NUMERICAL INVESTIGATION OF INTERNAL EROSION IN GRANULAR SOILS: FROM MICRO TO MACRO

ZHOU CHUANG

PhD

The Hong Kong Polytechnic University

This programme is jointly offered by The Hong Kong Polytechnic University and Tongji University

2025

The Hong Kong Polytechnic University

Department of Civil and Environmental Engineering

Tongji University

Department of Geotechnical Engineering

Numerical Investigation of Internal Erosion In Granular Soils: From Micro To Macro

Zhou Chuang

A thesis submitted in partial fulfilment of the requirements for the degree of

Doctor of Philosophy

September 2025

CERTIFICATE OF ORIGINALITY

I hereby declare that this thesis is my own work and that, to the best of my knowledge and belief, it reproduces no material previously published or written, nor material that has been accepted for the award of any other degree of diploma, except where due acknowledgement has been made in the text.

Signature:

Name: ZHOU CHUANG

Abstract of thesis entitled

Numerical Investigation of Internal Erosion in Granular Soils: From Micro to Macro

Internal erosion in sandy soils is a prevalent engineering hazard in which fine particles are transported and lost through the pore spaces of the soil skeleton under seepage flow, ultimately leading to soil deformation and structural failure. Given its multi-field, multi-phase, and multi-scale nature, internal erosion presents significant research challenges. To elucidate the micro- to macro-scale mechanisms governing erosion, this study systematically investigates particle migration behavior using a cross-scale approach, integrating Computational Fluid Dynamics-Discrete Element Method (CFD-DEM) and Finite Element Method (FEM). First, microscopic particle erosion mechanics are examined at the small-scale Representative Volume Element (RVE) level, accounting for the influence of soil stress anisotropy and fabric anisotropy. Building on these insights, the internal erosion processes and structural mechanical response of a water-soil-tunnel system are further investigated through a meso-scale CFD-DEM-FEM boundary value model, identifying key factors affecting system stability. Additionally, a novel erosion law is proposed based on CFD-DEM simulations, and a coupled seepage-erosion-mechanics numerical analysis method is developed within the framework of four-constituent medium theory. Finally, leveraging ABAQUS UEL subroutine development, this study enables large-scale numerical analysis of dam seepage erosion. By bridging discrete and continuum media and connecting microscopic particle behavior to macroscopic engineering responses, this research achieves a comprehensive cross-scale investigation of internal erosion, advancing both theoretical understanding and practical applications in geotechnical engineering.

LIST OF PUBLICATIONS DURING THE CANDIDATURE

Journal Papers

Zhou C, Qian J G, Yin Z Y. Microscopic investigation of the influence of complex stress states on internal erosion and its impacts on critical hydraulic gradients[J]. International Journal for Numerical and Analytical Methods in Geomechanics, 2022, 46(18): 3377-3401.

Zhou C, Qian J G, Yin Z Y, et al. Suffusion in gap-graded granular soils subjected to strain-controlled cyclic loading with coupled CFD-DEM method[J]. Transportation Geotechnics, 2023, 42: 101098.

ZHOU C, QIAN J, YIN Z. Computational fluid dynamics-discrete element fluid-solid coupling analysis on suffusion in anisotropic sandy soils[J]. Rock and Soil Mechanics, 2024, 45(1): 9.

Zhou C, Qian J G, Yin Z Y, et al. Effect of particle shape and bedding angle on suffusion in gap-graded granular soils by coupled CFD-DEM method[J]. International Journal for Numerical and Analytical Methods in Geomechanics, 2023, 47(8): 1373-1398.

Zhou C, Qian J G, Cheng M Y. Microscopic investigation on suffusion in granular soil subject to cyclic hydraulic reversal using CFD-DEM[J]. European Journal of Environmental and Civil Engineering, 2025: 1-28.

Zhou C, Qian J G, Yin Z Y et al. Novel erosion law based on CFD-DEM simulations and its application in hydromechanical modeling of gap-graded soils [J]. Canadian Geotechnical Journal. (Accepted)

Qian J G, **Zhou C**, Yin Z Y, et al. Investigating the effect of particle angularity on suffusion of gap-graded soil using coupled CFD-DEM[J]. Computers and Geotechnics, 2021, 139: 104383.

ACKNOWLEDGEMENTS

My doctoral journey at The Hong Kong Polytechnic University has been an invaluable and unforgettable experience. I am deeply grateful to all those who supported and accompanied me throughout this extraordinary chapter of my life.

First and foremost, I would like to express my sincerest gratitude to my supervisors, Professor Zhenyu Yin and Professor Jiangu Qian. Professor Yin's visionary guidance provided a clear direction for my research, and his unwavering dedication and passion for academic excellence have profoundly shaped not only my PhD work but also my future aspirations as a researcher. I am equally indebted to Professor Jiangu Qian for his meticulous mentorship over the years. From him, I have learned not only rigorous problem-solving methodologies but also the essence of critical thinking. His insightful revisions of my papers have greatly refined my academic writing, leaving an enduring impact on my scholarly development. Without their collective wisdom, encouragement, and support, the successful completion of this research would not have been possible.

I also extend my heartfelt thanks to my friends and colleagues at PolyU and Tongji University, whose camaraderie made my PhD journey both enriching and joyful. Their companionship brought balance and warmth to my academic pursuits. Finally, I reserve my deepest appreciation for my family and my girlfriend, whose unconditional love, patience, and understanding have

been my steadfast foundation. Their unwavering belief in me allowed me to dedicate myself fully to this endeavor without distraction.

TABLE OF CONTENTS

CHAPTER 1 INTRODUCTION **1**

1.1 Background **1**

1.2 Research objectives and methodologies **4**

1.3 Structure of the thesis **6**

CHAPTER 2 LITERATURE REVIEW **11**

2.1 Introduction **11**

2.2 DEM-based solid-liquid coupling numerical method **11**

2.3 Unresolved CFD-DEM method **14**

2.3.1 Governing equations for DEM 15

2.3.2 Governing equations for CFD 15

2.3.3 Fluid-particle interaction force 16

2.3.4 Coupling scheme of CFD–DEM 18

2.4 Application of CFD-DEM in RVE study about suffusion within the discrete media framework **18**

2.4.1 Effect of fine content 19

2.4.2 Effect of gap ratio 21

2.4.3 Effect of particle shape 22

2.4.4 Effect of hydraulic gradient 23

2.4.5 Effect of other factors 25

2.5 Application of CFD-DEM in BVP study about suffusion within the discrete media framework **27**

2.6 Numerical study of macroscopic suffusion under the continuum mechanics framework **29**

2.7 Summary **33**

CHAPTER 3 SUFFUSION MECHANISM UNDER ANISOTROPIC STRESS CONDITIONS **45**

3.1 Introduction **45**

3.2 Simulation of suffusion under anisotropic stress conditions **46**

3.2.1 Model setup 46

3.2.2 Simulation procedure of suffusion 49

3.3 Numerical Results and Discussion **50**

3.3.1 Mass loss of fine particles 50

3.3.2 Variation in void ratio 52

3.3.3 Critical hydraulic gradient 53

3.4 Microscopic analysis and mechanism **56**

3.4.1 Response of hydraulic drag force and contact force 56

3.4.2 Anisotropy of contact force 57

3.4.3 Response of coordination numbers 59

3.4.4 Erosion path and strong force chain network 62

3.5 Summary **64**

CHAPTER 4 INVESTIGATION ON INFLUENCE OF PARTICLE FABRIC ANISOTROPY ON SUFFUSION **80**

4.1 Introduction **80**

4.2 Suffusion simulation scheme for fabric anisotropic soil **81**

4.2.1 Model setup 81

4.3 Numerical results and discussion **83**

4.3.1 Cumulative eroded mass loss 83

4.3.2 Fine particles distribution 84
4.3.3 Soil deformation 86
4.3.4 Void ratio variation 86
4.3.5 Variation of hydraulic conductivity 88
4.3.6 Soil mechanical response to suffusion 89
4.3.7 Force chain networks 90
4.3.8 Variations in microscopic anisotropic parameters 92
4.3.9 Investigation of erosion law from a microscopic point of view 92
4.4 Summary 94
CHAPTER 5 STUDY ON TUNNEL SEEPAGE EROSION AND MECHANICAL RESPONSE BASED ON CFD-DEM-FEM 107
5.1 Introduction 107
5.2 Calculation framework of CFD-DEM-FEM method 109
5.3 Geometric conditions and simulation setup 111
5.3.1 Model geometric conditions 111
5.3.2 Simulation programe 114
5.4 Simulation results and discussions 117
5.4.1 The influence of crack size 117
5.4.2 The influence of crack position 123
5.4.3 The influence of burial depth and water level 125
5.5 Structure response to seepage erosion 129
5.6 Summary 132
CHAPTER 6 CFD-DEM-BASED CONTINUUM MODEL FOR SEEPAGE-EROSION-

MECHANICS COUPLING 160

6.1 Introduction 160

6.2 CFD-DEM simulations and novel erosion law 161

6.2.1 Testing soils and schemes 162

6.2.2 Results of the fines mass loss 163

6.2.3 The model of fines mass loss 164

6.3 Continuous medium theory framework for seepage-erosion-mechanical coupling 166

6.3.1 Four constituents model 167

6.3.2 Implementation of erosion law 170

6.3.3 Critical state-based and fines-dependent mechanical model 171

6.3.4 The establishment of framework for the coupling of seepage-erosion-mechanics 176

6.4 Validation and discussion 178

6.4.1 Description of laboratory suffusion tests 178

6.4.2 Comparison between simulations and experiments 180

6.5 Influence of soil initial state on suffusion response 183

6.6 Soil mechanical response subjected to suffusion 185

6.7 Summary 186

CHAPTER 7 FINITE ELEMENT SIMULATION OF INTERNAL EROSION IN LARGE-SCALE DAMS BASED ON ABAQUS 201

7.1 Introduction 201

7.2 Hydro-mechanical coupling governing equations 201

7.3 The derivation of the finite element form of the governing equations 203

7.4 Simulation of internal erosion in dams 207

7.5 Results and discussion 208

7.6 Summary 210

CHAPTER 8 FINDINGS, CONCLUSIONS, AND RECOMMENDATIONS 216

8.1 Findings and conclusions 216

8.1.1 Effect of initial stress anisotropy on suffusion 217

8.1.2 Effect of initial fabric anisotropy on suffusion 218

8.1.3 Soil-water-structure seepage erosion model 219

8.1.4 Seepage-erosion-mechanics coupling framework 220

8.1.5 ABAQUS simulations for internal erosion 221

8.2 Recommendations for future studies 222

REFERENCE 225

LIST OF FIGURES

Figure 1.1 Different manifestations of internal erosion 9

Figure 1.2 Geological disasters caused by internal erosion: (a) Erosion in dams; (b) Debris flow; (c) Tunnel leakage; (d) Ground subsidence 9

Figure 1.3 Outline of the research content in the thesis 10

Figure 2.1 Algorithm flowchart of CFD-DEM coupling 35

Figure 2.2 Contributory factors to suffusion (after Shire et al. (2014)) 35

Figure 2.3 Schematic diagram of the RVE suffusion model (after Liu et al. (2020)) 36

Figure 2.4 The influence of fine content on mass loss. 36

Figure 2.5 The evolution of local packings during suffusion for underfilled and overfilled samples: (a) Underfill: before suffusion; (b) Underfill: after suffusion; (c) Overfill: before suffusion; (d) Overfill: after suffusion 37

Figure 2.6 Fines clogging in pore channel for different gap ratios. (after Xie et al. (2023)) 37

Figure 2.7 The influence of gap ratio on mass loss 38

Figure 2.8 Internal pore structure captured by MIS (adapted from Chen et al.(2023a)): (a) Gap ratio=3.0; (b) Gap ratio=5.4; (c) Gap ratio=11.2 38

Figure 2.9 CFD-DEM models with shaped particles (a): models considering particle aspect ratio (after Xiong et al. (2021)); (b): models considering particle angularity (after Qian et al. (2021b)) 39

Figure 2.10 The influence of particle shape on mass loss: (a) Effect of aspect ratio; (b) Effect of angularity 39

Figure 2.11 Particle trajectory in the non-spherical sample (after Qian et al. (2021b)).....40

Figure 2.12 The influence of hydraulic gradient on mass loss.....40

Figure 2.13 Fluid streamline of samples with different hydraulic gradients (after Mu et al. (2023)) 41

Figure 2. 14 The coupled CFD-DEM suffusion model for hollow cylinder torsional shear test (after Song et al. (2024)) 41

Figure 2.15 Variation of eroded mass with rotation of the major principal stress axis (α) and intermediate principal stress ratio (*b*) (after Song et al. (2024)) 42

Figure 2.16 Eroded mass under different confining pressure and fines content (after Wang et al.(2022)) 42

Figure 2.17 Model of tunnel erosion (after Ibrahim and Meguid, (2023)) 43

Figure 2.18 (a) two-phase three-component mixture, (b) two-phase four-component mixture, (c) three-phase five-component mixture, (d) conceptual representation of a three-phase five-component mixture.....43

Figure 2.19 Scheme of the dike-on-foundation with a cavity located at the bottom. 44

Figure 2.20 Contours of (a) equivalent plastic shear strain and (b) erodible fines mass fraction (after Lei et al. (2020)) 44

Figure 3.1 Schematic of seepage flow along with different principal stresses in a dam 68

Figure 3.2 Particle size distribution curves for the tested soil 68

Figure 3.3 Assessment of unstable soils for samples used in this study by the Burenkova method 68

Figure 3.4 Stress states adopted in simulations 69

Figure 3.5 The imposed hydraulic gradient in CFD-DEM simulations 69

Figure 3.6 CFD-DEM simulation model 70

Figure 3.7 Schematic diagram of fines loss: (a) before suffusion; (b) after suffusion 70

Figure 3.8 Evolution of fines loss versus time 71

Figure 3.9 Ultimate fines loss under different stress ratios 71

Figure 3.10 Different layers of the specimen 72

Figure 3.11 Distribution of the void ratio: (a) $\sigma_r = 50\text{kPa}$; (b) $\sigma_r = 100\text{kPa}$; (c) $\sigma_r = 150\text{kPa}$ 72

Figure 3.12 Determination of the critical hydraulic gradient 73

Figure 3.13 Relationships between the initial hydraulic gradient and the shear stress ratio 73

Figure 3.14 Relationships between the initial hydraulic gradient and the initial void ratio 73

Figure 3.15 The evolution of total drag force and contact force at z-direction 74

Figure 3.16 Characterization of Particle Contact Orientation in 3D Space 74

Figure 3.17 Contact fabric information for specimens under (1st row of T1-D0-CP50; 2nd row of T2-D1-CP50-1; 3rd row of T4-D3-CP50-1;1st column for contact number; 2nd column for normal contact force): (a) $\alpha_c = 0.071$; (b) $\alpha_c = 0.094$; (c) $\alpha_c = 0.067$; (d) $\alpha_n = 0.029$; (e) $\alpha_n = 0.278$; (f) $\alpha_n = 0.174$ 75

Figure 3.18 Evolution of parameters defining the magnitude and principal direction of anisotropy during suffusion: (a) α_n ; (b) β_n 76

Figure 3.19 Evolution of force chains: (a) overall force chain distribution(*t*=0s); (b) local force chains (*t*=0s); (c) local force chains (*t*=6s); (d) local force chains (*t*=12s) 76

Figure 3.20 Evolution of particle connectivity 77

Figure 3.21 Evolution of coordination number with elapsed time: (a)T1-D0-CP50; (b) T4-D3-CP50-1;(c) T2-D1-CP50-1 77

Figure 3.22 Erosion path of fine particles: (a) T1-D0-CP50; (b) T2-D1-CP50-1; (c) T4-D3-CP50-1 78

Figure 3.23 Distribution of strong contact force: (a) T1-D0-CP50; (b) T2-D1-CP50-1; (c) T4-D3-CP50-1 79

Figure 4.1 Particle shape adopted in CFD-DEM 97

Figure 4.2 Definition of bedding angle 97

Figure 4.3 Generation of fabric anisotropic soils: (a) generating particles with fixed orientations and applying a pressure of 10kPa; (b) unlocking particle rotation and applying a pressure of 100kPa..... 98

Figure 4.4 3D orientation of coarse particles: (a)bedding angle=0°; (b) bedding angle=30°; (c) bedding angle=60°; (d) bedding angle=90°; (e) bedding angle=Isotropy..... 98

Figure 4.5 The diagram of soil suffusion 98

Figure 4.6 Loss of fine particles with elapsed time for samples with different bedding angles and aspect ratios: (a) aspect ratio=1.5; (b) aspect ratio=2.0 99

Figure 4.7 Comparison of ultimate mass loss for samples with different bedding angles..... 99

Figure 4.8 Distribution of particles: (a) simulated samples; (b)selected particle plane; (c) microscopic particle arrangement 99

Figure 4.9 Contours of fine content at different points for samples with AS=1.5 both before and

after erosion (the specific plane is x=0): (a) bedding angle=0°; (b) bedding angle=30°; (c) bedding angle=60°; (d) bedding angle=90°; (e) bedding angle=Isotropy..... 101
Figure 4.10 Comparison of fine particle distribution along with Z position: (a) bedding angle=0°; (b) bedding angle=30°; (c) bedding angle=60°; (d) bedding angle=90°; (e) bedding angle=Isotropy..... 101
Figure 4.11 Axial strain for samples with different bedding angles: (a) AR=1.5; (b) AR=2.0 102
Figure 4.12 Variation of e, e_c, e_f for samples with AS=1.5 at different bedding angles: (a) bedding angle=0°; (b) bedding angle=30°; (c) bedding angle=60°; (d) bedding angle=90°; (e) bedding angle=Isotropy..... 102
Figure 4.13 Hydraulic conductivity versus simulation time 103
Figure 4.14 Typical fine particle migration of different specimens 103
Figure 4.15 Fine particle trajectory: (a) particle trajectory of Mode I; (b) particle trajectory of Mode II; (c) particle trajectory of Mode III..... 103
Figure 4.16 Variation of strength and deformation characteristics expressed by stress ratio (deviatoric stress over mean effective stress) versus axial strain and volumetric strain versus axial strain: (a) before suffusion; (b) after suffusion..... 104
Figure 4.17 Peak stress ratio of samples with different bedding angles: (a) AR=1.5; (b) AR=2.0 104
Figure 4.18 Strong force chains network 105
Figure 4.19 Contributions to strong contact force by different contact types: (a) before suffusion; (b) after suffusion; (c) after triaxial shear 105

Figure 4.20 Evolution of soil fabric anisotropy: (a)-(b): during suffusion; (c)-(d): during triaxial shear 106

Figure 4.21 λ_e from CFD-DEM results: (a) Aspect ratio=1.5; (b) Aspect ratio=2.0 106

Figure 5.1 Algorithm flowchart of CFD-DEM-FEM coupling 136

Figure 5.2 Contact force on the tunnel element: (a) tunnel mesh with tetrahedral element; (b) contact between particle and trilateral element 137

Figure 5.3 Particle size distribution (PSD) curves of HK-CDG and enlarged PSD used in simulation 137

Figure 5.4 Simplified modeling of cracks between tunnel linings 138

Figure 5.5 Setup of the simulated numerical model: (a) configuration of the tunnel erosion model; (b) the definition of crack position angles 138

Figure 5.6 Setup of the fluid domain: (a) mesh part and boundary condition for CFD; (b) fluid velocity field 139

Figure 5.7 Distribution of initial void ratio 139

Figure 5.8 Process of tunnel excavation 140

Figure 5.9 The distribution of soil effective stress: (a) analytical distribution; (b) simulated results; (c)stress distribution after excavation 140

Figure 5.10 Analytical solution for tunnel pressure 141

Figure 5.11 Comparison of tunnel pressure distribution between analytical solution and simulation results: (a) analytical solution; (b) simulation results 141

Figure 5.12 Particle loss for different crack widths: (a) Crack width= $1.1d_{\max}$; (b) Crack width=

$1.2d_{max}$;(c) Crack width=$1.3d_{max}$; (d) Crack width=$1.4d_{max}$;(e) Crack width=$1.5d_{max}$ 142

Figure 5.13 Eroded mass loss versus simulation time for different crack widths..... 142

Figure 5.14 Final mass loss versus crack width 142

Figure 5.15 Particle trajectory during erosion for different crack widths: (a) Crack width=$1.1d_{max}$; (b) Crack width=$1.2d_{max}$;(c) Crack width=$1.3d_{max}$; (d) Crack width=$1.4d_{max}$;(e) Crack width=$1.5d_{max}$ 143

Figure 5.16 Distribution of soil displacement contour for different crack widths: (a) Crack width=$1.2d_{max}$; (b) Crack width=$1.3d_{max}$; (c) Crack width=$1.4d_{max}$; (d) Crack width=$1.5d_{max}$ 144

Figure 5.17 Surface displacement for different crack widths: (a) Crack width=$1.1d_{max}$; (b) Crack width=$1.2d_{max}$;(c) Crack width=$1.3d_{max}$; (d) Crack width=$1.4d_{max}$;(e) Crack width=$1.5d_{max}$ 145

Figure 5.18 Maximum displacement versus erosion time for different crack widths. 145

Figure 5.19 Distribution of fine content after erosion: (a) Initial state (b) Crack width=$1.1d_{max}$; (c) Crack width=$1.2d_{max}$; (d) Crack width=$1.3d_{max}$; (e) Crack width=$1.4d_{max}$; (f) Crack width=$1.5d_{max}$ 146

Figure 5.20 Distribution of soil effective stress for different crack widths: (a) Crack width=$1.1d_{max}$; (b) Crack width=$1.2d_{max}$;(c) Crack width=$1.3d_{max}$; (d) Crack width=$1.4d_{max}$;(e) Crack width=$1.5d_{max}$ 147

Figure 5.21 Soil contact force chain and soil arch effect: (a) $t=0$; (b) $t=1\text{s}$; (c) $t=2\text{s}$; (d) $t=5\text{s}$; (e) $t=10\text{s}$ 147

Figure 5.22 Contact force chain distribution in samples with different crack widths: (a) Crack width=$1.1d_{max}$;(c) Crack width=$1.3d_{max}$; (d) Crack width=$1.4d_{max}$;(e) Crack width=$1.5d_{max}$ 148

Figure 5.23 Distribution of normal contact for different crack widths: (a) Initial state; (b) Crack width=$1.1d_{max}$;(c) Crack width=$1.2d_{max}$;(d) Crack width=$1.3d_{max}$;(e) Crack width=$1.4d_{max}$;(f) Crack width=$1.5d_{max}$ 148

Figure 5.24 Particle loss with varying crack positions: (a) $\theta_a = 0^\circ$; (b) $\theta_a = 45^\circ$; (c) $\theta_a = 90^\circ$;(d) $\theta_a = 135^\circ$;(e) $\theta_a = 180^\circ$ 149

Figure 5.25 Eroded mass loss versus simulation time for different crack positions 150

Figure 5.26 The force on the particles during erosion 150

Figure 5.27 Particle trajectory during erosion for different opening angles: (a) $\theta_a = 0^\circ$;(b) $\theta_a = 45^\circ$;(c) $\theta_a = 90^\circ$;(d) $\theta_a = 135^\circ$;(e) $\theta_a = 180^\circ$ 151

Figure 5.28 Surface displacement for different opening angles: (a) $\theta_a = 0^\circ$; (b) $\theta_a = 45^\circ$; (c) $\theta_a = 90^\circ$;(d) $\theta_a = 135^\circ$;(e) $\theta_a = 180^\circ$ 152

Figure 5.29 Maximum displacement versus erosion time for different crack positions. 152

Figure 5.30 Distribution of soil effective stress for different opening angles: (a) $\theta_a = 0^\circ$; (b) $\theta_a = 45^\circ$; (c) $\theta_a = 90^\circ$;(d) $\theta_a = 135^\circ$;(e) $\theta_a = 180^\circ$ 153

Figure 5.31 Contact force chain distribution in samples with different crack positions: (a) $\theta_a = 0^\circ$; (b) $\theta_a = 45^\circ$; (c) $\theta_a = 90^\circ$;(d) $\theta_a = 135^\circ$;(e) $\theta_a = 180^\circ$ 153

Figure 5.32 Particle loss for different burial depths and water levels: (a) Burial depth=$1.0d_T$; (b) Burial depth=$1.5d_T$; (c) Burial depth= $2.0d_T$;(d) Water level= $0.5b_d$;(e) Water level=$1.0b_d$;(f)

Water level=$1.5b_d$ 154

Figure 5.33 Eroded mass loss versus simulation time: (a) Different burial depths; (b) Different water levels..... 154

Figure 5.34 Particle trajectory during erosion for different burial depths and water levels: (a) Burial depth= $1.0d_T$; (b) Burial depth= $1.5d_T$; (c) Burial depth= $2.0d_T$;(d) Water level= $0.5b_d$;(e) Water level=$1.0b_d$;(f) Water level=$1.5b_d$ 155

Figure 5.35 Surface displacement for different burial depths and water levels: (a) Burial depth= $1.0d_T$; (b) Burial depth= $1.5d_T$; (c) Burial depth= $2.0d_T$;(d) Water level= $0.5b_d$;(e) Water level=$1.0b_d$;(f) Water level=$1.5b_d$ 155

Figure 5.36 Maximum displacement versus erosion time for different burial depths and water levels: 156

Figure 5.37 Distribution of soil effective stress for different burial depths and water levels: (a) Burial depth= $1.0d_T$; (b) Burial depth= $1.5d_T$; (c) Burial depth= $2.0d_T$;(d) Water level= $0.5b_d$;(e) Water level=$1.0b_d$;(f) Water level=$1.5b_d$ 156

Figure 5.38 Contact force chain distribution in samples with different burial depths and water levels: (a) Burial depth=$1.0d_T$; (b) Burial depth=$1.5d_T$; (c) Burial depth= $2.0d_T$;(d) Water level= $0.5b_d$;(e) Water level=$1.0b_d$;(f) Water level=$1.5b_d$ 157

Figure 5.39 Mechanical response of tunnel with different crack widths: (a) Convergent deformation; (b) Normal stress of tunnel (crack width=$1.4d_{\max}$)..... 157

Figure 5.40 Mechanical response of tunnel with different crack positions: Convergent deformation: $\theta_a = 45^\circ$; (b) Normal stress: $\theta_a = 45^\circ$; (c) Convergent deformation: $\theta_a = 90^\circ$; (d)

Normal stress: $\theta_a = 90^\circ$; (e) Convergent deformation: $\theta_a = 135^\circ$; (f) Normal stress: $\theta_a = 135^\circ$; (d) Convergent deformation: $\theta_a = 180^\circ$; (h) Normal stress: $\theta_a = 180^\circ$ 158

Figure 5.41 Mechanical response of tunnel with different burial depths: (a) Convergent deformation; (b) Normal stress of tunnel (burial depth=1.0 D_t)..... 159

Figure 5.42 Mechanical response of tunnel with different water levels: (a) Convergent deformation; (b) Normal stress of tunnel (water level=1.5 H_s) 159

Figure 6.1 Grain-size distribution of soils in this study and experiment 191

Figure 6.2 Illustration of CFD-DEM model..... 191

Figure 6.3 Fine particle mass loss ratio for samples under different: (a)confining pressure; (b) hydraulic gradient; (c) stress ratio 192

Figure 6.4 The fitting curve of ultimate mass loss ratio for different: (a) seepage velocity; (b) confining pressure; (c) stress ratio 192

Figure 6.5 Fitting results of mass loss ratio versus time for cases under different: (a) seepage velocity; (b) confining pressure; (c) stress ratio..... 193

Figure 6.6 PSD of soils and suffusion samples in the study of Liang et al.(Liang et al., 2017b) 193

Figure 6.7 Comparison of results from experiments and fitting 194

Figure 6.8 Simplified modeling of saturated soils: (a) Mesoscale REV; (b) two-constituents continuum model; (c) four-constituents continuum model 194

Figure 6.9 Seepage-Erosion-Mechanics coupling calculation flowchart..... 195

Figure 6.10 Triaxial Seepage Erosion Testing Equipment(Chang and Zhang, 2011): (a) Triaxial

tesing system; (b) Water supply system; (c) Soil collection system; (d) Water collection system 195
Figure 6.11 Hydraulic gradient applied during suffusion tests 196
Figure 6.12 Deformation of specimen before and after suffusion (Chang and Zhang (Chang and Zhang, 2013b)) 196
Figure 6. 13 Determination of simulation parameters: (a) Determination of mechanical parameters; (b) Determination of CLS parameters 196
Figure 6.14 Comparison between experiments and numerical simulations: (a) cumulative mass; (b) evolution of hydraulic conductivity; (c) axial strain; (d) radial strain 197
Figure 6.15 Comparison of different erosion laws: (a) Eroded soil mass; (b)Hydraulic conductivity 197
Figure 6.16 Cumulative mass loss for sample with different (a) void ratio; (b) friction angle; (c) fine content; (d) size ratio 198
Figure 6.17 Results of drained triaxial tests for samples with different void ratios before and after erosion: (a,c) deviatoric stress versus axial strain; (b,d) void ratio versus axial strain 199
Figure 6.18 Results of drained triaxial tests for samples with different fine contents before and after erosion: (a,c) deviatoric stress versus axial strain; (b,d) void ratio versus axial strain. 200
Figure 7.1 8-node plane strain element 212
Figure 7.2 Diagram of FEM numerical model 213
Figure 7.3 Variation of fine content f_c during erosion : (a) Day=150; (b) Day=250; (c) Day=300;

(d) Day=350 213

Figure 7.4 Variation in soil displacement during erosion (m) (Deformation amplification factor =250): (a) Day=150; (b) Day=250; (c) Day=300; (d) Day=350 213

Figure 7.5 Changes in fine content and displacement at element nodes during erosion: (a) Fine content; (b) Displacement 214

Figure 7.6 Variation in shear strain during suffusion: (a) Day=150; (b) Day=250; (c) Day=300; (d) Day=350 215

LIST OF TABLES

Table 2.1 Comparison of different fluid/DEM modeling methods 34

Table 3.1 Summary of the simulated stress conditions 66

Table 3.2 Input parameters used in the simulation 67

Table 4.1 Summary of numerical simulation samples 97

Table 5.1 Summary of simulation scheme 135

Table 5.2 Parameters used in the simulation 135

Table 6.1 Summary of model parameters 189

Table 6.2 Summary of simulation samples 189

Table 6.3 Parameters of the mass loss ratio model 189

Table 6.4 Parameters used in the hydramechanical model 190

Table 7.1 The parameters of the numerical model 212

CHAPTER 1 INTRODUCTION

1.1 Background

Internal erosion is a common geological hazard in water-rich strata. It originates under conditions of heavy rainfall or infiltration, where cohesionless soil particles are transported and flow through the pores of the soil matrix, leading to internal particle loss. According to the research by Fell and Fery (2007), internal erosion in soils can be classified into four main types: concentrated leakage, backwards erosion, suffusion, and contact erosion. Figure 1.1 illustrates the possible forms of internal erosion that may occur at different locations in a dam.

According to Foster et al. (2000), approximately 46% of dam failures are initiated by suffusion, which is a specific form of internal erosion characterized by the migration of fine particles through the pore spaces of a coarse-grained soil matrix under seepage flow. This phenomenon predominantly occurs in gap-graded or widely graded soils, which exhibit a bimodal particle size distribution comprising distinct coarse and fine fractions. Such soil types are commonly encountered in embankment foundations, rockfill dam filters, and gravel-packed sand control layers used in oil and gas extraction. The loss of fine particles not only weakens the soil structure and reduces its strength but can also lead to local particle accumulation, decreasing the soil's permeability while increasing excess pore water pressure and reducing effective stress, thereby compromising stability. Furthermore, as continued erosion enlarges internal voids, suffusion may progress into piping, ultimately resulting in catastrophic soil failure. This process can induce severe engineering disasters, including dam breaches, debris flows, and ground subsidence (Al-

Saigh et al., 1994; Crosta and Prisco, 1999; Sheorey et al., 2000; Yoo, 2017; Albaba et al., 2019; Kong et al., 2021), as illustrated in Figure 1.2. Given its critical role in geotechnical hazards, this study focuses specifically on suffusion. Unless otherwise stated, the terms "internal erosion" and "seepage erosion" hereafter refer exclusively to suffusion.

Suffusion-related hazards pose significant research challenges due to their inherently multi-phase, multi-field, and multi-scale characteristic (Xiong et al., 2020). First, suffusion encompasses both microscale fluid-solid interactions at the particle level and macroscale soil deformation. Second, its occurrence necessitates a comprehensive understanding of the coupled hydraulic behavior and the mechanical interactions between soil particles. Furthermore, as suffusion involves the migration of grains, the soil exhibits the distinct features of granular media, requiring consideration of its discrete nature. However, in conventional soil mechanics theory, soil is typically modeled as a continuum. This assumption limits the ability of traditional theories and experiments to quantitatively capture localized particle transport and interactions within pore structures. These fundamental scientific limitations significantly hinder a deeper understanding of the mechanisms underlying suffusion and present substantial theoretical and technical barriers to the accurate prediction and effective mitigation of suffusion-induced hazards.

With the rapid advancement of numerical computation methods, a range of innovative numerical algorithms has emerged, offering new avenues for investigating suffusion. Among them, the Discrete Element Method (DEM), proposed by Cundall and Strack (1979), is grounded in a

micromechanical theoretical framework. DEM represents soil as an assembly of discrete particles and governs their motion and displacement through Newton's laws of motion combined with refined contact force models. This microscale numerical approach is particularly well-suited for capturing the inherent discreteness of granular systems. As such, it is highly effective in describing the dynamic behavior of particle migration during seepage-induced suffusion. By leveraging DEM, researchers can track and quantitatively characterize the spatiotemporal evolution of suffusion processes.

Building on this foundation, researchers have integrated fluid-phase modeling techniques, such as Computational Fluid Dynamics (CFD) (Hu et al., 2023; Tang et al., 2023; Xu et al., 2025; Zeng et al., 2025), Smoothed Particle Hydrodynamics (SPH) (Mao et al., 2022; Yu et al., 2023, 2024), and the Lattice Boltzmann Method (LBM) (Jäger et al., 2017; Stipić et al., 2022), with DEM to develop coupled fluid-solid algorithms capable of simulating suffusion. These coupling strategies effectively address the multi-field and multi-phase nature of the problem. However, due to the inherent computational complexity of DEM, the simulation scale remains limited to micro- or meso-scale domains (typically involving particle counts on the order of $10^5 - 10^6$, even under modern high-performance computing conditions. This limitation restricts the applicability of DEM-based approaches to real-world engineering problems, which often involve particle numbers on the order of 10^9 or higher (Alobaid et al., 2014; Brosh et al., 2014).

To overcome this limitation, researchers have turned to continuum-based numerical methods such as the Finite Element Method (FEM) and the Material Point Method (MPM) (Yerro et al., 2017; Shen et al., 2024; Qin et al., 2025). These approaches transform complex physical processes into solvable partial differential equations (PDEs), significantly enhancing computational efficiency and enabling the simulation of erosion problems at the engineering scale. However, the inherent assumption of soil as a continuum in these methods prevents the direct representation of critical micromechanical processes in suffusion, such as the transport and deposition of individual particles. This leads to a "scale-missing" problem. As a result, an effective multiscale numerical framework that bridges the gap between discrete microscale simulations and continuum-based macroscale engineering analysis for suffusion is still lacking.

1.2 Research objectives and methodologies

In order to enable a comprehensive micro-to-macro, cross-scale investigation of seepage-induced suffusion and advance the fundamental understanding of fine particle migration mechanisms in sandy soils, the following key issues are to be addressed:

(a) To investigate the suffusion evolution process in soils at the RVE scale under complex service conditions and provide micromechanical interpretations of the observed phenomena.

(b) To examine tunnel erosion phenomena and characterize the structural mechanical response to erosion at the mesoscopic scale

(c) To develop a novel erosion law incorporating stress-state effects on suffusion processes and implement it within the four-constituent theory framework to establish a coupled hydro-mechanical model.

(d) To establish a finite element analysis framework capable of simulating erosion processes and realizing large-scale investigations of suffusion in dams.

To achieve these research objectives, this thesis employs numerical modeling approaches implemented through the following methodology:

(a) To conduct a comprehensive literature review on numerical studies of suffusion in granular soils across multiple research scales.

(b) To establish CFD-DEM RVE models considering stress anisotropy and investigate the effects of complex stress states on suffusion evolution.

(c) To develop CFD-DEM RVE models incorporating initial soil fabric anisotropy and microscopically investigate the influence of bedding angle on suffusion behavior.

(d) To establish scaled-down BVP models of soil-water-tunnel systems using CFD-DEM-FEM and investigate the various factors that govern erosion development, as well as the structural mechanical response to erosion.

(e) To simulate soil suffusion under different stress states and hydraulic conditions using CFD-DEM, in order to formulate a new erosion law and integrate it with a fine-content-related constitutive model to achieve hydro-mechanical modeling.

(f) To develop an ABAQUS UEL subroutine for solving erosion governing equations and implement engineering-scale dam erosion models, enabling large-scale FEM analysis of internal erosion.

1.3 Structure of the thesis

This thesis comprises eight chapters, organized as follows:

Chapter 1 serves as the introduction, outlining the research background, objectives, methodologies, and the structure of the thesis.

Chapter 2 reviews existing research in numerical studies on suffusion, with a particular focus on unresolved CFD-DEM methodologies and their application to both RVE and BVP studies. The review further explores continuum-based numerical approaches for large-scale modeling of suffusion.

Chapter 3 presents a microscopic study of the influence of stress anisotropy on suffusion using CFD-DEM. The suffusion process under various initial stress states, including triaxial compression, triaxial extension, and isotropic confinement, is modeled. The simulation results are discussed in detail and interpreted from a microstructural perspective.

Chapter 4 uses CFD-DEM to explore the impact of fabric anisotropy on suffusion. In this study, the soil is modeled using ellipsoidal particles with specified bedding angles to replicate various soil fabrics. The chapter not only examines the evolution of suffusion but also investigates the mechanical response through triaxial test simulations under different bedding angles.

Chapter 5 establishes a water-soil-tunnel system using CFD-DEM-FEM to investigate tunnel erosion development and the structural mechanical response to erosion. The effects of various factors, including crack size, tunnel burial depth, crack position, and water levels, on the tunnel erosion process are examined. Tunnel convergence deformation and internal stress distribution are then analyzed through a finite element model.

Chapter 6 proposes a novel erosion law based on CFD-DEM simulations, considering soil stress state and hydraulic velocities. This erosion law is then integrated into a set of governing equations for suffusion, based on the four-constituent theory. Additionally, a fine-content-related critical state constitutive model is introduced to establish a hydro-mechanical framework. The

suffusion process is simulated using the proposed framework, and the results are compared with experimental data.

Chapter 7 develops an FEM framework for erosion simulations. The equations from Chapter 6 are solved using FEM through a secondary development ABAQUS UEL subroutine. The framework is then applied to establish a dam erosion model and facilitate large-scale analysis.

Chapter 8 summarizes the findings in this thesis and presents some recommendations for future research in the related area.

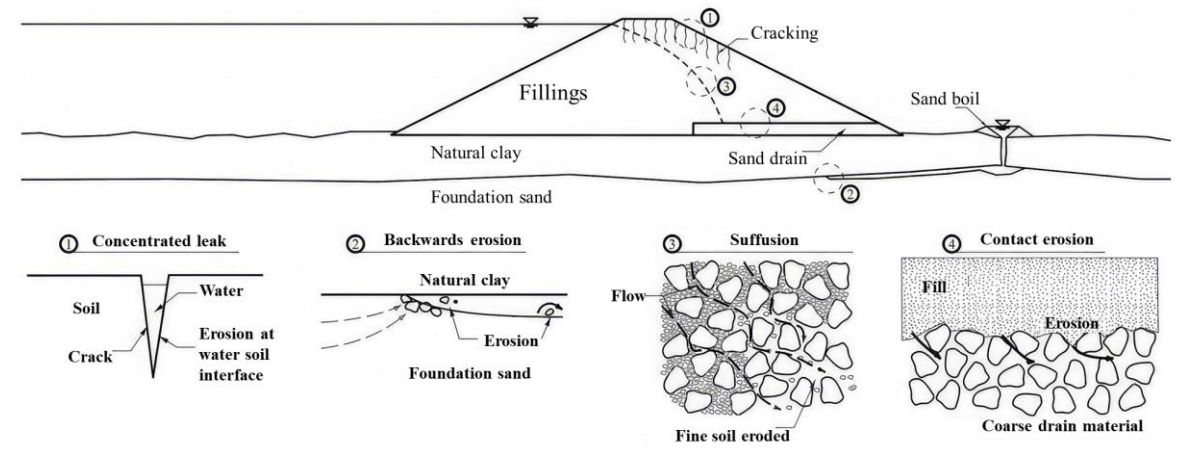

Figure 1.1 Different manifestations of internal erosion

(a)

(b)

(c)

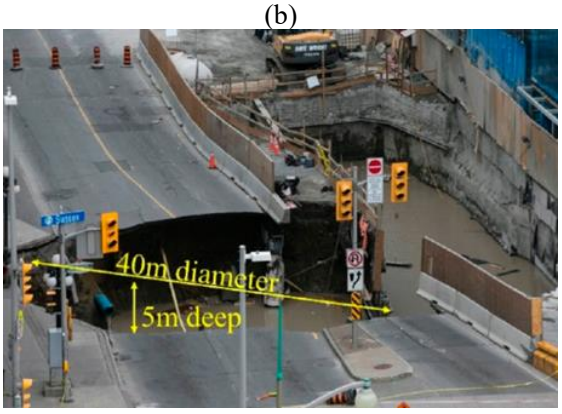

(d)

Figure 1.2 Geological disasters caused by internal erosion: (a) Erosion in dams; (b) Debris flow; (c) Tunnel leakage; (d) Ground subsidence

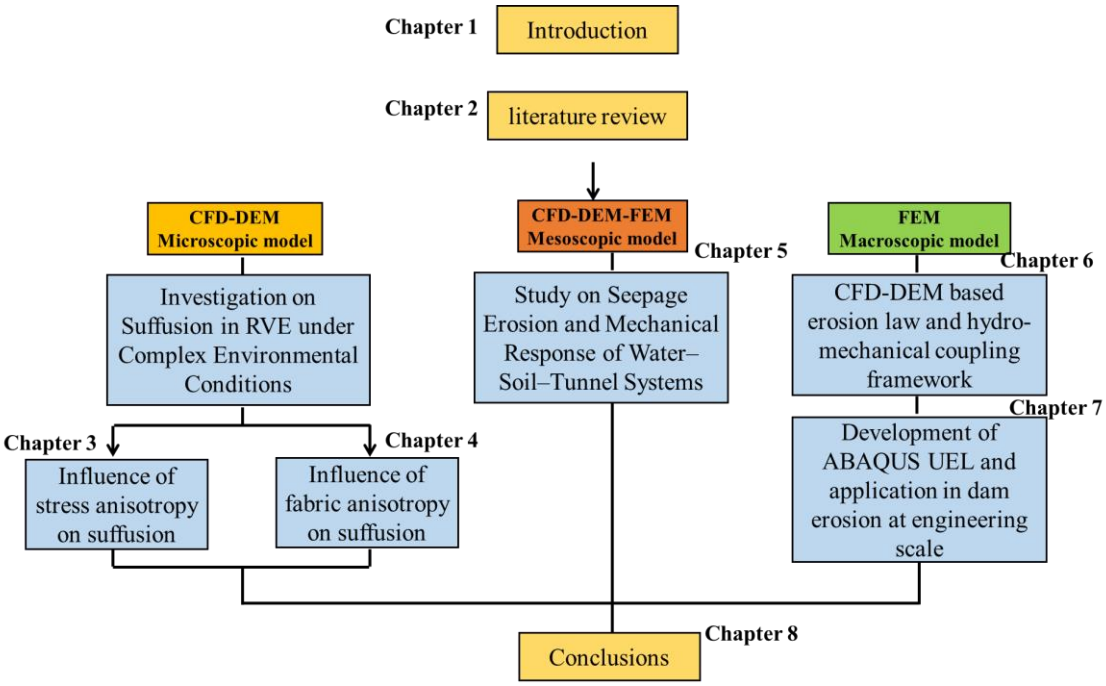

Figure 1.3 Outline of the research content in the thesis

CHAPTER 2 LITERATURE REVIEW

2.1 Introduction

This chapter presents a literature review of existing numerical investigations on suffusion. It begins by introducing and comparing commonly used fluid-solid coupling methods based on DEM. Next, the chapter synthesizes research on small-scale suffusion studies that employ RVE models within a discrete media framework. Subsequently, the review explores meso-scale BVP models, where DEM-based simulations investigate suffusion in complex, heterogeneous configurations. Finally, the chapter examines macroscopic suffusion modeling approaches grounded in continuum mechanics.

2.2 DEM-based solid-liquid coupling numerical method

DEM is a typical discontinuous numerical method to straightforwardly represent the nature of granular soils. By incorporating various fluid representation methods, the coupled fluid-DEM technique enables hydromechanical calculations. Current numerical simulation algorithms for soil-fluid coupling primarily include coupled CFD-DEM (Computational Fluid Dynamics-Discrete Element Method), SPH-DEM (Smooth Particle Hydrodynamics-Discrete Element Method), and LBM-DEM (Lattice Boltzmann Method- Discrete Element Method).

The coupled CFD-DEM method acquires the motions of particles and fluids in solid and fluid domains, respectively, by solving distinct governing equations and assessing their interactions (Kloss et al., 2012). This method can be further categorized into unresolved, fully resolved, and semi-resolved methods, based on the solution accuracy and the size of the fluid domain mesh

(Golshan et al., 2020). In the unresolved method, the flow around each particle is not explicitly resolved. Instead, the fluid velocity and pressure are volume-averaged within a local domain through the solution of locally averaged Navier-Stokes equations. An empirical drag force model is then employed to estimate the interaction forces exerted on the particles. Consequently, the size of the fluid mesh must be larger than the particle size to satisfy the local averaging assumption (Jing et al., 2016). On the contrary, in the fully resolved model, the velocity and pressure are solved precisely based on the Navier-Stokes equations. During the fluid solution process, the particles are treated as no-slip boundaries for the flow. The interaction force is directly evaluated by the integration of the fluid stress over the boundary surface of the particle, obviating the need for empirical drag models. As a result, the fluid mesh size must be at least 8-10 times smaller than the particle diameter to meet the integration requirement (Shen et al., 2022). The semi-resolved method lies between the un-resolved and fully-resolved methods, employing different solution strategies for fluids at different locations. Its most distinguishing feature is the use of either empirical drag models or exact integrals to compute fluid-particle interaction forces, determined by particle size (Yang et al., 2019b).

The LBM-DEM coupling method combines the lattice Boltzmann method with DEM to simulate fluid-particle interactions. In LBM, the fluid is represented as a collection of discrete particles that move on a fixed lattice, with their motion governed by a set of collision rules. Unlike CFD methods that rely on solving complex partial differential equations, the LBM is based on the Boltzmann transport equation, which describes the evolution of the probability distribution

function of the fluid particles (Yang et al., 2021). This equation is solved numerically using a discrete lattice, and the fluid velocity and pressure are calculated from the distribution function. In LBM, the fluid region is divided into regular lattices, and the fluid phase is considered a set of (fictitious) particle ensembles located at the lattice nodes. Each particle set includes several particles, as an example in the D3Q19 (Indraratna et al., 2021) model commonly used in 3D calculations, where there are 19 particles at each lattice node. By solving particle collisions and flows, the simulation of fluid can be computed.

Smooth particle hydrodynamics (SPH) is a Lagrangian approach that represents fluid particles in a mesh-free manner. In contrast to the Eulerian method, such as CFD, where the fluid domain is discretized into a grid, SPH models the fluid as a collection of interacting particles with mass, position, and velocity (El Shamy and Sizkow, 2021). The kinetic equations of the particle group are solved in a Lagrangian framework, making SPH well-suited for simulating complex fluid systems with free surfaces, large deformations, and multiphase flows. SPH uses kernel interpolation theory to handle fluid variables (Dehnen and Aly, 2012; Markauskas et al., 2018). By applying kernel functions, the continuity and momentum conservation equations are interpolated in an averaged form and assigned to the particle points as well as to other particles within a specific interaction length (Sun et al., 2013).

In general, whether it is CFD-DEM, SPH-DEM, or LBM-DEM, all of these methods treat soil as a discrete material, and thus, their application to suffusion is carried out within the framework

of discrete media. The advantage of these approaches is that they accurately reflect the discrete nature of particle flow. On the other hand, the interaction between the fluid and the solid can be directly modeled through interaction forces, rather than relying on complex constitutive models. Additionally, the internal structural evolution of the soil during erosion can be reconstructed using DEM, which provides a way to explore the microscopic mechanisms of erosion that traditional experiments cannot address.

It should be noted that while the aforementioned methods are capable of simulating soil seepage erosion, they exhibit significant variations in computational accuracy and resource demands. Table 2.1 provides a comprehensive comparison of these numerical approaches across multiple aspects. As expected, there exists a trade-off between simulation fidelity and computational expense—higher accuracy typically entails greater computational costs. Among these methods, the unresolved CFD-DEM approach has emerged as the predominant technique for suffusion studies, owing primarily to its superior computational efficiency. The unresolved CFD-DEM approach has been widely adopted in published studies of suffusion (Zhang et al., 2020; Fu et al., 2022; Chen et al., 2023b; Liu et al., 2023a; Liu and Yin, 2024; Wang et al., 2024). Consequently, this chapter will primarily focus on research findings derived from unresolved CFD-DEM simulations. The following section will first introduce the fundamental methodology of the unresolved approach.

2.3 Unresolved CFD-DEM method

As previously highlighted, the unresolved CFD-DEM approach has stood out for its efficiency

and is widely adopted in studies related to suffusion. In this research, the unresolved scheme is thus employed for simulating. The ensuing section provides a fundamental overview of this methodology.

2.3.1 Governing equations for DEM

The simulation of dispersed particles' behavior is achieved by employing the fundamental principles of Newton's second law. At any given time *t*, the translational and rotational motion of particles is governed by the following equations:

$$m_i \frac{\mathrm{d}\mathbf{v}_i}{\mathrm{d}t} = \sum_{j=1}^{N} \mathbf{f}_i^j + \mathbf{f}_i^{f\to p} \tag{2.1}$$

$$I_i \frac{\mathrm{d}\boldsymbol{\omega}_i}{\mathrm{d}t} = \sum_{j=1}^{N} \mathbf{M}_i^j + \mathbf{M}_i^{f\to p} \tag{2.2}$$

where m_i and I_i denotes the mass and moment of inertia of particle *i*, respectively. $\mathbf{v}_i$ and $\boldsymbol{\omega}_i$ are the translational and angular velocities. $\mathbf{f}_i^j$ is the contact force exerted on particle *i* by the contact *j*. *N* is the total number of contacts particle *i* engaged, including particle-particle and particle-wall contact. In a similar way, $\mathbf{M}_i^j$ is the torque applied from contact *j* to particle *i*. $\mathbf{f}_i^{f\to p}$ is the interaction force applied to the particle by the flow. $\mathbf{M}_i^{f\to p}$ is the additional torque due to the fluid phase velocity gradient.

2.3.2 Governing equations for CFD

The CFD solves the following continuity equation and locally averaged Navier–Stokes equation accounting for the presence of particles in the fluid:

$$\frac{\partial \rho_f \alpha_f}{\partial t} + \nabla \cdot \left(\rho_f \alpha_f \mathbf{u}_f \right) = 0 \tag{2.3}$$

$$\frac{\partial \left(\alpha_f \rho_f \mathbf{u}_f \right)}{\partial t} + \nabla \cdot \left(\alpha_f \rho_f \mathbf{u}_f \mathbf{u}_f \right) = -\alpha_f \nabla p + \nabla \cdot \left(\alpha_f \tau_f \right) + \mathbf{f}^{p\to f} \tag{2.4}$$

where α_f represents the fluid volume fraction, p and $\mathbf{u}_f$ are the averaged pressure and velocity of the fluid, respectively. ρ_f stands for fluid density. τ_f is the shear stress tensor of the fluid. $\mathbf{f}^{p\to f}$ denotes the source term of momentum from interaction with the particulate phase, given as:

$$\mathbf{f}^{p\to f} = -\frac{\sum_{p=1}^{N}\mathbf{f}^{f\to p}}{V_c} \tag{2.5}$$

where V_c is the cell volume, N is the number of particles inside the fluid cell. $\mathbf{f}^{f\to p}$ accounts for the forces generated by the fluid on the particles, the calculation of which would be introduced later.

2.3.3 Fluid-particle interaction force

The interaction force $\mathbf{f}^{f\to p}$ between particles and fluid typically comprises several components, including the drag force, pressure gradient force, virtual mass force, and lift force (Ishii and Mishima, 1984; Mei, 1992). However, in dense particle flows such as those encountered in suffusion phenomena, the dominant governing factor is the pressure gradient force $\mathbf{f}_{\nabla p}$ and drag force $\mathbf{f}_d$:

$$\mathbf{f}^{f\to p} = \mathbf{f}_d + \mathbf{f}_{\nabla p} \tag{2.6}$$

in which the drag force $\mathbf{f}_d$ and pressure gradient force $\mathbf{f}_{\nabla p}$ are calculated as follows:

$$\mathbf{f}_p = -V_p \nabla p \tag{2.7}$$

$$\mathbf{f}_d = \frac{1}{2} C_D \rho_f A' \left|\mathbf{u}_f - \mathbf{v}_p\right| \left(\mathbf{u}_f - \mathbf{v}_p\right) \tag{2.8}$$

where V_p and $\mathbf{v}_p$ are the volume and velocity of the particle, respectively. A' is the project area of the particle in the direction of flow. C_D stands for the drag coefficient. Since this equation is only applicable to spherical particles in dilute flows (e.g., single particle motion in fluid), the

drag coefficient must be modified based on the particle Reynolds number Re_p for dense particle flows (Chhabra et al., 1999). The particle Reynolds number is defined as:

$$\mathrm{Re}_p = \frac{\rho_f \left|\mathbf{u}_f - \mathbf{v}_p\right| d_p^{equ}}{\mu_f} \tag{2.9}$$

where μ_f represents the fluid viscosity, d_p^{equ} denotes the equivalent spherical diameter of the particle volume. For spherical particles, d_p^{equ} corresponds to the actual particle diameter, while for non-spherical particles, it can be calculated based on the particle's actual volume. Building upon this foundation, Ergun et al. (1952) proposed a modified drag coefficient model that incorporates the fluid volume fraction:

$$C_{D,\,\mathrm{Ergun}} = \frac{200\alpha_s}{\alpha_f \phi_s^{\,2} Re} + \frac{7}{3\phi_s} \tag{2.10}$$

$$\phi_s = \frac{A_{\mathrm{equ}}}{A_{\mathrm{p}}} \tag{2.11}$$

where ϕ_s represents particle sphericity, and A_{p} denotes particle surface area. A_{equ} is the equivalent spherical surface area for the particle volume. For spherical particles, $\phi_s = 1$; for non-spherical particles, ϕ_s is calculated based on the surface area of a sphere with equivalent volume. α_s represents particle concentration. Eqs. (2.10)-(2.11) apply to dense particle flows where solid fraction $\alpha_s > 0.2$. Building on this foundation, Wen and Yu (1966) derived an expression for dilute flows ($\alpha_s < 0.2$) based on fluidized bed experimental data:

$$C_{D,\mathrm{Wen}} = \alpha_f^{-1.65} \max\left\{\frac{24}{\alpha_f \mathrm{Re}_p}\left[1 + 0.15\left(\alpha_f \mathrm{Re}_p\right)^{0.687}\right], 0.44\right\} \tag{2.12}$$

Lu and Gidaspow (2003) established a blended formulation that smoothly bridges Eqn. (2.10) and Equation (2.12) through a mixing function, achieving a continuous transition between high-concentration and low-concentration regimes. The final expression takes the form:

$$C_{D_{\mathrm{Lu\&Gidaspow}}} = \psi \mathrm{C}_{\mathrm{D}_{\mathrm{Ergun}}} + (1-\psi)\mathrm{C}_{\mathrm{D}_{\mathrm{Wen\&Yu}}} \tag{2.13}$$

$$\psi = \frac{1}{\pi}\arctan\left[150\times 1.75\left(0.8-\alpha_f\right)\right]+0.5 \tag{2.14}$$

2.3.4 Coupling scheme of CFD–DEM

The parallel calculation of DEM and CFD is enabled by a staggered scheme to exchange the solid fractions and interaction force. As shown in Figure 2.1, the initial particle assembly and fluid field are generated according to the input file. The interparticle contact force is calculated based on the contact area (i.e., overlap) and contact law. In contrast, the interaction force (pressure gradient force and drag force) is determined based on the initial fluid field. Then the solid volume fraction will be transferred back to the CFD domain to iteratively solve the N-S equation and update the pressure and velocity of the fluid. To ensure solution accuracy, CFD calculates multiple timesteps within each DEM timestep.

2.4 Application of CFD-DEM in RVE study about suffusion within the discrete media framework

Based on different simulation scales, studies about suffusion using CFD-DEM can be broadly divided into two categories: research on small-scale RVE model and research on meso-scale BVP model. The following sections will present the current status of both categories of research.

The representative volume element is a fundamental unit of a material or system that is used to study its properties and behavior (Yio et al., 2017). It is a small but representative portion of the material which is assumed to have the same statistical characteristics and behaviors as the larger one. In CFD-DEM investigations of suffusion, RVE models typically constitute small-scale

cubic or cylindrical specimens. These computational specimens are specifically designed to evaluate the micromechanical response of virtual granular assemblies (Guo and Zhao, 2016).

Previous studies have pointed out that suffusion is closely related to soil geometry conditions, hydraulic conditions, and stress states (as illustrated in Figure 2.2). The geometric conditions mainly refer to soil properties, like fines content and soil porosity. The hydraulic condition is also known as the critical hydraulic gradient, i.e., soil particles will migrate only when the fluid gradient is greater than a certain critical value. The mechanical condition is linked to the soil loading state, for example, its effective stresses. In addition, research has also revealed that suffusion only occurs in soils classified as internally unstable under specific conditions (Burenkova, 1993). Among such soils, those with a gap-graded sandy distribution are more susceptible and vulnerable to erosion compared to well-graded ones. Consequently, the majority of studies on suffusion have focused on gap-graded soils (Chang and Zhang, 2011, 2013a; Chaplot, 2013). These studies have conducted comprehensive analyses of various factors influencing suffusion, including fine particle content, gap ratio (size ratio between coarse and fine particles), particle morphology, hydraulic gradient, and so on. This study will systematically review these research efforts in the following sections.

2.4.1 Effect of fine content

For gap-graded soils, the content of fine particles is closely related to the transmission of microscopic forces. According to Shire et al. (2014), soils can be divided into underfilled and overfilled cases, and for different filling states, there are significant differences in the role played

by fine particles, with underfilled states in which fine particles primarily contribute to maintaining the structural stability of coarse particles and are minimally involved in direct force transfer, while in overfilling, fine particles share the force chain transfer with coarse particles. Therefore, when suffusion occurs in soils with varying fine content, the evolutionary characteristics will differ based on the fine content. Skempton and Brogan's work (1994a) has established a critical range of fines content, ranging from 24% to 29%, that demarcates underfilling and overfilling states in soils. Building on this insight, Liu et al. (2020) performed a series of simulations using CFD-DEM on RVEs with fine contents of 20% and 35%. These two values were chosen to represent typical underfilled and overfilled samples, respectively. The established model is illustrated in Figure 2.3. The simulation model is set as a cubical sample with six stress-controlled boundaries. The CFD domain overlaps the DEM domain to ensure it entirely covers the particles.

A direct assessment of the hazard posed by suffusion is the statistical mass loss. To investigate the effect of fines content on soil erosion, indicators of mass loss caused by suffusion are plotted against normalized erosion time. As depicted in Figure 2.4, the results from the related studies (Hu et al., 2019; Xiong et al., 2020) are presented, from which it can be found that fines content not only determines the magnitude of the final mass loss but also alters the trend of erosion development. In the underfilled condition, soil mass loss reaches stability in a short period and exhibits a convergence trend, while in the overfilled condition, mass loss is difficult to converge, indicating the possibility of excessive soil loss. This effect induced by fine content is attributed

to the difference in microscopic contact force buckling by Liu et al. (2020), which resulted in a sudden change in the contribution of inter-particle force networks. Further analysis was conducted by examining the contact force chain through Figure 2.5 in their study. Results indicated that for underfilled samples, the magnitude of the contact force chain remained stable throughout the suffusion process (as can be observed through the marked red force chains and chained particles in Figure 2.5(a)-(b)). The bearing load skeleton was primarily composed of coarse-coarse contacts. The loss of the fines had little influence on coarse-coarse contacts. However, for overfilled conditions, the loss of particles resulted in a decrease in contact force, indicating an adjustment in soil structure and posing a challenge to soil stability. Therefore, the mass loss of overfilled soil was hard to stabilize.

2.4.2 Effect of gap ratio

The gap ratio is defined as the ratio of the size of coarse particles to fine particles in the soil. Previous experimental observations have confirmed that the susceptibility of gap-graded soils to suffusion is critically influenced by the gap ratio (Wan and Fell, 2008). Most of the judging criteria that determine whether the soil has a potential for internal erosion are also based on the size ratio (Kenney and Lau, 1985; Burenkova, 1993; Israr and Indraratna, 2017). Numerical research has demonstrated that gap-graded soils with high gap ratios exhibit greater susceptibility to suffusion than those with low gap ratios. This is attributed to the high percentage of void spaces in soils with high gap ratios, which provides a conducive environment for fines to mobilize and migrate through the soil matrix. Furthermore, the gap ratio determines the structure of the pore channels through which the fines migrate. As the gap ratio decreases, fines may

aggregate and cause infiltration and clogging, which can inhibit the progression of suffusion, as depicted in Figure 2.6.

Based on the available CFD-DEM cases in the literature, the mass loss versus gap ratio is plotted in Figure 2.7. Since the channel size for fine particle transportation increases with the increasing gap ratio, the final total eroded particle percentage is higher for larger particle size ratios. Chen et al.(2023a) analyzed the pore structure using the maximal inscribed sphere (MIS) method for samples with different gap ratios (as is shown in Figure 2.8). They also confirmed that the increase in average MIS size is found to have a clear linear correlation with the percentage of the mass eroded value, and the pore channel was divided into the 'narrow void filter', 'intermediate void filter' and 'wide void filter', which represent the connectivity of the internal pore structure. It's vividly shown that the soil with a small gap ratio has a dense stacking, increasing the likelihood of clogging at the pore throat and decreasing the fine loss.

2.4.3 Effect of particle shape

Currently, most of the DEM studies simplify real sandy soil particles to spherical particles by introducing rolling resistance (Iwashita and Oda, 1998) to equivalently consider shape effects with the consideration of calculation efficiency. However, frequent particle contact and relative sliding occur in soils under the scour of infiltrative water flow during suffusion, in which the simplified spherical particles tend to ignore the contact limitation arising from the particle shape, and therefore underestimate the erosion hazard. According to Barrett (1980), the indexes to quantify the shape of particles mainly include form (aspect ratio), roundness (angularity), and

roughness (Nguyen et al., 2020). For the effect of particle shape on suffusion, Qian et al. (2021b) and Xiong et al.(2021) established the CFD-DEM models using polyhedral particles to realize the coupling of non-spherical particles and fluids, and investigated the influence of particle angularity and aspect ratio, respectively (as is shown in Figure 2.9). The results are shown in Figure 2.10, from which it is found that the aspect ratio of particles has an inhibitory effect on erosion rate. The channels through which fines are transported and lost in a spherical case are typically more obvious than those of non-spherical particles (Xiong et al., 2021). This is because, as particles become more spherical in shape, the formation of continuous voids becomes increasingly facile. In contrast, non-spherical particles tend to experience restricted connectivity between voids due to increased interparticle contact. The fluid resistance within these voids is also amplified, further hindering the transport of fines. The angularity is found to facilitate the particle interlock and resistance to rolling (Jensen et al., 1999), thus also inhibiting the development of erosion. As shown in Figure 2.11, in the non-spherical specimen, the migration trajectory of the eroded fine particles will show multiple blockages, and therefore, the loss probability of shaped particles is smaller compared to that of spherical particles.

2.4.4 Effect of hydraulic gradient

The study of the hydraulic gradient in suffusion includes two main aspects, one is the determination of the critical gradient that leads to the movement of fines before erosion, and the other is the influence of the level of hydraulic gradient on the migration of particles after the onset of suffusion. The critical hydraulic gradient was first determined by Terzaghi (1925) according to the classical geotechnical theory and the effective stress balance, but the theory can

only consider the critical value of soil piping, and can not give the critical hydraulic gradient corresponding to the migration of fine particles (i.e., suffusion). Cheng et al. (2021) performed the CFD-DEM studies and investigated the critical hydraulic gradient through the monitoring of superficial velocity provided by the CFD solver. The results demonstrate that as the hydraulic gradient increases, the fluid surface velocity gradually rises. Upon reaching a critical threshold, the water is able to induce particle migration, thereby altering the internal flow field and causing a significant surge in the superficial velocity. This turning point may be identified as the critical hydraulic gradient that triggers suffusion (Nguyen and Indraratna, 2020; Zhou et al., 2022).

The impact of varying hydraulic gradient levels on the mass loss of specimens was also investigated in the literature. As depicted in Figure 2.12, the total mass loss generally increases with increasing hydraulic gradient. Notably, the hydraulic gradient exhibits a significant influence on the loss rate during the initial stages of seepage. At low hydraulic levels, the mass loss process develops gradually and slowly, whereas at high hydraulic gradients, the specimen mass loss increases rapidly, followed by a swift stabilization of the loss rate. However, it should be noted that the increase in hydraulic gradient does not lead to an indefinite increase in mass loss. For example, when the hydraulic gradient is increased from 8 to 16m/m, there is no significant change in erosion mass. According to Mu et al. (2023), the relatively low hydraulic gradient is inclined to induce clogging within the sample, which in turn forms the hydraulic tortuosity of flow. As depicted in Figure 2.13, the higher the hydraulic gradient, the lower the hydraulic tortuosity. Once fluid flows through the specimen with a more tortuous path, it is less

likely to lead to the overall migration of particles. Therefore, the increase in gradient usually accompanies high mass loss.

2.4.5 Effect of other factors

Apart from the widely studied influencing factors mentioned earlier, recent literature has also reported some specific conditions that consider more complex seepage and soil scenarios during suffusion. These include suffusion under varying seepage flow directions, confining pressure, and torsional shear conditions. This section aims to provide a review of these studies.

In the context of dams and foundations, the direction of water flow often deviates from the direction of soil gravity, which can have a notable impact on the migration of fine particles. Xiong et al. (2020) were the first to conduct CFD-DEM simulations to examine particle transport under different infiltration directions. In their study, water flowed downward while the direction of gravity was altered in DEM to mimic different diverse angles between seepage flow and gravity. They found that the maximum mass loss was obtained with an angle of 0°, where the direction of gravity was aligned with the flow. However, contrary to expectations, the minimum mass loss did not occur in the sample with an angle of 180°, where the gravitational force acted in the opposite direction to the flow. Instead, the sample exhibited the least amount of fine particle loss when the gravitational force was perpendicular to the flow. Xiong et al. suggested that this behavior could be attributed to the fact that the perpendicular gravitational force tended to push the detached fine particles away from the seepage channel, resulting in the aggregation of particles at the side of the sample.

Song et al. (2024) conducted the first-ever investigation into the impact of suffusion under torsional shear conditions. As illustrated in Figure 2. 14, a numerical model of the Hollow Cylinder Torsional Shear Test (HCTST) was developed. The study examined both the rotation of the major principal stress axis (α) and the intermediate principal stress ratio (*b*) to explore the development of suffusion under different stress states. The eroded fine mass is shown in Figure 2.15, where it is evident that as the major principal stress rotates from the vertical to the horizontal direction (i.e., as α increases), fewer fine particles are washed away by the fluid flow. In contrast, under identical loading conditions, more fine particles are eroded in cases with smaller *b* values. Song et al. attributed this to the stronger restriction on particles in the horizontal plane when α and *b* are larger, leading to the greatest cumulative mass of eroded fines.

Many researchers have shown that increasing confining pressure reduces the soil void ratio, thereby mitigating suffusion. However, in gap-graded soils consisting of coarse and fine grains, the impact of confining pressure is more complex. Coupling effects may be triggered by the fines content, as demonstrated by Wang et al. (2022). In their numerical experiments, a wide range of fines content was considered under varying confining pressures. The results showed that the eroded mass generally decreased with increasing confining pressure. However, in soils with high fines content, a reverse trend was observed. Soils under high pressure exhibited even greater mass loss compared to those under low-pressure levels, as shown in Figure 2.16. This is because, for soil with high fines content, the fine particles become part of the force chains. As the

confining pressure increases, the contact forces between fine particles are strengthened. Once high-stressed fine particles become detached, force chains will be subjected to highly unbalanced forces and some of them will collapse. Therefore, the final erosion amplitude will increase as the confining pressure increases.

2.5 Application of CFD-DEM in BVP study about suffusion within the discrete media framework

The previous section presented simulation results using the CFD-DEM method at the RVE scale. In this section, this study will analyze results obtained from BVP models at larger scales. These models feature more DEM particles, specific structures, and complicated boundary conditions, attempting to reproduce the scenery of in-site engineering. At present, the establishment of a one-to-one model with CFD-DEM remains unfeasible due to the limitations of computational capabilities. To address this challenge while preserving model complexity and computational efficiency in BVP simulations, two methods are commonly employed. The first method involves constructing a model at a smaller scale under constant gravitational acceleration, whereas the second method entails building a model at a reduced scale subjected to centrifugal acceleration.

For example, shield-driven tunnels assembled with segmental lining in saturated soils are at risk of suffering from suffusion through circumferential and longitudinal segmental joints (Zhang et al., 2019). Ibrahim and Meguid (2023) conducted a study on tunnel suffusion using the CFD-DEM approach. Unlike previous studies that employed simplified bonding models to address particle loss (Tucker, 2004; Wynn et al., 2008; Gu et al., 2019), Ibrahim and Meguid (2023)

developed a comprehensive model of the tunnel structure, encompassing sand particles, tunnel lining, infiltration flow, and pipe joints. To alleviate the computational cost, a small-scale model was constructed based on particle diameter, measuring 0.2m by 0.2m with a thickness of $10D_{50}$ (D_{50} at 50% mass passing), comprising approximately 40,000 particles and 3,200 fluid meshes. Liu et al. (2023a) conducted a comparable study in which they also modeled the opening of tunnels under 1g acceleration. Their BVP model measured $25D_{50} \times 3D_{50} \times 22D_{50}$, consisting of about 20,000 particles. Erosion was simulated by introducing pre-set cracks within the tunnel walls. As shown in Figure 2.17, the infiltrative water flow caused the loss of soil surrounding the cracks, leading to substantial displacement and settling of the surrounding soil. Parametric analysis of sand erosion was then presented, including the impact of water level, crack width, height of the sand layer, and crack angle. Compared with conventional approaches such as indoor tests and FEM analyses, the CFD-DEM method offers significant advantages in accounting for the discrete characteristics of infiltrated soil around the tunnel. However, the limitations of the approach are also noteworthy. Due to the small size of the simulated structure, the boundary effects on the overall response are pronounced, particularly in the longitudinal direction along the tunnel, where the constraint between longitudinal particles cannot be considered, leading to an overestimation of the seepage-induced ground loss and surface settlement (Liu et al., 2023a).

Another method to reduce the particle number in CFD-DEM numerical simulations is to introduce centrifugal acceleration. Centrifuge tests on small-scale model structures allow researchers to study full-scale structures by taking advantage of the centrifuge scaling laws.

Referring to centrifuge experiments, several researchers (Abate et al., 2015; Sakaguchi et al., 2018; Yin et al., 2020b) have developed scaled-down simulation models by increasing the acceleration of gravity. In a pioneering study, Qian et al. (Qian et al., 2021a) investigated suffusion in tunnels using the CFD-DEM under an elevated gravity of 100g. The tunnel model comprising over 1,000,000 particles, measured 350mm × 420mm with a burial depth of 280 mm. These dimensions corresponded to a prototype size of 35m × 42m, similar to actual engineering structures. According to the similarity criterion, the force state in the prototype can also be replicated by the scaled-down model. The CFD-DEM simulations utilizing centrifugal acceleration appear to be more realistic than the small-scale models under 1g, and the obtained results could provide valuable insights for disaster prevention in engineering projects. However, determining fluid properties such as density and viscosity during erosion remains a significant challenge. Qian et al.(2021a) and Fu et al.(2022) both encountered similar difficulties, since the fluid properties at 1g were utilized in their studies despite the acceleration having been increased in the modeling, resulting in errors in fluid interactions. Addressing this issue and determining accurate fluid parameters after increasing the centrifugal acceleration will be a critical factor in the application of CFD-DEM in BVP. Thus, further research is needed to overcome these challenges and improve the accuracy and reliability of this modeling approach (Marshall et al., 2010).

2.6 Numerical study of macroscopic suffusion under the continuum mechanics framework

As evidenced by the preceding analysis, numerical simulations of suffusion based on the discrete media framework inherently suffer from scale limitations. Neither the RVE model nor the BVP

model can achieve substantial breakthroughs in simulation scale. This limitation arises from the fundamental principles of the DEM since it requires independent calculations for the interaction force and displacement of each particle. When the model size increases, the number of particles grows exponentially, leading to a dramatic surge in computational demand. Despite efforts by researchers to accelerate calculations using methods such as GPU parallel computing, these improvements still cannot fundamentally eliminate the substantial gap between discrete medium simulations and real engineering scales. Consequently, the application and broader adoption of discrete media-based research findings in engineering practice face significant skepticism.

For this reason, scholars have made numerous new attempts to study suffusion within the continuum medium framework in order to improve the scale of simulations. The advantage of this approach is that continuum mechanics can describe the erosion process using a series of partial differential equations, transforming the complex physical problem into the solution of control equations. Moreover, continuum mechanics offers efficient solving methods such as the FEM and the Material Point Method (MPM). Compared to the DEM, these methods are more convenient for simulating suffusion phenomena at real-world scales. This section will introduce the relevant work in this regard.

Current continuum-based modeling of erosion is fundamentally grounded in mixture theory. The mixture theory provides a framework for describing systems where multiple constituents, including soils and fluent, coexist within the same space simultaneously. Volume fractions are

used to represent the relative proportions of each constituent. The suffusion process is fully deterministic and described by the mass balance of the mixture system. Vardoulakis et al. (1996) pioneered a mathematical model for sand production problems, in which saturated soil is treated as a two-phase, three-constituent continuum medium. The two phases consist of fluid and solid, while the three constituents comprise the water, soil skeleton, and fluidized soil particles. Subsequent studies have developed various multiphase models (Papamichos et al., 2001; Cividini and Gioda, 2004; Uzuoka et al., 2012; Ibrahim and Meguid, 2023), with some incorporating erodible fine-particle constituents attached to the soil skeleton, thereby establishing two-phase, four-constituent models (Steeb et al., 2007; Schaufler et al., 2013; Lei et al., 2020). In recent years, this theoretical framework has been extended to unsaturated soils, where the inclusion of pore gas enables the development of three-phase, five-constituent models. Figure 2.18 schematically illustrates these different mixture theory approaches.

Beyond establishing continuum models for granular soils, researchers have progressively incorporated erosion-dependent constitutive models and hydraulic models to characterize infiltration processes (Yin et al., 2016a, 2020a). To solve the governing equations, an erosion law must be introduced to quantitatively describe the rate of fine particle detachment from the solid matrix and subsequent transition into the fluid phase. However, deriving an exact mathematical expression for this law remains particularly challenging, as it involves microscopic-scale particle mass transfer. Current solutions in the literature typically rely on semi-empirical formulations derived from laboratory experiments (Vardoulakis et al., 1996;

Reddi et al., 2005; Cividini et al., 2009). Upon establishing the erosion law, this formulation can be numerically implemented to solve the coupled mass balance equations governing the multi-phase particulate system.

Yang et al. (2017, 2020a) employed the Galerkin-weighted residual method to derive the finite element standard formulation for solving the mass balance equations. They developed a user-defined eight-node quadratic Serendipity element within the finite element software ABAQUS to solve for the unknown variables. To validate the method's applicability to engineering problems, it was applied to an internal erosion case in a foundation dam, as illustrated in Figure 2.19. The fluid from the upstream to the downstream side causes fine particle migration, ultimately leading to dam failure. Subsequently, Yang et al. further applied this model to the study of internal erosion in tunnel engineering (Yang et al., 2022).

Lei et al. (2020) developed a set of governing equations for suffusion within the MPM framework. As a mesh-free numerical approach, MPM demonstrates superior capability over FEM in simulating large soil deformations caused by seepage erosion. The proposed computational framework was applied to model unsaturated slope erosion under rainfall infiltration, with a slope geometry of 7m height and 35° inclination. To minimize boundary effects, an additional layer of material points was incorporated at the slope base, while roller boundary conditions were imposed on both sides and fixed boundary conditions were applied at the bottom to simulate an impermeable substratum. Figure 2.20 presents the results of MPM

simulations showing the plastic shear strain and the mass of eroded fine particles. The results reveal that, following erosion, plastic strain extends from the base to the top of the slope. Due to particle loss, severe damage and large deformations occur at the slope crest. Furthermore, significant loss of fine particles is observed near the slope surface, resulting in downslope movement under the combined influence of gravity and water infiltration. Similarly, Xie et al. (2022) established a seepage-erosion-hydro coupling model using an explicit two-phase MPM formulation, which was subsequently applied to analyze a practical engineering case involving twin-tunnel construction in China.

2.7 Summary

This chapter provides a review of numerical studies on suffusion at different scales. It is evident that within the framework of discrete medium mechanics, the DEM method enables detailed characterization of particle migration and fluid-solid interactions, which facilitates the reproduction of the micro- and macro-mechanisms underlying internal erosion. However, limitations in computational power hinder the application of this method at larger scales, particularly those comparable to physical model tests or real-world engineering projects. In contrast, numerical modeling for macroscopic erosion still needs to be developed within the classical continuum mechanics framework. Yet, compared to the DEM, continuum mechanics struggles to provide refined descriptions of particle migration and micro-scale contact evolution. To address the abovementioned research gaps, a CFD-DEM-FEM coupled method, and the cross-scale analysis framework should be established.

.

Table 2.1 Comparison of different fluid/DEM modeling methods

	Un-resolved CFD-DEM	Resolved CFD-DEM	Semi-resolved CFD-DEM	LBM-DEM	SPH-DEM
Mesh size	$l \geq (3-4)D_{max}$	$l \leq d_{min}$ / (8 – 10)	$l \geq (1-2)d_{max}$	$l \leq d_{min}$	/
Solution accuracy	Low	High	Medium	High	Low
Handling of bypassed fluids	Mesh averaging	Precise solution	Mesh averaging for fine particles; Precise solution for coarse particles	Precise solution	Calculating each fluid particle
Computing capabilities	Up to 10^5 -10^6 particles	10^2 -10^3 particles	No more than 10^4 particles	10^2 -10^4 particles	Up to 10^5 -10^6 particles
Computational efficiency:	2h[a] for 19,500 particles and 650 fluid meshes; 4h[b] for 219,000 particles and 650 fluid meshes	45.8h[c] for 299 particles and 506,250 fluid meshes	12*24h[b] for 19,500 particles and $6*10^5$ fluid meshes; 120*24h[b] for 219,000 particles and $6*10^5$ fluid meshes	160h[d] for 26,728 particles and $6.4*10^7$ lattice	4h46min[e] for 1000 DEM particles and 240,771 SPH particles
Advantage	Powerful computational efficiency; Dense particulate flow; Huge particle number	High predictive accuracy in estimating the interaction between particles and fluid	Higher accuracy compared to unresolved CFD-DEM and lower computational cost compared to fully-resolved CFD-DEM	Simulating complex fluid flows with irregular boundaries and interfaces	Fluid with free surfaces; large deformations of particles
Limitation	Unavailability of pore fluid information; failure to use for the coupling of complex particle shapes	Extremely large computational burden; Single or very few particles; The demand for high-performance solvers; High calculation costs	The bypassing fluid around the small particles is not solved; A large demand for fluid meshes	Difficult to simulate systems with high particle concentrations	Less accurate in modeling the fluid near walls and boundaries
Application	Fluidized bed; Geotechnical Engineering; Chemical pharmaceuticals; Grain storage	Dam break wave impact on a rock pile	Determination of critical hydraulic gradient	Fluidized bed; transport of sediment	Debris flows; avalanches; landslides

Note: D_{max} is the maximum diameter of the coarse particle; d_{min} and d_{max} is the minimum and maximum diameter of the fine particle; [a] Performed on 8 CPUS (Intel Xeon CPU E5-2680 v2 @ 2.80 GHz) (Cheng et al., 2018); [b] Performed on 64 CPUS (Intel Xeon CPU E5-2680 v2 @ 2.80 GHz) (Cheng et al., 2018); [c] Performed on 30 CPUS (Intel Xeon E5-2690 @ 2.90 GHz) (Shen et al., 2022); [d] Performed on Intel Xeon(R) CPU E5-2620 v4@2.10 GHz (Ma et al., 2021) [e] Performed on NVIDIA GeForce RTX 2070 Mobile (Xu and Dong, 2021)

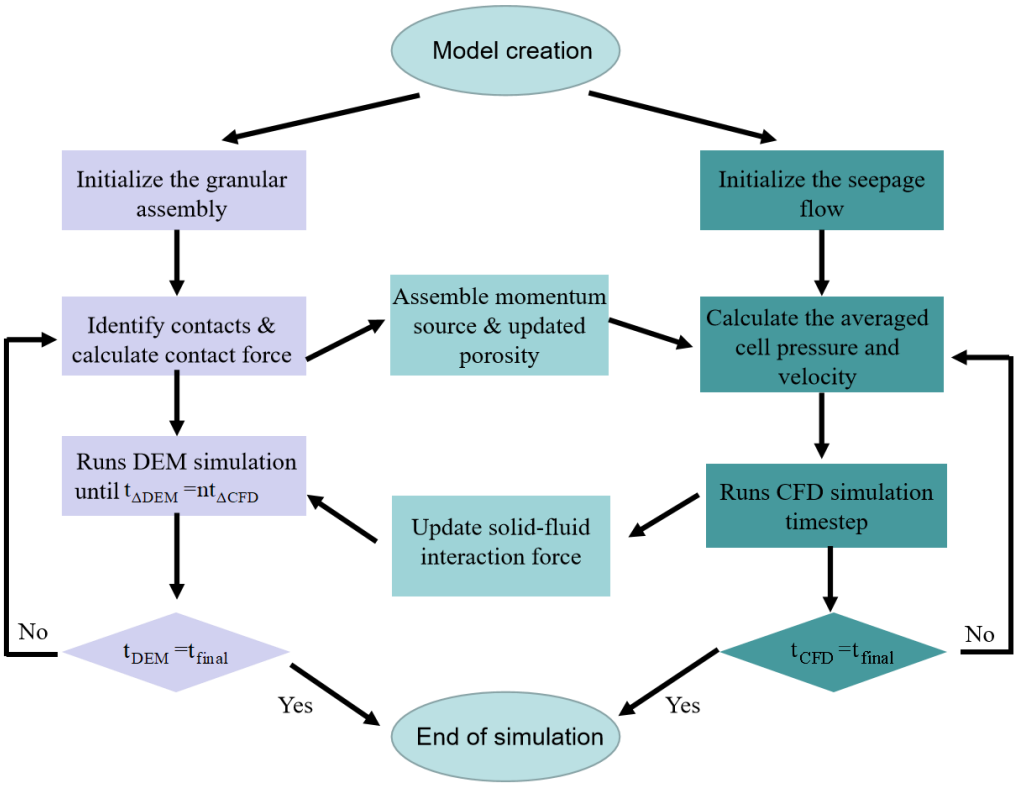

Figure 2.1 Algorithm flowchart of CFD-DEM coupling

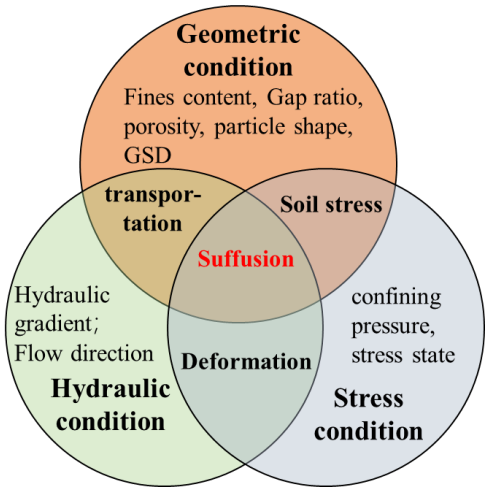

Figure 2.2 Contributory factors to suffusion (after Shire et al. (2014))

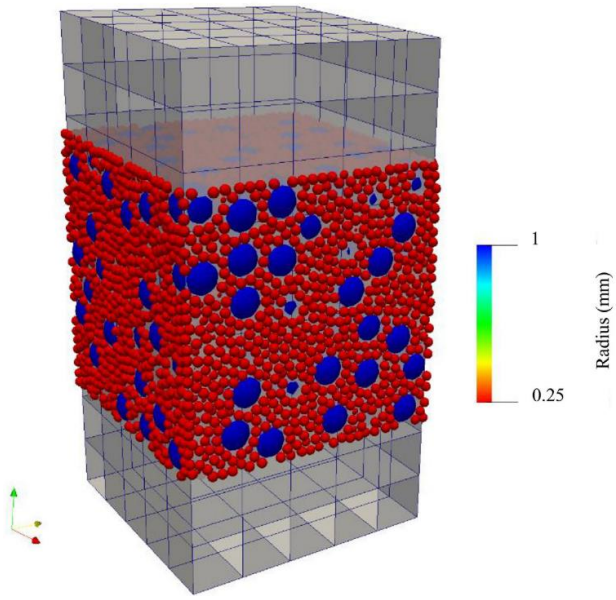

Figure 2.3 Schematic diagram of the RVE suffusion model (after Liu et al. (2020))

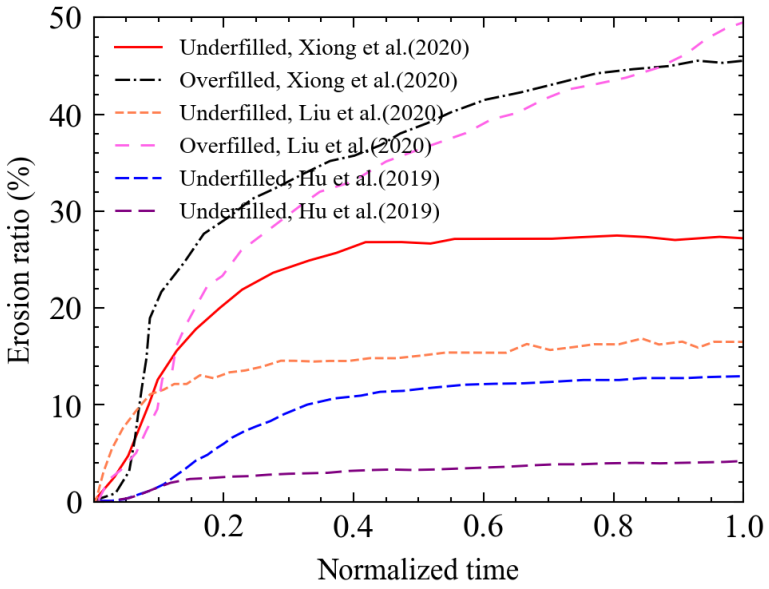

Figure 2.4 The influence of fine content on mass loss.

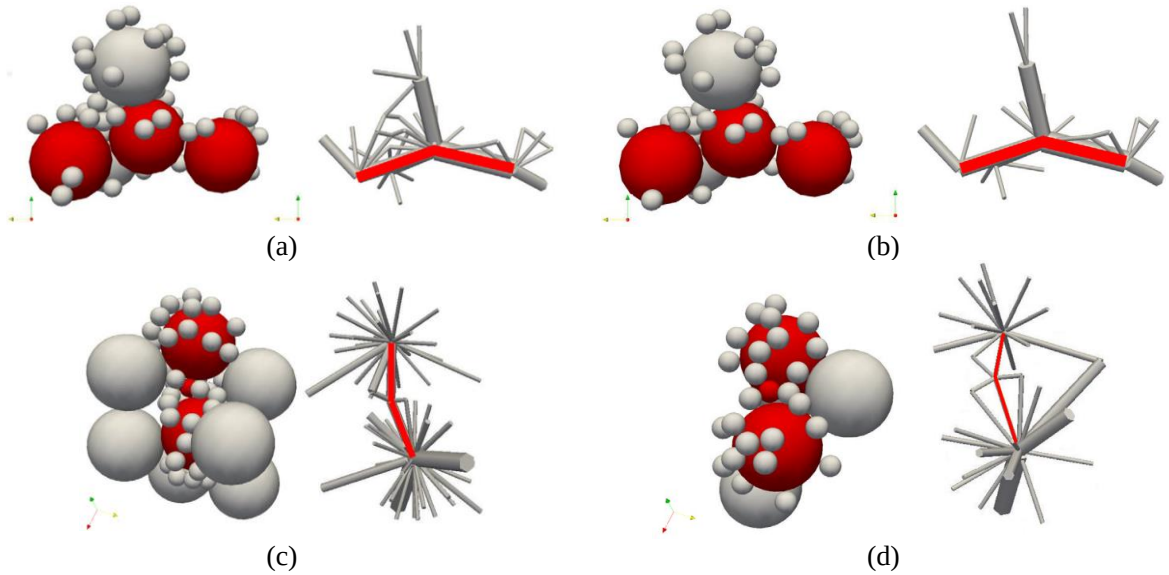

(a) (b) (c) (d)

Figure 2.5 The evolution of local packings during suffusion for underfilled and overfilled samples: (a) Underfill: before suffusion; (b) Underfill: after suffusion; (c) Overfill: before suffusion; (d) Overfill: after suffusion

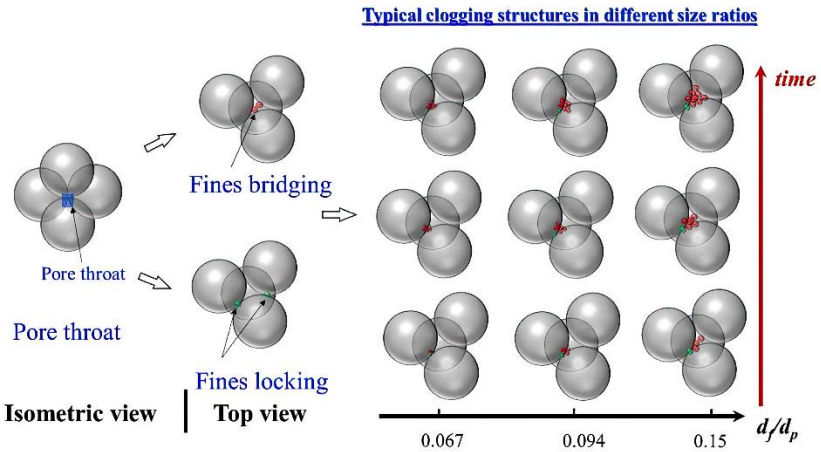

Figure 2.6 Fines clogging in pore channel for different gap ratios. (after Xie et al. (2023))

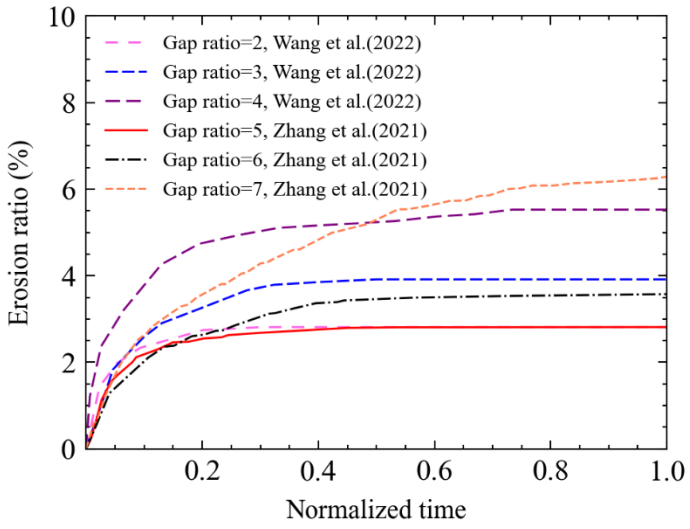

Figure 2.7 The influence of gap ratio on mass loss

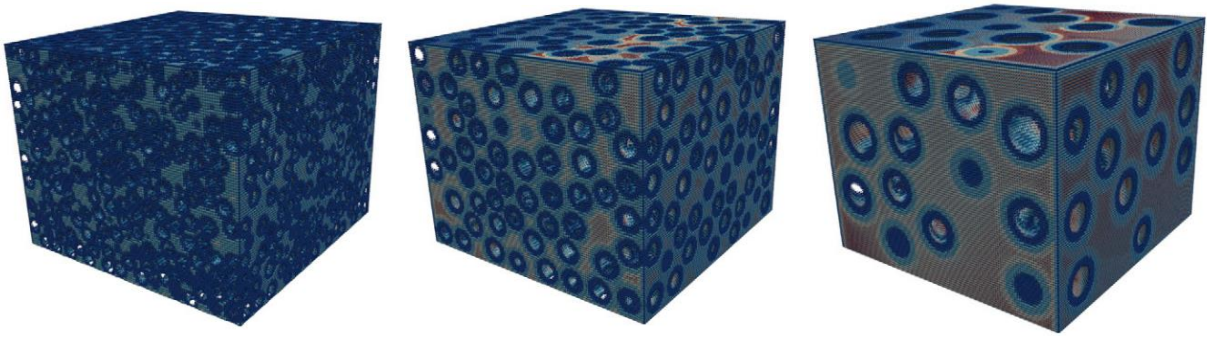

(a) (b) (c)

Figure 2.8 Internal pore structure captured by MIS (adapted from Chen et al.(2023a)): (a) Gap ratio=3.0; (b) Gap ratio=5.4; (c) Gap ratio=11.2

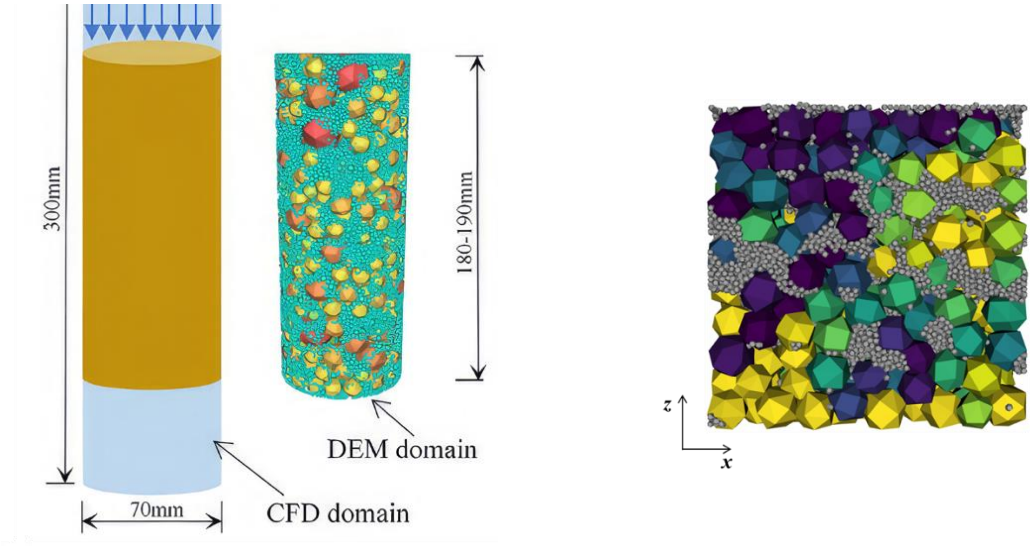

(a) (b)

Figure 2.9 CFD-DEM models with shaped particles (a): models considering particle aspect ratio (after Xiong et al. (2021)); (b): models considering particle angularity (after Qian et al. (2021b))

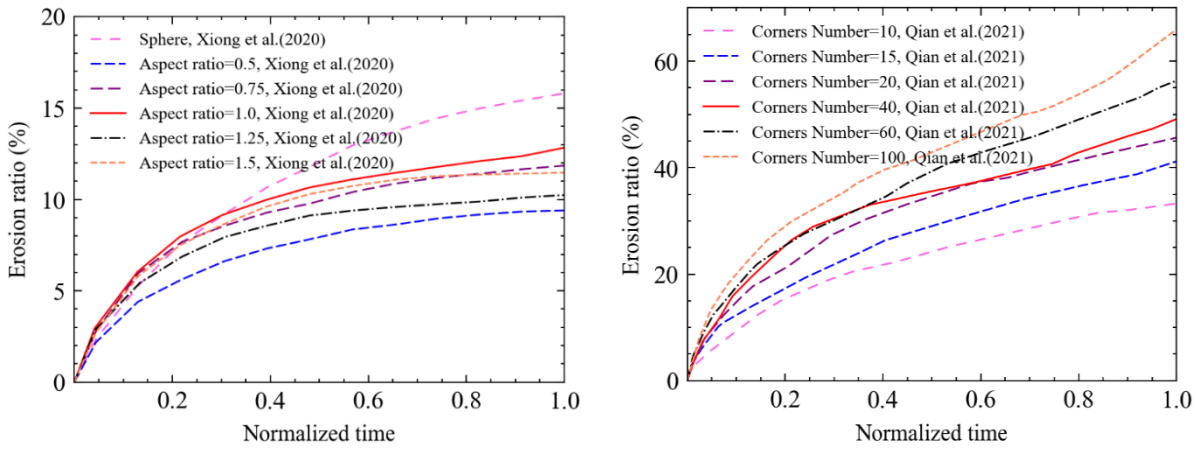

(a) (b)

Figure 2.10 The influence of particle shape on mass loss: (a) Effect of aspect ratio; (b) Effect of angularity

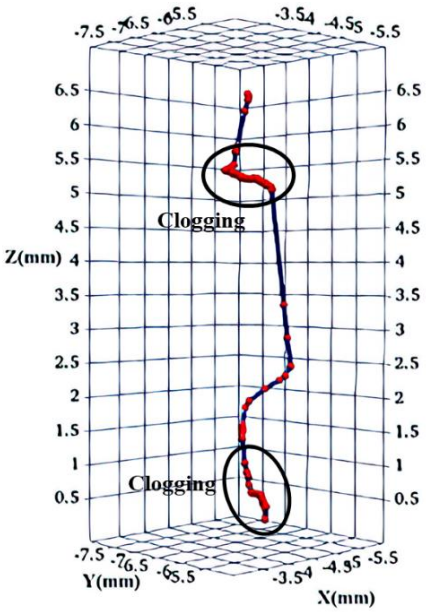

Figure 2.11 Particle trajectory in the non-spherical sample (after Qian et al. (2021b))

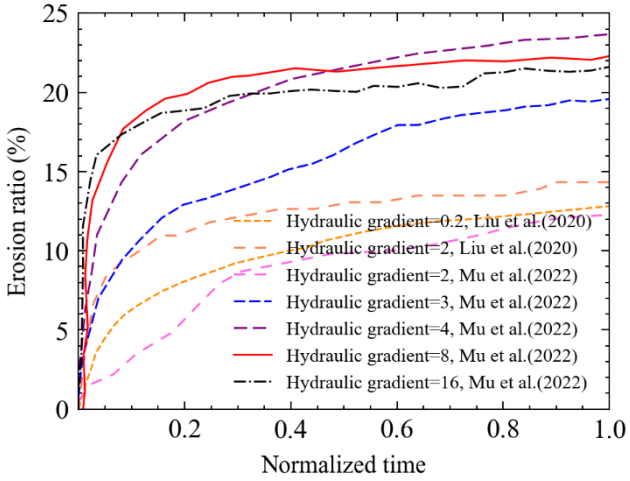

Figure 2.12 The influence of hydraulic gradient on mass loss

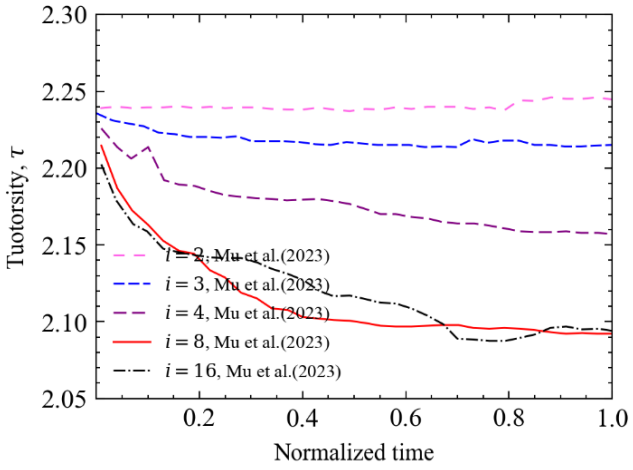

Figure 2.13 Fluid streamline of samples with different hydraulic gradients (after Mu et al. (2023))

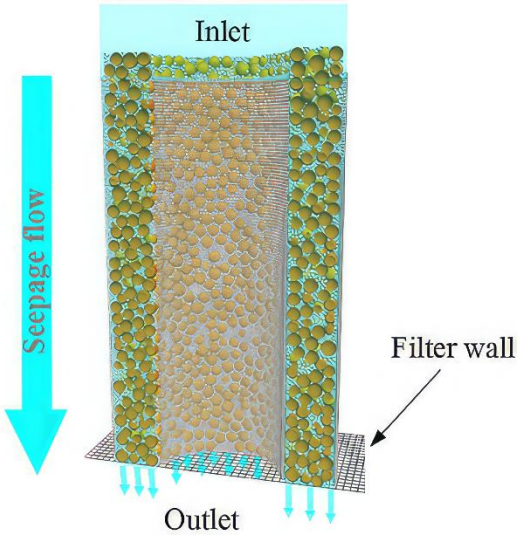

Figure 2. 14 The coupled CFD-DEM suffusion model for hollow cylinder torsional shear test (after Song et al. (2024))

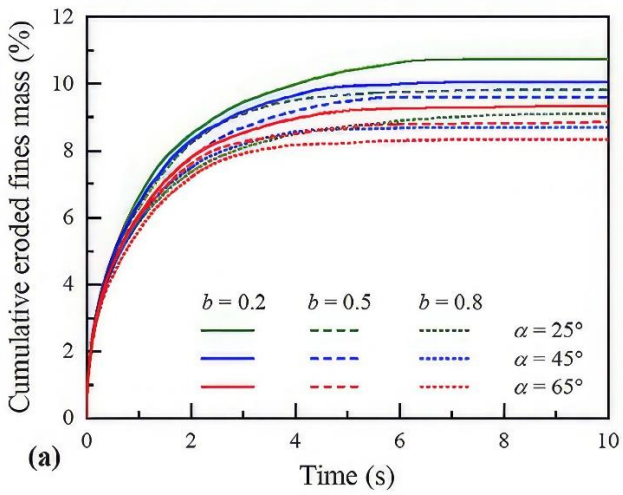

Figure 2.15 Variation of eroded mass with rotation of the major principal stress axis (α) and intermediate principal stress ratio (*b*) (after Song et al. (2024))

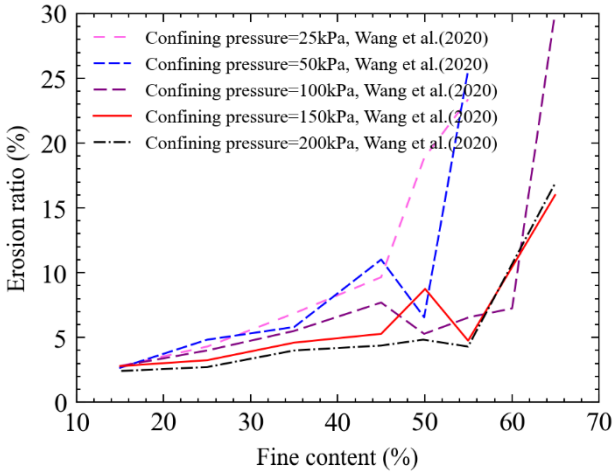

Figure 2.16 Eroded mass under different confining pressure and fines content (after Wang et al.(2022))

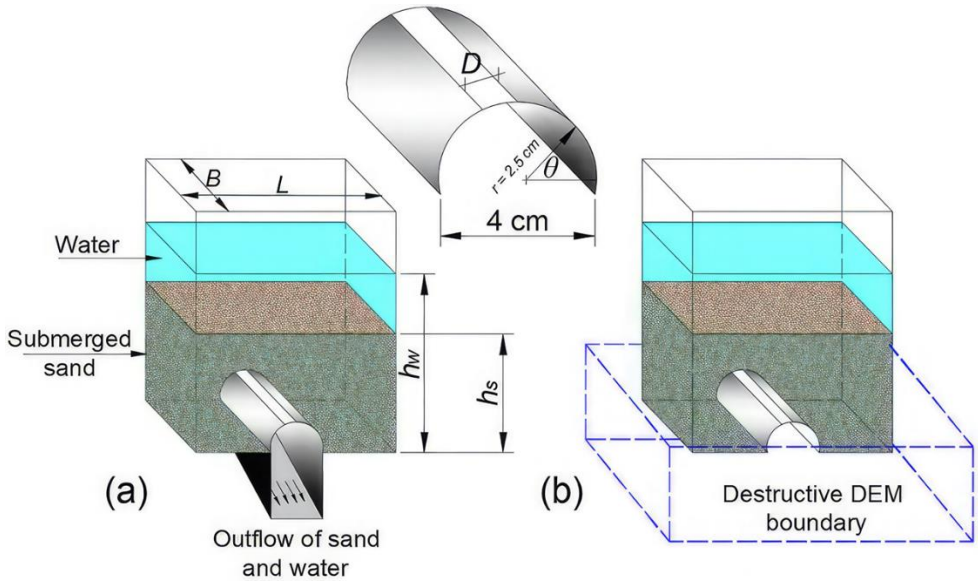

Figure 2.17 Model of tunnel erosion (after Ibrahim and Meguid, (2023))

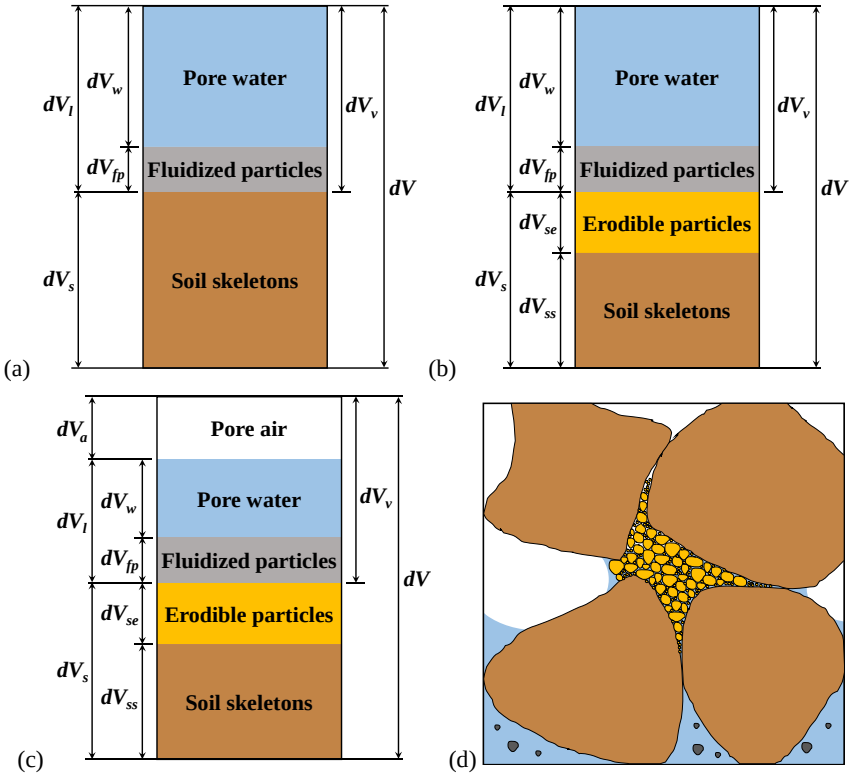

Figure 2.18 (a) two-phase three-component mixture, (b) two-phase four-component mixture, (c) three-phase five-component mixture, (d) conceptual representation of a three-phase five-component mixture

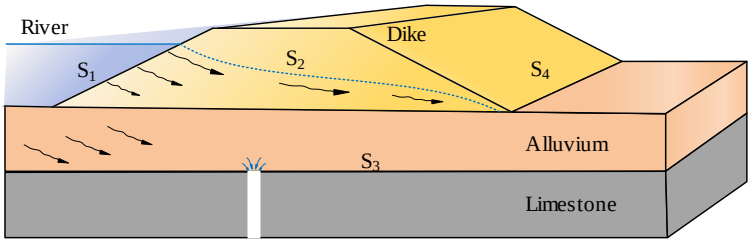

Figure 2.19 Scheme of the dike-on-foundation with a cavity located at the bottom.

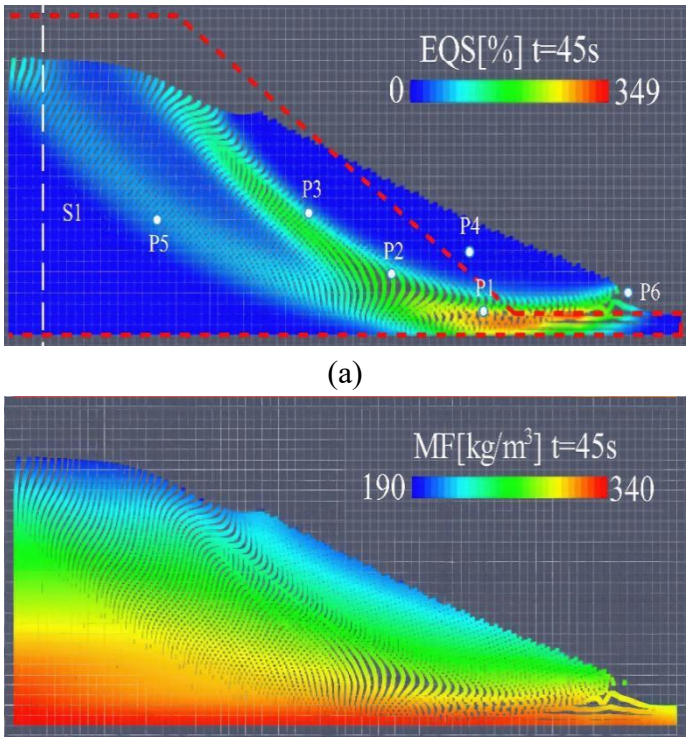

Figure 2.20 Contours of (a) equivalent plastic shear strain and (b) erodible fines mass fraction (after Lei et al. (2020))

CHAPTER 3 SUFFUSION MECHANISM UNDER ANISOTROPIC STRESS CONDITIONS

3.1 Introduction

One of the key factors influencing the development of internal erosion in sandy soils is the soil stress state. This is particularly relevant in hydraulic structures such as dams and reservoirs, where the soil in different regions is often subjected to different stress environments. Consequently, during groundwater seepage, the flow direction may vary in orientation relative to the principal stresses in the soil. As illustrated in Figure 3.1, for foundation soils, the seepage direction is parallel to the direction of the minimum principal stress, whereas in the core walls of dams, the seepage direction is perpendicular to the minimum principal stress. Therefore, the stress anisotropy of the soil will inevitably affect the development process of suffusion.

Over the past few decades, researchers have conducted laboratory experiments to investigate how anisotropic stress states influence the evolution of erosion. For example, Moffat and Fannin (2011) performed internal erosion tests under K_0 -stress conditions, and observed that the critical hydraulic gradient required to initiate suffusion increases with the applied effective overburden stress. Furthermore, under triaxial shear stress conditions, Chang and Zhang (2013b) used an improved triaxial apparatus to conduct erosion tests on soils subjected to complex stress states. Their results showed that samples under anisotropic stress conditions exhibited greater mass loss than those under isotropic stress. Based on experimental observations, Chang and Zhang classified suffusion under anisotropic stress conditions into four distinct stages: the stable stage,

initiation stage, development stage, and failure stage. They also identified three corresponding critical hydraulic gradients. Luo et al. (2020) conducted similar erosion tests, however, their results revealed some differences compared to those of Chang and Zhang. Firstly, they found that the entire erosion evolution process could be divided into six stages rather than four. Secondly, the critical hydraulic gradients determined by Luo et al. were significantly lower than those reported by Chang and Zhang. These discrepancies highlight the necessity of gaining a more accurate understanding of the influence of stress anisotropy on suffusion.

The analysis above reveals that studying the impact of stress anisotropy on erosion inherently involves both particle transport, represented by the DEM, and fluid motion, represented by CFD. Thus, to comprehensively understand the erosion process under varying stress conditions, this section utilizes the previously introduced CFD-DEM coupling method to undertake pertinent investigations and delve into the evolution mechanism from a microscopic standpoint.

3.2 Simulation of suffusion under anisotropic stress conditions

3.2.1 Model setup

In this section, the subject of investigation is a gap-graded soil sample composed of a mixture of coarse and fine particle groups. The diameter of the coarse particles ranges from 1.8 to 2.0mm, while the diameter of the fine particles ranges from 0.3 to 0.33mm. The fine content f_c is set at 25%. According to the study by Skempton and Brogan (1994), the mechanical behavior of soils with fine content less than 24% differs significantly from those with fine content greater than 29%. Since the primary objective of this chapter is to investigate the influence of stress

anisotropy—rather than the variation in f_c—the fine content is set near the transitional boundary between the two filling states, in order to minimize the influence of fine content on the results. The particle size distribution curve of the sample is shown in Figure 3.2. According to the research by Fannin and Moffat (2006), a soil can be classified as internally unstable, i.e., prone to internal erosion under seepage conditions if the ratio $D_{15c}/d_{85f}>4$, where D_{15c} is the diameter of coarse particles corresponding to 15% by mass, and d_{85f} is the diameter of fine particles corresponding to 85% by mass. In the sample used in this study, $D_{15c}/d_{85f}=6$, satisfying the aforementioned criterion. Furthermore, based on the findings of Burenkova (1993), if d_{90}/d_{60} of the soil satisfies the following condition, it can also be identified as an internally unstable soil:

$$0.76\log\left(d_{90}/d_{15}\right)+1<d_{90}/d_{60}<1.86\log\left(d_{90}/d_{15}\right)+1 \tag{3.1}$$

where, d_x (x=15, 60,or 90) denotes the particle diameter corresponding to x% by mass of the soil sample. The above criterion divides soil types into three distinct regions, as illustrated in Figure 3.3. It can be observed that the gradation of the soil sample used in this study also falls within the region classified as internally unstable.

In this study, three different stress states are considered to investigate the influence of anisotropic stress conditions on suffusion. These stress states correspond to triaxial extension, triaxial compression, and isotropic compression, as illustrated in Figure 3.4. A total of 15 sample groups are simulated. Each group is initially subjected to isotropic confining pressure, with the mean stress controlled at $p=50$kPa, 100kPa, 150kPa. Subsequently, the radial pressure σ_r is kept

constant while the axial pressure σ_a is increased to vary the deviatoric stress q, thereby achieving the desired stress ratio η （$\eta = q / p$） to simulate different stress conditions. In the case of triaxial compression, the maximum η value is 0.63; for triaxial extension, the minimum η is -0.5; and for isotropic compression, η=0. A detailed overview of the different sample configurations is provided in Table 3.1.

As suffusion is a long-term process, continuously varying hydraulic gradients are adopted to investigate the progressive evolution of sandy soils (Ke and Takahashi, 2014a; Hu et al., 2019). As shown in Figure 3.5, the hydraulic gradient is applied in a staged manner, covering a wide range from 0.1 to 10m/m to take into account, as far as possible, the seepage conditions that may be encountered in practical projects. A non-linear gradual increase in the hydraulic gradient is used to investigate critical hydraulic gradient during erosion, i.e., 0.1 per 0.5s for $i \le 0.5$, 0.15 per 0.5s for $0.5 < i \le 1.1$, 0.3 per 0.5s for $1.1 < i \le 2.0$, 0.5 per 0.5s for $2 < i \le 10.0$.

Fifteen samples with different stress states and variable hydraulic heads are considered in this study to investigate the influence of stress anisotropy and critical gradient. Each gap-graded sample measures approximately 15mm×15mm×19mm ($8D_{50} \times 8D_{50} \times 10D_{50}$), consisting of roughly 55000 particles. There is a slight difference in dimensions between specimens due to different stress states. In the present study, the soils are simulated as perfect spheres for reasonable calculation efficiency. Instead, the influence of particle shape is taken into consideration by applying rolling resistance (Wang et al., 2019; Peng et al., 2020; Yin et al.,

2020b; Qian et al., 2021a; Zhang and Yin, 2021). The soils are confined and loaded by six rigid walls. The friction coefficient between the particles and walls is 0.5, the same as between particles and particles. The Hertz-Mindlin contact model is employed to describe the interparticle contact behavior. Young's modulus equals 1×10^{9}, ensuring the total overlap of particles is within 2% (Chand et al., 2012; Peng et al., 2021). Other parameters adopted in this study are listed in Table 3.2. The fluid flows upward from the bottom to the top to eliminate the effect of gravity (Xiong et al., 2020). Since the number of particles used in the numerical calculations is relatively low due to limitations in computational power, and if downward seepage is considered, the loss of particles due to gravity will offset the discrepancy at different stress states. There is an extra height in the CFD domain to enclose the DEM sample (as shown in Figure 3.6). According to the benchmark of Qian et al. (Qian et al., 2021b), the size of the fluid cell is set $2mm\times2mm\times2mm$, which is equal to the largest particle diameter, and is 6 times the smallest particle.

3.2.2 Simulation procedure of suffusion

The overall simulation scheme mainly consists of the following steps:

Step 1: Sample generation. Soil particles are initially randomly dispersed in a large cuboid with a size of 15mm×15mm×80mm. Then the top and bottom walls are driven to compress the loose soil under a small stress level of 10kPa, after which the axial and radial stresses are increased under a servo mechanism up to a predetermined value. Gravity is switched off during this stage to generate a homogeneous sample.

Step 2: Gravity balance. Gravitational acceleration is activated and applied to the particles during this step, allowing the sample to reach internal stress equilibrium under its self-weight. This process lasts approximately 4 seconds. It is worth noting that, although some fine particles inevitably migrate downward through internal pores under the influence of gravity, the previously applied confining pressure during the preloading stage significantly reduces particle movement.

Step 3: Internal erosion. During suffusion, the top wall is first replaced by a filter wall with holes through which fine particles can be washed away by the fluid (as shown in Figure 3.7). The size of the hole is 2.5 times the diameter of the largest fine particles but less than the diameter of the coarse particle. Suffusion lasts 14s, and during this process, the soil stress state is kept unchanged.

3.3 Numerical Results and Discussion

3.3.1 Mass loss of fine particles

Figure 3.8 plots the cumulative mass loss of fine particles with elapsed time. In the present study, the fine particle loss m_e is calculated by the ratio of eroded fines mass and total fines mass. Samples under different stress ratios but the same confining stress of 50kPa are taken as examples to elaborate on the soil response to stress states. For a comparative analysis, the figure also shows the results of physical experiments conducted by Chang and Zhang (2013b) (see the red curves in Figure 3.8). It can be observed that the cumulative loss of fine particles obtained from the experiment is greater than that from the numerical simulation. This discrepancy is primarily due to two factors: first, in the physical experiment, seepage was applied in the same

direction as gravity, which intensified the migration of fine particles; second, the stress ratio in the physical test reached as high as 1.5, which is significantly greater than the stress ratio used in the simulation. As a result, there is a numerical difference between the experimental and simulation outcomes. However, it is important to note that both the experimental and numerical results exhibit a consistent evolution pattern of fine particle loss, namely that stress anisotropy significantly intensifies the erosion and migration of fine particles. Specifically, the total fine particle loss for T2-D1-CP50-1 and T4-D3-CP50-1 under anisotropic state is 6.9% and 8.1%, respectively, while T0-D0-CP50 under the isotropic confining stress state has a fine particle loss of only 4.1%. Furthermore, Figure 3.9 shows the final mass loss for all the samples, from which it can also be concluded that samples with stress anisotropy will have more fines eroded and that the higher the stress ratio, the greater the mass loss. In Section 3.4, this study will give a specific microscopic explanation for the macroscopic phenomenon that stress anisotropy increases fine particle loss.

As the hydraulic gradient continues to increase, the loss of fine particles also shows different phasing characteristics. For example, for specimen T4-D3-CP50-1, no fine particle loss (i.e., $m_e=0$) occurs from 0 to 1.3s (corresponding to $i=0\sim0.36\text{m/m}$). The specimen undergoes significant fine particle loss from 1.3s to 5.2s (corresponding to $i=0.36\sim1.82$). The loss rate then slows down until 10.7s ($i=7.2\text{m/m}$) when the fine particle loss again accelerates slightly and finally reaches equilibrium (fines loss is essentially constant). Such an evolution process is consistent with the four stages and three critical hydraulic gradients summarized in the

experimental study by Chang and Zhang (2013b). However, it is important to clarify that this evolution process does not apply uniformly to samples under all stress conditions. For instance, in the case of sample T2-D1-CP50-1, the mass loss curve displays more distinct transitional stages. Similarly, the laboratory seepage erosion tests conducted by Luo et al. (2020) also demonstrated that the development of fine particle loss involves more than just four stages. Given the ongoing debate surrounding the applicability of the four-stage erosion evolution model, this study focuses solely on analyzing the critical gradient corresponding to the initial onset of fine particle migration—referred to as the initial critical hydraulic gradient. The details of this analysis are presented in Section 3.3.3.

3.3.2 Variation in void ratio

After applying a hydraulic gradient to the sample, fine particles are driven by the hydraulic force to migrate through the coarse particle skeleton, thereby causing a change in the sample's void. To facilitate the analysis of the void ratio variation, the specimens are divided into four equal portions along the Z-axis, and the void ratios are counted separately (see Figure 3.10). Figure 3.11 plots the pre- and post-erosion void ratio at different positions under different σ_r, from which it can be seen that the initial distribution of void ratio for samples under a relatively small confining pressure (50kPa) is more inhomogeneous compared to samples with a relatively large confining pressure (100kPa and 150kPa). This is because, the particles used in this study are a mixture of coarse and fine parts, and the size ratio between them is up to 6. Therefore, the fines can move freely through the pore because of gravity, especially when the confining pressure is low. However, it should be noted that through the method used in the aforementioned sample

generation stage, the maximum porosity deviation before erosion is controlled to be around 0.05 (for the T1-D0-CP50 sample), which is permissible for specimens with a size ratio of 6 (Hu et al., 2019). By observing the void ratio after suffusion, it can be found that at the fourth layer near the filter, samples under different conditions show a significant increase in porosity, indicating that fine particle loss is more severe at this location. For the isotropic and triaxial extension stress states of the specimens (e.g., samples of T1-D0-CP50 and T4-D3-CP50-1), the difference in void ratio between the different layers decreases compared to pre-erosion. In contrast, the void ratio difference increases for the triaxial compression stress state, as in T2-D1-CP50-1, where the maximum difference in the void ratio is up to 0.1 after internal erosion. This characteristic can be found in different σ_r, indicating that for samples under triaxial compression states, the erosion path for the fines at the bottom is obscure and therefore the particle loss is mainly from the upper fines. This can be further evidenced by the microscopic particle trajectories in Section 3.4.

3.3.3 Critical hydraulic gradient

As the hydraulic gradient increases, fine particles in the soil begin to erode when the applied gradient is greater than a critical value, which is known as the critical hydraulic gradient. However, there are some discrepancies in determining the critical hydraulic gradient in previous laboratory physical experiments. Some scholars determine the critical value solely based on the turning point on the mass loss curve (Chang and Zhang, 2013b; Liang et al., 2019), but this method largely relies on the subjectivity of the experimenter, which can lead to deviations. Therefore, this study combines mass loss and microscopic surface velocity change to propose a new method for determining critical hydraulic gradients, avoiding the disturbance of subjectivity

in the results. Figure 3.12 plots the cumulative mass loss (in black line) and soil surface velocity (in red line) versus simulation time. The surface velocity is defined as the z-directional average velocity of the fine particles close to the filter. In the initial stages of seepage erosion, the drag force exerted by the hydraulic gradient is less than the weight of the particles so that the fine particles move downward with a negative surface velocity without fines loss ($m_e = 0$). The surface velocity is positive from $t = t_1$ and does not reappear negative for the phase $t > t_1$, indicating that the upward drag force is greater than the particle's gravity, and the particle moves upward. At the same time, the mass loss occurs at $t = t_1$ ($m_e > 0$), so the hydraulic gradient corresponding to t_1 is determined as the critical value. It is also worth noting that there are other points where the rate of mass loss changes significantly in the cumulative mass loss curve (e.g., $t = t_2 \sim t_4$). At $t = t_3$, for example, the surface velocity remains almost constant but the mass loss is still significantly accelerated. Previous scholars usually take the hydraulic gradient corresponding to $t = t_3$ as another critical value, thus summarizing the erosion process into different stages (Chang and Zhang, 2013b). However, the conclusion is not corroborated by similar experimental results from other scholars, so the hydraulic gradients corresponding to $t = t_2 \sim t_4$ are not taken as a critical value in this study. Through the above method, the critical hydraulic gradient corresponding to the occurrence of erosion can be accurately defined, eliminating the subjectivity in observation that arises from relying solely on the inflection point on the mass loss curve.

Figure 3.13 shows the critical hydraulic gradients of samples under different stress states

determined using the above method. It can be observed that as the confining pressure increases from 50kPa to 150kPa, the critical hydraulic gradient of samples with the same stress ratio η also increases. For example, when $\eta = 0$, the gradient of soil under $\sigma_r = 50\text{kPa}$ is 0.45m/m, while that of soil under $\sigma_r = 150\text{kPa}$ grows to 0.70m/m, indicating that the increase in confining pressure enhances the erosion resistance of soil. In addition, it's observed that the critical hydraulic gradient of the triaxial extension specimens ($\eta < 0$) is close to that in isotropic compression ($\eta = 0$) under the same σ_r. In contrast, the critical hydraulic gradient is significantly higher in triaxial compression ($\eta > 0$). As shown in Figure 3.13, for example, the critical values for T4-D3-CP50-1 and T1-D0-CP50 are 0.38 and 0.45m/m, respectively, while the critical gradient for T2-D1-CP50-1 grows to 0.62m/m, about 1.6 times that of T4-D3-CP50-1 and 1.4 times that of T1-D0-CP50. Moreover, it is generally accepted that the onset of internal erosion is directly related to the initial void ratio, that is, the smaller the void ratio, the greater the critical hydraulic gradient (Liu et al., 2021), but this rule does not apply when the effect of stress anisotropy is taken into account. As shown in Figure 3.14, the critical hydraulic gradient and the void ratio are negatively correlated for specimens under the same stress state. However, for specimens with different stress ratios, even if they have the same initial void ratio, the critical hydraulic gradient is not the same. Specifically, the void ratio of T6-D0-CP100 is 0.461, which is less than that of T2-D1-CP50-1 (0.485). Nevertheless, the former has a critical hydraulic gradient of 0.55m/m, smaller than the latter's 0.62m/m. This phenomenon was also observed in the physical experiments (Chang and Zhang, 2013b). This study investigates the phenomenon from the microscopic perspective of force chain distribution and particle coordination numbers, which

will be presented in Section 3.4.

3.4 Microscopic analysis and mechanism

3.4.1 Response of hydraulic drag force and contact force

To explore the influence of the stress state on internal erosion at a microscopic level, the evolution of contact force and hydraulic force (drag force) is first analyzed. Since coarse particles do not get lost and show less movement compared to fine particles, it would be more interesting to see the drag force and contact force on fine particles considering their most significant role in suffusion. For analysis purposes, the contacts that fine particles involve are divided into coarse-fine (c-f) particle contacts and fine-fine (f-f) particle contacts, and the average force of these two types of contact is counted separately. As shown in Figure 3.15, with the variation in the hydraulic gradient, the average drag force shows a distinct step change. It is worth noting that as suffusion develops and the hydraulic gradient increases, the coarse-fine contact force gradually decreases, while the fine-fine contact force shows the exact opposite trend, gradually increasing (in absolute terms). This is because, during the initial stage of suffusion, fine particles primarily act as filler between particles and are distributed within the pores formed by the coarse skeleton, contributing very little to the overall stress transmission of the soil, with minimal inter-particle forces. However, after the fluid action, fine particles with weaker inter-particle contact forces are eroded, and the remaining fine particles form close contact with surrounding particles under the action of the drag force. As a result, their inter-particle interactions increase as erosion progresses. In contrast, the coarse-fine contact force is relatively large before erosion, indicating that it bears part of the force transmission. However, this contact type is not stable (in related

studies, it is referred to as a metastable structure (Hu et al., 2020b; Qian et al., 2021b)), so once the fluid infiltrates, the soil structure can be easily disrupted, leading to a continuous reduction in the average coarse-fine contact force. Additionally, it can be observed that the coarse-fine contact force exhibits significant fluctuations at $t = 1.3\text{s}$, which coincides with the previously determined critical hydraulic gradient time point. Therefore, the main reason for the fluctuation in contact force is that after fine particles begin to be lost, the particles undergo redistribution and adjustment. During the period of $t > 6.5\text{s}$, the average contact force decreases slowly without noticeable fluctuations. Correspondingly, there is no significant change in the mass loss rate on the mass loss curve (as shown in Figure 3.8).

3.4.2 Anisotropy of contact force

As introduced in Section 3.3.1, samples under triaxial extension and triaxial compression states typically experience more mass loss than those under isotropic compression states, indicating that the initial stress anisotropy of the sample reduces soil erosion resistance. The above simulation phenomenon can be explained by the anisotropy of particle contacts at the microscopic level. To characterize the anisotropy of particle contacts, the angles on the *xoy* plane θ and the *yoz* plane φ are used to represent the orientations of particle contacts in 3D space (as shown in Figure 3.16). Then, the spatial distribution function $E(\theta,\varphi)$ is used to quantify the particle contact information (Xiong et al., 2020). Considering the symmetry along the z-axis, the variable θ can be eliminated by averaging the function as $\overline{E}\left(\theta,\varphi\right) = \int_0^{2\pi} E\left(\theta,\varphi\right)d\theta \,/\, \int_0^{2\pi} d\theta$. Then, the simplified distribution function on the basis of the second Fourier component is written as:

$$\overline{E}(\varphi) = \frac{1}{2\pi}[1 + \alpha\cos 2(\varphi - \beta)] \tag{3.2}$$

where $\int_0^{2\pi} \overline{E}(\varphi) d\varphi = 1$. The parameter α defines the magnitude of the anisotropy and β determines the principal direction, which are calculated as:

$$\alpha = 2\sqrt{\left[\int_0^{2\pi} \bar{E}(\varphi)\cos 2\varphi d\varphi\right]^2 + \left[\int_0^{2\pi} \bar{E}(\varphi)\sin 2\varphi d\varphi\right]^2} \tag{3.3}$$

$$\beta = \frac{1}{2}\arctan\frac{\int_0^{2\pi} \bar{E}(\varphi)\sin 2\varphi d\varphi}{\int_0^{2\pi} \bar{E}(\varphi)\cos 2\varphi d\varphi} \tag{3.4}$$

Figure 3.17 shows the spatial distribution of contact configuration (contact number and contact force magnitude) for the $\sigma_r = 50\text{kPa}$ samples. Before suffusion begins, the contact number in the newly generated cubic sample is relatively evenly distributed in all directions, so the anisotropy coefficient of the contact number, α_c, is small, and the differences between samples under different stress states are not significant.

The initial orientation of the normal contact force is consistent with the stress states applied to the sample. For the T2-D1-CP50-1 and T4-D3-CP50-1 samples under stress anisotropic states, the contact force anisotropy coefficient, α_n, is much greater than that of the isotropic T1-D0-CP50 sample. More importantly, the anisotropic principal directions, β_n, for the T2-D1-CP50-1 and T4-D3-CP50-1 samples are 1.51° and 90.8°, respectively, which align with their maximum principal stress directions. The evolution of anisotropic parameters α_n and β_n for the normal contact force versus time is presented in Figure 3.18. It can be observed that for the isotropic sample T1-D0-CP50, α_n remains almost constant throughout the process, with a very small value. In contrast, for the anisotropic stress state samples T2-D1-CP50-1 and T4-D3-CP50-1, α_n decreases continuously after the hydraulic gradient is applied, indicating that for the initial

anisotropic samples, fine particle loss leads to adjustments in particle contact, resulting in a trend from initial stress anisotropy to stress isotropy. Such a change in contact force inevitably leads to a corresponding adjustment in particle position, which in turn increases particle-to-particle misalignment and therefore a significant increase in the likelihood of fine particles passing through the pores between coarse particles' matrix. Ultimately, at the macroscopic level, specimens with initial stress anisotropy appear to lose significantly more fine particles than specimens with isotropic stress. Furthermore, Figure 3.19 plots the evolution of the local contact forces during suffusion, from which the transformation of the contact force from anisotropic to isotropic can be clearly seen. The local force chains illustrated in Figure 3.19(b)-(d) are the selected areas marked in Figure 3.19(a). At the beginning ($t = 0\text{s}$), under the stress state of triaxial extension ($\sigma_r > \sigma_a$), the local contact force chain has a significant horizontal anisotropy distribution. Then at $t = 6\text{s}$, the fine particle loss triggers a structure adjustment (i.e., the contact force chains form an isotropic three-dimensional structure in space). As seepage continues, this isotropic structure does not change in form but is further strengthened as the contact forces in all three directions increase, indicating that this stable structure could well resist seepage erosion.

3.4.3 Response of coordination numbers

Connectivity, the number of contacts per particle with its neighboring particles, can be used to measure how difficult it is for particles to be mobilized by seepage flow. It is generally acknowledged that fine particles with low connectivity are vulnerable to hydraulic forces (Hu et al., 2019). Figure 3.20 illustrates the variation of connectivity of fine particles. The vertical axis represents the total number of particles with particular connectivity. With the progress of erosion,

the number of fine particles with low connectivity (as shown in Figure 3.20, the cut-off point between high and low connectivity is roughly around 3 in this study) gradually decreases, while at the same time, the number of fine particles with high connectivity is increasing. There are two main reasons for the reduction in the number of low-connectivity fine particles. First, the seepage fluid directly erodes some of the weakly connected fine particles, resulting in a decrease in the total number of these particles. Second, due to internal structural adjustments, some weakly connected fine particles establish new contact connections with surrounding particles, transforming into high-connectivity fine particles in order to resist the erosion. On a macroscopic level, the mass loss rate on the curve in Figure 3.8 slows down, which can be explained by the change in the connectivity of particles at the microscopic level. In the initial stage, the fluid erodes fine particles with low connectivity. These particles have weak connections with surrounding particles and are easily eroded, so they are quickly lost. However, as these particles are completely eroded, the subsequent loss primarily involves high-connectivity particles. Since these particles are tightly connected with their surroundings and are more resistant to erosion, the mass loss slows down.

Unlike particle connectivity, the particle coordination number Z represents the average number of contacts for all particles, and can be calculated using the following formula:

$$Z = \frac{2C}{N} \tag{3.6}$$

where C is the total contact number and N is the total particle number in the soil matrix. For gap-graded soils, coarse particle loss is not involved, therefore, the change in coordination

number is primarily caused by the erosion of fine particles. When analyzing the change in coordination number, it is necessary to distinguish between the two types of soil particles. For this purpose, the contact types are divided into three categories: the contacts between two coarse particles (Z_{c-c}), the contacts between two fine particles (Z_{f-f}), and the contacts between coarse particles and fine particles (Z_{c-f}). Figure 3.21 shows that Z_{c-c} is almost constant during erosion regardless of the stress state, indicating that the contact between the coarse particles is more stable. In contrast, Z_{f-f} keeps increasing, which is consistent with the pattern reflected by the connectivity mentioned above (Figure 3.20). Among the three contact types, Z_{c-f} has the largest value because, in the gap-graded soils, the size ratio between coarse and fine particles is significant, and the coarse particles are surrounded by multiple fine particles, resulting in the highest number of coarse-fine contact types.

It is worth noting that once the permeating fluid is introduced, Z_{c-f} exhibits a significant response, with a marked sudden drop. Under the impact of the applied fluid water, weakly connected fine particles rapidly detach from the coarse particles (the inset in Figure 3.21 shows the process of fine particles detaching from coarse particles), and the intensity of the fluid's impact on the particles differs under different stress states. For example, for the isotropic (T1-D0-CP50) and triaxial extension stress state (T4-D3-CP50-1) samples, Z_{c-f} decreases by 0.492 and 0.523, respectively, while for the triaxial compressive sample (T2-D1-CP50-1), Z_{c-f} only decreases by 0.408. This phenomena indicate that coarse-fine contacts significantly respond to the effect of the water flow, and the Z_{c-f} change in samples T1-D0-CP50 and T4-D3-CP50-1 is

more pronounced than in sample T2-D1-CP50-1, suggesting that more fine particles in the former two samples detach from the coarse particles, and these fine particles are more sensitive to erosion. It is precisely due to this variation process that the initial critical hydraulic gradient under triaxial compression stress state is larger than under triaxial extension and isotropic compression stress state.

3.4.4 Erosion path and strong force chain network

The migration trajectory records the path formed by particles as they pass through the pores of the soil during suffusion. By recording the particle positions inside the soil at equal time intervals and plotting them as points in the spatial coordinates, a line diagram can be formed by connecting the coordinates at different time points. Figure 3.22 shows the migration trajectories of fine particles under different stress states. The three longest migration trajectories in each stress state are selected for plotting to avoid the influence of randomness on the results. In the figure, the red dots represent the position of the particles at a certain moment. Since the sampling intervals are consistent, the longer the line between two points, the smoother the particle migration at that location. Conversely, the denser the red dots, the slower the particle velocity, indicating greater clogging, making it more difficult for particles to pass through. Furthermore, Figure 3.23 shows the strong force chain network inside the sample. In this study, $1.2\left\langle \overline{f_n} \right\rangle$ is used as the cut-off point for strong and weak force chains, where $\left\langle \overline{f_n} \right\rangle$ is the average value of the contact force chain. Since strong force chains are primarily responsible for stress transmission and are relatively stable, they offer better resistance to seepage erosion. They can effectively inhibit particle loss and migration, and from a stress perspective, can explain the migration paths formed

by the lost fine particles.

As shown in Figure 3.22(a), for sample T1-D0-CP50, there is no obvious clogging in either the horizontal or vertical migration trajectories. At the same time, the distribution of the strong force chain network (Figure 3.23(a)) reveals a relatively uniform pattern, with no clear aggregation or dominant direction of force transmission. However, for the triaxial compression sample T2-D1-CP50-1, Figure 3.22(b) clearly shows clogging in the vertical direction of particle migration, and the upward migration paths are not smooth. This is because, as shown in the strong force chain network in Figure 3.23(b), under triaxial compression, a large number of strong force chains are formed in the vertical direction within the sample. As a result, particles face greater resistance when moving upward, slowing their velocity; in other words, a larger hydraulic gradient is required to drive their migration. In contrast, for the triaxial extension sample, horizontal clogging is observed in Figure 3.22(c), but the upward migration trajectories remain relatively smooth. This is because, according to the force chain distribution in Figure 3.23(c), the strong force chains form a principal force transmission direction in the horizontal plane, which restricts particle movement in that direction. From the above observations, it is clear that if the strong force chain network does not form a principal force transmission direction aligned with the flow direction, particle migration trajectories tend to be smoother and face less obstruction. As a result, erosion can occur at a lower critical hydraulic gradient. This explains why the initial critical hydraulic gradient under triaxial compression is greater than that under isotropic compression or triaxial extension.

3.5 Summary

This chapter conducted a coupled CFD-DEM simulation with the aim of investigating the influence of initial stress anisotropy on suffusion of gap-graded sandy soil. Three stress states (i.e., isotropic, triaxial compression, and triaxial extension) were considered. A continuous variable water head was introduced to study the critical hydraulic gradient for samples under different stress conditions. The observed macroscopic phenomenon of mass loss, void ratio variation, and the difference between critical gradients is interpreted from a microscopic perspective, including connectivity, contact fabric, local force chains, and erosion path. According to the analysis, the following conclusions can be drawn:

(a) Under isotropic compression and triaxial extension stress states, the difference in void ratio between different layers decreases after suffusion compared to before suffusion. In contrast, under triaxial compression stress, the difference in void ratio between different layers increases.

(b) Compared to the initial isotropic stress state, the sample with initial stress anisotropy experiences a significant increase in final mass loss. As particle loss progresses, the degree of initial stress anisotropy gradually decreases and tends toward isotropy. This microscopic mechanism can be attributed to the formation of an internally stable, spatially isotropic force structure.

(c) The turning point of the mass loss curve, along with the turning point of the average particle surface velocity, can serve as characteristic states for defining the initial critical hydraulic

gradient. When comparing the erosion behavior under the three stress states, the critical hydraulic gradient under the triaxial extension stress state is closer to that under the isotropic stress state, but lower than that under the triaxial compression stress state. This microscopic mechanism can be attributed to the fact that under triaxial compression stress, the strong force chain network tends to align with the main direction of seepage, thereby increasing the resistance to erosion. At the same time, after the seepage flow is applied, the response of the coordination number is greater under triaxial extension and isotropic compression stress states than under triaxial compression, leading to more fine particles detaching from coarse particles. As a result, the critical hydraulic gradient required for triaxial extension and isotropic compressive states is smaller than that for triaxial compression

Table 3.1 Summary of the simulated stress conditions

Test	σ_r(kPa)	σ_a(kPa)	Consolidation ratio (σ_a/σ_r)	Stress ratio (η)	Flow direction
T1-D0-CP50	50	50	1	0	Up
T2-D1-CP50-1	50	75	1.5	0.43	Up
T3-D1-CP50-2	50	90	1.8	0.63	Up
T4-D3-CP50-1	50	37.5	0.75	-0.27	Up
T5-D3-CP50-2	50	28.7	0.57	-0.50	Up
T6-D0-CP100	100	100	1	0	Up
T7-D1-CP100-1	100	150	1.5	0.43	Up
T8-D1-CP100-2	100	180	1.8	0.63	Up
T9-D3-CP100-1	100	75	0.75	-0.27	Up
T10-D3-CP100-2	100	57.3	0.57	-0.50	Up
T11-D0-CP150	150	150	1	0	Up
T12-D1-CP150-1	150	225	1.5	0.43	Up
T13-D1-CP150-2	150	270	1.8	0.63	Up
T14-D3-CP150-1	150	112.5	0.75	-0.27	Up
T15-D3-CP150-2	150	86	0.57	-0.5	Up

Table 3.2 Input parameters used in the simulation

	Parameter	Unit	Value
DEM domain			
	Young's modulus	N/m^2	1×10^8
	Poisson's ratio	-	0.3
	Particle density	kg/m^3	2650
	Friction coefficient	-	0.5
	Restitution coefficient	-	0.3
	Particle diameter	1.6~2.0 mm	1.6~2.0 0.03~0.33
	Timestep	s	2×10^{-7}
CFD domain			
	Density	kg/m^3	998
	Dynamic viscosity	Pa·s	1×10^{-3}
	Timestep	s	2×10^{-5}
Wall boundary			
	Young's modulus	N/m^2	1×10^{10}
	Friction coefficient	-	0

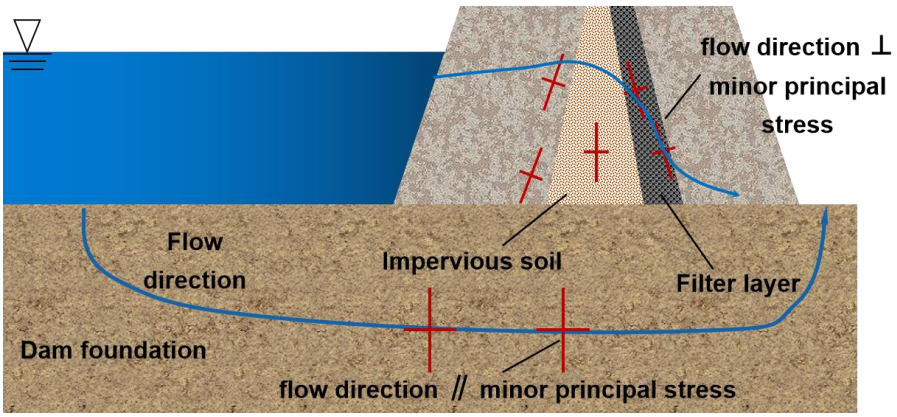

Figure 3.1 Schematic of seepage flow along with different principal stresses in a dam

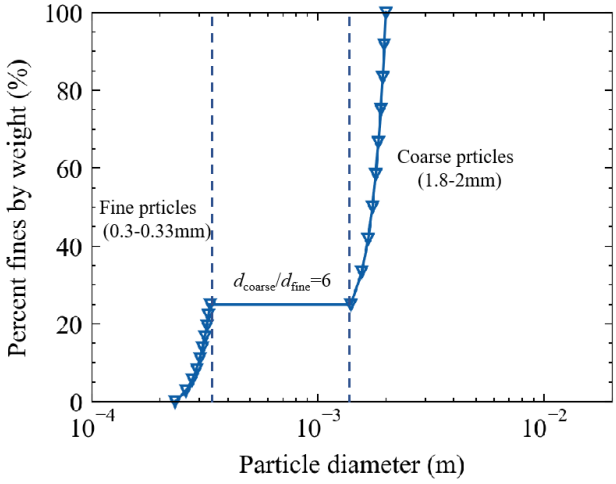

Figure 3.2 Particle size distribution curves for the tested soil

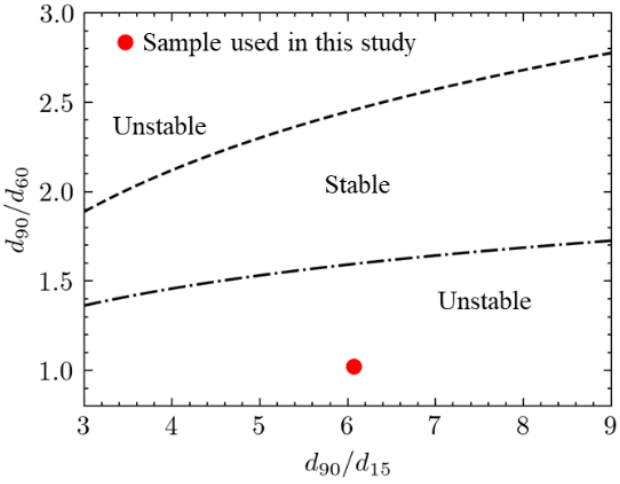

Figure 3.3 Assessment of unstable soils for samples used in this study by the Burenkova method

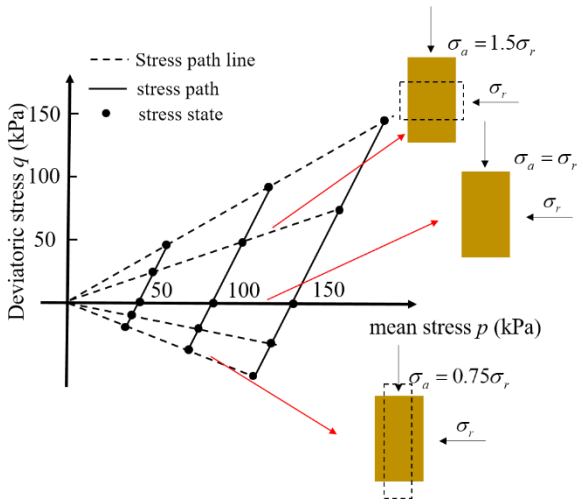

Figure 3.4 Stress states adopted in simulations.

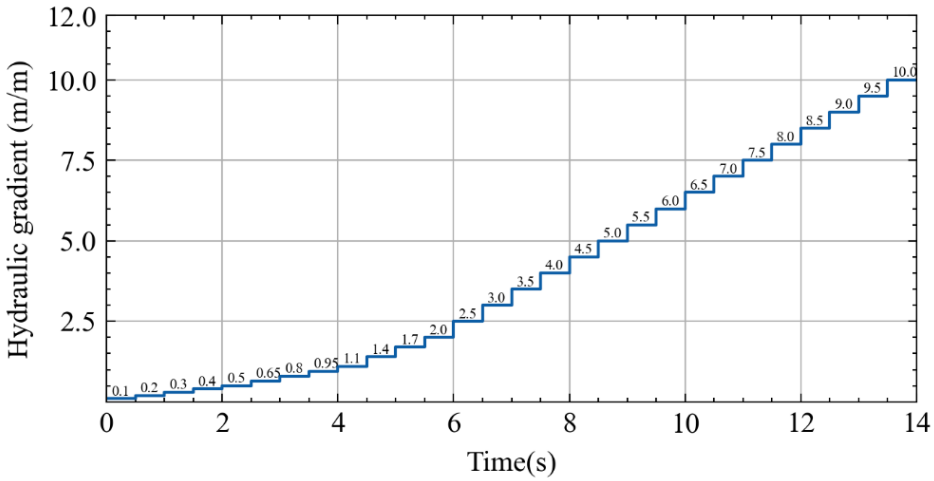

Figure 3.5 The imposed hydraulic gradient in CFD-DEM simulations

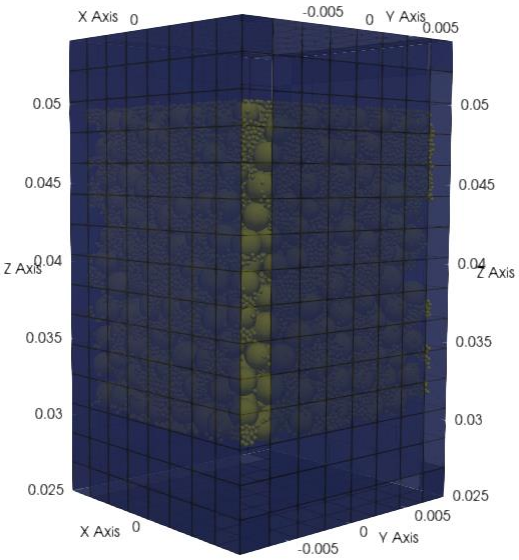

Figure 3.6 CFD-DEM simulation model

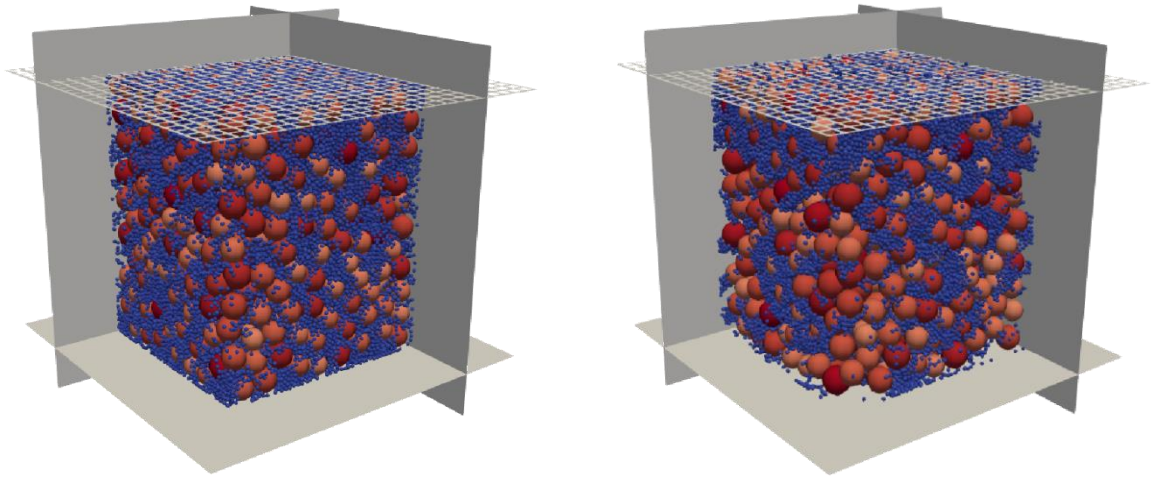

(a) (b)

Figure 3.7 Schematic diagram of fines loss: (a) before suffusion; (b) after suffusion

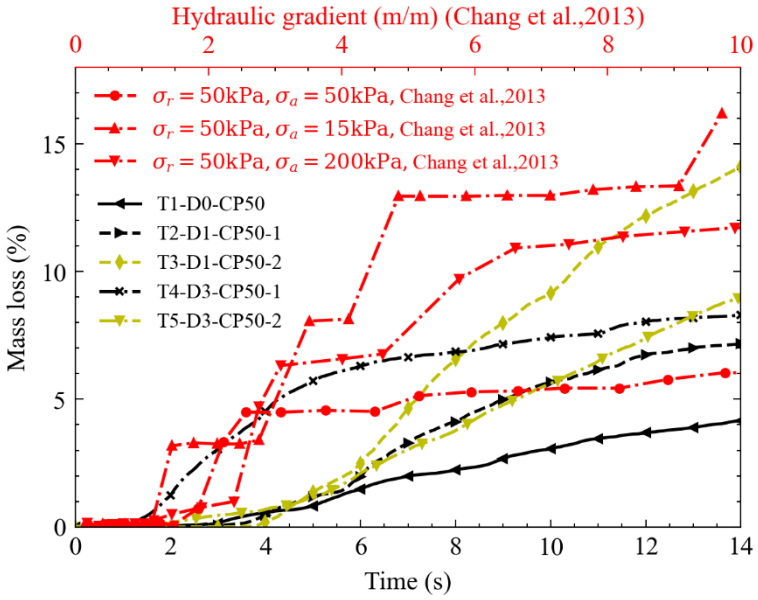

Figure 3.8 Evolution of fines loss versus time

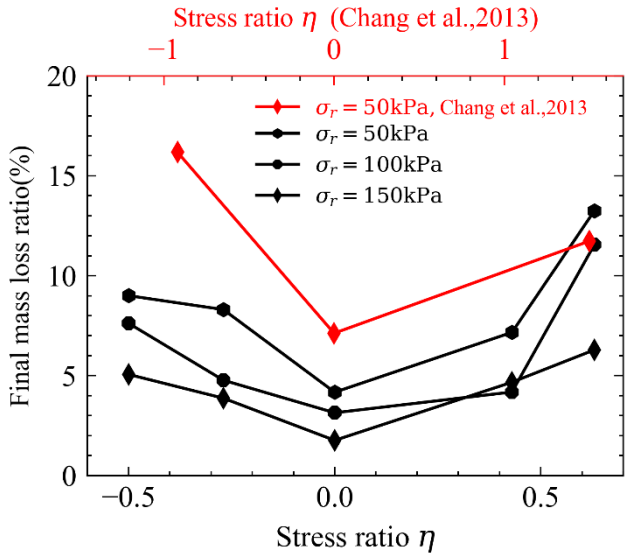

Figure 3.9 Ultimate fines loss under different stress ratios

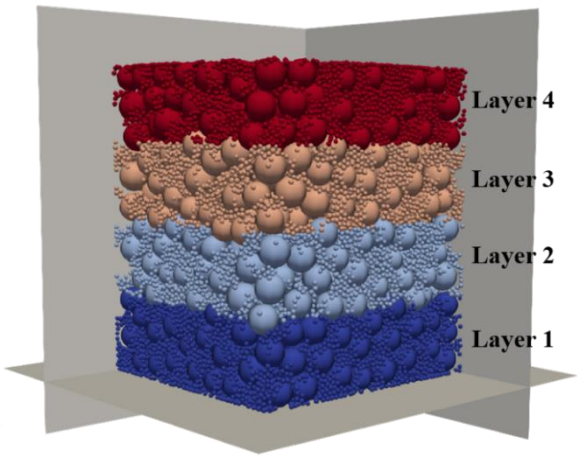

Figure 3.10 Different layers of the specimen

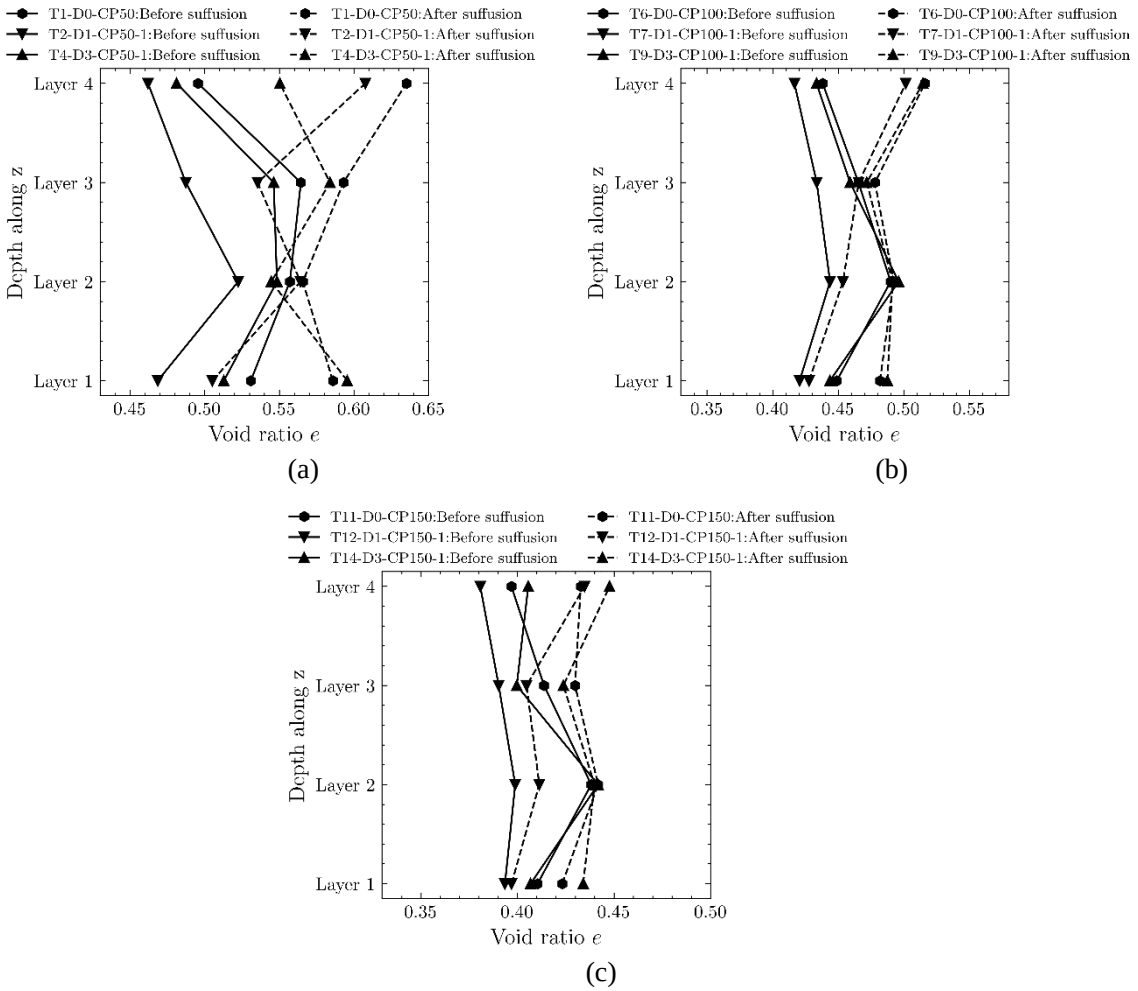

Figure 3.11 Distribution of the void ratio: (a) $\sigma_r = 50$kPa ; (b) $\sigma_r = 100$kPa ; (c) $\sigma_r = 150$kPa

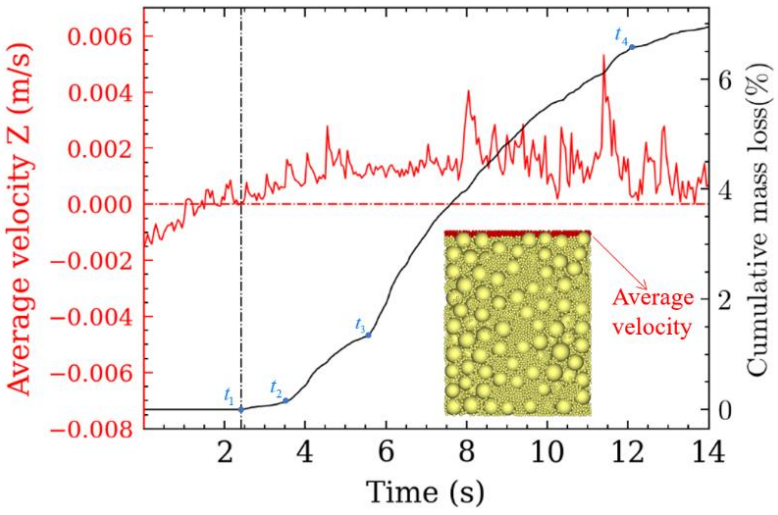

Figure 3.12 Determination of the critical hydraulic gradient

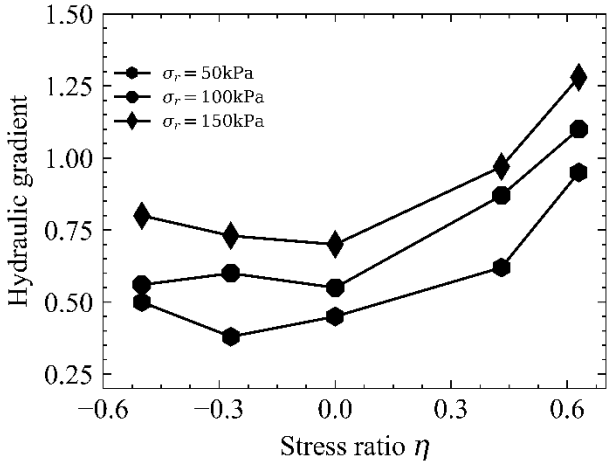

Figure 3.13 Relationships between the initial hydraulic gradient and the shear stress ratio

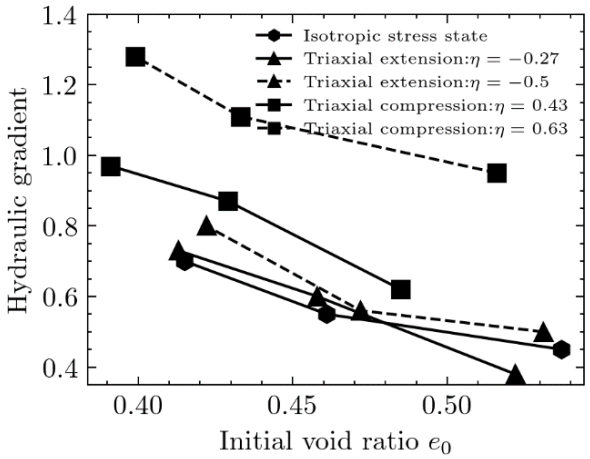

Figure 3.14 Relationships between the initial hydraulic gradient and the initial void ratio

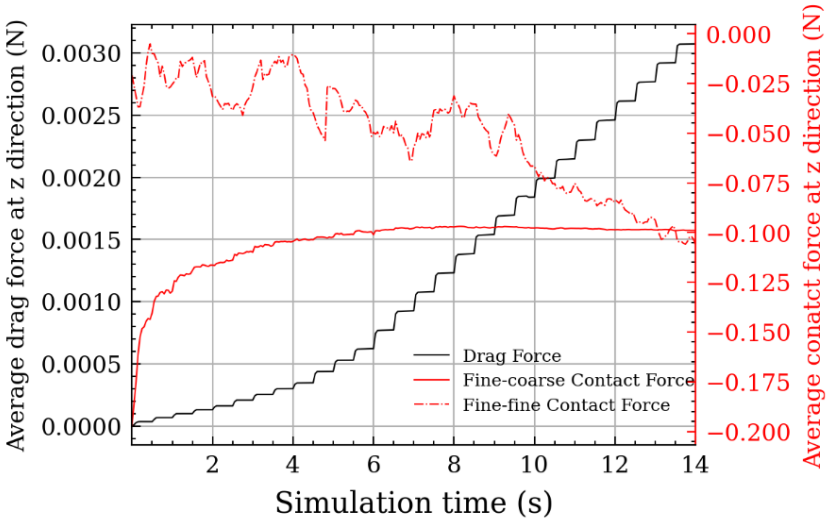

Figure 3.15 The evolution of total drag force and contact force at z-direction

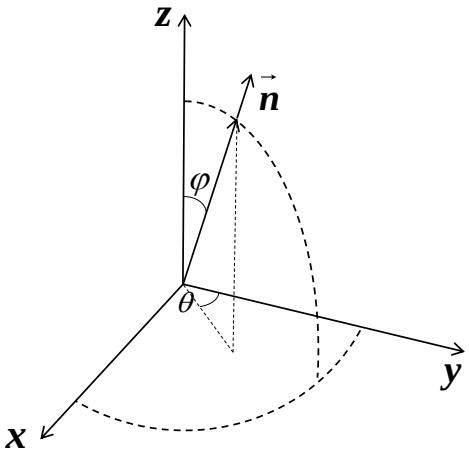

Figure 3.16 Characterization of Particle Contact Orientation in 3D Space

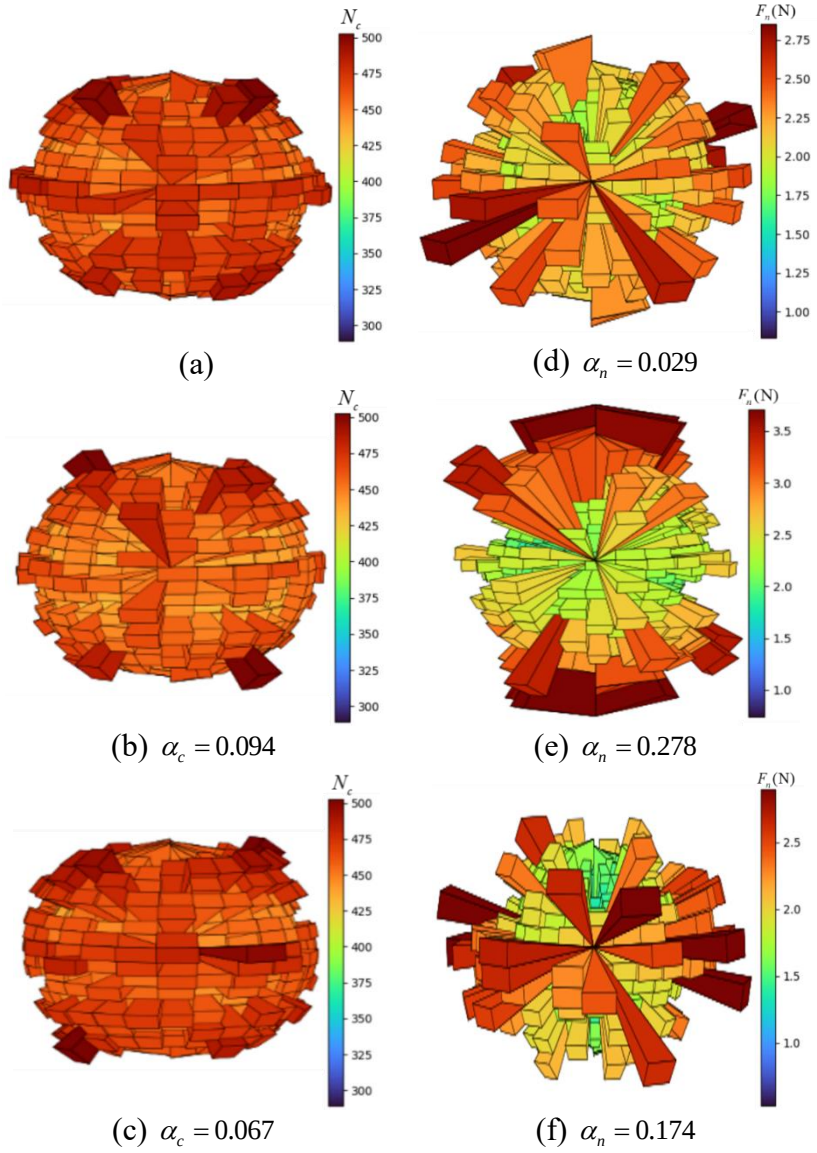

(a) (d) $\alpha_n = 0.029$

(b) $\alpha_c = 0.094$ (e) $\alpha_n = 0.278$

(c) $\alpha_c = 0.067$ (f) $\alpha_n = 0.174$

Figure 3.17 Contact fabric information for specimens under (1st row of T1-D0-CP50; 2nd row of T2-D1-CP50-1; 3rd row of T4-D3-CP50-1;1st column for contact number; 2nd column for normal contact force):

(a) $\alpha_c = 0.071$; (b) $\alpha_c = 0.094$; (c) $\alpha_c = 0.067$; (d) $\alpha_n = 0.029$; (e) $\alpha_n = 0.278$; (f) $\alpha_n = 0.174$

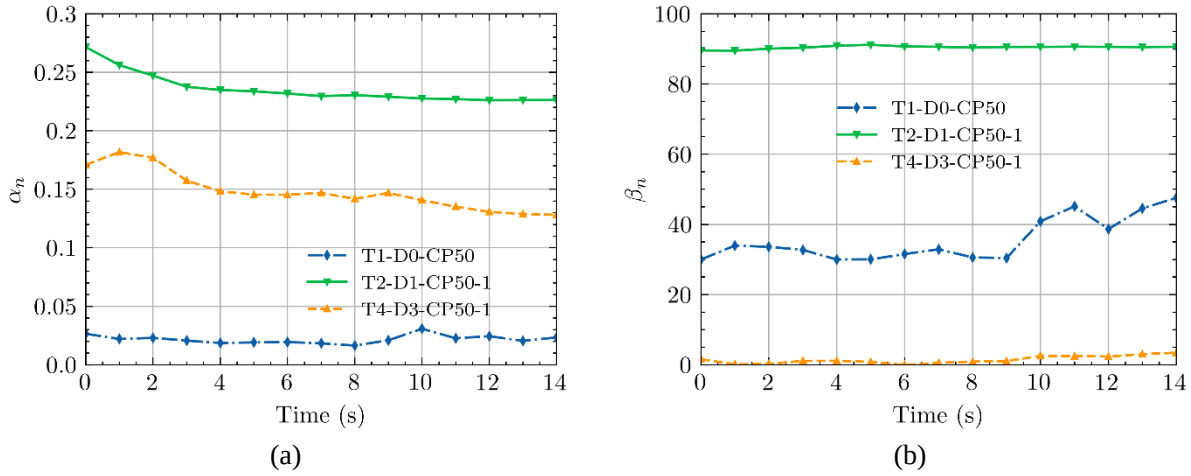

Figure 3.18 Evolution of parameters defining the magnitude and principal direction of anisotropy during suffusion: (a) α_n; (b) β_n

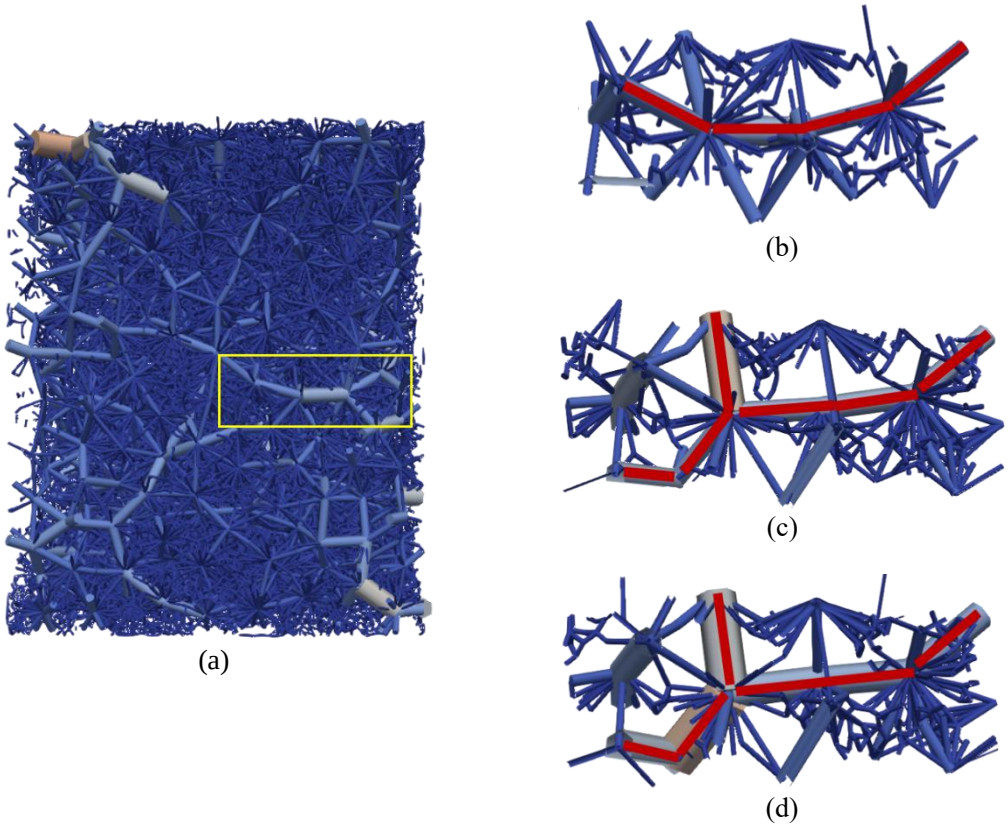

Figure 3.19 Evolution of force chains: (a) overall force chain distribution(t=0s); (b) local force chains (t=0s); (c) local force chains (t=6s); (d) local force chains (t=12s)

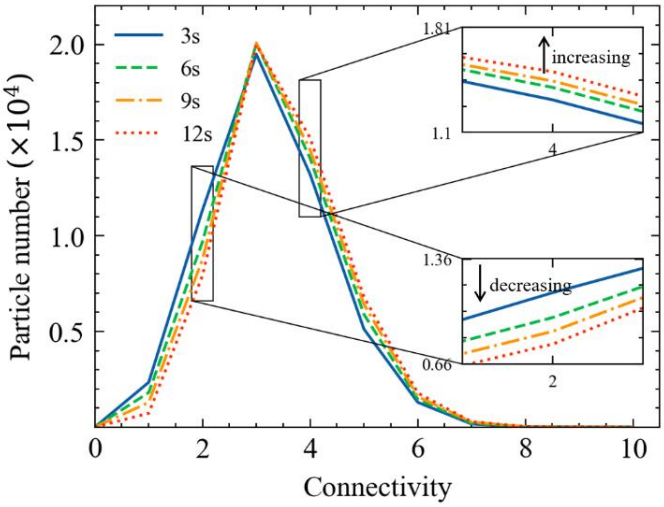

Figure 3.20 Evolution of particle connectivity

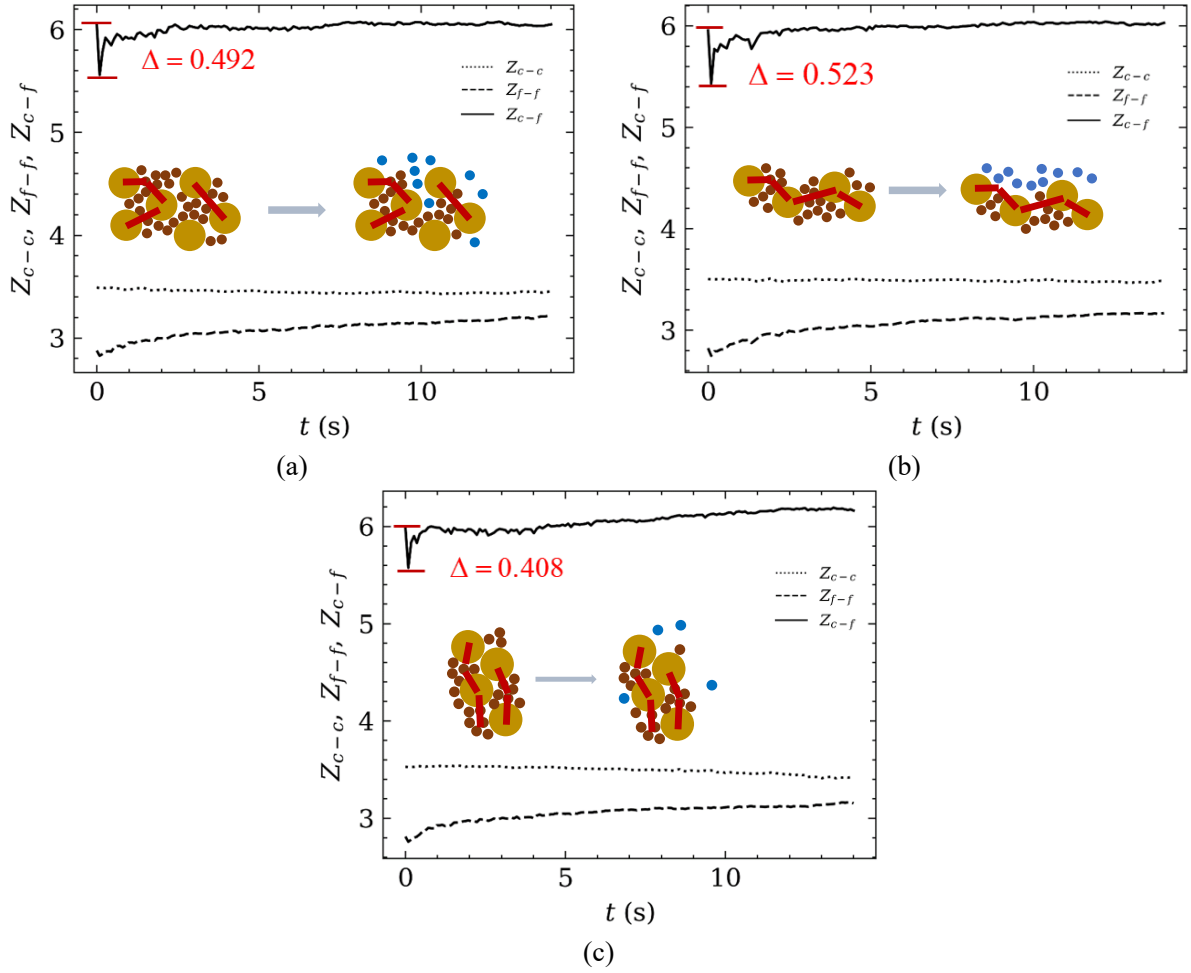

Figure 3.21 Evolution of coordination number with elapsed time: (a)T1-D0-CP50; (b) T4-D3-CP50-1;(c) T2-D1-CP50-1

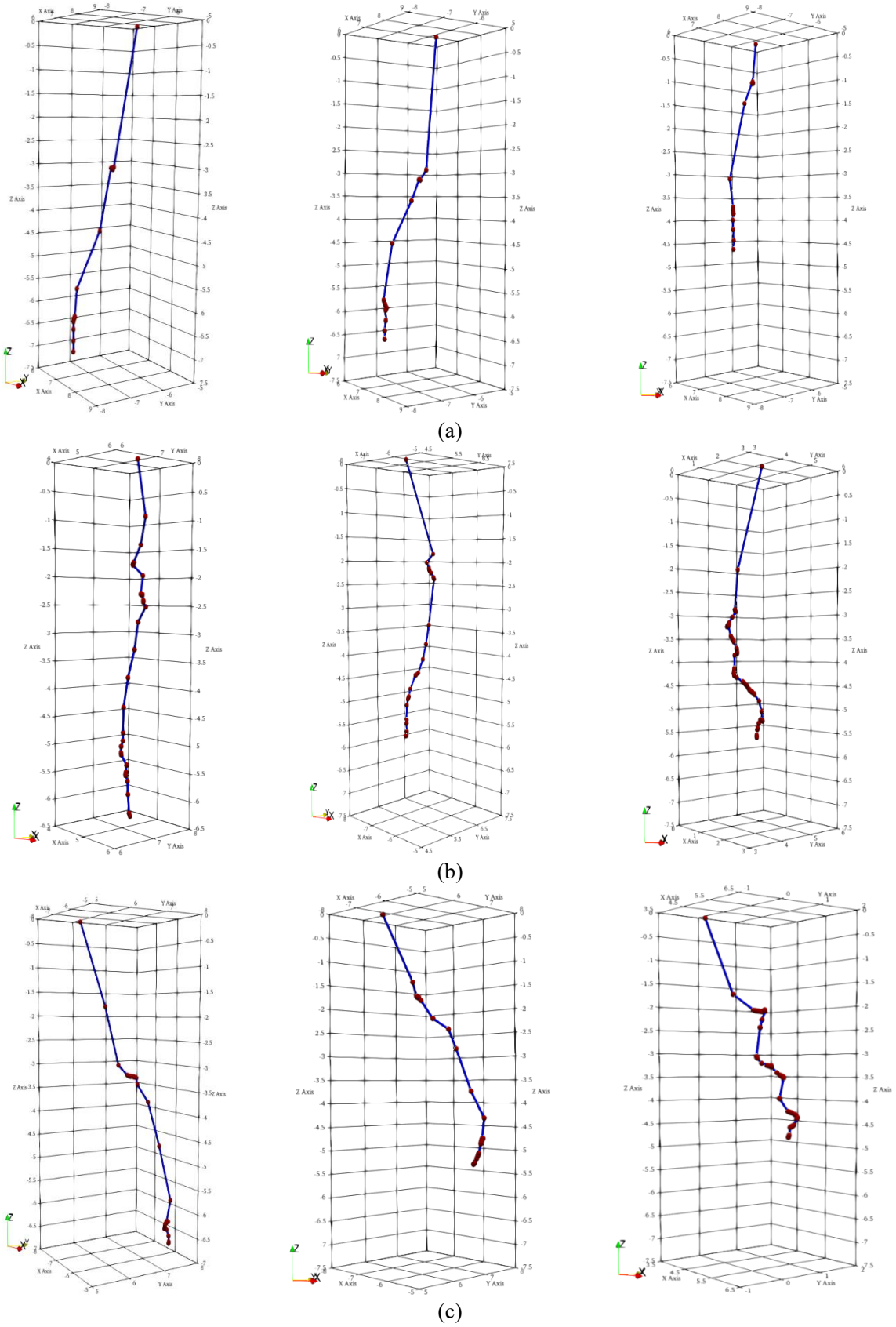

Figure 3.22 Erosion path of fine particles: (a) T1-D0-CP50; (b) T2-D1-CP50-1; (c) T4-D3-CP50-1

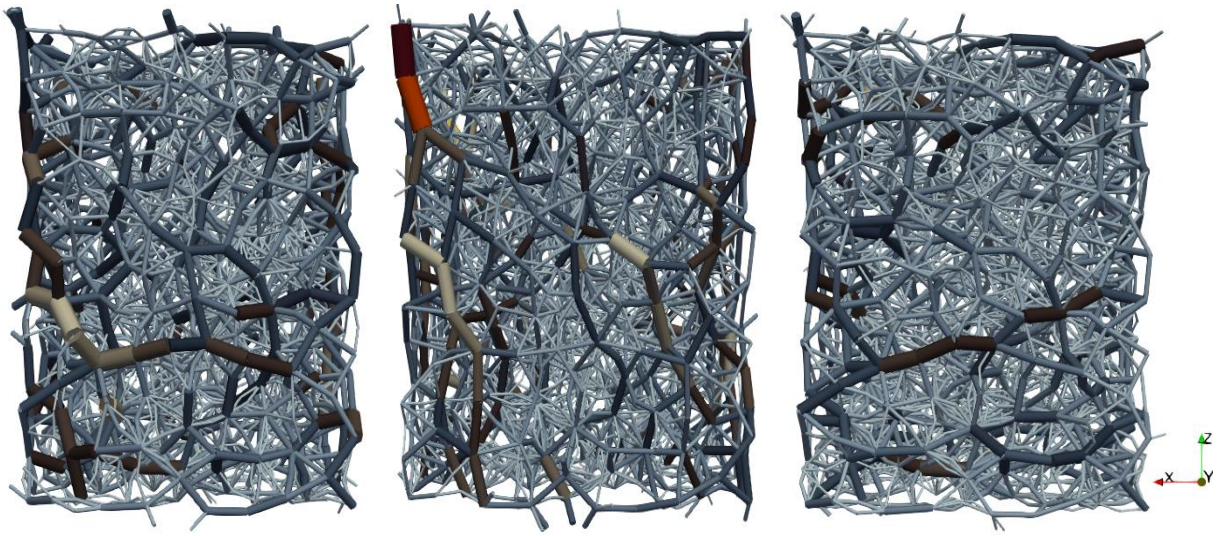

(a) (b) (c)

Figure 3.23 Distribution of strong contact force: (a) T1-D0-CP50; (b) T2-D1-CP50-1; (c) T4-D3-CP50-1

CHAPTER 4 INVESTIGATION ON INFLUENCE OF PARTICLE FABRIC ANISOTROPY ON SUFFUSION

4.1 Introduction

Due to the influence of deposition, natural sand typically exhibits significant fabric anisotropy characteristics. Microscopically, this feature manifests as the oriented arrangement of particles, while macroscopically, it is reflected in the presence of multiple sedimentary layers or different bedding planes in the soil. Existing studies have shown that the fabric anisotropy of sand is closely related to the shear strength, dilatancy, and critical state of the soil (Anandarajah and Kuganenthira, 1995; Yang et al., 2008; Pegah et al., 2024). Ahmed's research (2013) shows that soil permeability is also affected by fabric, specifically, greater fabric anisotropy leads to higher permeability. Therefore, when suffusion occurs in sand with initial fabric anisotropy, the fabric anisotropy not only affects the soil's strength and resistance to erosion and but also alters the seepage characteristics of the fluid. Liang et al. (2017a) further suggested that the fabric anisotropy of the soil may accelerate the development of dominant seepage channels, thus increasing the likelihood of erosion damage to the soil. Although fabric anisotropy is widespread in sand, its impact on suffusion and particle migration has not been fully studied. To address this, this chapter will use CFD-DEM method to explore the effect of initial particle fabric anisotropy on the suffusion process.

4.2 Suffusion simulation scheme for fabric anisotropic soil

4.2.1 Model setup

The primary objective of this chapter is to investigate the influence of particle fabric anisotropy on erosion. Since fabric anisotropy arises from the regular arrangement of particles, the simplified spherical particles typically used in DEM simulations cannot accurately replicate the fabric anisotropy of natural sand (Liang et al., 2021). To address this, non-spherical particles—specifically, elongated polyhedral particles (Figure 4.1)—are employed. Initial samples with controlled fabric structures are generated by prescribing the orientation of these non-spherical particles. Two aspect ratios (AR) are selected to produce samples with varying bedding directions: AR = 1.5 and AR = 2.0. The aspect ratio is defined as the ratio of the particle's long-axis length to its short-axis length in the x-z plane. Additionally, the particle bedding direction is defined as the angle between the particle's major axis and the horizontal direction (Figure 4.2). This study retains the same gap-graded soil as in Chapter 3, with the particle size distribution shown in Figure 3.2.

In order to generate the anisotropic sample, particles with initial orientation are firstly dispersed in a cube enclosed by rigid walls, then the top and bottom walls are driven to pre-compress the soil to a medium-dense state under a low-stress level (10kPa). During this process, the rotation of particles is locked (as shown in Figure 4.3(a)) and the gravity is disabled to ensure the soil's fabric structure. The stress is then gradually increased to a pressure of 100kPa, while the limitation of rotation is also removed to permit the particles to adapt to a dense state, consistent

with natural soil conditions (as shown in Figure 4.3(b)). There are 10 groups of specimens in total, considering 5 different anisotropy degrees and 2 different aspect ratios. Table 4.1 lists the description of all cases. Considering that the soil on site is usually in a K_0 stress state, the surrounding walls, therefore, remain stationary in the simulation. Subsequently, the gravity is switched on and ensures that the specimen reaches gravitational equilibrium before suffusion. Note that the fines are filled in the voids of the soil matrix, meaning that it is hard for them to remain an obvious anisotropy after applying the external loading and gravity, especially compared to the coarse matrix. While it's also worth noting that it is the coarse fraction that plays a significant role in impeding particle migration, indicating that it's more meaningful to focus on the anisotropy degree of coarse particles. Figure 4.4 exhibits 3D rose figure of orientation for coarse particles, from which it can be seen that the fabric anisotropy of the soil matrix is consistent well with the predefined bedding angle after reaching the equilibrium state.

The setup of the fluid domain is similar to that in Chapter 3. The CFD domain has the same length and width as the DEM domain but has an extra height of 20mm so that the particle assembly can be completely covered by the fluid. Then the CFD area is discretized into cells with a size of 2mm×2mm×2mm. The pressure-inlet and pressure-outlet conditions are specified for the bottom and top boundary, respectively, then a laminar flow is triggered due to the pressure difference. A constant hydraulic gradient of 8m/m is adopted to induce adequate particle loss for soils under constant axial stress of 100kPa within a limited simulation time. As shown in Figure 4.5, under the action of the seepage flow, fine particles continuously migrate out through the

upper filter. The filter mesh size is 1.2mm×1.2mm, which ensures that fine particles can pass through freely, while coarse particles cannot. As for the parameters used in the numerical model, all parameters remain consistent with those set in Chapter 3 (see Table 3.2), except for the rolling resistance. Since the effect of particle shape is already accounted for by the aspect ratio of the particles, the rolling resistance r_c is set to zero in this chapter.

4.3 Numerical results and discussion

4.3.1 Cumulative eroded mass loss

The evolution of fine particle loss versus elapsed time is illustrated in Figure 4.6. As is to be expected, the slope of the curve is high at the beginning and the difference between soil samples with different particle shapes and bedding angles is negligible during this phase. Subsequently, the slope of the curve gradually decreases and levels off. However, compared to cases with an aspect ratio of 2.0, the specimen with an aspect ratio of 1.5 still has a larger rate of fines loss at the end of suffusion, which means that it probably needs more simulation time to reach the final steady state. It can be found that the mass loss of the specimens increases with increasing bedding angle for a particular aspect ratio. For example, the mass loss for the sample with bedding angle=0° and AR=1.5 is only 20.36%, whereas, for a bedding angle of 90°, the mass loss increases to 35.36%, suggesting that the fabric arrangement of the coarse particles can play a role in hindering the migration of the internal fine particles. The ultimate mass loss for all specimens is calculated in Figure 4.7, from which it can be seen that the effect of bedding angle on specimen mass loss decreases as the aspect ratio increases from 1.5 to 2.0. The difference between the maximum and minimum mass loss is 15% at AR=1.5, while at AR=2.0 this

difference is reduced to approximately 7.7%. In addition, the final mass loss of the specimens with AR=2.0 is overall less than that of the specimens with AR=1.5 (except at a bedding angle of 0). Therefore, the increase in the particle aspect ratio can also help to restrict soil particle loss (Qian et al., 2021b; Xiong et al., 2024).

4.3.2 Fine particles distribution

Figure 4.8 shows the variation of particle distribution at different levels. Firstly, a specific plane is chosen from the initial samples and scaled up to study the transportation of particles. It can be seen from Figure 4.8(b) that in the early stages of seepage erosion, the velocity of particles is relatively high, while as the suffusion develops, there is a significant decrease in velocity in the range of 4s~10s. This is because, when a hydraulic pressure differential is applied and suffusion is triggered, the erodible fine particles with low connectivity, respond immediately by migrating with the permeable water flow. As a result, the fine particles in the upper part move at a high velocity. As the number of particles with a low connectivity decreases, the remaining are more resistant to erosion and therefore, the rate of particle migration gradually decreases. Furthermore, the results also indicate that the loss of particles is extremely inhomogeneous, for example, in the region annotated in Figure 4.8(b), significant loss of fine particles occurs and vast pores are formed between coarse particles due to a lack of filling. More specifically, Figure 4.8(c) plots the local particle distribution, from which it is clear that at individual location points the fine particles are completely eroded and the soil skeleton, consisting of coarse particles, is exposed. Nevertheless, it is also noteworthy that at some location points, such as those at the bottom of the specimen, there appears to be no significant change in the fine content. In Figure 4.9, the

contours of fine content are plotted, from which it can be seen that the initial fine particle distribution of the specimens with different bedding angles is relatively uniform before suffusion, while after suffusion, the fine content varies considerably. Firstly, there is a sharp reduction in the area near the outlet boundary, from an initial level of around 25% to less than 10%. On the contrary, near the bottom boundary, there is instead a massive growth in the fines content, up to 50% at some locations. It can therefore be seen that although, on the whole, the specimen suffers particle loss, the migration of fine particles within the soil can be very disordered due to the presence of the particle skeleton, i.e., over-loss as well as over-filling (clogging) can occur simultaneously. A similar observation has also been reported by other studies (Ke and Takahashi, 2014a; Rochim et al., 2015; Liang et al., 2019; Hu et al., 2020a; Liu et al., 2020).

Figure 4.10 presents fine particle distribution along the Z direction pre- and post-suffusion. Taking specimens with AR=1.5 as an example, it can be seen that the number of fine particles (N_f) before suffusion is homogeneously distributed at different depths, with no obvious aggregation, except at the top and bottom boundaries, where there are slightly more fine particles due to particle-wall contact. After suffusion, the distribution of fine grains shows a distinct 'triangle-like' characteristic (Xiong et al., 2020; Zhang et al., 2020), i.e., the closer to the top seepage outlet boundary, the fewer particles. It is noteworthy that when the deposition direction has a large angle with the infiltration flow (e.g., specimens with bedding angles of 0° and 30°), the change in fine particle number at the bottom before and after suffusion is not as pronounced as for specimens with smaller bedding angles, indicating that when the long axis of coarse

particles is aligned horizontally, it can have a stronger obstructive effect on fines, limiting their movement and thus reducing particle loss.

4.3.3 Soil deformation

During suffusion, the soil maintains the K_0 stress state, and a fixed pressure of 100kPa is applied to the upper and lower plates to simulate the overlying soil weight. Therefore, when there is particle loss, the sample will deform axially under the pressure. As illustrated in Figure 4.11, the axial strain for specimens with different aspect ratios increases with increasing bedding angle. Compared to the aspect ratio, the bedding angle has a more profound effect on suffusion since the axial deformation of the isotropic specimen is 0.94% at an aspect ratio of 1.5 and 1.27% at 2.0. Whereas, when the fabric angle changes from 0° to 90°, the axial deformation increases from 0.4% to 1.28% and 0.67% to 1.4% for AR=1.5 and AR=2.0, respectively. In addition, specimens with AR=1.5 exhibit smoother axial strain evolution compared to those with AR=2.0, which show a more staged progression. As can be seen in Figure 4.11(b), the specimens' deformation rate is high for the first two seconds, then drops rapidly and rises again in the final period. This is because the loss of fines will destabilize the original load-bearing skeleton, then the coarse particles have to adjust the contact direction to form a new force structure, and if the particles have a relatively high aspect ratio, the particle misalignment will release more strain energy (Liu et al., 2020), resulting in a substantial deformation.

4.3.4 Void ratio variation

In the case of mixtures of coarse and fine particles, the former may form a solid skeleton that bears the main external load, while the bulk of the fine particles may be confined to the matrix

between the coarse, acting merely as fillers (Skempton and Brogan, 1994; Taha et al., 2019). Therefore, a global void ratio e may not be sufficient to characterize the evolution of different compositions (Thevanayagam and Mohan, 2000). According to Taha et al.(Taha et al., 2019), the intergranular void ratio $e_{c,}$ defined by assuming all the fine particles acted as the inter-coarse voids, and the inter-fine void ratio e_f, defined by assuming the coarse particles are of zero volume, are introduced in this study to investigate the density of the coarse-grained matrix and fine-grained matrix, respectively. The above parameters can be written as:

$$e = \frac{V_V}{V_s^f + V_s^c} \tag{4.1}$$

$$e_c = \frac{V_V + V_s^f}{V_s^c} = \frac{e + f_c}{1 - f_c} \tag{4.2}$$

$$e_f = \frac{V_V}{V_s^f} = \frac{e}{f_c} \tag{4.3}$$

where V_V is volume of actual voids; V_s^c or V_s^f is volume of coarse or fine particles.

Figure 4.12 shows the variation of e, e_c, e_f versus simulation time for specimens with AR=1.5. It's found that both void ratio e and inter-fine void ratio e_f are gradually rising due to particle loss. While void ratio e remains relatively consistent across samples with different bedding angles, inter-fine void ratio e_f shows significant variation, indicating the inter-fine void ratio can be a more accurate description of the loss of the fines for gap-graded soils. In addition, it can be seen that inter-coarse void ratio e_c keeps decreasing during suffusion, which indicates that while the fine-grained matrix is getting looser, the coarse-grained matrix is getting denser. This is mainly attributed to the fact that the loss of fines leads to the coarse particles taking on more force transmission and therefore the coarse-grained skeleton shrinks, increasing the contact forces.

4.3.5 Variation of hydraulic conductivity

For non-cohesive soils, suffusion may render a loose soil structure with increased porosity and hydraulic conductivity due to the large amounts of loss in fines. In turn, the increased hydraulic conductivity can further exacerbate soil erosion. Figure 4.13 shows the evolution of the overall hydraulic conductivity for samples at different bedding angles. The hydraulic conductivity k considered in this study is calculated as follows:

$$k = \frac{q_w}{A_c i} \tag{4.4}$$

where q_w is the volume flow rate; A_c is the area of the sample cross-section, and i is the hydraulic gradient.

As can be seen from the results, there is a clear step change in the hydraulic conductivity for different specimens. This is because, particle blockages can form at local locations within the specimen, and as the particles continue to be lost, more and more flow channels will be formed, leading to the local blockages being flushed out and resulting in a sudden increase in permeability. Furthermore, the evolution in conductivity of specimens with different bedding angles varies considerably. For example, when the bedding angle is 0°, the permeability shows limited change in the early stage of seepage and then increases significantly in the later stage. When the bedding angle is 90°, the permeability experiences a rapid increase at the beginning of erosion but remains relatively stable in the subsequent process. When the bedding angles are 30° and 60°, the permeability progressively increases throughout the process. Based on these different variations, three typical modes of particle transport at the microscopic level can be identified (as shown in Figure 4.14, note that these illustrated particle clumps are selected from the same position of

samples): (I) When the coarse particles are arranged perpendicular to the direction of the seepage flow, fluid is hindered, and the fine particles around the coarse matrix basically do not migrate throughout the suffusion, corresponding to a stable conductivity. Figure 4.15 illustrates the trajectory of fine particles, from which it can also be seen that the paths of the fine particles in this mode are more dispersed and no major dominant seepage channels are formed within the specimen; (II) When the coarse particles are aligned in the 30° and 60° directions, a preferential flow channel is formed along the long axis of the coarse particles (as shown in Figure 4.15(b)), and fine particles gradually flow away from the pore space following the coarse particle contours. The migration of fine particles and hydraulic conductivity of the sample shows a progressive variation; (III) When the coarse particles are configured in the same direction as flow, the soil matrix has a little hindering effect on erosion. Therefore, in the early stages of suffusion, the fine particles will transport following a vertical path (Figure 4.15(c)), so that hydraulic conductivity experiences significant growth at the very beginning.

4.3.6 Soil mechanical response to suffusion

The mechanical response of the soil will inevitably be affected by the escaping of fines, as the stress-strain relationship is closely related to the fines content for coarse-fine mixture according to previous studies (Gong et al., 2019). In this study, a series of drained triaxial tests, both for pre- and post-erosion samples, are carried out to explore the effect of bedding angle and suffusion on the soil's mechanics. Taking specimens with AR=1.5 as examples, it can be found in Figure 4.16 that all the samples, both before and after erosion, exhibit a stiff response at the beginning

and then reach a peak stress ratio at the axial strain of about 7%, followed by softening until a critical state is reached. The corresponding volume strain change also has similarities, that is, shear dilatation occurs after shear contraction. Comparing the stress ratios before and after erosion, it can be seen that the specimens that have undergone suffusion show a significant reduction in peak strength. Furthermore, as listed in Figure 4.17, the strength is not only reduced by the fines loss but is also influenced by the particles' fabric, as the maximum stress ratio decreases with the increase of bedding angle both for samples with AR=1.5 and 2.0. These results are consistent well with physical experiments (Oda, 1972; Yin et al., 2010). Moreover, the effect of fabric on soil strength becomes more pronounced as the particle shape changes. Because as the bedding angle has increased from 0° to 90°, the peak stress ratio decreases from 1.91 to 1.82 for samples with AR=1.5, a reduction of 4.7%, whereas for samples with AR=2.0, the peak ratio decreases from 1.97 to 1.78, a reduction of 9.6%.

4.3.7 Force chain networks

The redistribution of the force chain within the soil will be triggered because of the fines loss, which is an important potential hazard for engineering safety. The microscopic strong force chain is analyzed in Figure 4.18. Comparing the results of pre- and post-suffusion, it can be found that the loss of fine particles results in a dispersed force structure, especially near the seepage outlet, where the number of strong force chains decreases. However, overall, the impact of erosion on the force chain network is relatively limited. This is primarily because coarse particles are the key components of the force chains. Within the constraints of fixed boundaries and constant stresses, the migration of coarse particles is minimal, so that the loss of fine particles does not

lead to the collapse of the soil matrix. The damage caused by erosion to the soil is progressive, as it transfers some of the load originally carried by the fine particles and increases the contact forces between the coarse particles. In contrast, Figure 4.18 also shows the distribution of the force chains after triaxial shear, from which it can be seen that the force chain network has been totally reconstructed after shear.

To further study the changes in strong force chains in different contact types (coarse particle-coarse particle contact, coarse particle-fine particle contact, and fine particle-fine particle contact) after erosion, Figure 4.19 shows the proportion of different contact types in the strong contact force chains. It can be seen that coarse particles are involved in the vast majority of the strong chain, but it is worth noting that the f-f contact still contributes about 20% of the strong chain before erosion. In addition, the greater the fabric bedding angle, the higher the contribution of f-f and the lower the contribution of c-f, indicating that the role of fine particles in the soil structure is closely related to the arrangement of coarse particles. When the coarse particles are aligned along the direction of load application (bedding angle is 90°), it is not conducive to load transfer and soil strength (as can also be seen from the analysis of the maximum stress ratio in Figure 4.17), so the fine particles then need to be involved in more strong chain contacts to maintain soil stability. The reduction in the percentage of f-f contact after suffusion is consistent with the cumulative mass loss, however, the transfer of forces occurs mainly in the c-f contact rather than the c-c contact. Thus, although the loss of fine particles initially has a small impact on the stress structure of the soil body, subsequent loss of fines has the potential to lead to the overall

destruction of the soil structure (as the remaining fines take on increasing force transfer) and therefore erosion problems in engineering need to be intervened in early and dealt with as soon as possible. It's also worth noting that, after the soil has been damaged to a critical state, the f-f contact only acts as a filler, contributing almost nothing to the load transfer (as can be seen in Figure 4.19c).

4.3.8 Variations in microscopic anisotropic parameters

This section uses the microscopic parameters α and β defined in Section 3.4.2 to explore the evolution of the soil's microscopic anisotropy, where α represents the degree of anisotropy and β represents the principal direction of anisotropy. Figure 4.20(a)-(b) show the fabric anisotropy (particle orientation) of the soil skeleton (coarse particles) during suffusion. It's clear that for samples with a specific bedding angle, the α is significantly greater than the sample without a bedding angle. In addition, the β is also consistent with the predefined angles, indicating that the aforementioned generation method produces soil samples with initial anisotropy very well. It's found that the orientation of the coarse particles remains almost unchanged throughout the seepage erosion process, despite the continuous loss of fine particles. While during triaxial shear, as shown in Figure 4.20(c)-(d), α of samples with initial anisotropy shows a tendency to evolve to isotropy. In contrast, α of samples without anisotropy tends to develop to anisotropy. In the meantime, the anisotropy principal direction β inclines to be perpendicular to the large principal stress.

4.3.9 Investigation of erosion law from a microscopic point of view

The erosion law describes the rate of fine particle loss during the erosion process. It can be used

to solve the mass balance equation in multi-field theory, thus simulating macroscopic seepage problems based on FEM (detailed introduction is provided in Chapter 6 of this thesis). This section will explore the impact of fabric anisotropy on the constants of the erosion law based on the CFD-DEM simulations. Uzuoka and Borja (2012), based on the results of laboratory experiments, proposed a semi-empirical expression for the erosion law:

$$\hat{n} = -\lambda_e (1-\phi)\left(f_c - f_{c\infty} \right)|q_w| \tag{4.5}$$

where f_c is the fines content and $f_{c\infty}$ is the final fines content when there is no more particle loss; ϕ represents the porosity; q_w denotes the volume flow rate; λ_e is a material constant. Eqn. (4.5) can be rewritten as:

$$\lambda_e = \frac{-\hat{n}}{(1-\phi)\left(f_c - f_{c\infty} \right)|q_w|} \tag{4.6}$$

Eqn. (4.6) indicates that the erosion law constant λ_e can be obtained through inverse analysis. In CFD-DEM simulations, the fine particle loss rate $\hat{n}$ can be obtained from the mass loss curve. Similarly, f_c, $f_{c\infty}$, ϕ and q_w can also be calculated in DEM and CFD, and based on this, the results of λ_e can be obtained. Figure 4.21 shows the λ_e of samples with different aspect ratios at different bedding angles. Since in this study, the f_c at t=10s from the numerical simulation is used to replace the $f_{c\infty}$ in Eqn (4.6), the results in Figure 4.21 only show the range from t=0-9s to avoid a zero denominator in the formula at t=10s. It can be observed that the λ_e calculated by CFD-DEM exhibits abnormal fluctuations at t=8-9s, mainly because the simulation cannot be run for as long as the laboratory experiments, which makes it impossible to ensure that the erosion rate is zero at the end of the erosion, leading to fluctuations in the final stages. However, between t=0-8s, the results obtained by CFD-DEM show little fluctuation and can be approximated as a constant. More importantly, this constant calculated by CFD-DEM is

numerically close to values adopted in other studies (Yang, 2019), indicating that CFD-DEM can effectively reflect the changes in fine particle erosion rates. This lays the foundation for proposing a new erosion law based on CFD-DEM in the following sections. By comparing samples with different bedding angles, it can be observed that although the particle fabric anisotropy can affect the final fine particle loss, soil strain, and so on, the impact of fabric anisotropy on the erosion law constant is minimal. The constants calculated for samples with different bedding angles are similar. This is mainly because the erosion law represents the mass (volume) of fine particles lost from the soil skeleton under the action of seepage water per unit time and per unit volume. Although an increase in particle fabric anisotropy reduces the fine content f_c and increases porosity ϕ, the volume flow rate also increases due to particle loss. Therefore, in Eqn (4.6), $(1-\phi)\left(f_c - f_{c\infty}\right)$ decreases, while $\left|q_w\right|$ increases, which ultimately leads to little variation in the erosion law constant across samples with different fabric anisotropies. This pattern suggests that when establishing a new erosion law in the future, the effect of sample fabric anisotropy can be neglected, simplifying the calculations.

4.4 Summary

Coupled CFD-DEM investigations into the influence of soil initial fabric anisotropy on suffusion were carried out in this chapter. Samples of gap-graded soils with particles of two different aspect ratios under five different bedding angles (0°,30°,60°,90°, and isotropic) were generated to simulate soil anisotropy and then eroded by an upward seepage flow with a constant hydraulic gradient. In addition, drained triaxial tests were conducted on samples before and after erosion to explore the stress-strain response to suffusion. Key concluding remarks are made as follows:

(a) The mass loss ratio is observed to decrease from 35.4% to 20.4% for AR=1.5, and from 29.6% to 23.2% for AR=2.0 as the bedding angle decreases from 90° to 0°. Meanwhile, the soil strain also decrease as the bedding angle decreases. The migration of fine particles causes the spatial distribution of fine particles in the sample to become more uneven, manifesting as localized over-erosion and local clogging phenomena.

(b) During the erosion process, the compaction of coarse and fine particles changes differently. Fine particles become more loosely packed due to particle loss, while coarse particles become more compacted as they bear more external forces. Compared to the average void ratio e, distinguishing it into fine particle inter-pore ratio e_f and coarse particle inter-pore ratio e_c can better reflect the variation patterns between different components of the gap-graded soil.

(c) By comparing the triaxial shear tests of samples before and after erosion, it is found that the peak strength of the samples is negatively correlated with the bedding angle, and the erosion of fine particles leads to a decrease in the peak strength of the soil. Additionally, during the triaxial shear process, comparing particles with different aspect ratios reveals that increasing the aspect ratio of particles can significantly improve the shear strength and erosion resistance. For samples with initial fabric anisotropy, their degree of anisotropy decreases during the shear process, while samples with initial isotropy exhibit gradually increasing anisotropy during this process.

(d) CFD-DEM numerical simulations can be used to determine the material constants in the erosion law, thus providing a theoretical basis for establishing a new erosion law based on microscopic results. The study also found that the effect of fabric anisotropy on the erosion law constant is not significant, so when proposing an erosion law, the influence of fabric anisotropy can be neglected for simplification.

Table 4.1 Summary of numerical simulation samples

Soil samples	Aspect ratio (AR)	Bedding angle	Initial void ratio
S-15as-0	1.5	0°	0.393
S-15as-30		30°	0.385
S-15as-60		60°	0.389
S-15as-90		90°	0.394
S-15as-iso		Isotropy	0.394
S-20as-0	2.0	0°	0.394
S-20as-30		30°	0.401
S-20as-60		60°	0.396
S-20as-90		90°	0.392
S-20as-iso		Isotropy	0.401

Particle shape	*x-z* Plane	*y-z* Plane
Aspect ratio=1.5		
Aspect ratio =2.0		

Figure 4.1 Particle shape adopted in CFD-DEM

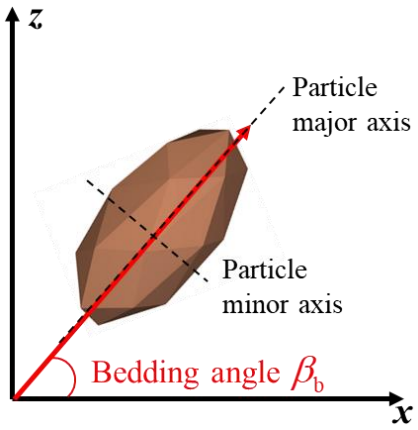

Figure 4.2 Definition of bedding angle

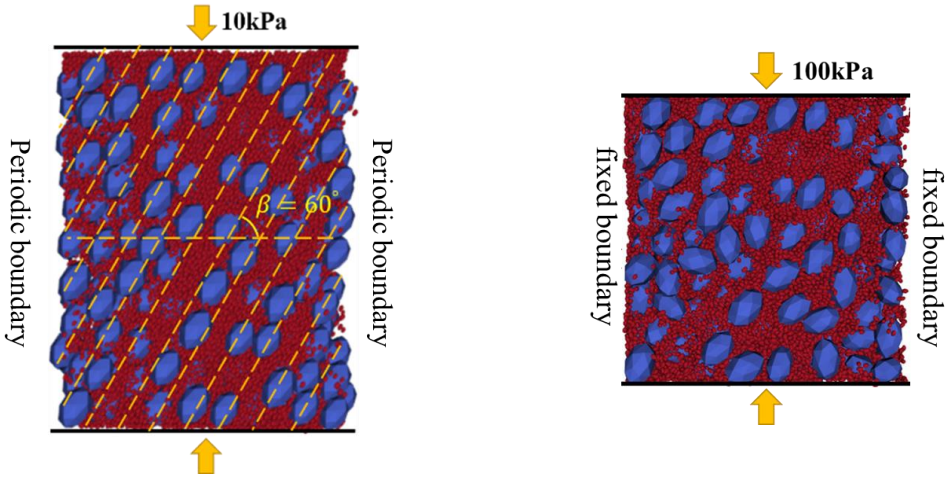

(a) (b)

Figure 4.3 Generation of fabric anisotropic soils: (a) generating particles with fixed orientations and applying a pressure of 10kPa; (b) unlocking particle rotation and applying a pressure of 100kPa.

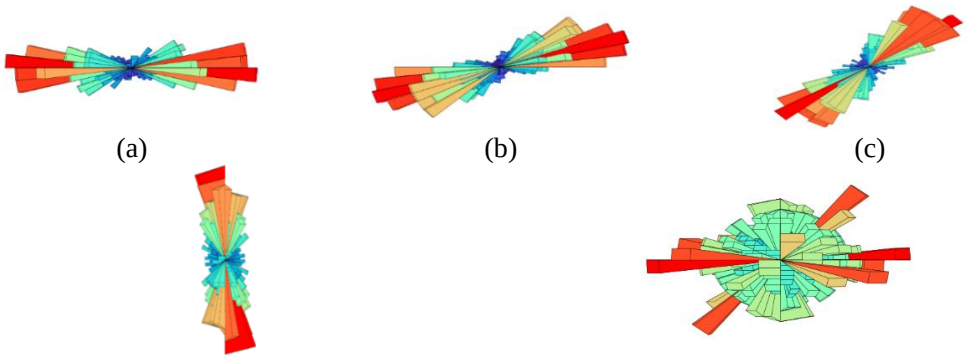

(a) (b) (c)

(d) (e)

Figure 4.4 3D orientation of coarse particles: (a)bedding angle=0°; (b) bedding angle=30°; (c) bedding angle=60°; (d) bedding angle=90°; (e) bedding angle=Isotropy

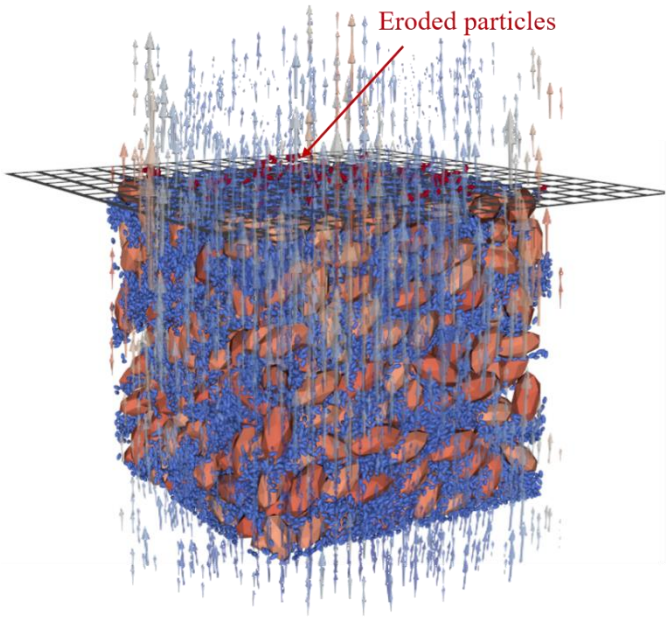

Figure 4.5 The diagram of soil suffusion

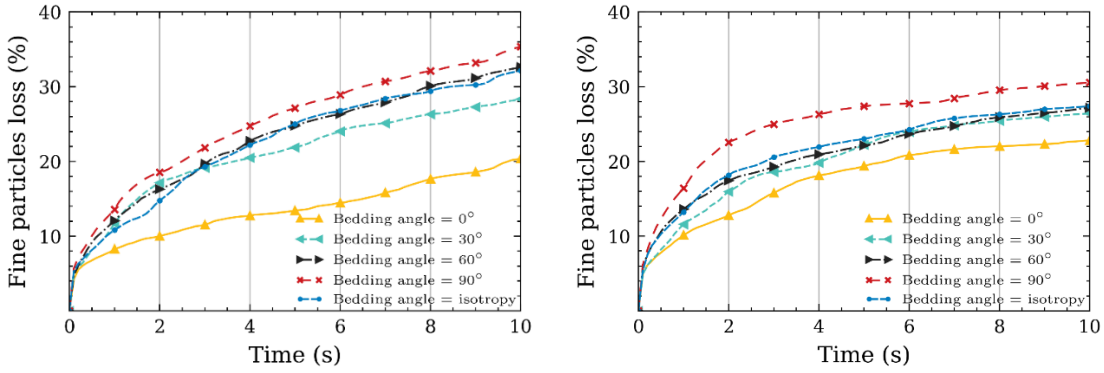

Figure 4.6 Loss of fine particles with elapsed time for samples with different bedding angles and aspect ratios: (a) aspect ratio=1.5; (b) aspect ratio=2.0

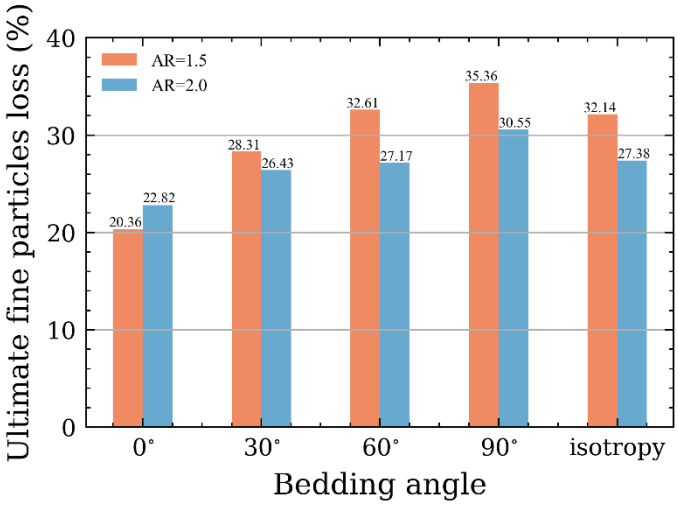

Figure 4.7 Comparison of ultimate mass loss for samples with different bedding angles

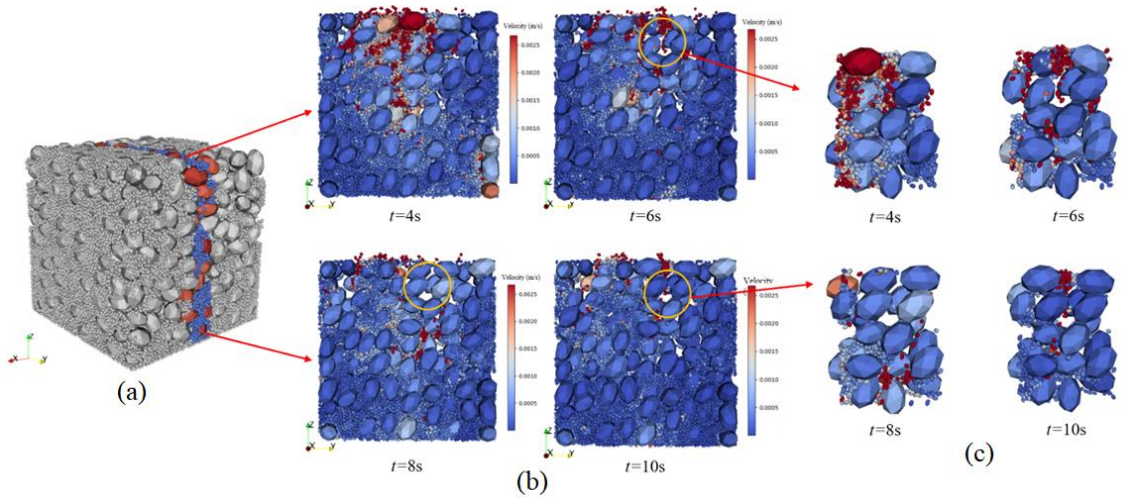

Figure 4.8 Distribution of particles: (a) simulated samples; (b)selected particle plane; (c) microscopic particle arrangement

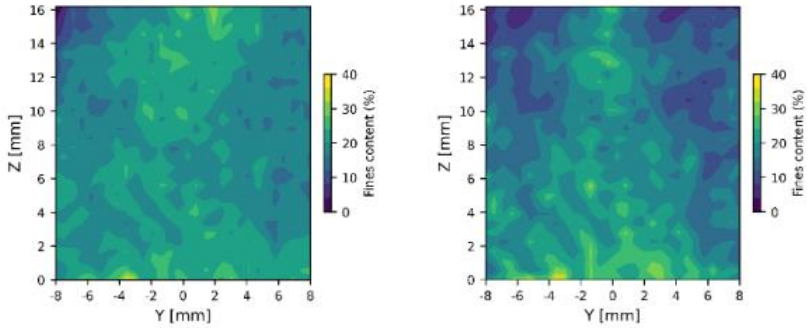
Z [mm]
Y [mm]
Fines content (%)
0
10
20
30
40

(a)

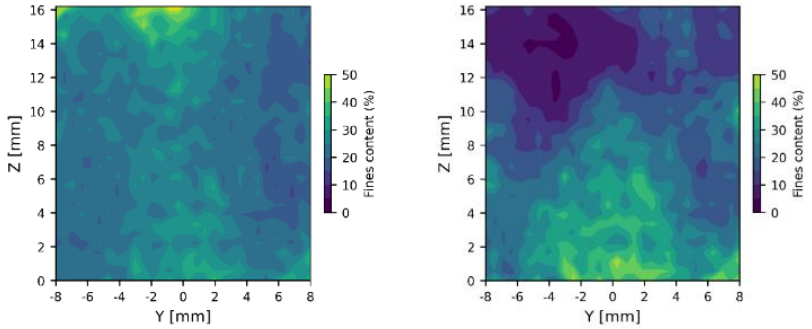
Z [mm]
Y [mm]
Fines content (%)
0
10
20
30
40
50

(b)

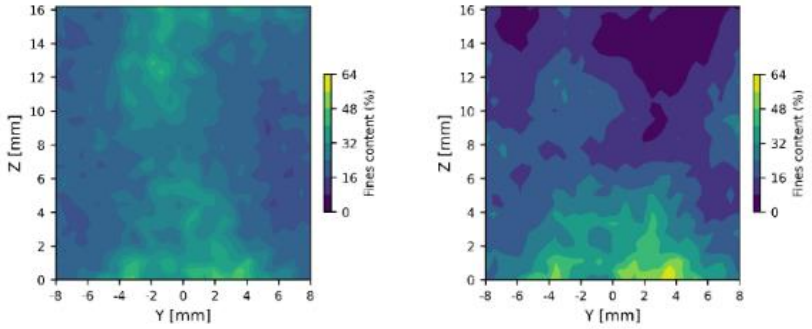
Z [mm]
Y [mm]
Fines content (%)
0
16
32
48
64

(c)

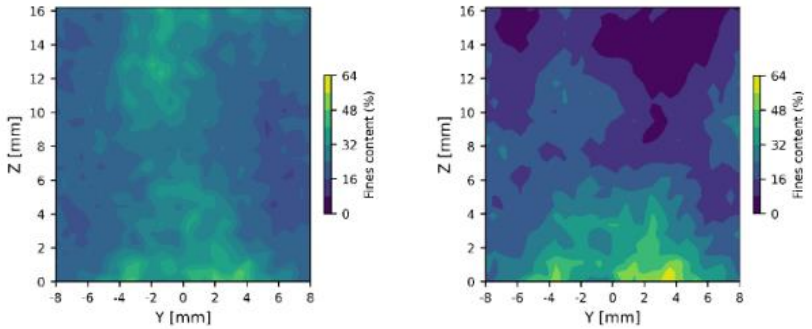
Z [mm]
Y [mm]
Fines content (%)
0
16
32
48
64

(d)

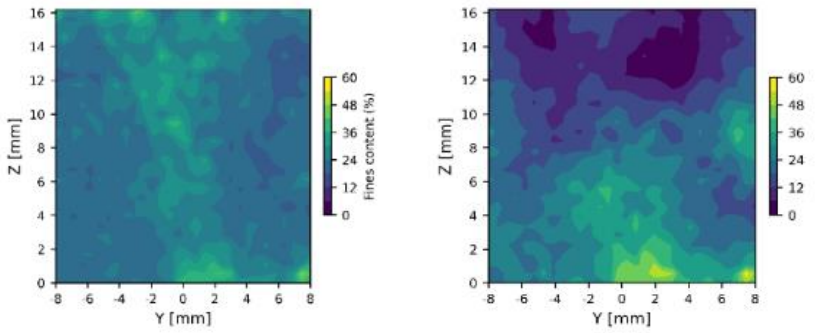

(e)

Figure 4.9 Contours of fine content at different points for samples with AS=1.5 both before and after erosion (the specific plane is *x*=0): (a) bedding angle=0° ; (b) bedding angle=30° ; (c) bedding angle=60° ; (d) bedding angle=90° ; (e) bedding angle=Isotropy

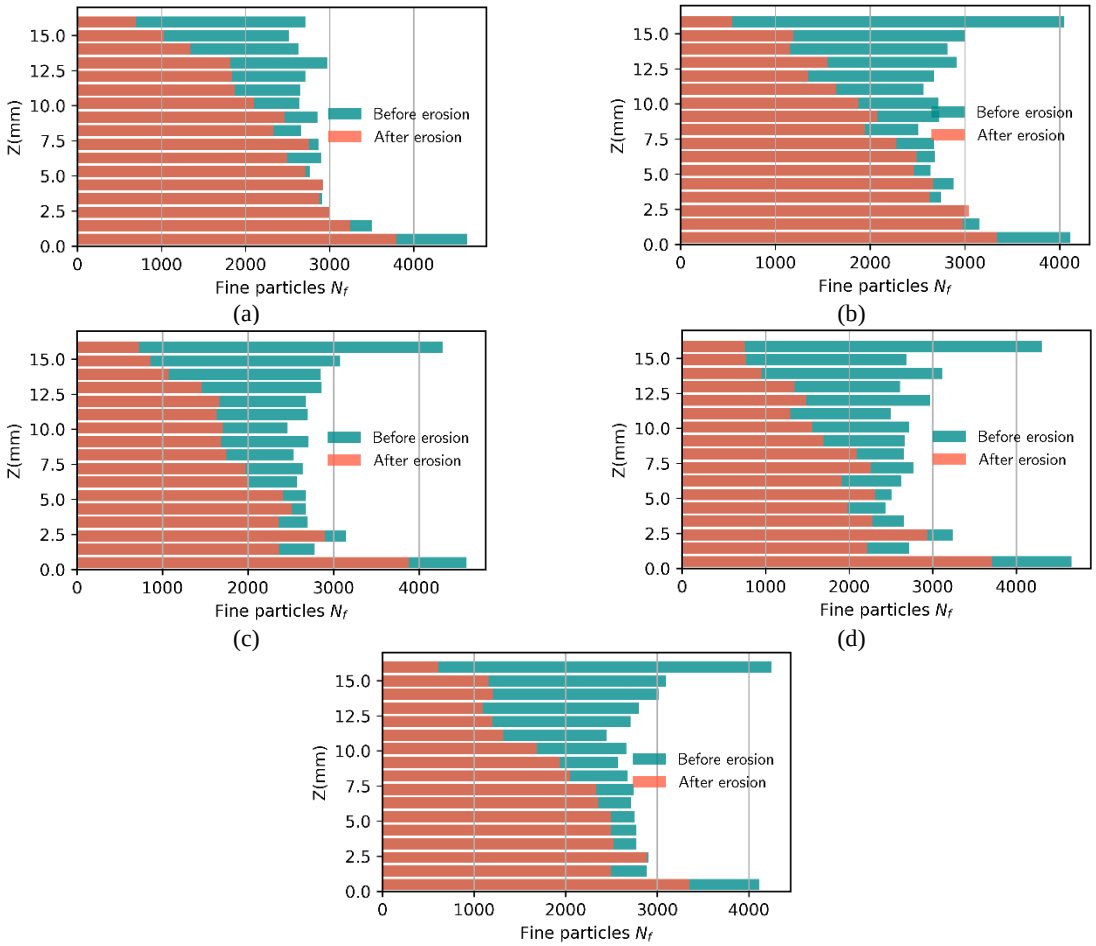

(a) (b) (c) (d) (e)

Figure 4.10 Comparison of fine particle distribution along with Z position: (a) bedding angle=0° ; (b) bedding angle=30° ; (c) bedding angle=60° ; (d) bedding angle=90° ; (e) bedding angle=Isotropy

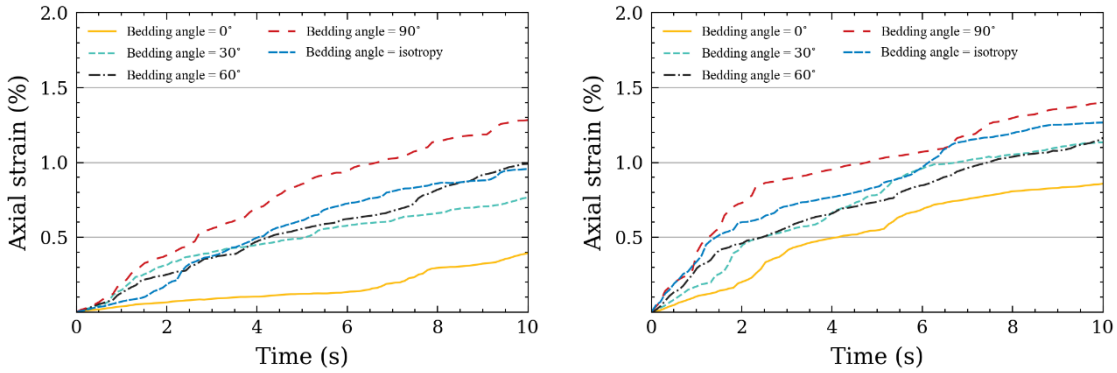

Figure 4.11 Axial strain for samples with different bedding angles: (a) AR=1.5; (b) AR=2.0

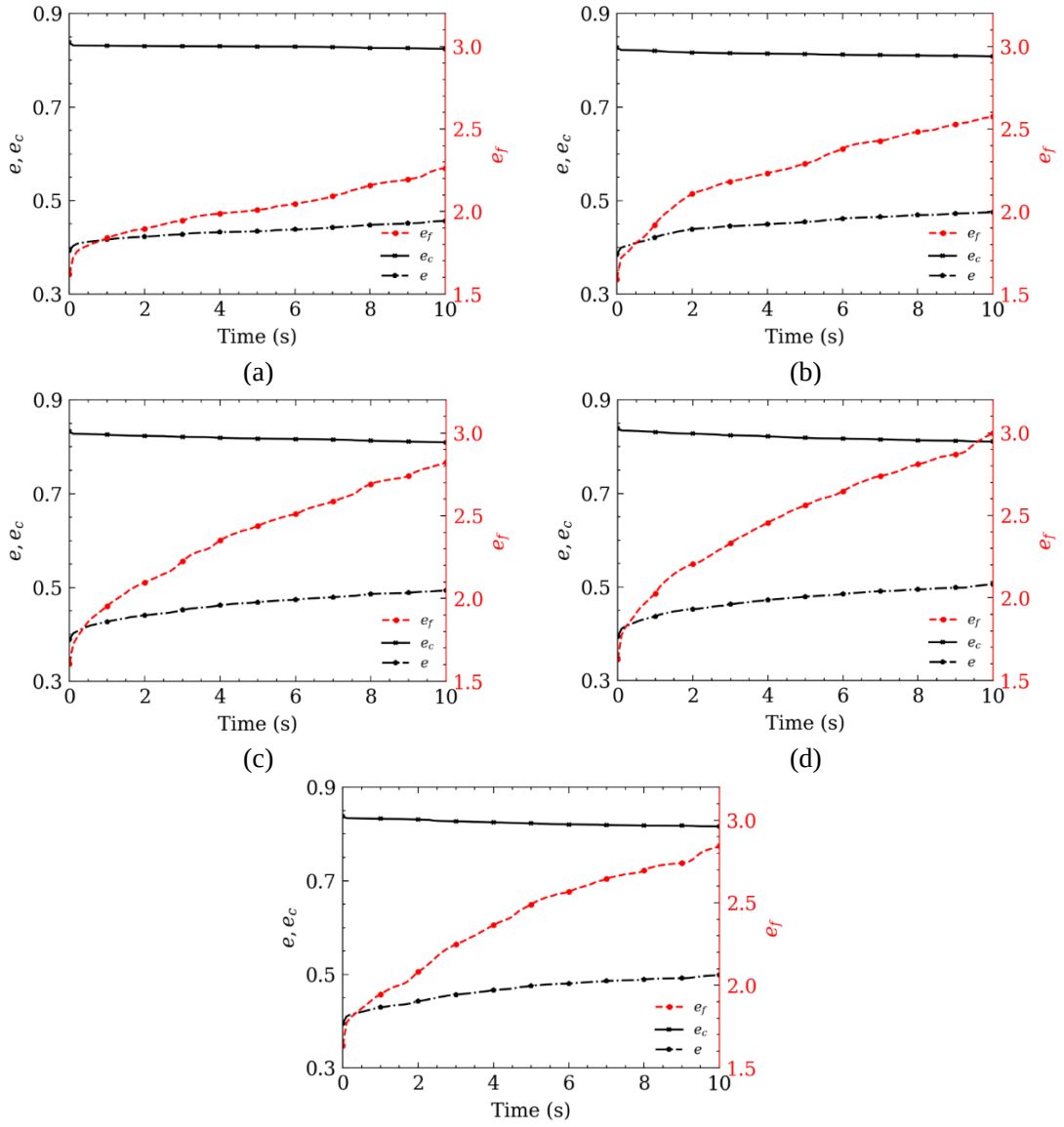

Figure 4.12 Variation of e, e_c, e_f for samples with AS=1.5 at different bedding angles: (a) bedding angle=0° ; (b) bedding angle=30° ; (c) bedding angle=60° ; (d) bedding angle=90° ; (e) bedding angle=Isotropy

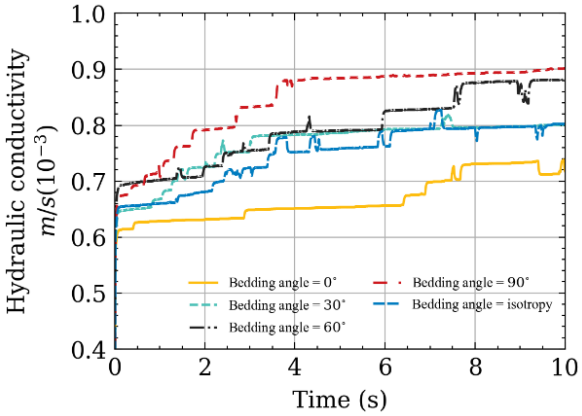

Figure 4.13 Hydraulic conductivity versus simulation time

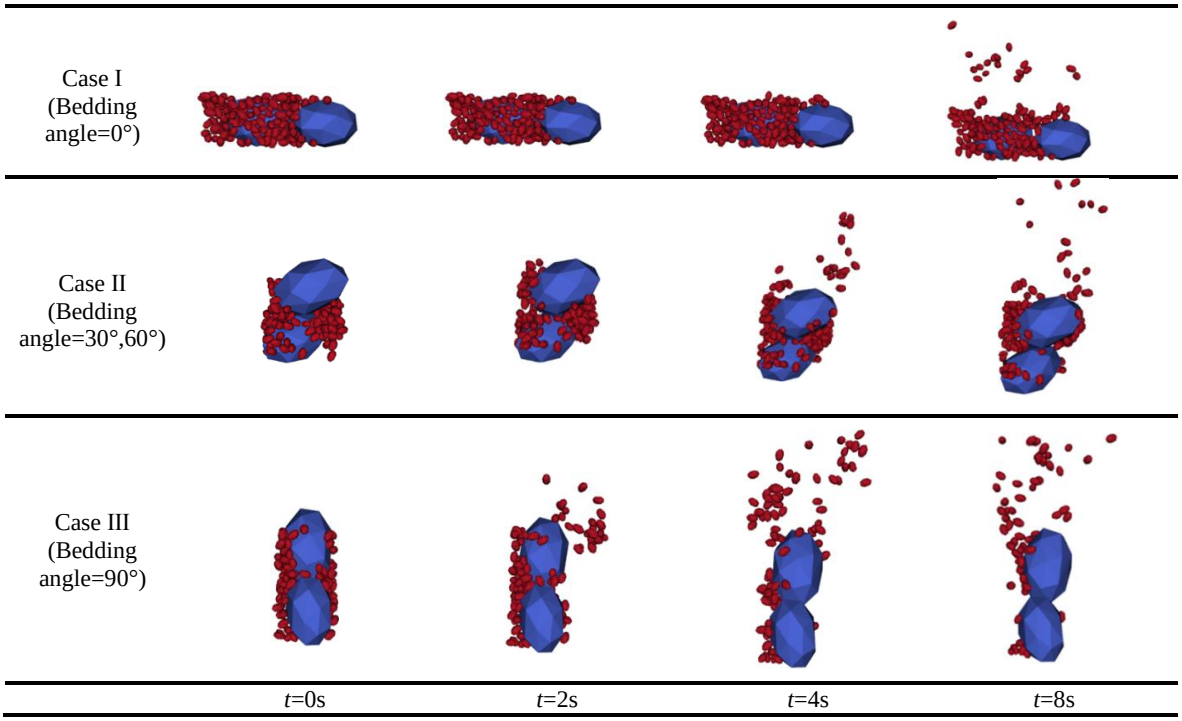

Figure 4.14 Typical fine particle migration of different specimens

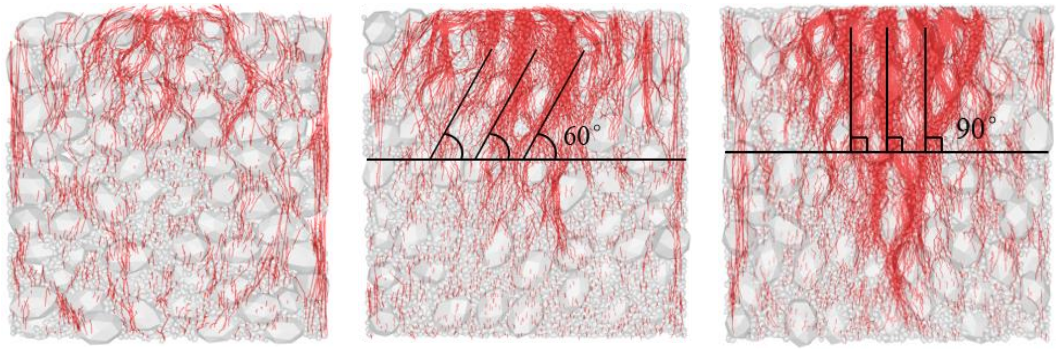

(a) (b) (c)

Figure 4.15 Fine particle trajectory: (a) particle trajectory of Mode I; (b) particle trajectory of Mode II; (c) particle trajectory of Mode III

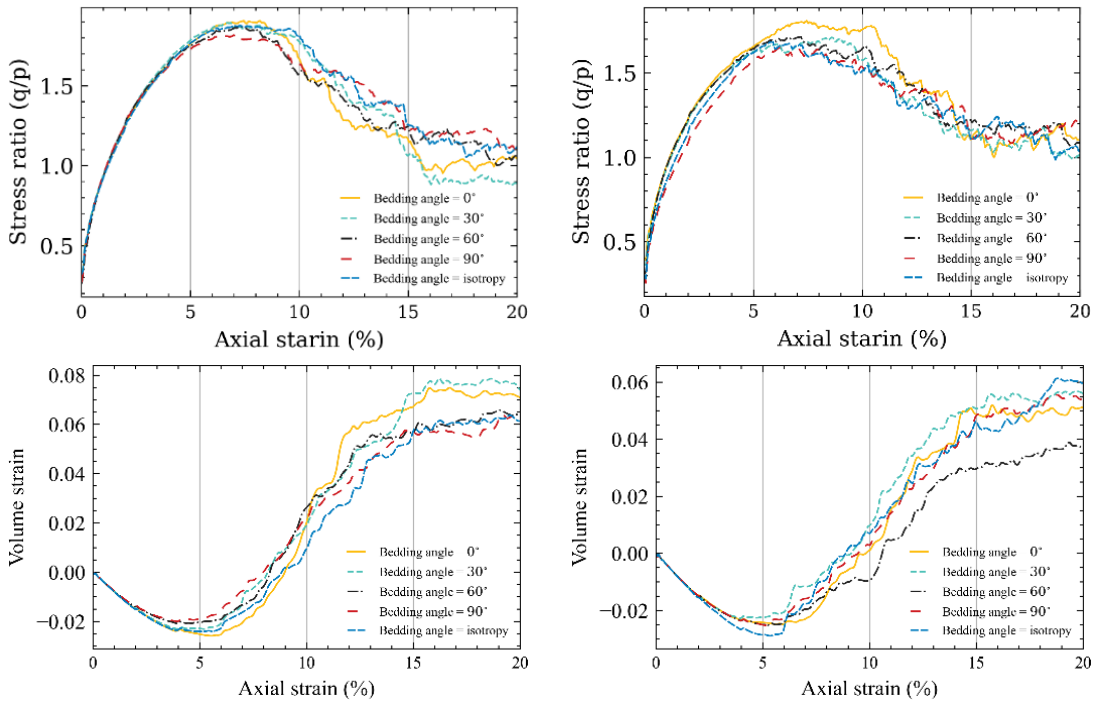

Figure 4.16 Variation of strength and deformation characteristics expressed by stress ratio (deviatoric stress over mean effective stress) versus axial strain and volumetric strain versus axial strain: (a) before suffusion; (b) after suffusion

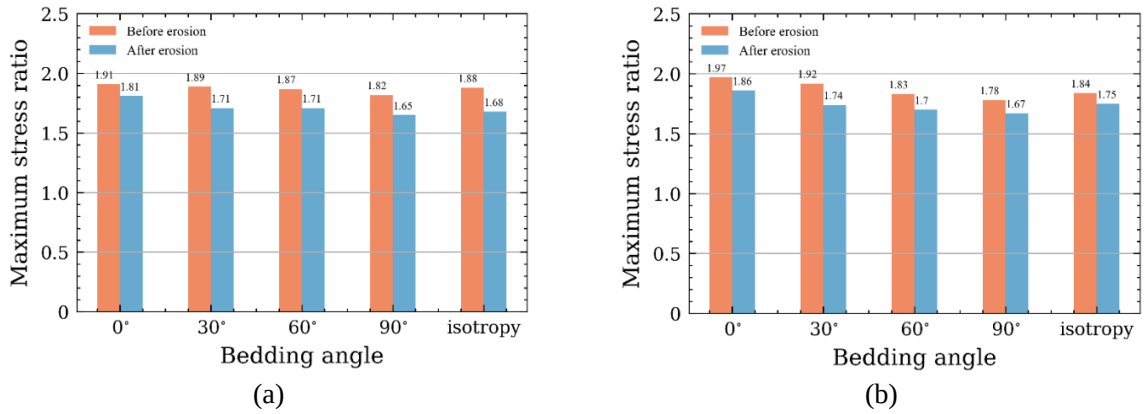

Figure 4.17 Peak stress ratio of samples with different bedding angles: (a) AR=1.5; (b) AR=2.0

Bedding angle	Before suffusion	After suffusion	After triaxial shear
0°	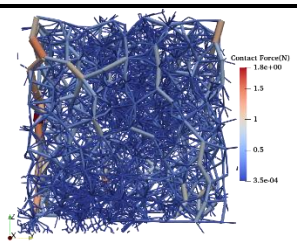	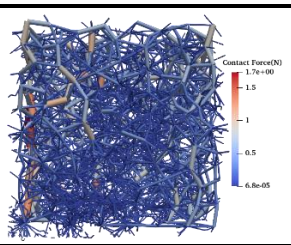	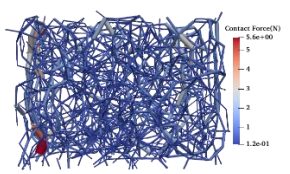
30°	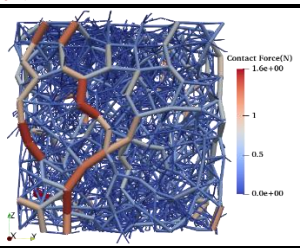	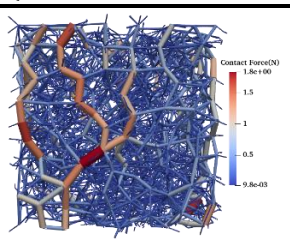	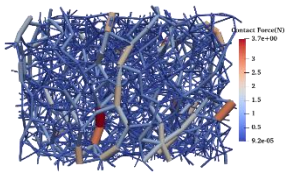

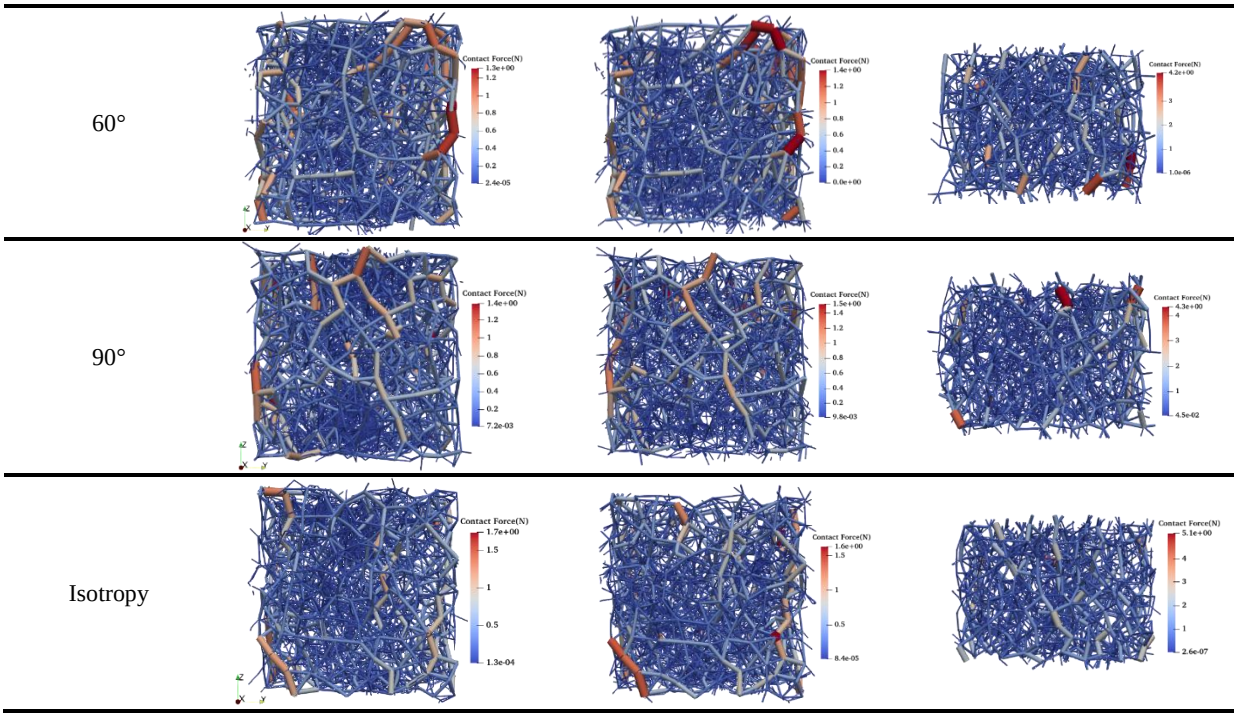

Figure 4.18 Strong force chains network

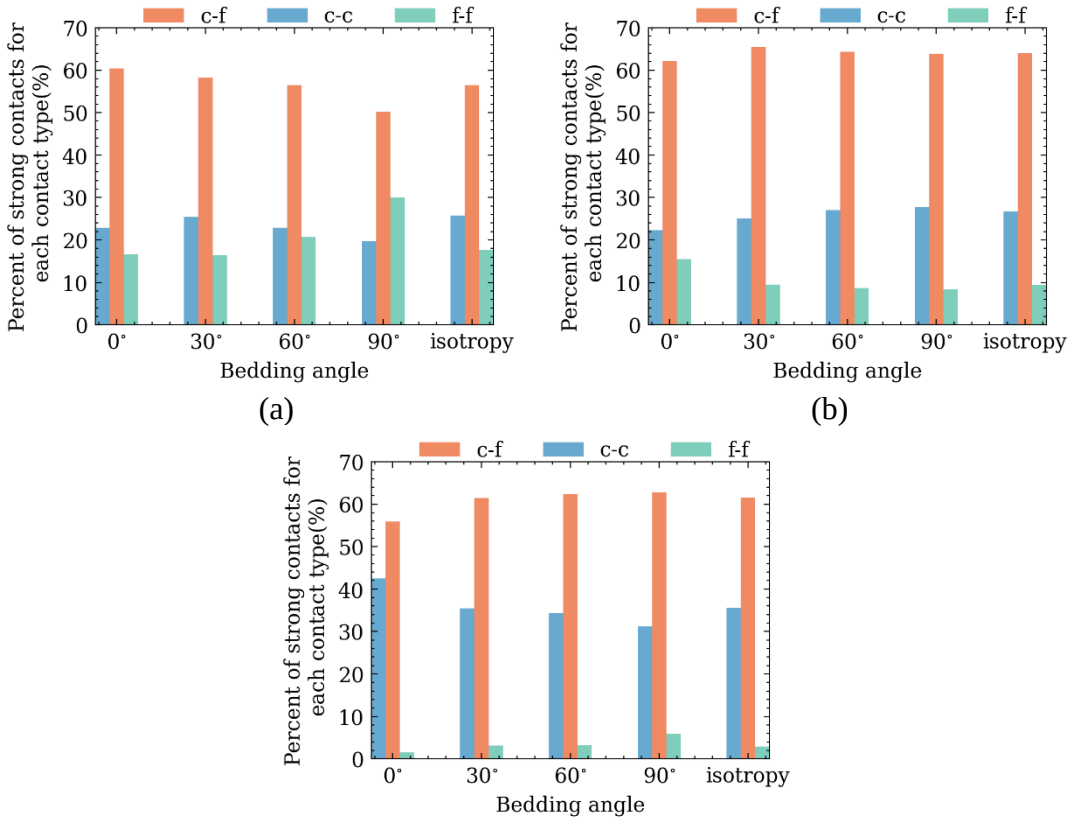

Figure 4.19 Contributions to strong contact force by different contact types: (a) before suffusion; (b) after suffusion; (c) after triaxial shear

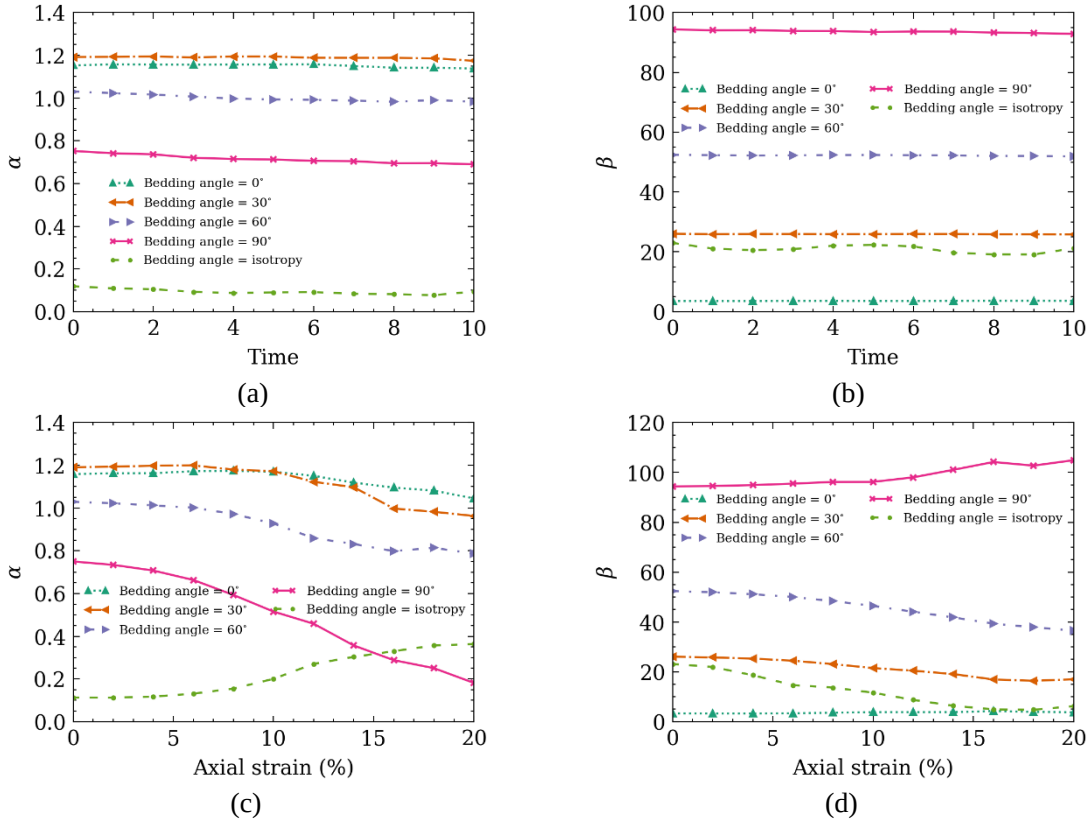

Figure 4.20 Evolution of soil fabric anisotropy: (a)-(b): during suffusion; (c)-(d): during triaxial shear

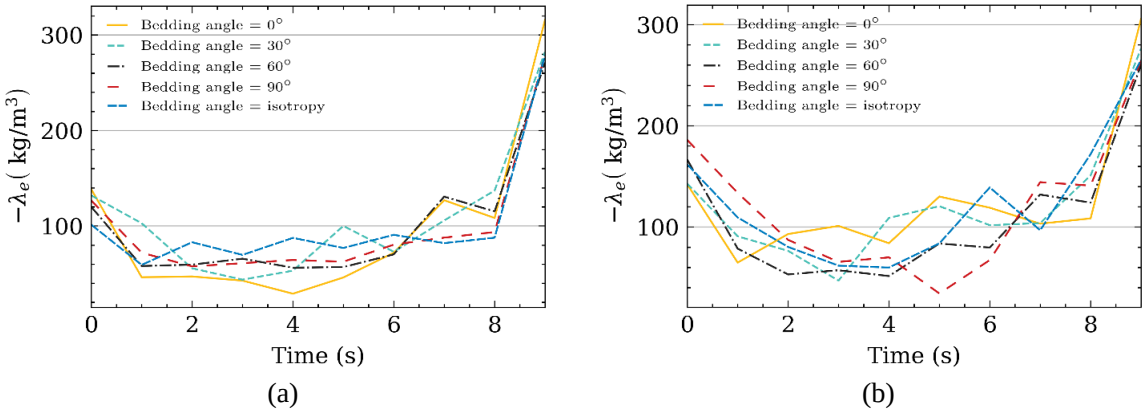

Figure 4.21 λ_e from CFD-DEM results: (a) Aspect ratio=1.5; (b) Aspect ratio=2.0

CHAPTER 5 STUDY ON TUNNEL SEEPAGE EROSION AND MECHANICAL RESPONSE BASED ON CFD-DEM-FEM

5.1 Introduction

With the development of underground space, shield tunnels have been widely used in underground engineering projects such as subways and urban lifelines (Shin et al., 2006; Liao et al., 2009; Cheng et al., 2020). However, due to the complex service environment, tunnel failure disasters occur frequently. Research suggests that one of the primary causes of tunnel failure is soil erosion caused by groundwater seepage in water-rich sand, which is exacerbated by tunnel lining cracks and faults (Davies et al., 2001; Korff et al., 2011; Zhang et al., 2021). According to statistics, such issues are prevalent in over 80% of operational tunnels in southwest China that have been in service for more than ten years (Gao et al., 2019). Cracks in the tunnel lining can lead to the migration of surrounding soil, resulting in the formation of underground cavities and subsidence. Furthermore, particle migration can significantly alter soil-structure interactions, causing convergent deformation of the tunnel and exacerbating structural damage (Meguid and Dang, 2009; Ye and Liu, 2020), which poses substantial risks to both infrastructure integrity and public safety (Cividini et al., 2009; Midgley et al., 2013). For instance, on February 7, 2018, a tunnel failure on Foshan Metro Line 2 in China, triggered by groundwater leakage, led to the formation of a 900m² by 6m sinkhole, resulting in 11 fatalities and 8 injuries (Peng et al., 2023). Therefore, it is crucial to investigate the evolution of soil erosion caused by tunnel leakage and examine the mechanical response of the tunnel structure to ensure long-term functionality and serviceability.

Over the past decades, scholars have employed various approaches, including analytical (Park et al., 2008; Zhang et al., 2015, 2017; Gan et al., 2021), experimental (Mukunok et al., 2009; Leung and Meguid, 2011; Lü et al., 2020; Zhang et al., 2022) and numerical methods (Ye and Liu, 2020, 2021; Qian et al., 2021a) to assess the impact of seepage-induced tunnel erosion on the surrounding environment. The analytical method typically treats the tunnel as a 2D circle on a semi-infinite plane, with the soil modeled as an isotropic porous medium. By using conformal mapping, the Laplace equation for Darcy's flow can be solved to derive flow velocity and pore pressure distributions (Huangfu et al., 2010). Although analytical methods offer insights into the fundamental mechanisms of seepage infiltration and are computationally efficient, their oversimplification of tunnel structures and neglect of soil transport limit their practicality in engineering applications. In contrast, scaled-down laboratory experiments are more direct and can better reflect in-site scene. The tunnel structure can be carefully designed, and the migration of soil can be visually observed (Zheng et al., 2017a; Gao et al., 2019). Sato and Kuwano (2015) developed a new apparatus that allows soil to discharge from pipe cracks by imposing uniform seepage from the ground surface. Notably, the front of the soil chamber was replaced with a transparent acrylic plate to facilitate observation. Their study investigated the progressive expansion of underground cavities and the mutual effects of structures on seepage accidents. However, the limitation of such experiments is that phenomenological observations often fail to provide microscopic interpretations, particularly regarding soil transportation and the interaction forces between soil particles and seepage flow. As a result, scholars have sought to develop advanced numerical methods to conduct in-depth studies, focusing on micro-level information

during erosion. Qian et al. (2021a) employed CFD-DEM to investigate the effects of tunnel burial depth and grain size distribution on seepage erosion, providing innovative insights into the microscopic mechanics of tunnel erosion. Similarly, Ibrahim and Meguid (2023) explored the erosion development in tunnels under a constant groundwater table, developing simplified relationships for estimating the total mass of eroded soil. While these studies provide valuable insights into the evolution of erosion, most focus primarily on soil migration or changes in flow behavior, neglecting the tunnel's mechanical response. As highlighted by Ye and Liu (2021), the occurrence of joint cracks and soil loss significantly impacts tunnel stability. The migration of particles induces variations in soil stress, altering the forces exerted on the tunnel, which in turn can lead to deformation and tensile stress. Therefore, a more systematic investigation is required to better understand the erosion mechanisms, evaluate their effects on tunnel structures, and assess the safety of erosion-affected tunnels.

This chapter employs a CFD-DEM-FEM coupling approach to develop a mesoscale BVP model for tunnel seepage erosion. The study systematically examines the influence of key factors, including crack width, crack position, tunnel burial depth, and groundwater level, on the erosion process.

5.2 Calculation framework of CFD-DEM-FEM method

This study will explore tunnel seepage erosion and the mechanical response of tunnel structures. The fluid (seepage water) and solid (soil) are simulated using the aforementioned CFD-DEM method. After completing the seepage erosion simulation, the particle-structure interaction forces

and fluid pressures are read and used as nodal forces, which are then re-input into the FEM tunnel model for analysis. The CFD-DEM-FEM computational framework is shown in Figure 5.1, where the CFD-DEM computation still uses the two-way coupling scheme, while the FEM part calculates the nodal displacements based on the forces at the nodes of the discretized tunnel structure elements (Yao et al., 2021; Adhav et al., 2024), given by:

$$\{F\}=[K]\{d\} \tag{5.1}$$

where $\{F\}$ is the vector of global nodal force, $[K]$ is the structure's total stiffness matrix, and $\{d\}$ is the structure's nodal displacements. The tunnel is discretized using a tetrahedral element with 4 nodes, as is shown in Figure 5.2. Therefore, contact between the DEM soil particle and the triangle face is mainly point-to-node, point-to-edge, and point-to-face (Zheng et al., 2017b). The element node force can be calculated using the contact force and the area coordinates. As is shown in Figure 5.2(b), when the spherical soil particle is in contact with the surface, it will exert a contact force $\boldsymbol{F}_c$ at the contact point. The nodal force for the contact element is given as (Yang et al., 2023):

$$\boldsymbol{F}_i = N_i \bullet \boldsymbol{F}_c \ \ (i=1,2,3) \tag{5.2}$$

where $\boldsymbol{F}_i$ is the equivalent nodal force. N_i is the shape function of the trilateral element, given as:

$$\boldsymbol{N} = (N_1, N_2, N_3) = (\frac{S_1}{S}, \frac{S_2}{S}, \frac{S_3}{S}) \tag{5.3}$$

where S_i is the area coordinate of the contact point, and S is the area of the surface.

5.3 Geometric conditions and simulation setup

5.3.1 Model geometric conditions

The simulation model comprises three key components: soil, fluid, and tunnel structure. The soil used in this study is derived from gap-graded sandy soils of Hong Kong's completely decomposed granite (HK-CDG) mixtures (Chang and Zhang, 2011, 2013a), characterized by a bimodal distribution of coarse and fine particles, with a fine content of 35% (Figure 5.3). However, directly applying the particle size distribution (PSD) of HK-CDG in DEM simulations is computationally infeasible due to the broad range of the PSD (10^{-4} to 10^{-2} m), which would necessitate an impractically large number of particles. To improve computational efficiency, a simplified, narrower PSD is selected to approximate the key characteristics of the original HK-CDG soil. Nevertheless, this modification alone is insufficient for simulating boundary value problems (e.g., tunnel erosion). A common strategy to reduce computational costs in DEM simulations is to scale up particle sizes while preserving the relative proportions of the PSD (Jiang and Yin, 2012; Yin et al., 2020b). Consequently, the simulated soil is enlarged by a factor of 40, resulting in fine particles of 0.8 cm and coarse particles of 4.8 cm, as shown in Figure 5.3. It is essential to highlight that such scaling up would inevitably lead to disparities between simulated scenarios and practical settings. Nevertheless, the validation, to be detailed in the subsequent section, demonstrates that the primary characteristics derived from the simplified numerical model are consistent with engineering expectations.

To simulate erosion between tunnel linings, the flawed tunnel is modeled as a ring with a circumferential crack, as shown in Figure 5.4. The entire computational domain is configured as a cuboid with the following dimensions: a length of 1.8 meters, a depth of 2.5 meters, and a width of 0.36 meters, as illustrated in Figure 5.5(a). In accordance with the recommendations of Shire et al. (2014), the minimum size ratio between the particles and the model domain must exceed 6.5 to satisfy the boundary conditions. As such, the model width is set to be 7.5 times the largest particle size and 18 times the average particle size. The total number of particles is approximately 2,000,000. The tunnel's external diameter is 0.62 meters, while the internal diameter measures 0.59 meters. An aperture with a 30° opening angle is introduced within the designated tunnel segment to simulate a tunnel crack. The crack's width in the longitudinal direction varies across different samples to examine the impact of crack size on tunnel erosion.

This study conducts a comprehensive analysis of tunnel seepage erosion, focusing on four key influencing factors: tunnel depth, crack size, crack position, and water table depth. A total of 13 test groups are considered, encompassing five different crack angles θ_c (0°, 45°, 90°, 135°, and 180°), three differnet burial depths (1.0 d_T ,1.5 d_T , and 2.0 d_T , where d_T denotes the outer diameter of tunnel), five different crack widths (1.1 $d_{\max}$, 1.2 $d_{\max}$, 1.3 $d_{\max}$, 1.4 $d_{\max}$, and 1.5 $d_{\max}$, where $d_{\max}$ denotes the maximum particle diameter), and three different water levels (0.5 b_d ,1.0 b_d , and 1.5 b_d , where b_d is tunnel burial depth). The crack angle θ_c is defined as the angle between the crack's midpoint and the tunnel's axis, as illustrated in Figure 5.5(b). A summary of the simulated samples is provided in Table 5.1. It should be noted that the minimum crack size

in this chapter is set to 1.1 times the maximum particle diameter, so coarse particles will also be eroded during the seepage process. This is because, according to the studies in Chapters 3 and 4, fine particles in gap-graded soils generally serve as a filling function, and considering only the loss of fine particles has a relatively small effect on the forces applied to the tunnel structure. Therefore, this section investigates the most unfavorable conditions for tunnel seepage erosion, where both coarse and fine particles are allowed to be lost simultaneously.

The fluid domain shares the same width and length dimensions as the soil domain, while the fluid depth varies in cases No. 7, No. 12, and No. 13 to simulate different water levels. To capture the flow behavior near the tunnel, the fluid mesh is locally refined, while a coarser orthogonal hexahedral mesh is employed in regions farther from the tunnel, as depicted in Figure 5.6(a). Considering practical engineering conditions, the seepage region is sufficiently large such that the seepage point does not influence surface water pressure. As a result, the top and bottom boundaries of the fluid domain are prescribed as constant-pressure boundaries, while the side boundaries are treated as impermeable walls. At the fluid-tunnel interface, a pressure outlet boundary is imposed at the crack location to simulate the seepage point, while the remaining interface is modeled as a no-slip wall. Driven by the differential pressure of infiltrating water, groundwater flows through the pressure outlet, as shown in Figure 5.6(b).

In this study, DEM employs spherical particles to represent sandy soil, ensuring computational efficiency. To account for discrepancies in contact forces due to the simplified particle

morphology, a rotational resistance model is implemented (Ai et al., 2011), incorporating a rolling resistance coefficient in the calculation of interparticle forces and momentum. The bulk density of HK-CDG soil is determined to be 2610 kg/m³, based on the calibration by Chang and Zhang (2011). However, other key micro-scale parameters, such as interparticle friction, Young's modulus, and restitution coefficient, have not been explicitly calibrated for HK-CDG. Consequently, these parameters are derived from similar sandy gap-graded materials reported in the literature (Qian et al., 2021a; Xiong et al., 2022; Chen et al., 2023a). The fluid is modeled as pure water, with a density of 1000kg/m³ and a dynamic viscosity of 0.001Pa·s. The tunnel structure is assigned a density of 2500kg/m³, with a Young's modulus of 1.92×10^{8} Pa and a Poisson's ratio of 0.192. A comprehensive summary of material properties and simulation parameters is provided in Table 5.2.

5.3.2 Simulation program

The seepage erosion simulation is composed of four primary steps: generation of initial soil specimens, saturated consolidation, tunnel excavation, and tunnel erosion.

In the first step, the initial loose soil layer is generated using the sand-fall method. To avoid initial pore inhomogeneity, which may arise from the migration of fine particles from the upper to lower layers under self-gravity, particle gravity is disabled during this stage. The resulting initial sample measures approximately 3m×1.8m×0.36m, which exceeds the target size in the depth direction for the erosion phase. Following this, gravity is applied to the soil, and CFD is employed to simulate hydrostatic pressure. This initiates the saturated consolidation process,

which lasts approximately 10 seconds until the soil reaches a steady state. Figure 5.7 presents the void ratio distribution after consolidation, demonstrating a relatively uniform profile along the depth direction. Upon completing the saturated consolidation phase, a thin-walled tube, matching the outer diameter of the tunnel, is placed at the designated tunnel location. A circular plate is then deployed along the tunnel perimeter and moved at a constant rate to excavate and remove the soil within the tunnel, as illustrated in Figure 5.8. During excavation, the tube adjusts vertically under the combined effects of gravity and soil pressure to counterbalance residual forces. After soil removal, the model undergoes an additional consolidation phase and rebalancing to achieve a steady state.

To validate the accuracy of the sampling method, Figure 5.9 presents a comparison between the theoretical vertical effective stress of the soil and the simulation results. The theoretical value of the effective stress is calculated using the following equation:

$$\sigma_z = \frac{(d_s - 1)\gamma_w}{1 + e} h \tag{5.4}$$

where $d_s = 2.61$ represents the particle density based on experimental data. $e = 0.28$ denotes the average void ratio of the soil, and *h* is the depth of the soil.

The comparison presented in Figure 5.9(a) and (b) demonstrates that the effective stresses in the soil obtained from the simulation closely align with the theoretical values. Additionally, Figure 5.9(c) shows the effective stress distribution after tunnel excavation, where a small degree of stress concentration is observed around the tunnel due to the excavation effect. To further assess the reliability of the sample generation method, the soil pressure exerted on the tunnel is

compared with analytical results. As shown in Figure 5.10, soil and water pressures are calculated based on the saturated soil density. In this study, the particle density is set to 2.61g/cm³, and the saturated density is computed as 22.3kN/m³. The vertical soil pressure is determined based on the tunnel depth, while the horizontal soil pressure is calculated using the lateral pressure coefficient ($K_0 = 0.5$ in this work). The distributions of soil pressure around the tunnel, obtained from both analytical solutions and simulations, are presented in Figure 5.11. The simulation results exhibit less homogeneity compared to the analytical solutions, which can be attributed to the fact that DEM treats the soil as a discrete assembly, causing the interaction forces between particles and the structure to be non-uniform at the same depth. Moreover, the DEM captures the natural structural behavior of the soil, including localized soil arches that can withstand additional pressure. This results in discrepancies near the bottom of the tunnel between the analytical and simulated results. Despite these differences, the DEM successfully captures the pressure increase trend from the top to the bottom of the tunnel, with both the minimum and maximum pressures showing a reasonable match to the analytical solution. Therefore, the sample generation process can be considered suitable for accurately reflecting the stress conditions around tunnel structures.

Upon completion of the sampling process, a cracked tunnel model is introduced in place of the circular tube, and a fluid domain, identical to the DEM domain, is incorporated to initiate seepage erosion. During the seepage erosion process, variations in soil stress may induce rigid body displacement of the tunnel, resulting in misalignment between the DEM and CFD domains. To

mitigate this issue and avoid the computational complexity associated with implementing a dynamic fluid mesh, the rigid body displacement of the tunnel is restricted.

5.4 Simulation results and discussions

5.4.1 The influence of crack size

5.4.1.1 Seepage-induced soil mass loss

After the initiation of seepage erosion, soil particles outside the tunnel gradually migrate into the tunnel through cracks under the action of infiltration fluent. Figure 5.12 illustrates the eroded soil mass for varying crack widths at the end of erosion. It is observed that as the crack width increases, the volume of soil particles entering the tunnel also increases. When the crack width exceeds $1.3d_{max}$, a pronounced V-shaped settlement funnel develops in the soil, accompanied by significant displacement of soil surface. At a crack width of $1.5\,d_{max}$, severe soil erosion occurs, severe soil erosion occurs, with eroded soils completely filling the tunnel cavity.

Figure 5.13 illustrates the cumulative mass loss versus seepage time. It's found that for a crack width of $1.1\,d_{max}$, the particle loss remains minimal. For crack widths ranging from $1.2\,d_{max}$ to $1.4\,d_{max}$, more pronounced soil loss occurs, with the loss rate increasing rapidly initially, followed by a plateau phase where the mass loss curve stabilizes. As shown in Figure 5.12(b)-(d), at the end of the erosion for these cases, the tunnel is not fully filled with soil while the mass loss ceases. This indicates that particles near the tunnel opening can form an effective aggregation, which inhibits the continuous loss of particles into the tunnel. Such aggregation is responsible for the stabilization observed in the mass loss curve. In contrast, while the mass loss curve for a

crack width of $1.5d_{max}$ also exhibits a stable phase, the underlying mechanism differs from that of the $1.2\,d_{max}$ to $1.4\,d_{max}$ cases. As shown in Figure 5.12(e), the stabilization occurs because the tunnel becomes completely filled with eroded soil, preventing further loss of external particles. At this stage, no effective structure forms around the tunnel crack to inhibit erosion, therefore the loss of particles shows a non-convergence of the characteristics.

According to the above observations, the evolution of tunnel erosion can therefore be divided into 3 different patterns. As is illustrated in Figure 5.14, when the crack width is less than $1.1\,d_{max}$, the tunnel soil remains structurally stable, with negligible mass loss due to erosion. Second, for crack widths between $1.2\,d_{max}$ and $1.4\,d_{max}$, seepage erosion drives incremental mass loss that gradually stabilizes, reflecting a convergent pattern of erosion. Finally, when the crack width exceeds $1.5\,d_{max}$, soil particles are continuously eroded. The particle structure becomes destabilized as external particles fail to effectively mitigate the loss, resulting in a dispersive pattern of soil erosion.

5.4.1.2 Seepage-induced particle displacement

Figure 5.15 illustrates the particle transport trajectories during the erosion process. As the crack width increases, the range of particle migration expands vertically, eventually reaching the surface. Concurrently, the lateral extent of particle migration also increases. The particle trajectories primarily concentrate above the crack, exhibiting a symmetric, funnel-shaped distribution. Figure 5.16 presents the contour plots of particle displacement (note that displacement data is not shown for a crack width of $1.1\,d_{max}$ due to negligible displacement). As

the crack width increases, both the displacement area and the displacement distance expand. For instance, at a crack width of $1.2\,d_{max}$, the particle displacement area is limited, with displacements all less than 0.15m. As the crack width increases to $1.4\,d_{max}$ and $1.5\,d_{max}$, the soil disturbed area expands significantly. In addition, a comparison of the $1.4\,d_{max}$ and $1.5\,d_{max}$ cases reveals that while the overall disturbed area is similar, the region with displacements greater than 0.35m is markedly larger for the specimen with a crack width of $1.5\,d_{max}$. These results suggest that increasing crack width considerably enhances the likelihood of subsurface cavity formation, thereby escalating the potential hazards of the erosion process.

Figure 5.17 shows the surface sedimentation at different time intervals. The sedimentation curve is V-shaped, with the maximum sedimentation occurring near X = 0. When the crack width reaches $1.5\,d_{max}$, the maximum surface settlement can reach approximately 0.15m, indicating that seepage erosion can trigger substantial uneven ground settlement. Moreover, the development of ground settlement is primarily concentrated in the early stages of erosion (i.e., from 0 to 5 seconds), after which the settlement ceases to progress. This observation suggests that seepage erosion is characterized by a rapid onset, and once seepage begins, particle loss and ground settlement occur quickly. Therefore, it is crucial to implement disaster prevention and control measures early in the erosion process to prevent sudden soil loss and mitigate ground settlement.

Figure 5.18 illustrates the development of maximum settlement over time for specimens with

varying crack widths. It is evident that the maximum settlement exhibits a pronounced nonlinear progression. For instance, in the specimen with a width of $1.3d_{max}$, the maximum settlement increases gradually between *t*=0-2s, accelerates rapidly from *t*=2-5s, and then stabilizes between *t*=5-10s. In comparison, the mass loss curves in Figure 5.13 show that the rate of mass loss remains relatively constant between *t*=0-5s, indicating a temporal hysteresis between the settlement development and mass loss. Furthermore, the turning point, where the maximum displacement transitions from a slow to a rapid increase, occurs progressively earlier with an increase in crack width. This behavior can be attributed to the formation of a soil arch effect within the specimen, a phenomenon that will be further discussed in the following section.

5.4.1.3 Variation of soil fine content

The soil samples used in this study consist of gap-graded sandy soils. Figure 5.19 analyzes the changes in fine content due to erosion, with Figure 5.19(a) showing the initial distribution of fine content before erosion. Initially, the fine content is relatively uniformly distributed. However, following seepage erosion, the fine particles above the tunnel crack are significantly reduced. As the width of the cracks increases, the area of the soil that shows a decrease in fine content expands. When the tunnel crack is $1.1\,d_{max}$, the decrease in fine content is more pronounced than $1.2\,d_{max}$, although the area of the soil where the fine content changes is smaller. This can be attributed to the minimal loss of coarse particles in the $1.1\,d_{max}$ case (as is shown in Figure 5.12(a)), where soil migration and particle reorganization are limited. The soil loss primarily affects the fine particles within the coarse particle skeleton, resulting in a significant reduction in fine particle content above the tunnel. For width=$1.5\,d_{max}$, it can be found that the fine particle content above

the crack of the tunnel instead appears to increase. This is because, as shown in Figure 5.12(d), the eroded soil particles completely fill the tunnel under this condition, resulting in the subsequent soil gathering around the crack. Therefore, the fine particles, after being transported with the infiltrating flow, become clogged near the crack, leading to an increase in the fine content.

5.4.1.4 Soil stress variation and microscopic contact information

To investigate the impact of seepage erosion on soil stresses, the vertical effective stress distribution for varying crack widths is shown in Figure 5.20, while the initial effective stress distribution is presented in Figure 5.9(c). The results indicate a notable stress reduction in the region above the tunnel cracks due to particle loss. Conversely, an increase in effective stress is observed in the areas adjacent to the tunnel. This behavior is attributed to the arching effect induced by particle migration (Liu et al., 2022b, 2022a). To further elucidate the soil arch effect that emerges during the seepage process, the microscopic contact force chains of particles at various time intervals are illustrated in Figure 5.21. Using the crack=1.4 $d_{\max}$ as an example, the distribution of the contact force chains prior to seepage erosion (t=0) appears relatively uniform. Upon the initiation of seepage erosion (t=1s), particle loss results in the development of a distinct stress relaxation zone above the tunnel cracks. By t=2s, continued particle loss leads to the formation of a pronounced soil arch, which bears the overlying soil pressure and limits surface settlement. The presence of this soil arch contributes to the temporal hysteresis observed between settlement and particle loss, as shown in Figure 5.14 and Figure 5.18. As particle loss continues to increase, the internal soil arch becomes incapable of maintaining the stability of the soil body,

ultimately leading to its collapse. This collapse results in a shift in the dominant direction of particle contact forces above the tunnel, as shown in Figure 5.21(d), transitioning from the vertical to the transverse direction due to the compression exerted by the overlying collapsed soil. The increase in lateral contact forces enhances inter-particle friction, which improves the soil's resistance to seepage erosion. Consequently, the soil body achieves a relatively stable state once again. Therefore, comparing Figure 5.21Figure 5.21 Soil contact force chain and soil arch effect: (a) $t=0$; (b) $t=1\text{s}$; (c) $t=2\text{s}$; (d) $t=5\text{s}$; (e) $t=10\text{s}$(e) and Figure 5.21 Figure 5.21 Soil contact force chain and soil arch effect: (a) $t=0$; (b) $t=1\text{s}$; (c) $t=2\text{s}$; (d) $t=5\text{s}$; (e) $t=10\text{s}$(d), it can be seen that the structure of the earth body force chain is no longer significantly adjusted.

Figure 5.22 illustrates the microscopic force chain distribution of specimens with varying crack widths following seepage erosion. When the crack width is $1.1\,d_{\max}$, the force chain distribution closely resembles the initial state, indicating minimal impact of erosion on the structural integrity of the force chains. As the crack width increases to $1.2\,d_{\max}$, a distinct soil arch effect remains evident within the specimen even after seepage erosion. However, for crack widths ranging from $1.3\,d_{\max}$-$1.5\,d_{\max}$, the extent of erosion becomes substantial enough to destabilize the internal soil arch, leading to its collapse. Figure 5.23 presents the statistical analysis of the particle normal contact distribution. The analysis shows that the microscopic contact distribution evolves from initial anisotropy to isotropy. Notably, prior to erosion, vertical contacts are significantly greater than those in the horizontal direction. However, as soil is lost, the contact distribution changes due to the arch effect. The increase in horizontal contact forces indicates that the earth pressure,

initially borne by the lost particles, is transferred to the soil body on both sides of the crack.

5.4.2 The influence of crack position

5.4.2.1 Seepage-induced soil mass loss

Figure 5.24 plots the loss of particles at different crack positions, where the position angle θ_a = 0°, 45°, 90°, 135°, 180° (the definition of position angle θ_a could be found in Figure 5.5(b)). After the completion of erosion, particle loss decreases progressively as the crack position angle increases. At θ_a =0°, a distinct "V"-shaped sinkhole forms within the soil. In contrast, at θ_a =45°, 90°, 135°, the sinkholes are offset to the side where cracks appear, showing an asymmetric distribution. Notably, the influence of seepage erosion diminishes with increasing distance from the tunnel opening, resulting in less pronounced particle loss in regions farther from the crack. As the crack position increases to θ_a =135°, 180°, the soil layer above the tunnel no longer exhibits significant subsidence. Figure 5.25 presents the evolution of mass loss versus the erosion time for different position angles, it can be observed that the smaller the position angle, the greater the soil loss and the longer it takes for the erosion to reach a plateau. At θ_a =0°, erosion produces 5% soil loss and the mass loss does not gradually stop until $t = 5\text{s}$, while at θ_a =180°, erosion produces only 1.5% soil loss and the soil loss gradually stops at $t = 2\text{s}$. The reduction in final soil loss with increasing crack angle can be attributed to the increasing angle between the gravitational force $F_{gravity}$ acting on the particles and the seepage force $F_{seepage}$, as shown in Figure 5.26. A larger position angle increases the gravitational component that opposes the seepage force, thereby making soil particles more challenging to be driven and eroded.

5.4.2.2 Seepage-induced particle displacement

Figure 5.27 depicts the particle migration trajectories at different position angles. As the crack position angle increases from 0° to 180°, the particle migration route progressively shifts toward the crack position. The bigger the position angle, the smaller the migration range induced by erosion. In addition, the effect of particle erosion on the surface is significantly reduced with increasing position angle. This behavior is attributed to the change in the alignment of seepage forces with particle self-gravity. As the position angle increases from 0° to 180°, the seepage force shifts from being aligned with the gravitational force to opposing it. At θ_a=180°, the self-gravity of the particles can counteract the seepage force, making particle migration more difficult. The surface settlements at different time intervals are shown in Figure 5.28. It is observed that the maximum surface settlement decreases with increasing crack position angle, and the location of maximum settlement shifts from the midpoint of the soil to the edge of the model. At θ_a=180°, surface settlement is nearly negligible, despite there are still some particles being eroded into the tunnel. These findings suggest that the most critical location for tunnel erosion occurs at the top of the tunnel, where seepage erosion leads to substantial particle loss and significant surface settlement. Figure 5.29 further depicts the evolution of maximum settlement over time. At θ_a =0°, 45°, and 90°, the settlement rate is initially slow, then increases before reaching a plateau. This trend indicates a hysteresis effect, where the development of maximum settlement lags behind mass loss in these specimens. In contrast, at θ_a=135° and 180°, no significant hysteresis is observed. The previous analysis suggests that the observed hysteresis effect primarily results from soil arching within the soil mass. Consequently, when cracks develop at larger angles, effective soil arches fail to form within the specimen.

5.4.2.3 Soil stress variation and microscopic contact information

The effective stress distribution of the soil after seepage erosion at various angles is shown in Figure 5.30. It can be observed that a stress relaxation zone is formed near the crack position, and the smaller the position angle, the greater the reduction in stress. At θ_a =0°, the soil effective stress above the entire crack is almost reduced to the range of 0-5 kPa. This is mainly because after severe particle loss, the self-weight of the soil decreases. On the other hand, from the force chain distribution in Figure 5.31, it can be seen that when θ_a = 0°, the soil arch above the crack also disperses the soil pressure towards the arch foot, which further reduces the effective stress in the soil. Additionally, when θ_a = 90°, 135°, and 180°, erosion also creates stress concentration zones at positions opposite the crack, leading to an increase in stress in those areas. This is because, when the crack appears at these positions, the particle migration zone becomes deeper. When distant particles move towards the soil loss area to replenish the particles, they are significantly constrained by the presence of the tunnel structure or the sample boundary, which causes particle accumulation and blockage, resulting in stress concentration.

5.4.3 The influence of burial depth and water level

5.4.2.1 Seepage-induced soil mass loss

Figure 5.32 presents the cumulative mass loss of soil at varying tunnel depths and water levels, demonstrating that particle loss increases with both tunnel depth and water table elevation. It's found that the effect of the water level on particle erosion is particularly pronounced. As shown in Figure 5.32(d)-(f), the erosion mode transitions from convergent to divergent. When the water table is at $0.5b_d$, particle loss is minimal at 1.2%, whereas at $1.5b_d$, the mass loss increases

significantly to 6.2%. Figure 5.33 shows the change in cumulative mass loss over time. It can be observed that for samples with different burial depths, the time required for the mass loss to stabilize is relatively similar. However, for samples with different groundwater levels, the higher the water level, the more time it takes for the mass loss to stabilize. Additionally, the rate of mass loss in the initial stage also increases with the rise in groundwater level. This change occurs because, for samples with different tunnel burial depths, the ratio of soil pressure to groundwater pressure is consistent. Therefore, even at different burial depths, the erosion development pattern is very similar. On the other hand, an increase in groundwater level will raise the water pressure at the crack location, altering the ratio of soil pressure to water pressure. As a result, under the same burial depth and crack width, samples with a higher groundwater level will experience greater seepage forces, making it harder for the soil to resist groundwater seepage.

5.4.3.2 Seepage-induced particle displacement

Figure 5.34 plots the particle migration trajectory at different burial depths and water table levels, respectively. It can be found that with the increase of tunnel depth, the scope of the particle migration zone triggered by seepage erosion increases, which is mainly due to the fact that the migration zone will start from the seepage point, and extend upward at a specific angle (as shown in Figure 5.34(a)-(c)), and finnaly extend to the ground surface. Therefore, the deeper the tunnel is, the larger the scope of the disturbance zone formed. In contrast, the particle migration zone in Figure 5.34(d) is limited when the water table is $0.5b_d$. This is because, in this case, the water table is situated below the surface, resulting in increased effective stress in the soil above the water table. This leads to stronger contact between soil particles, preventing large-scale granular

migration. As the water table rises, the effective stress of the soil above the tunnel decreases, while the increased water table also accelerates the seepage rate at the cracks, triggering a larger range of granular flow. Comparing the angle between the extent of granular flow and the horizontal line, it can be observed that the angle remains relatively constant at different tunnel depths, around 65°, but notably decreases as the height of the water table increases. This is because changes in tunnel depth do not significantly affect the effective gravity of the soil, meaning that microscopically, the particles maintain a similar resistance to fluid erosion. In contrast, an increase in the water table height raises the pore fluid pressure, which reduces the effective stress between the particles. This reduction in effective stress weakens the soil's resistance to erosion, thereby expanding the extent of the disturbed zone.

Figure 5.35 illustrates the surface settlement for different tunnel depths and water table levels. Comparing the effects of different burial depths, it can be found that although the mass loss of soil is much smaller when the tunnel is shallowly buried (e.g., burial depth $=1.0d_T$) compared to when it is deeply buried (e.g., burial depth = $1.5d_T$), the surface settlement caused by the shallow burial is nearly the same as that caused by the deeper burial. This suggests that a shallower tunnel depth poses a greater hazard of surface settlement due to seepage loss. Additionally, when the tunnel burial depth is shallow, the surface settlement curve takes on a U-shape. In contrast, for deeper tunnels, the surface settlement curve becomes V-shaped. This behavior can be explained by the ratio of the tunnel crack opening range W ($W = \theta * R$, where θ is the opening angle, and R is the radius of the tunnel) to the burial depth b_d. For shallow tunnels, W / b_d is large, leading

to a more uniform surface settlement across the entire opening. However, for deeply buried tunnels, W/b_d is much smaller, causing the cracks to behave like single seepage points, with the maximum settlement occurring directly above these points. As a result, the surface displacement curve exhibits a V-shape. Regarding the impact of varying water levels, surface settlement shows a significant increase as the water level rises. Additionally, a higher water level causes a broader area of surface settlement. Specifically, when the water level is $1.0b_d$ (Figure 5.35(e)), the settlement near the boundary (i.e., X=±0.8 m) remains minimal. However, when the water level increases to $2.0b_d$ (Figure 5.35(f)), settlement near this boundary increases substantially. Figure 5.36 shows the variation of maximum settlement with time for different burial depths and water levels. As seen in Figure 5.36(a), the curves for different burial depths exhibit similar evolution, indicating that the impact of tunnel depth on soil settlement primarily affects the magnitude of settlement. In contrast, increasing the water level not only shifts the turning point to an earlier time but also accelerates the rate of settlement increase. The higher the water level, the faster the development of surface settlement.

5.4.3.3 Soil stress variation and microscopic contact information

Figure 5.37 illustrates the variations in effective stress within the soil at different burial depths and water table levels. As the tunnel burial depth increases, the extent of effective stress reduction becomes more pronounced. This phenomenon arises because deeper tunnels induce large-scale particle flow, resulting in looser particle arrangements and weakened interparticle contact forces, thereby leading to a more significant reduction in effective stress. Similarly, the range of stress reduction caused by seepage erosion becomes more extensive with rising water table levels. The

microscopic contact force chains in Figure 5.38(a)-(c) reveal that increasing tunnel depth amplifies the lateral contact force above the seepage point, indicating that greater tunnel depths necessitate the transfer of higher upper earth pressures. Regarding the influence of groundwater level, Figure 5.38(d) shows that a stable soil arch structure is maintained when the groundwater level is $0.5b_d$. However, as the water level rises, the clear soil arch structure disappears, as seen in Figure 5.38(e) and (f), and is replaced by a transverse contact force chain formed after the collapse of the soil arch. These observations suggest that lowering the groundwater level enhances the soil's resistance to erosion.

5.5 Structure response to seepage erosion

Following the completion of tunnel seepage erosion, the contact forces between particles and the tunnel structure are extracted and applied as nodal external forces in a finite element analysis to evaluate the mechanical response of the tunnel under seepage erosion, including the tunnel convergent deformation and normal stress. Since the tunnel model in this study is three-dimensional, the deformation along the longitudinal axis is non-uniform. To focus on the deformation around the cracks, the structural lining deformation within a 100 mm range, encompassing the tunnel crack, is analyzed. The average value of this deformation is calculated and defined as the convergent deformation of the tunnel lining. These results are presented in the subsequent figures.

As shown in Figure 5.39(a), when the crack is located at the top of the tunnel, the influence of varying crack widths on deformation is primarily concentrated in the upper part of the tunnel.

The maximum top convergent deformation occurs when the crack width=$1.1d_{max}$. This is due to the reduction in structural stiffness caused by the crack, while particle loss remains minimal at this width, and the soil pressure around the crack does not significantly decrease compared to pre-erosion conditions, resulting in more pronounced deformation. In contrast, the smallest top deformation is observed when the crack width=$1.2d_{max}$. This can be attributed to the fact that the sample retains a stable soil arch after erosion, as shown in Figure 5.22(b), effectively supporting the overlying soil pressure and reducing deformation at the tunnel's top. Figure 5.39(b) plots the normal stress distribution along the ring direction of the tunnel (taking the case of crack=$1.4d_{max}$ as an example). It’s found that after the seepage erosion, the tunnel only shows a small tensile stress zone at the location below the waist, which indicates that for the condition where the crack occurs at the top, the effect of particle erosion on the structural damage is relatively small.

Figure 5.40 illustrates the mechanical response of the tunnel at various crack positions. When the crack is located at the 45° and 90° positions, the convergent deformation at the crack is minimal, while significant deformation occurs beneath it. This is due to the limited upward migration of soil particles beneath the crack, as shown in Figure 5.27(b)-(c), resulting in only a small reduction in soil pressure at that location. Consequently, larger deformation is observed below the crack. In contrast, when the crack is located at the 135° and 180° positions, the maximum convergent deformation occurs primarily at the tunnel's top. This is because, after the loss of soil near the crack, the soil above the tunnel migrates downward. However, due to the tunnel's support, the soil pressure above cannot be entirely transferred downward, leading to

increased pressure at the top of the tunnel and consequently greater deformation. Examining the internal force distribution in Figure 5.40(f) and (h), it is evident that when the crack is located at 135° and 180°, numerous tensile stress zones appear within the tunnel after erosion. Although the soil loss triggered by the crack at the above positions is relatively small (as shown in Figure 5.24(d)-(e)), the inability to transfer the soil pressure downward results in increased pressure heterogeneity within the structure, thereby causing greater structural damage.

Figure 5.41 shows the structural response at different burial depths. It can be seen that the tunnel burial depth mainly affects the deformation of the tunnel waist. As the burial depth increases, the convergence deformation of the waist increases. This is because, on the one hand, the increase in tunnel depth will lead to an increase in the lateral earth pressure at the waist of the tunnel. On the other hand, the deeper the tunnel is, the more serious the particle loss is, that is, the more obvious the reduction of earth pressure above the tunnel is. Therefore, under the combined effect of the two, when the tunnel is buried deeper, the seepage erosion causes more significant deformation. As a result, tensile stress zones are also mainly concentrated at the tunnel waist, as seen in Figure 5.41(b). At the same time, some tensile stress zones also appear above the tunnel, which is due to the fact that the lateral compression of the tunnel will lead to a tendency of expansion at the top, and hence it is also susceptible to tensile damage.

Figure 5.42 presents the results for varying water table levels. When the water table is at $0.5b_d$, the soil effective stress above the tunnel is the largest, and the tunnel crown experiences the

highest earth pressure. However, the deformation at the crown is minimal, while the most significant deformation occurs at the tunnel waist. This is due to the formation of a stable soil arch within the soil (e.g., Figure 5.38(d)) after erosion, which redistributes the soil pressure and reduces deformation at the crown. As the groundwater table rises, the stability of the soil arch is compromised, leading to an increase in deformation at the tunnel crown and a decrease near the waist. A comparison with Figure 5.39(b) (water level=$1.0b_d$) shows that even with the water level raised to $1.5b_d$ (Figure 5.42(b)), the impact of seepage erosion on the structural tensile stress zone remains minimal. This indicates that the spatial location of the tunnel crack and the burial depth are the primary factors governing the development of tensile stress zones within the tunnel structure. In contrast, variations in crack size and groundwater table depth have only a secondary influence on the distribution of structural stresses.

5.6 Summary

In this study, a tunnel seepage erosion model was initially developed using a combination of CFD-DEM. The evolution of erosion under various conditions, such as different tunnel crack widths, crack positions, burial depths, and groundwater tables, was examined at a microscopic scale. Subsequently, the tunnel's response to erosion was analyzed using the FEM, enabling an investigation of tunnel convergence deformation and normal stress distribution. Based on the analysis of the simulation results, the following conclusions are drawn:

(a) The increase in tunnel crack width significantly accelerates cumulative soil loss. Based on crack size, the soil erosion pattern can be classified into three regimes: stable mode, convergent

erosion, and divergent erosion. As the crack position gradually shifts from the crown to the bottom of the tunnel, the soil mass loss gradually decreases. When the crack appears at the bottom of the tunnel, the amount of soil lost is the least. Additionally, mass loss increases with greater tunnel burial depth and higher water levels;

(b) In the early stages of seepage erosion, an earth arch structure forms within the soil, supporting the pressure of the overlying soil layer. Under the influence of the earth arch, there is a delay in the maximum surface settlement relative to the loss of mass. However, as particle loss continues, the stability of the soil arch deteriorates, leading to a rapid increase in surface settlement. Increasing the crack width and raising the water table height significantly accelerate the collapse of the soil arch, making sudden surface settlement more likely than changes in crack position or tunnel burial depth;

(c) Seepage erosion significantly alters the soil force transfer structure. The soil pressure originally borne by the eroded particles will be transferred to the soil on both sides of the crack under the action of soil arching. As a result, the stress changes induced by erosion exhibit heterogeneity. Specifically, stress relaxation occurs near the cracks, while stress concentration zones emerge around the cracks;

(d) Increasing the crack width and water table height has a minimal effect on the increase in tunnel convergence deformation and tensile stress zones. In contrast, increasing tunnel burial

depth amplifies the convergence deformation at the tunnel girdle, making the occurrence of tensile stress zones more likely. The most significant factor affecting the mechanical response of the tunnel is the location of the cracks. As the crack location shifts from the top to the bottom of the tunnel, although particle mass loss decreases, the ability to transfer the overlying earth pressure diminishes. This results in more pronounced tunnel deformation and greater tensile stress damage.

Table 5.1 Summary of simulation scheme

	No.	Crack position (θ_a)	Burial depth	Crack width	Water head
Crack position	1	0°	2.0 d_T	1.4 $d_{\max}$	1.0 b_d
	2	45°	2.0 d_T	1.4 $d_{\max}$	1.0 b_d
	3	90°	2.0 d_T	1.4 $d_{\max}$	1.0 b_d
	4	135°	2.0 d_T	1.4 $d_{\max}$	1.0 b_d
	5	180°	2.0 d_T	1.4 $d_{\max}$	1.0 b_d
Burial depth	6	0°	1.0 d_T	1.4 $d_{\max}$	1.0 b_d
	7	0°	1.5 d_T	1.4 $d_{\max}$	1.0 b_d
	8	0°	2.0 d_T	1.4 $d_{\max}$	1.0 b_d
Crack width	9	0°	2.0 d_T	1.1 $d_{\max}$	1.0 b_d
	10	0°	2.0 d_T	1.2 $d_{\max}$	1.0 b_d
	8	0°	2.0 d_T	1.3 $d_{\max}$	1.0 b_d
	1	0°	2.0 d_T	1.4 $d_{\max}$	1.0 b_d
	11	0°	2.0 d_T	1.5 $d_{\max}$	1.0 b_d
Water head	12	0°	1.5 d_T	1.3 $d_{\max}$	0.5 b_d
	7	0°	1.5 d_T	1.3 $d_{\max}$	1.0 b_d
	13	0°	1.5 d_T	1.3 $d_{\max}$	1.5 b_d

Note: d_T is the outer diameter of the tunnel; $d_{\max}$ is the diameter of the maximum particle size; b_d is the burial depth of the tunnel.

Table 5.2 Parameters used in the simulation

Parameters	Unit	Value

DEM domain	Particle Young's modulus E_p	Pa	1×10^8
	Particle Poisson's ratio υ_p	-	0.3
	Particle density ρ_p	$kg\cdot m^{-3}$	2.61×10^3
	Particle-to-particle friction coefficient μ_p	-	0.5
	Particle-to-wall friction coefficient μ_w	-	0.5
	Restitution coefficient e_p	-	0.3
	Rolling resistance r_c	-	0.1
	Diameter of particles d_p	mm	0.3-2
	Timestep of DEM Δt_{DEM}	s	2.4×10^{-7}
	Gravity acceleration	m/s^2	9.8
	Particle number	-	2,000,000
CFD domain	Fluid density ρ_f	$kg\cdot m^{-3}$	1000
	Dynamic viscosity ν_f	$Pa\cdot s$	1000
	Timestep of CFD Δt_{CFD}	s	2.4×10^{-5}
FEM domain	Structure density ρ_s	$kg\cdot m^{-3}$	2500
	Structure Young's modulus E_s	Pa	1.92×10^8
	Structure Poisson's ratio υ_s	-	0.182

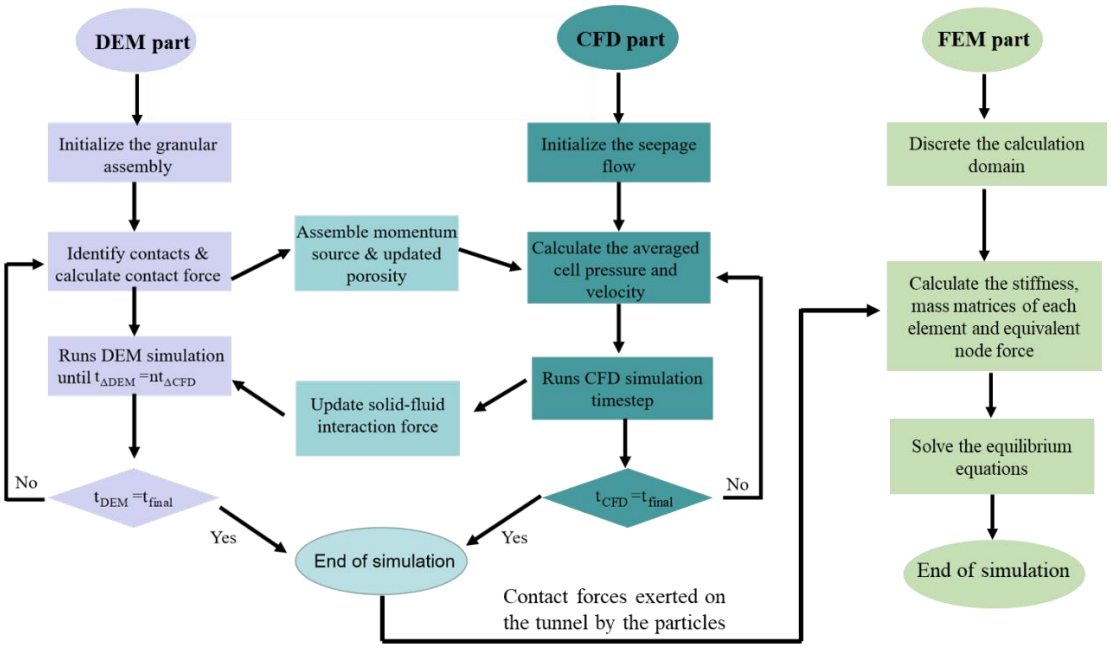

Figure 5.1 Algorithm flowchart of CFD-DEM-FEM coupling

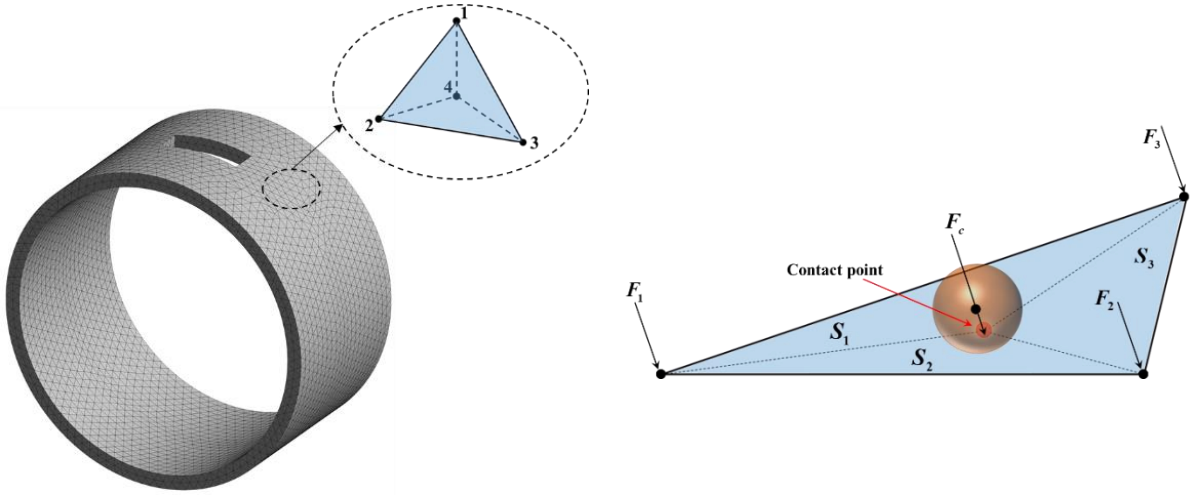

(a) (b)

Figure 5.2 Contact force on the tunnel element: (a) tunnel mesh with tetrahedral element; (b) contact between particle and trilateral element

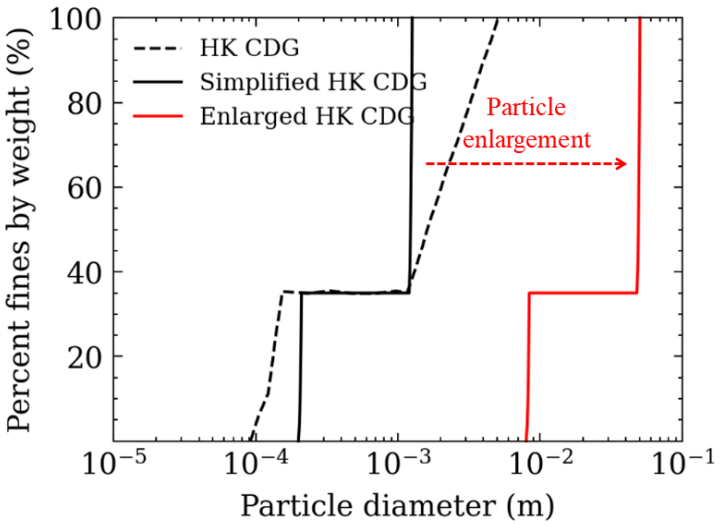

Figure 5.3 Particle size distribution (PSD) curves of HK-CDG and enlarged PSD used in simulation

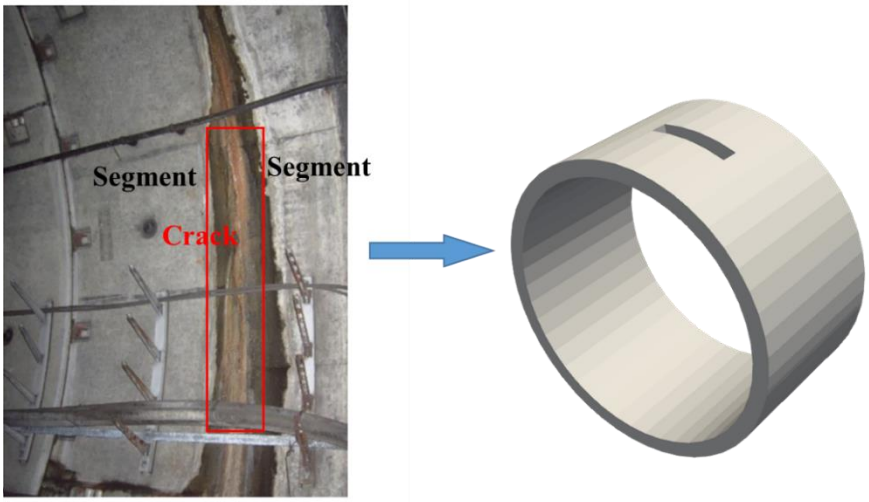

Figure 5.4 Simplified modeling of cracks between tunnel linings

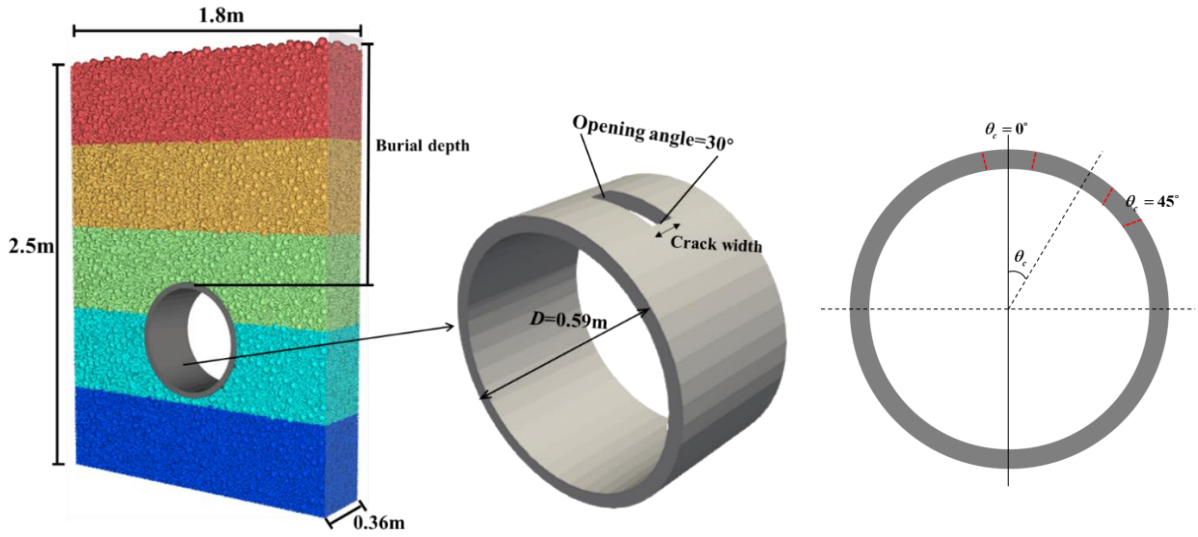

Figure 5.5 Setup of the simulated numerical model: (a) configuration of the tunnel erosion model; (b) the definition of crack position angles

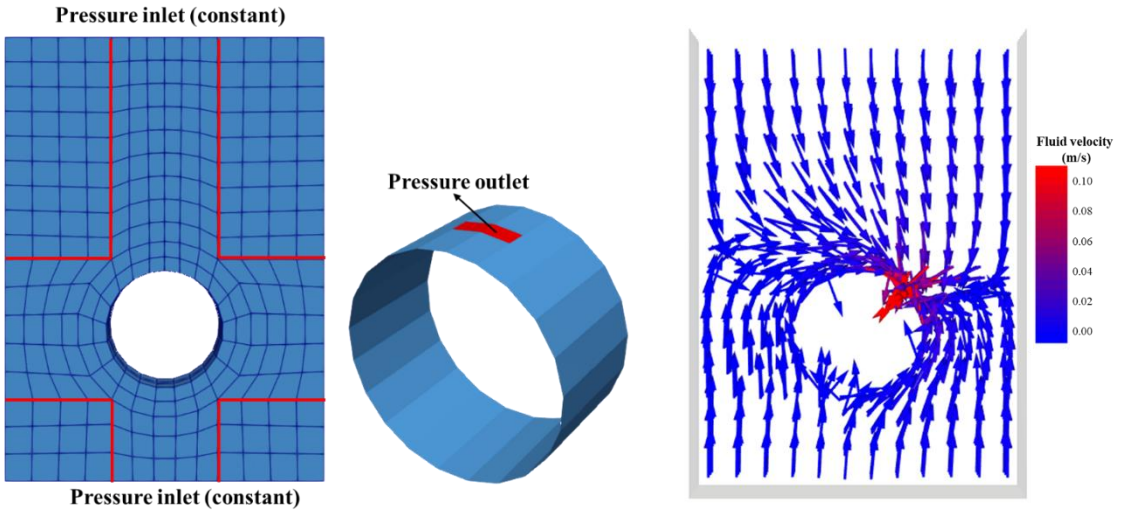

(a) (b)

Figure 5.6 Setup of the fluid domain: (a) mesh part and boundary condition for CFD; (b) fluid velocity field

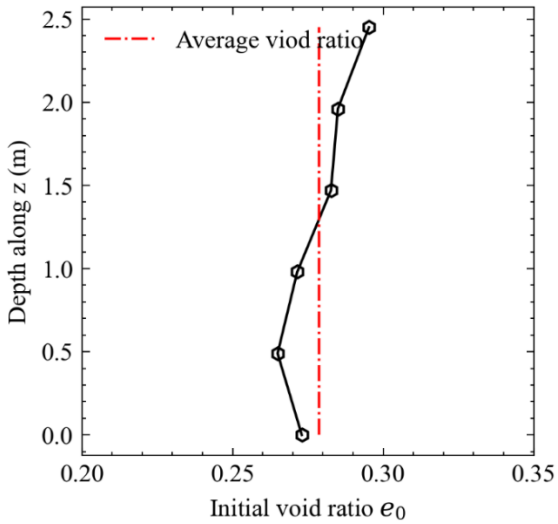

Figure 5.7 Distribution of initial void ratio

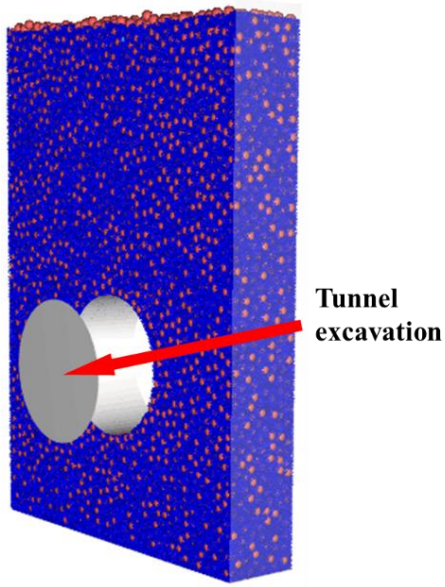

Figure 5.8 Process of tunnel excavation

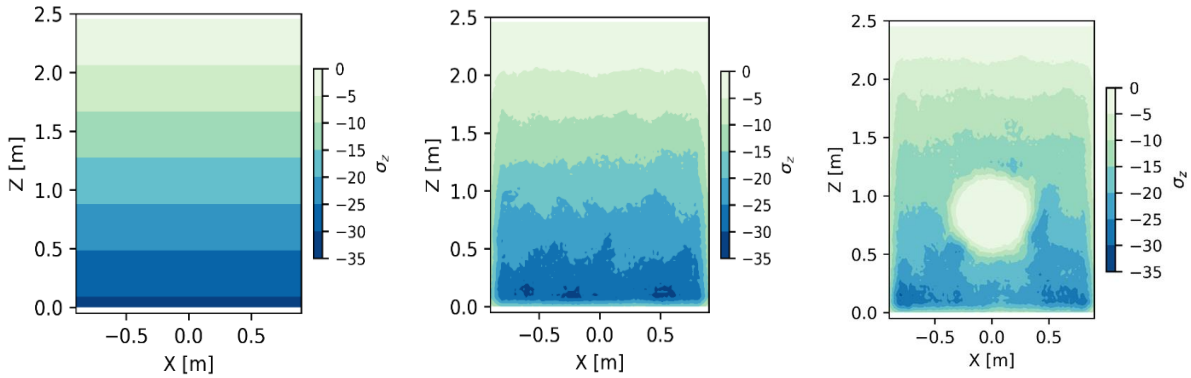

Figure 5.9 The distribution of soil effective stress: (a) analytical distribution; (b) simulated results; (c)stress distribution after excavation

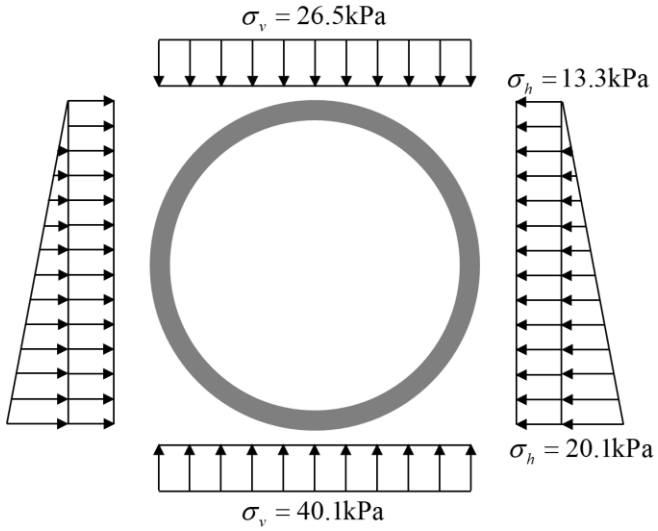

Figure 5.10 Analytical solution for tunnel pressure

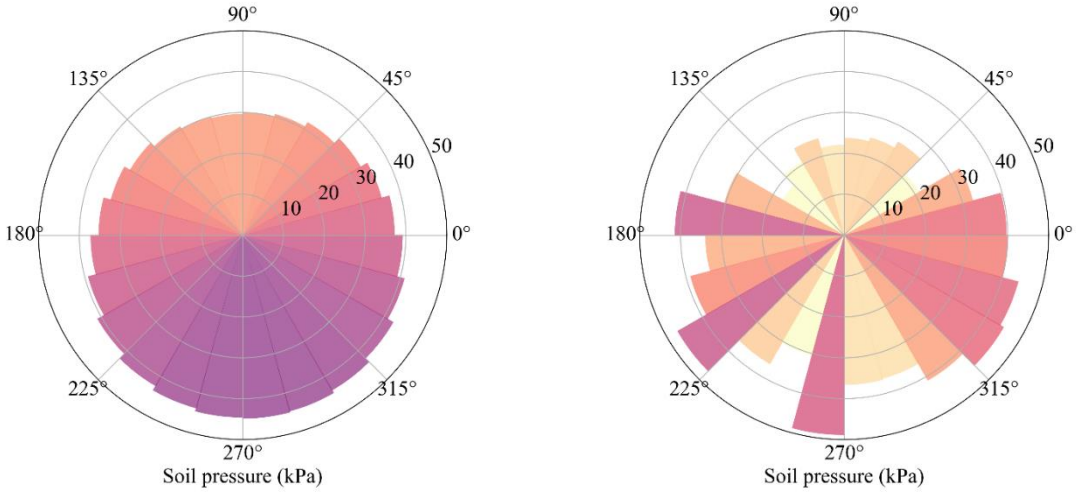

Figure 5.11 Comparison of tunnel pressure distribution between analytical solution and simulation results:

(a) analytical solution; (b) simulation results

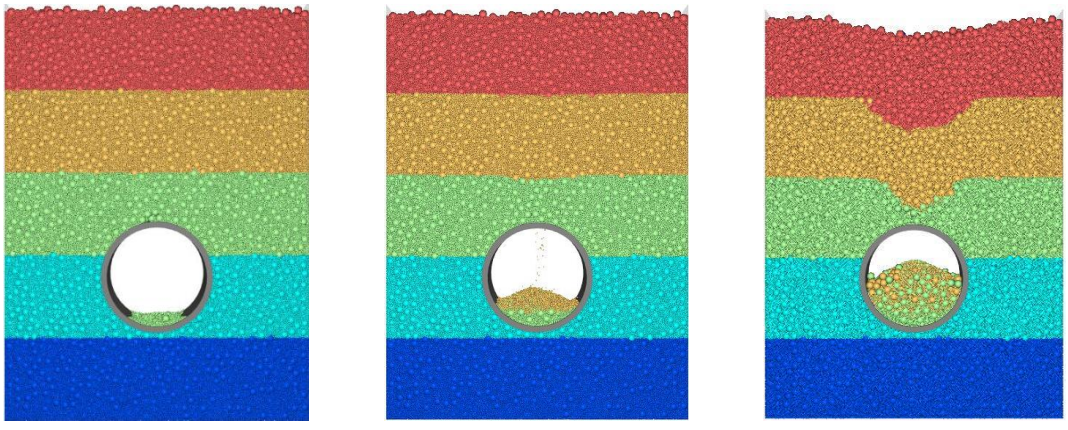

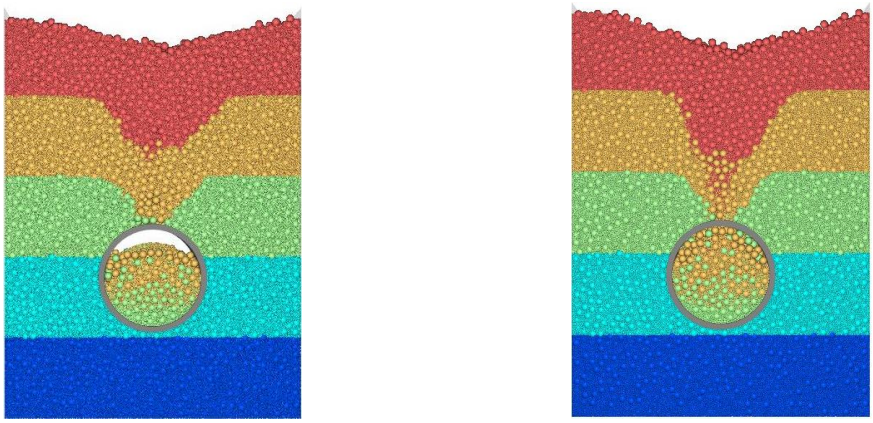

(d) (e)

Figure 5.12 Particle loss for different crack widths: (a) Crack width=$1.1d_{max}$; (b) Crack width=$1.2d_{max}$;(c) Crack width=$1.3d_{max}$; (d) Crack width=$1.4d_{max}$;(e) Crack width=$1.5d_{max}$

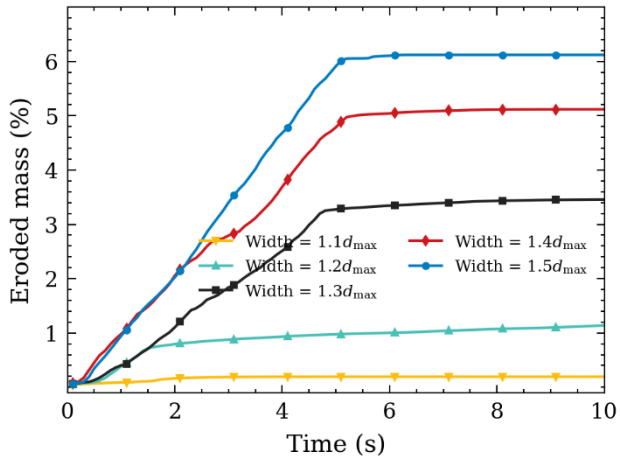

Figure 5.13 Eroded mass loss versus simulation time for different crack widths

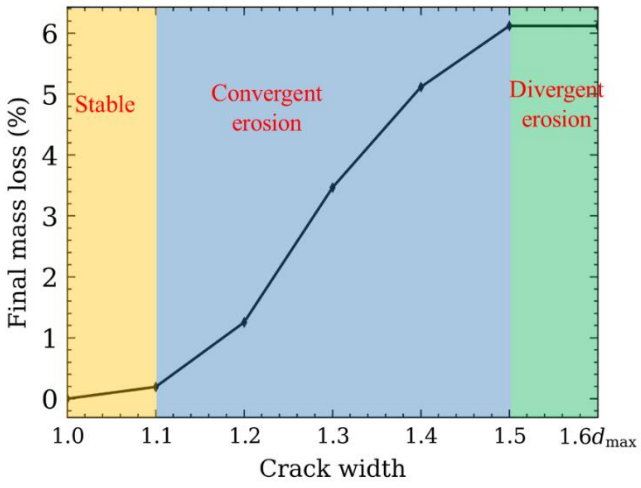

Figure 5.14 Final mass loss versus crack width

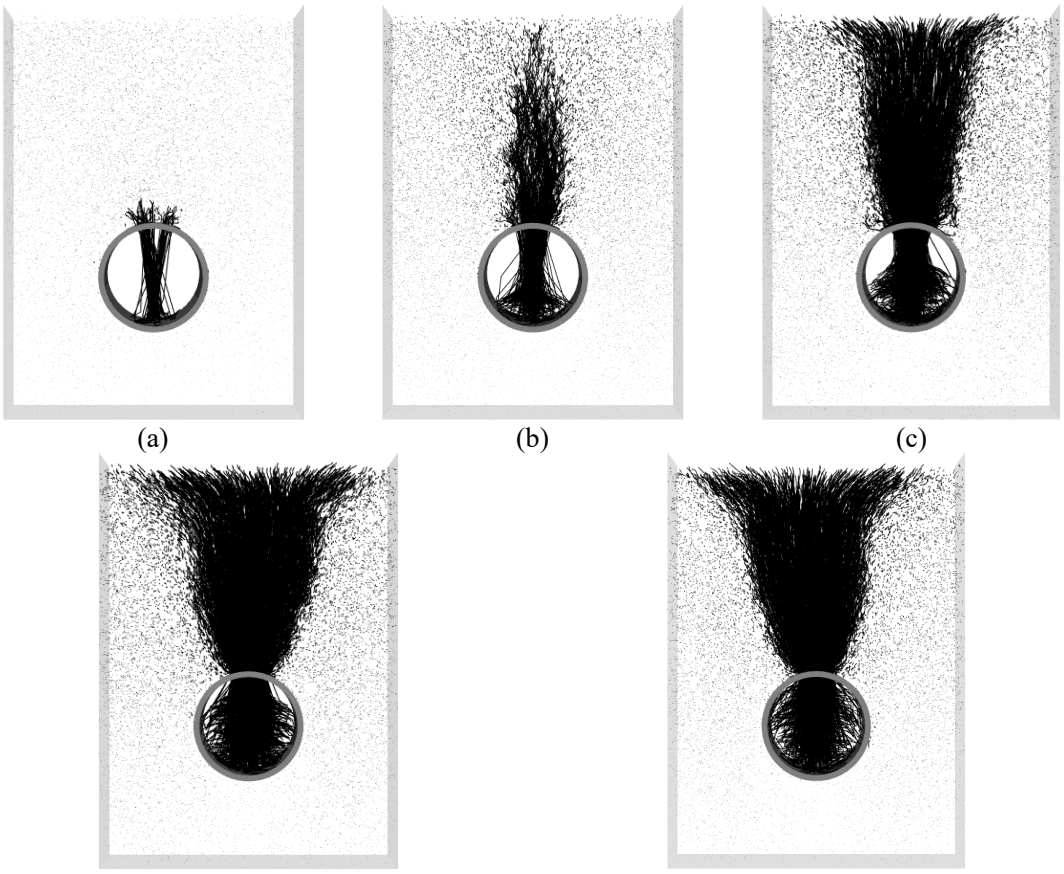

(a) (b) (c)

(d) (e)

Figure 5.15 Particle trajectory during erosion for different crack widths: (a) Crack width=$1.1d_{max}$; (b) Crack width=$1.2d_{max}$;(c) Crack width=$1.3d_{max}$; (d) Crack width=$1.4d_{max}$;(e) Crack width=$1.5d_{max}$

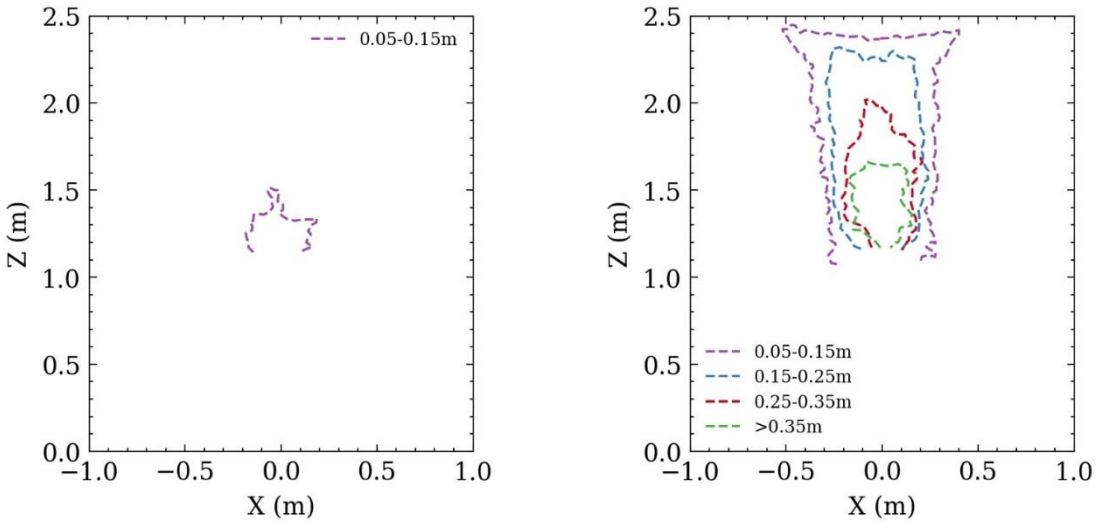

(a) (b)

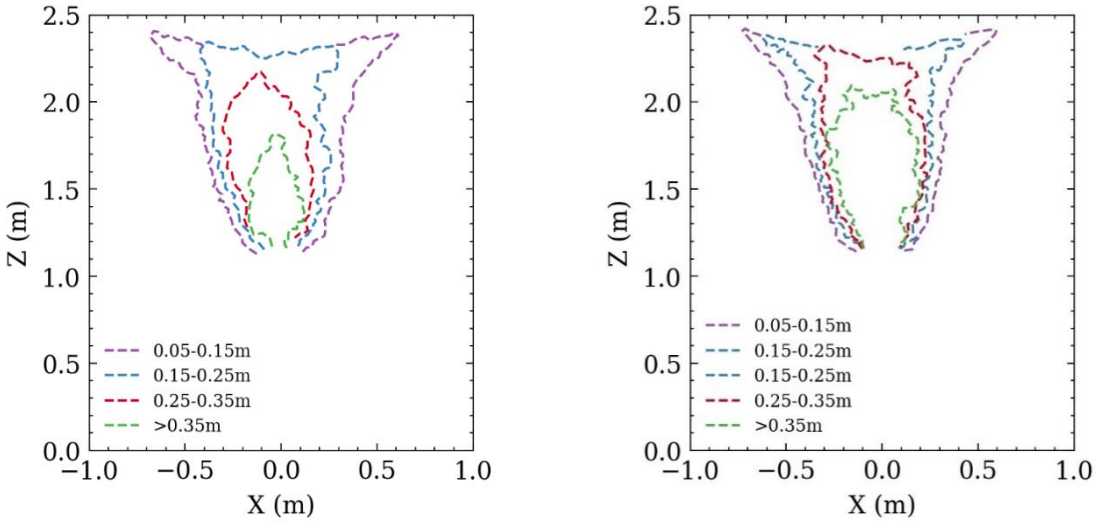

(c) (d)

Figure 5.16 Distribution of soil displacement contour for different crack widths: (a) Crack width=$1.2d_{max}$; (b) Crack width=$1.3d_{max}$; (c) Crack width=$1.4d_{max}$; (d) Crack width=$1.5d_{max}$

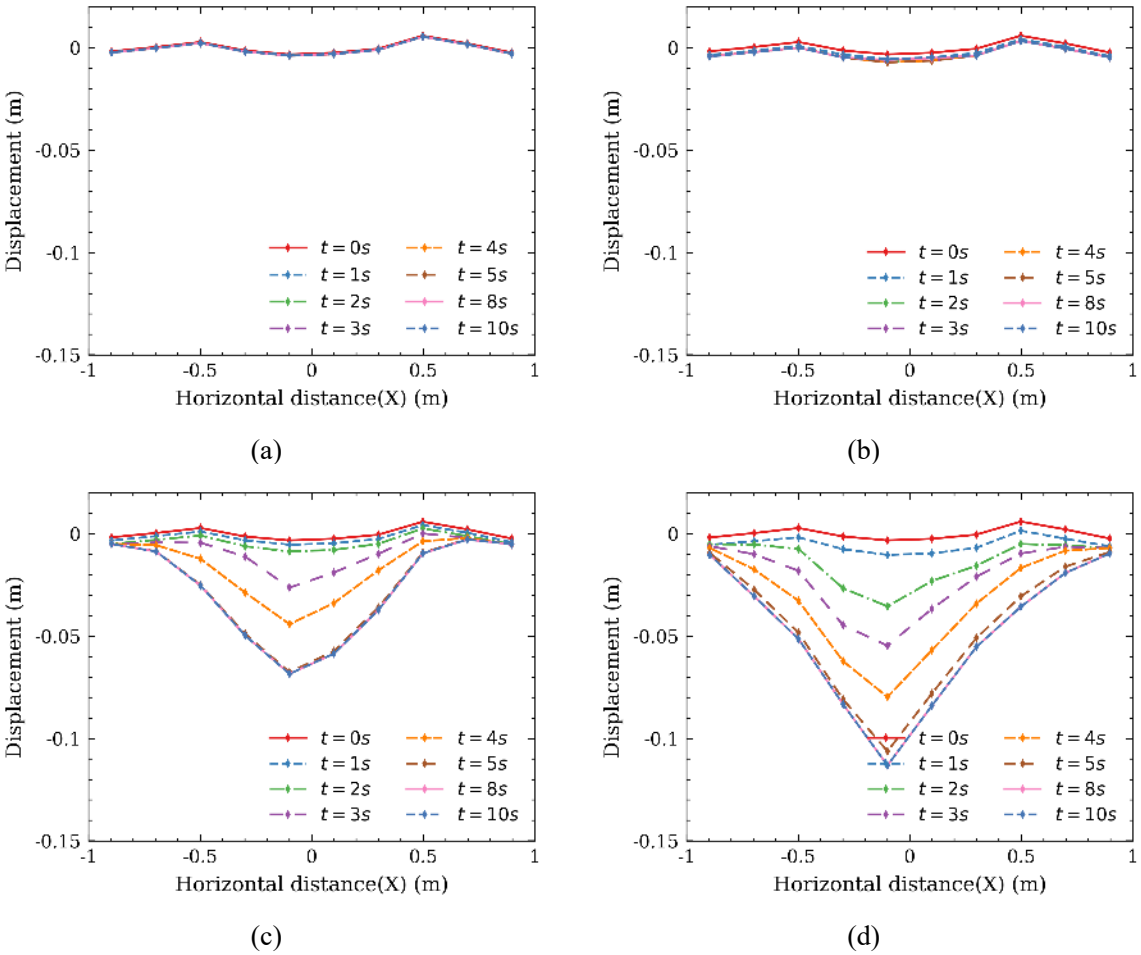

(a) (b)

(c) (d)

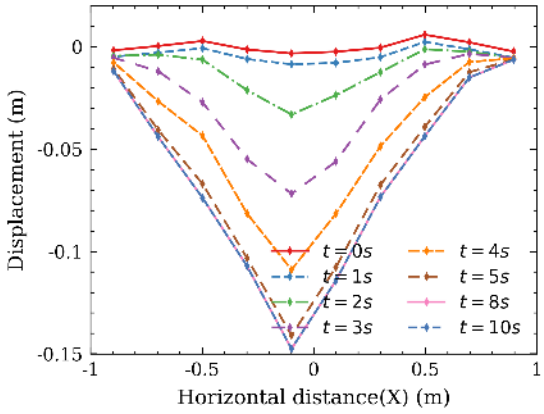

(e)

Figure 5.17 Surface displacement for different crack widths: (a) Crack width=$1.1d_{max}$; (b) Crack width= $1.2d_{max}$;(c) Crack width=$1.3d_{max}$; (d) Crack width=$1.4d_{max}$;(e) Crack width=$1.5d_{max}$

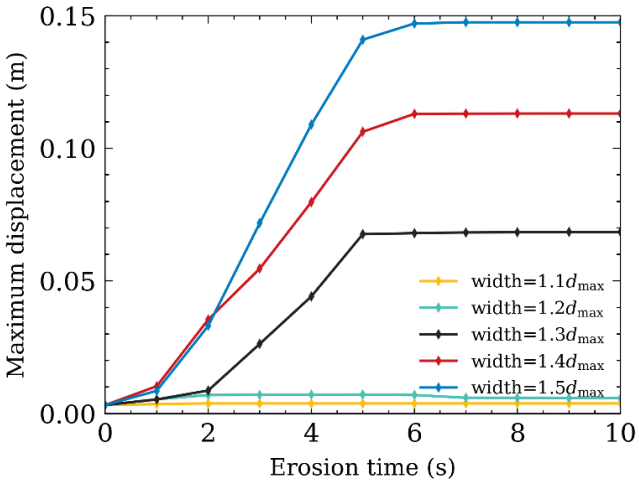

Figure 5.18 Maximum displacement versus erosion time for different crack widths.

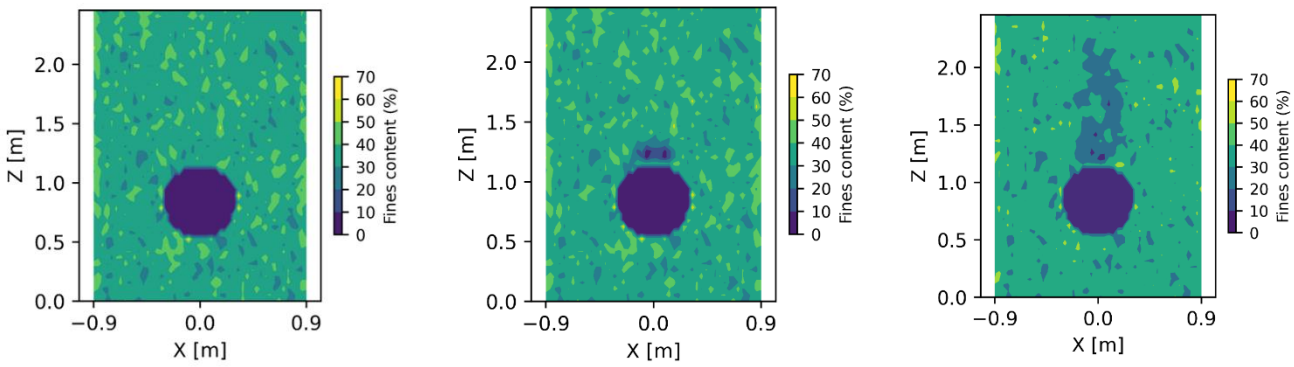

(a) (b) (c)

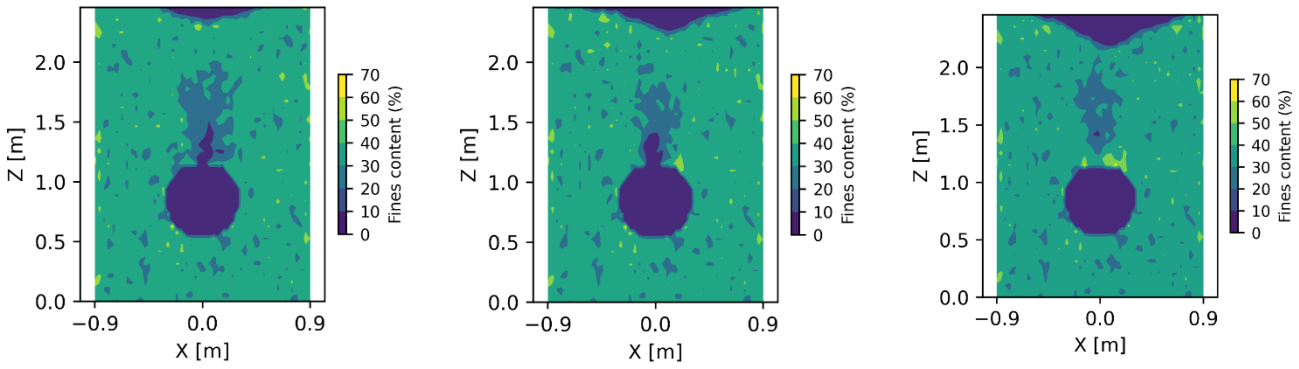

(d) (e) (f)

Figure 5.19 Distribution of fine content after erosion: (a) Initial state; (b) Crack width=$1.1d_{max}$; (c) Crack width=$1.2d_{max}$; (d) Crack width=$1.3d_{max}$; (e) Crack width=$1.4d_{max}$; (f) Crack width=$1.5d_{max}$

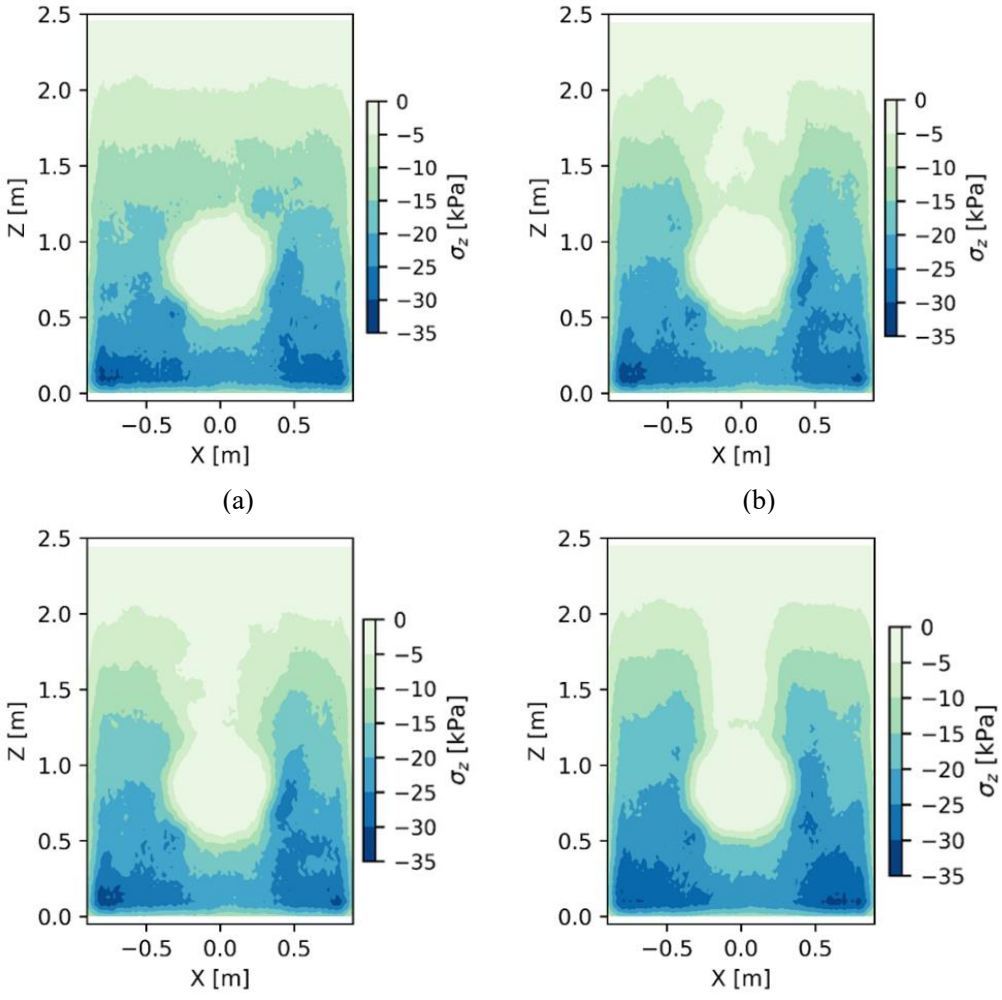

(a) (b)

(c) (d)

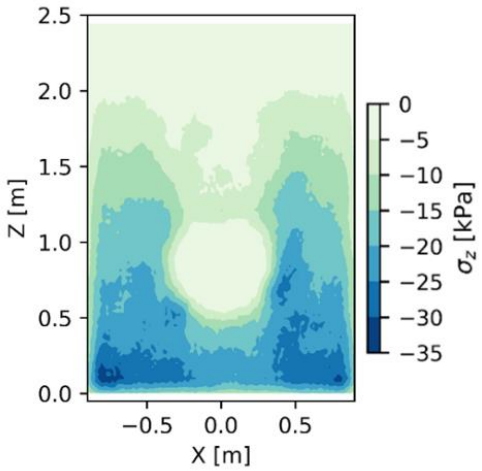

(e)

Figure 5.20 Distribution of soil effective stress for different crack widths: (a) Crack width=$1.1d_{max}$; (b) Crack width=$1.2d_{max}$;(c) Crack width=$1.3d_{max}$; (d) Crack width=$1.4d_{max}$;(e) Crack width=$1.5d_{max}$

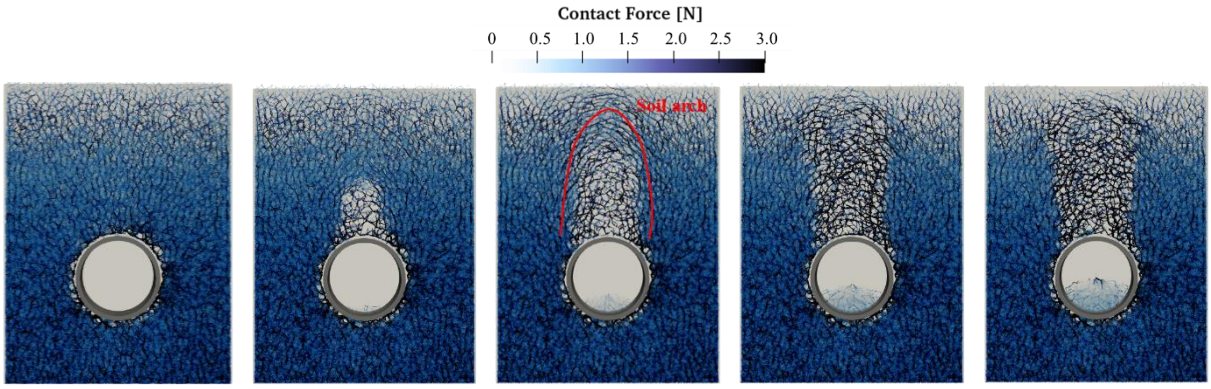

(a) (b) (c) (d) (e)

Figure 5.21 Soil contact force chain and soil arch effect: (a) $t=0$; (b) $t=1$s ; (c) $t=2$s ; (d) $t=5$s ; (e) $t=10$s

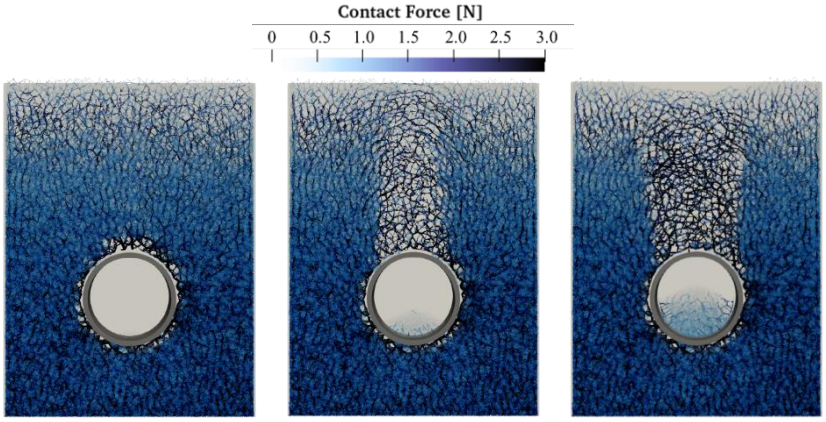

(a) (b) (c)

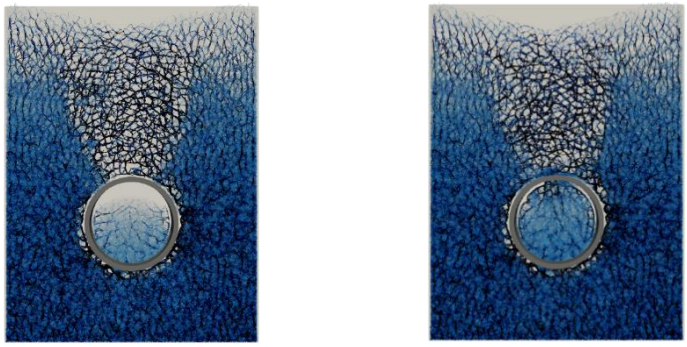

(d) (e)

Figure 5.22 Contact force chain distribution in samples with different crack widths: (a) Crack width= $1.1d_{max}$;(c) Crack width= $1.3d_{max}$; (d) Crack width= $1.4d_{max}$;(e) Crack width= $1.5d_{max}$

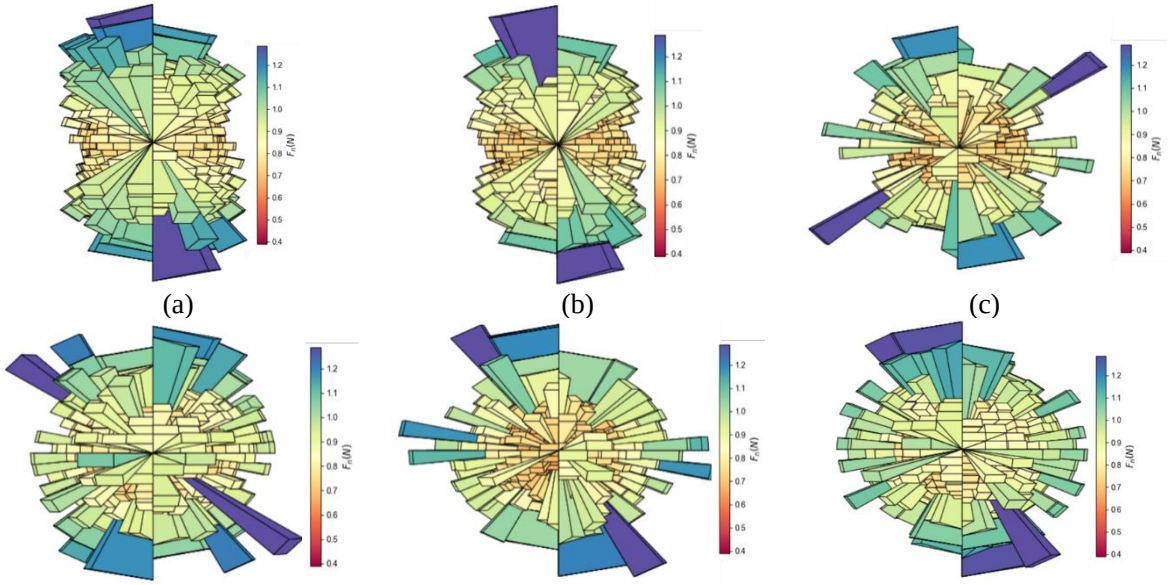

(a) (b) (c)

(d) (e) (f)

Figure 5.23 Distribution of normal contact for different crack widths: (a) Initial state; (b) Crack width= $1.1d_{max}$;(c) Crack width= $1.2d_{max}$;(d) Crack width= $1.3d_{max}$;(e) Crack width= $1.4d_{max}$;(f) Crack width= $1.5d_{max}$

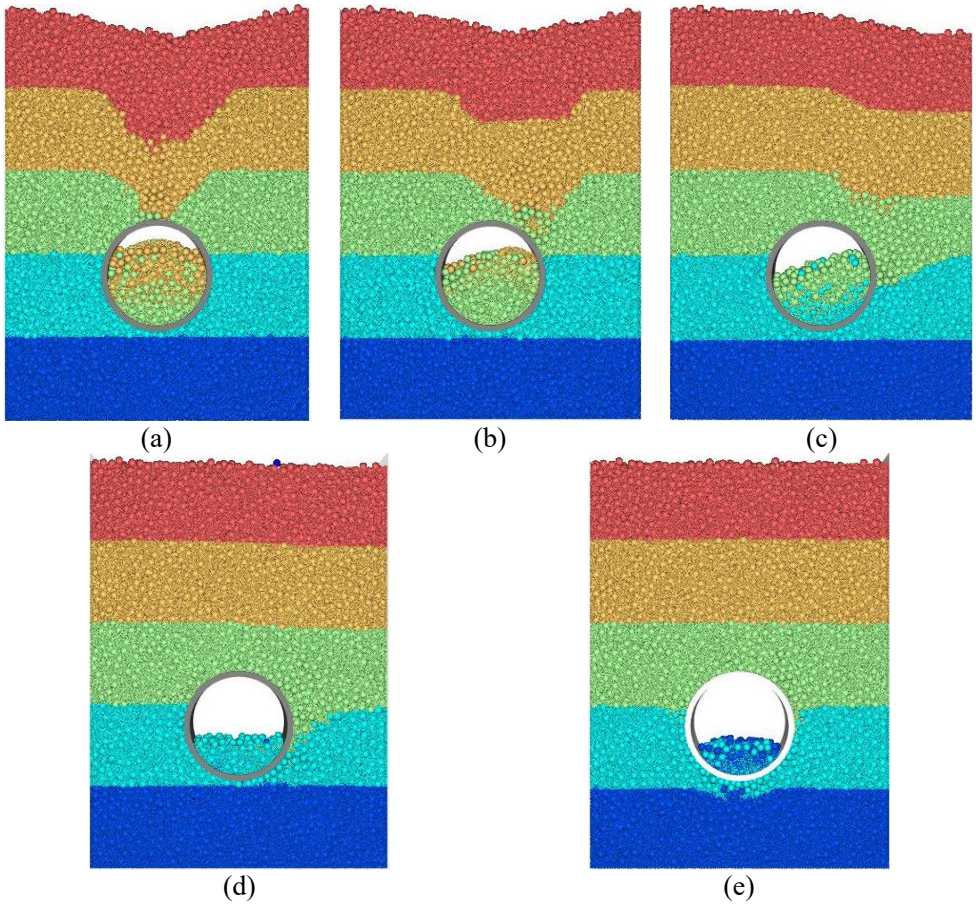

Figure 5.24 Particle loss with varying crack positions: (a) $\theta_a = 0^\circ$; (b) $\theta_a = 45^\circ$; (c) $\theta_a = 90^\circ$;(d) $\theta_a = 135^\circ$;(e) $\theta_a = 180^\circ$

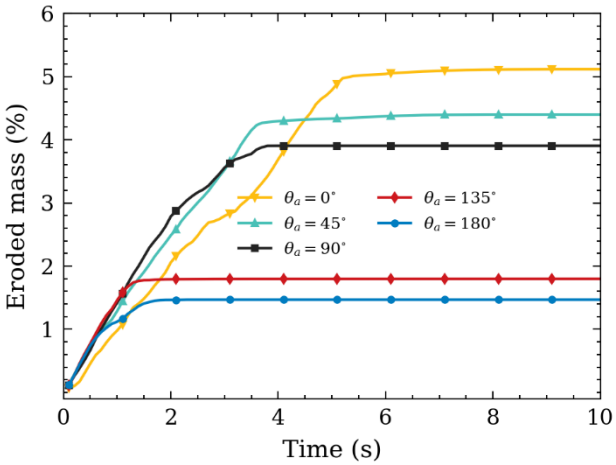

Figure 5.25 Eroded mass loss versus simulation time for different crack positions

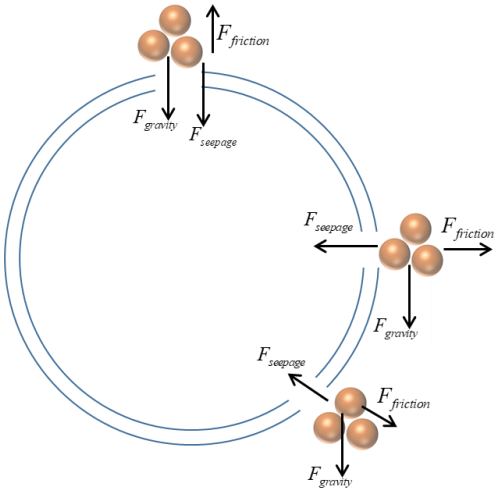

Figure 5.26 The force on the particles during erosion

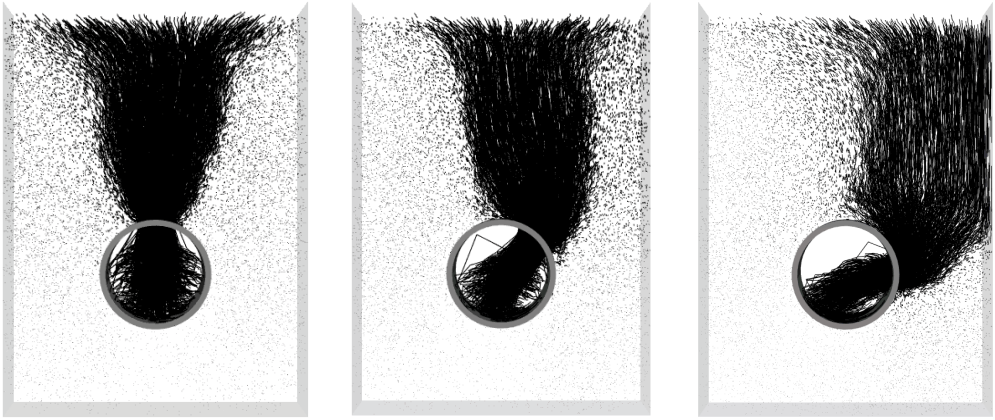

(a) (b) (c)

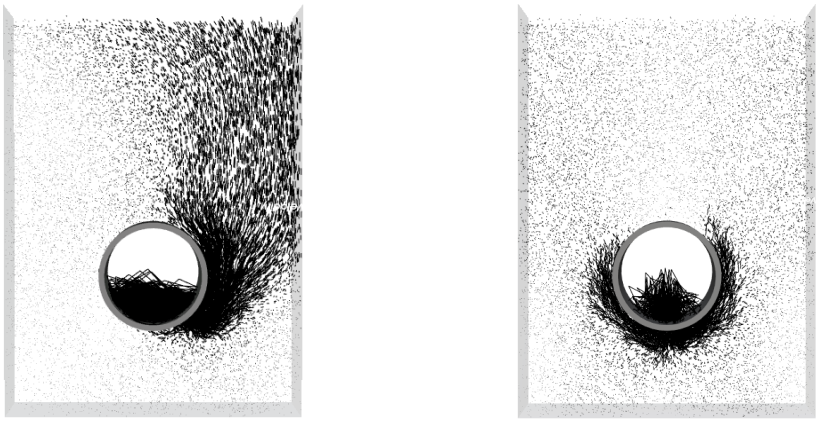

(d) (e)

Figure 5.27 Particle trajectory during erosion for different opening angles: (a) $\theta_a = 0^\circ$;(b) $\theta_a = 45^\circ$;(c) $\theta_a = 90^\circ$;(d) $\theta_a = 135^\circ$;(e) $\theta_a = 180^\circ$

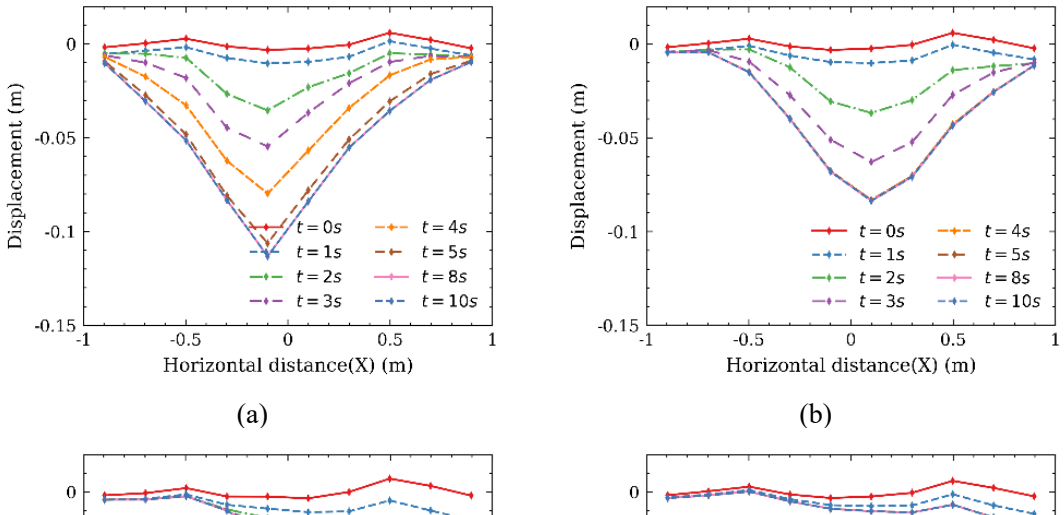

(a) (b)

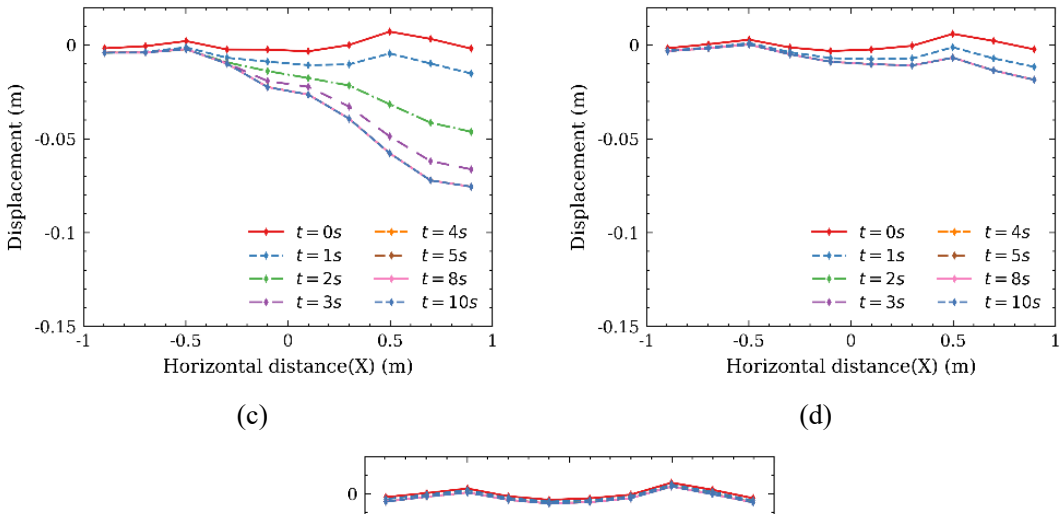

(c) (d)

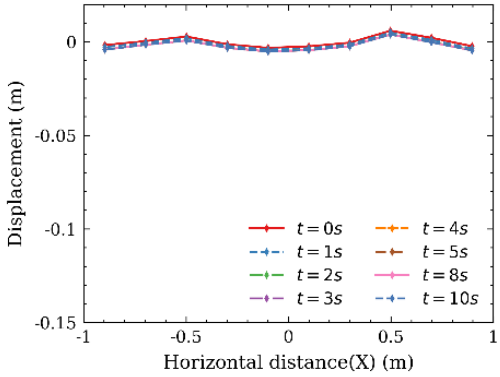

(e)

Figure 5.28 Surface displacement for different opening angles: (a) $\theta_a = 0^\circ$; (b) $\theta_a = 45^\circ$; (c) $\theta_a = 90^\circ$;(d) $\theta_a = 135^\circ$;(e) $\theta_a = 180^\circ$

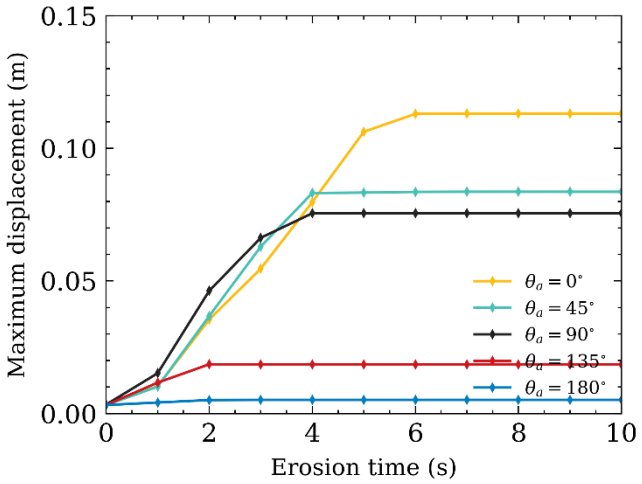

Figure 5.29 Maximum displacement versus erosion time for different crack positions.

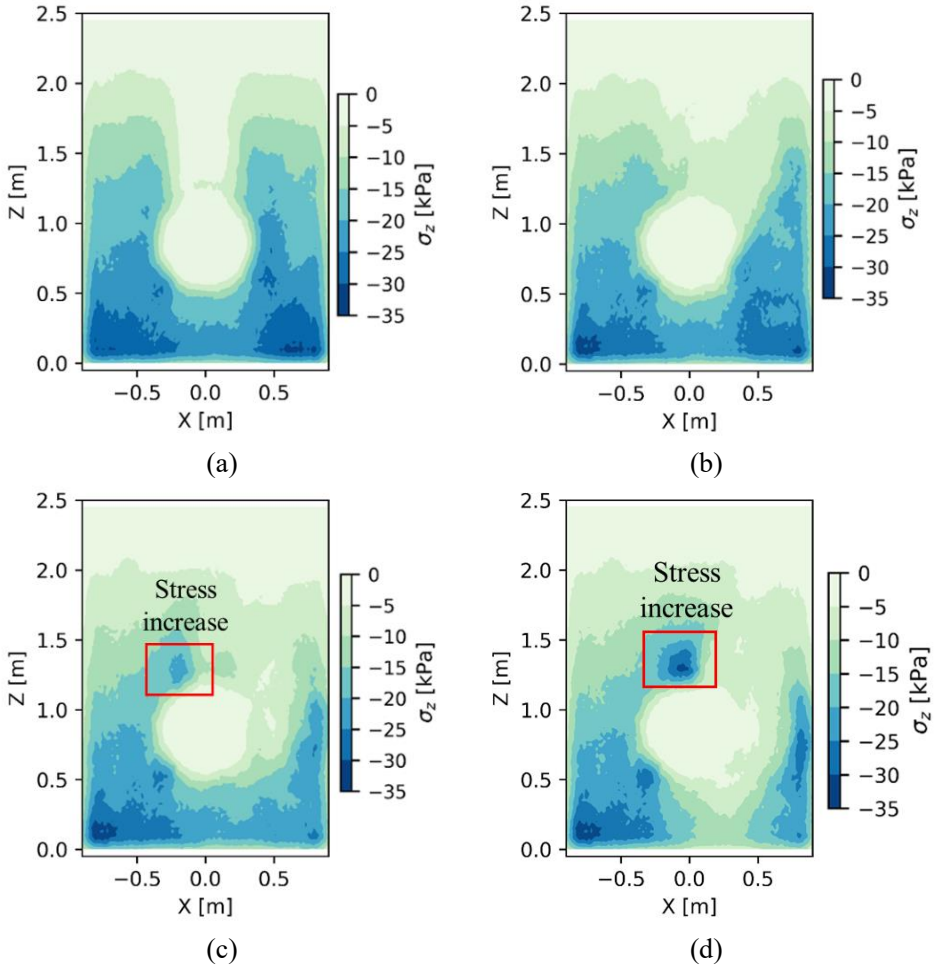

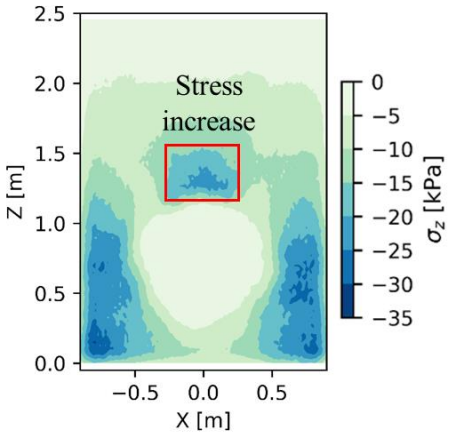

(e)

Figure 5.30 Distribution of soil effective stress for different opening angles: (a) $\theta_a = 0^\circ$; (b) $\theta_a = 45^\circ$; (c) $\theta_a = 90^\circ$;(d) $\theta_a = 135^\circ$;(e) $\theta_a = 180^\circ$

(a) $\theta_a = 0^\circ$ (b) $\theta_a = 45^\circ$ (c) $\theta_a = 90^\circ$

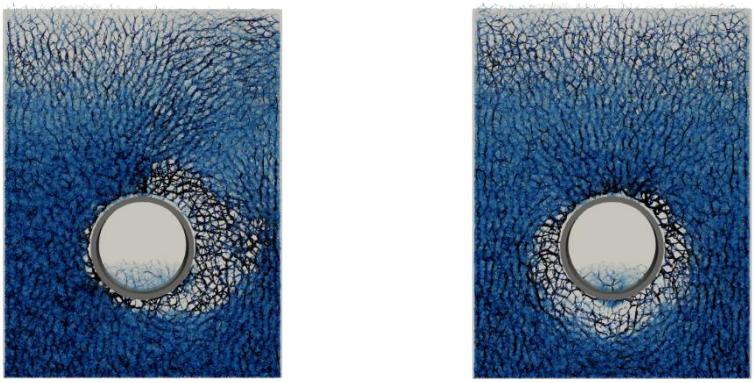

(d) $\theta_a = 135^\circ$ (e) $\theta_a = 180^\circ$

Figure 5.31 Contact force chain distribution in samples with different crack positions: (a) $\theta_a = 0^\circ$; (b) $\theta_a = 45^\circ$; (c) $\theta_a = 90^\circ$;(d) $\theta_a = 135^\circ$;(e) $\theta_a = 180^\circ$

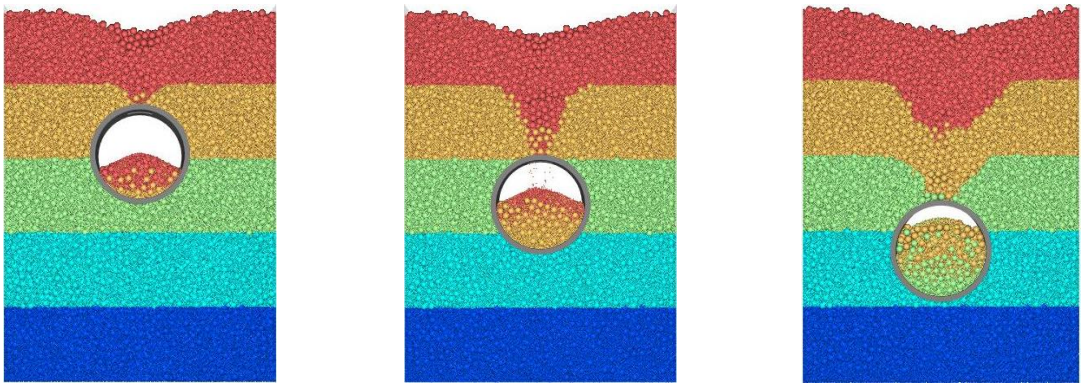

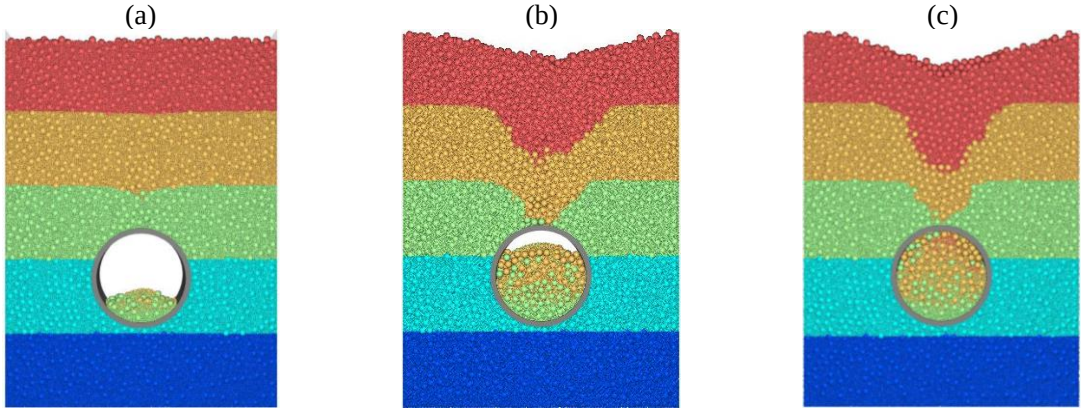

(a) (b) (c)

(d) (e) (f)

Figure 5.32 Particle loss for different burial depths and water levels: (a) Burial depth=$1.0d_T$; (b) Burial depth=$1.5d_T$; (c) Burial depth= $2.0d_T$;(d) Water level=$0.5b_d$;(e) Water level=$1.0b_d$;(f) Water level=$1.5b_d$

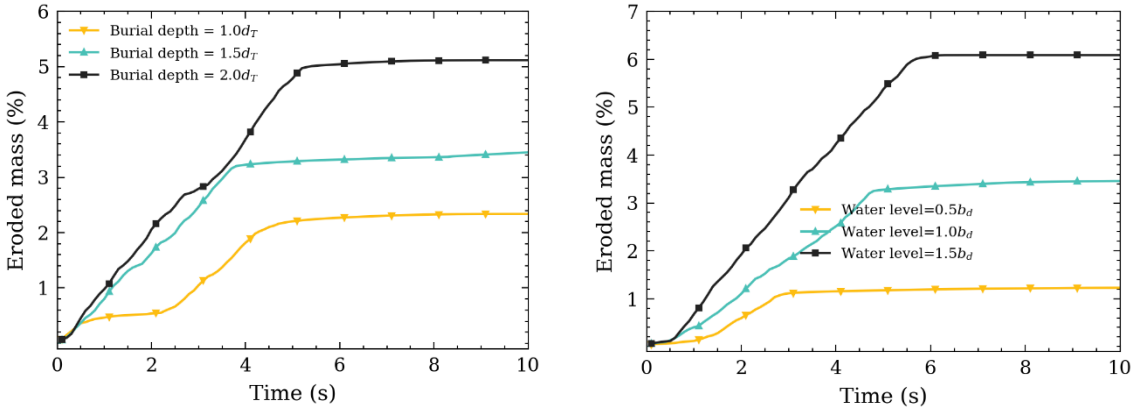

(a) (b)

Figure 5.33 Eroded mass loss versus simulation time: (a) Different burial depths; (b) Different water levels

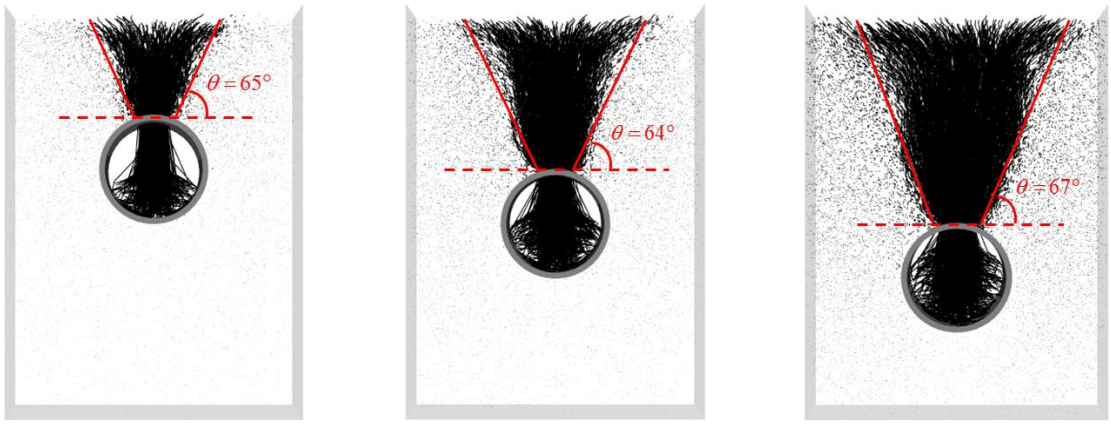

(a) Burial depth=$1.0d_T$ (b) Burial depth=$1.5d_T$ (c) Burial depth= $2.0d_T$

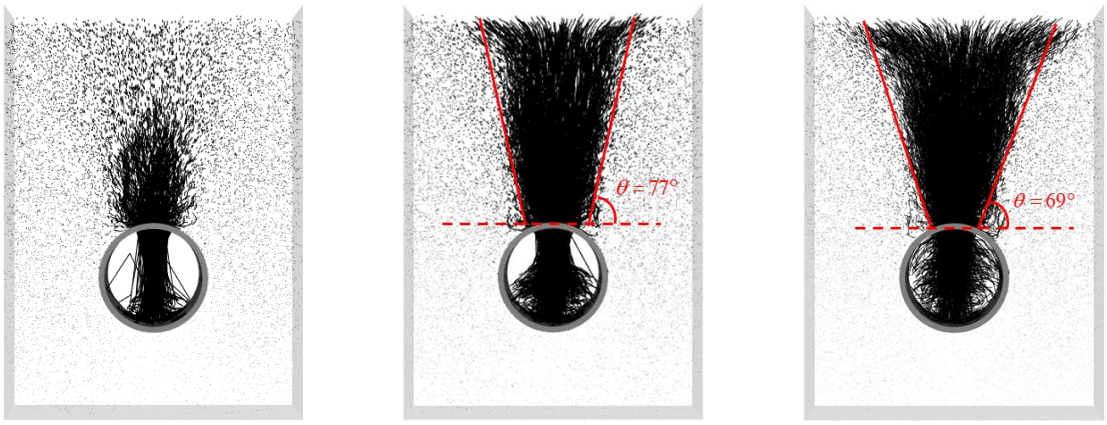

(d) Water level= $0.5b_d$ (e) Water level= $1.0b_d$ (f) Water level= $1.5b_d$

Figure 5.34 Particle trajectory during erosion for different burial depths and water levels: (a) Burial depth= $1.0d_T$; (b) Burial depth= $1.5d_T$; (c) Burial depth= $2.0d_T$;(d) Water level= $0.5b_d$;(e) Water level= $1.0b_d$;(f) Water level= $1.5b_d$

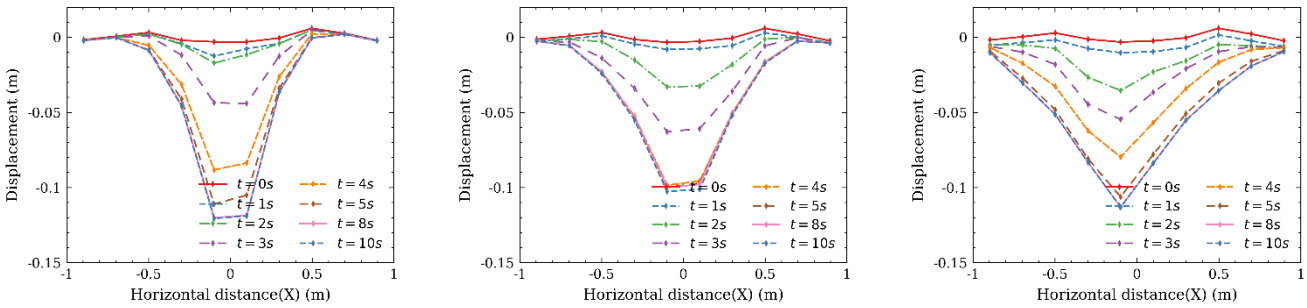

(a) Burial depth= $1.0d_T$ (b) Burial depth= $1.5d_T$ (c) Burial depth= $2.0d_T$

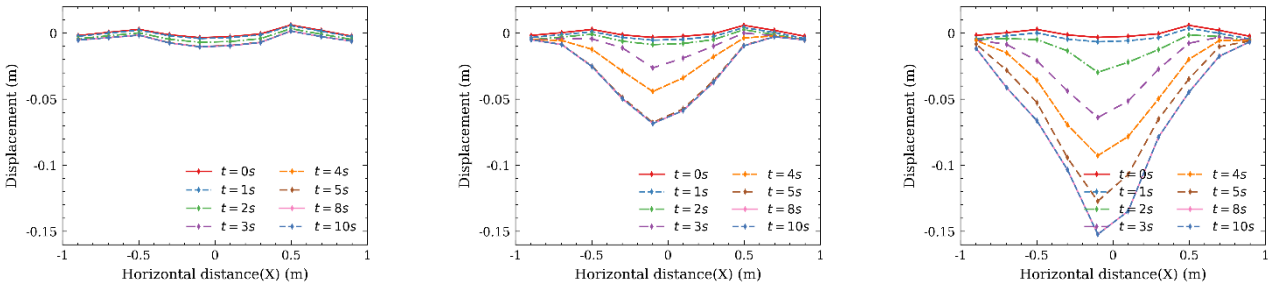

(d) Water level= $0.5b_d$ (e) Water level= $1.0b_d$ (f) Water level= $1.5b_d$

Figure 5.35 Surface displacement for different burial depths and water levels: (a) Burial depth= $1.0d_T$; (b) Burial depth= $1.5d_T$; (c) Burial depth= $2.0d_T$;(d) Water level= $0.5b_d$;(e) Water level= $1.0b_d$;(f) Water level= $1.5b_d$

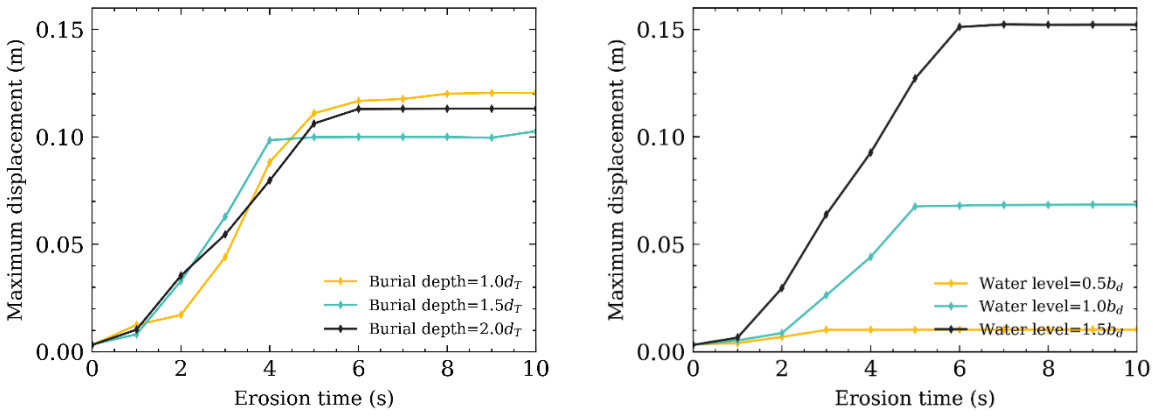

(a) (b)

Figure 5.36 Maximum displacement versus erosion time for different burial depths and water levels:

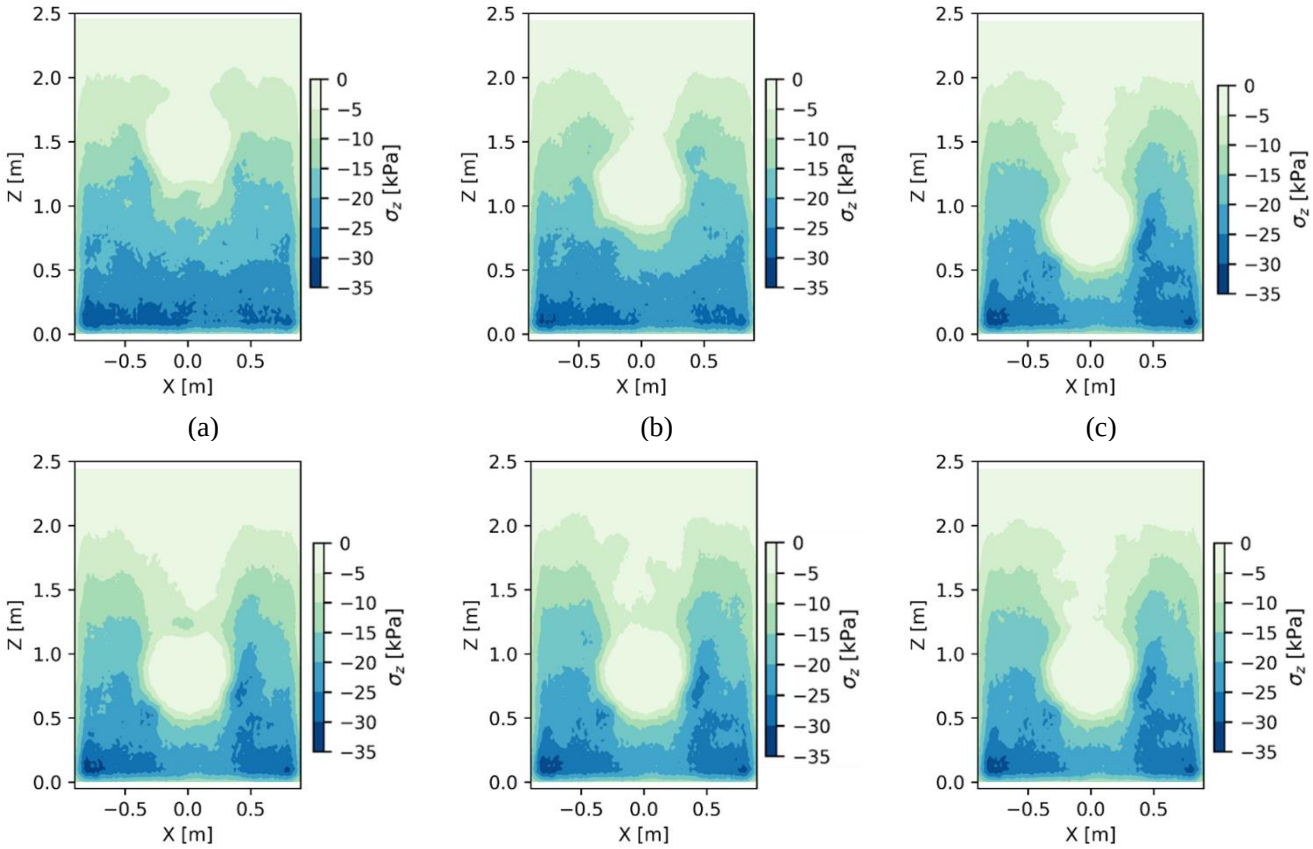

(a) (b) (c)

(d) (e) (f)

Figure 5.37 Distribution of soil effective stress for different burial depths and water levels: (a) Burial depth= $1.0d_T$; (b) Burial depth= $1.5d_T$; (c) Burial depth= $2.0d_T$;(d) Water level= $0.5b_d$;(e) Water level= $1.0b_d$;(f) Water level= $1.5b_d$

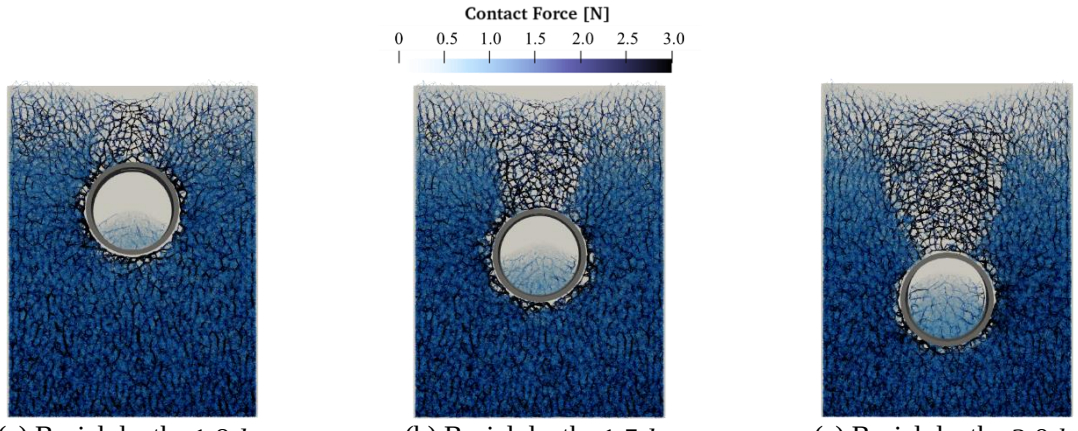

(a) Burial depth= $1.0d_T$ (b) Burial depth= $1.5d_T$ (c) Burial depth= $2.0d_T$

(d) Water level=$0.5b_d$ (e) Water level=$1.0b_d$ (f) Water level=$1.5b_d$

Figure 5.38 Contact force chain distribution in samples with different burial depths and water levels: (a) Burial depth=$1.0d_T$; (b) Burial depth=$1.5d_T$; (c) Burial depth= $2.0d_T$;(d) Water level=$0.5b_d$;(e) Water level=$1.0b_d$;(f) Water level=$1.5b_d$

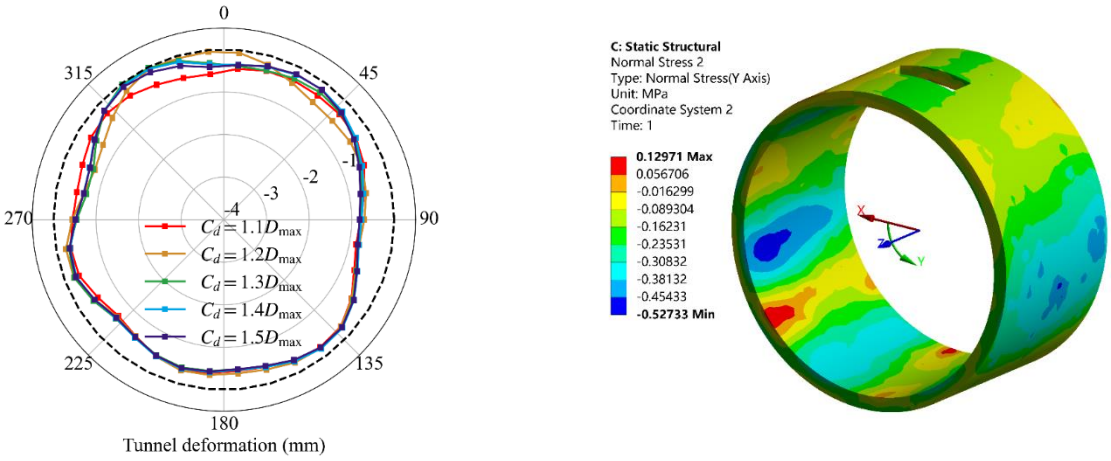

(a) (b)

Figure 5.39 Mechanical response of tunnel with different crack widths: (a) Convergent deformation; (b) Normal stress of tunnel (crack width=$1.4d_{max}$)

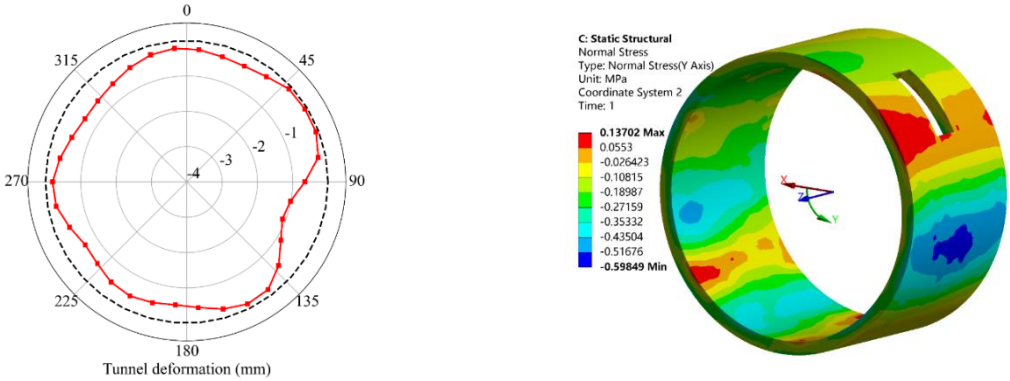

(a) (b)

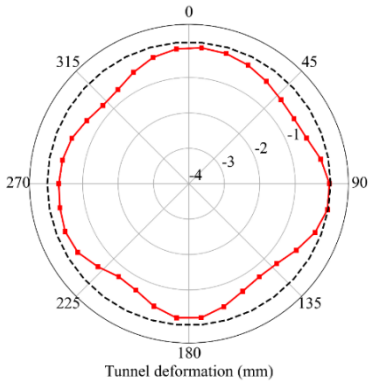

(c)

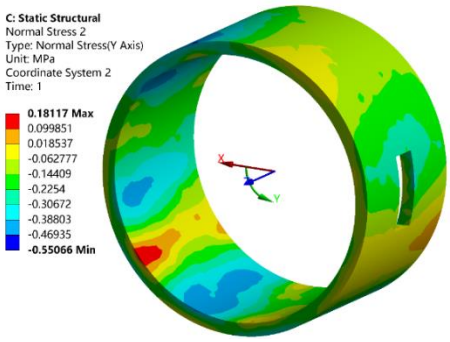

(d)

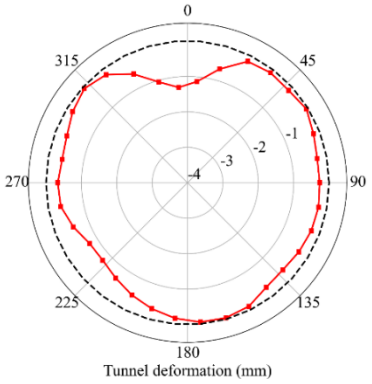

(e)

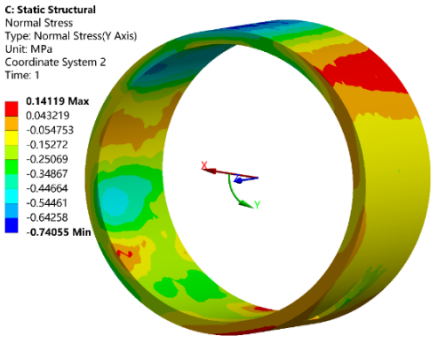

(f)

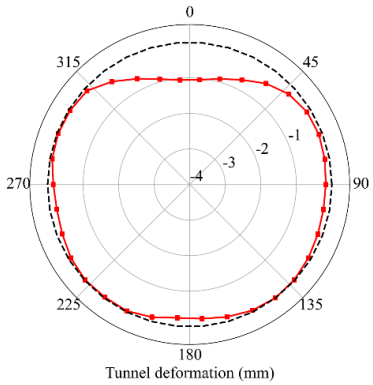

(d)

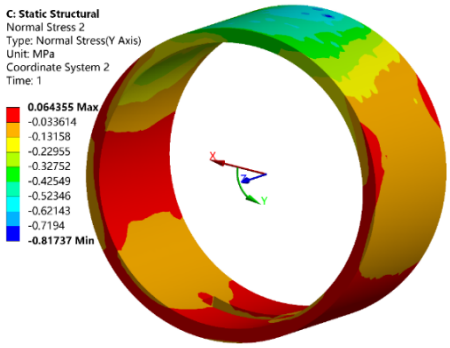

(h)

Figure 5.40 Mechanical response of tunnel with different crack positions: Convergent deformation: $\theta_a = 45^\circ$; (b) Normal stress: $\theta_a = 45^\circ$; (c) Convergent deformation: $\theta_a = 90^\circ$; (d) Normal stress: $\theta_a = 90^\circ$; (e) Convergent deformation: $\theta_a = 135^\circ$; (f) Normal stress: $\theta_a = 135^\circ$; (d) Convergent deformation: $\theta_a = 180^\circ$; (h) Normal stress: $\theta_a = 180^\circ$

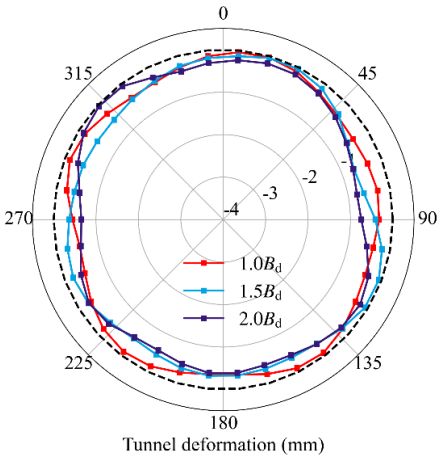

(a) Convergent deformation

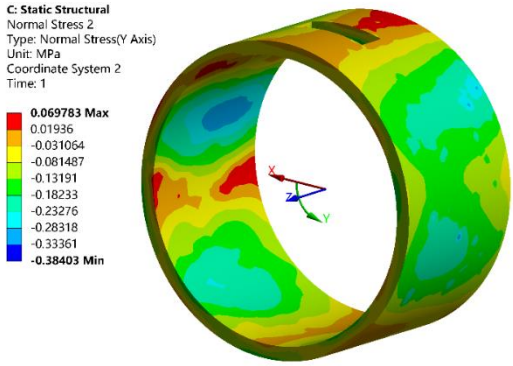

(b) Normal stress of tunnel (burial depth=1.0 D_t)

Figure 5.41 Mechanical response of tunnel with different burial depths: (a) Convergent deformation; (b) Normal stress of tunnel (burial depth=1.0 D_t)

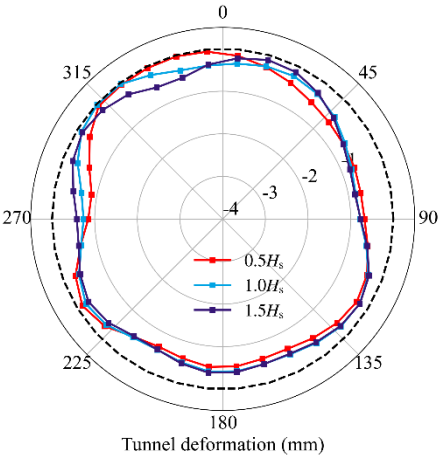

(a) Convergent deformation

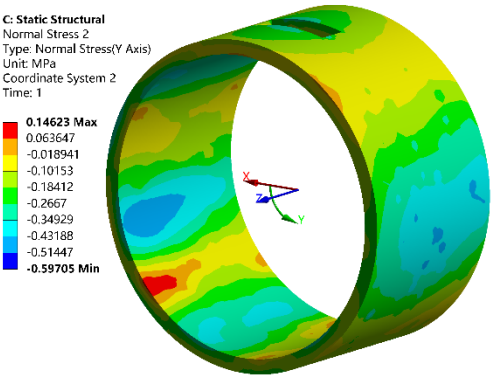

(b) Normal stress of tunnel (water level=1.5 H_s)

Figure 5.42 Mechanical response of tunnel with different water levels: (a) Convergent deformation; (b) Normal stress of tunnel (water level=1.5 H_s)

CHAPTER 6 CFD-DEM-BASED CONTINUUM MODEL FOR SEEPAGE-EROSION-MECHANICS COUPLING

6.1 Introduction

Seepage erosion in soil represents a complex, coupled problem that involves multiple phases (solid, fluid), multiple fields (seepage, mechanical), and multiple scales (particle level, engineering level). As demonstrated in previous chapters, while the CFD-DEM method efficiently addresses the numerical solution of multiphase and multifield problems, its modeling capacity remains constrained by computational power, restricting its application to small-scale RVE problems or mesoscopic BVP issues. To investigate internal erosion at the engineering scale, researchers have developed a four-phase medium theory within the continuum mechanics framework (de Boer, 2000; Uzuoka and Borja, 2012). By employing the finite element method, this theory facilitates the simulation of erosion at macroscopic engineering scales. Within this framework, the loss of fine particles is represented by mass exchange between the solid and liquid phases, while the progression of erosion is governed by a series of mass balance equations. Importantly, when solving the governing equations, explicit expressions for the mass exchange rates between the phases, referred to as the erosion law, are essential. Numerous studies on erosion laws have been proposed (Azadbakht et al., 2020; Deng et al., 2023), most of which are based on semi-empirical formulas derived from laboratory experiments (Sterpi, 2003; Cividini et al., 2009; Uzuoka et al., 2012; Khalil et al., 2013). For instance, Sterpi (2003) proposed a functional relationship for the fine particle erosion rate, which is dependent on the hydraulic gradient and erosion time. Liang et al. (2019) applied this model to simulate their experimental

observations. However, the model fails to predict experimental results under varying hydraulic conditions using a unified set of soil parameters, thus limiting its generalizability. Building upon Sterpi's model, Uzuoka et al. (2012) incorporated the effects of soil porosity and fine particle content, formulating an improved model for the fine particle loss rate as a function of fluid velocity. Nevertheless, this model neglects the influence of the soil's stress state. Notably, the research presented in Chapter 3 of this paper demonstrates that the stress state of the soil plays a critical role in the progression of erosion. In response, Deng et al.(2023) recently proposed an erosion law that factors in the overburden pressure of the soil at K_0 state, but the inclusion of mean stress and deviatoric stress, which are commonly encountered in soil testing, has not yet been addressed. Therefore, there is an urgent need for further research to develop a new erosion law that encompasses the soil stress state.

This study aims to propose a novel erosion law that facilitates the hydro-mechanical modeling of suffusion within the framework of the four-constituent continuum theory. Notably, the erosion law is derived from the results of CFD-DEM simulations rather than physical experiments. The newly proposed model incorporates both hydraulic conditions and the soil's stress state. At the same time, by integrating a constitutive model that can account for the effects of erosion, a simulation framework for seepage-erosion-mechanical coupling is ultimately established.。

6.2 CFD-DEM simulations and novel erosion law

The erosion law describes the rate at which fine particles detach from the soil skeleton and become flowing particles during seepage. As discussed in previous chapters, the CFD-DEM

approach effectively captures fine particle migration at the microscopic scale. Building on this capability, the present chapter develops a novel erosion law derived from microscopic CFD-DEM simulations. Additionally, to couple erosion with mechanics, the erosion law must account for both hydraulic conditions and stress states. Therefore, before establishing the erosion law, this chapter first conducts CFD-DEM erosion simulations on samples under different hydraulic gradients and stress states.

6.2.1 Testing soils and schemes

Given that HK-CDG, as a gap-graded soil, has been extensively studied in laboratory experiments focusing on its erosion development (Chang and Zhang, 2013b), this chapter proposes an erosion law based on HK-CDG soil. The particle size distribution of HK-CDG is shown in Figure 6.1. To facilitate CFD-DEM simulation, the initial gradation is simplified to narrow the particle size range. The simplified model consists of fine particles with a diameter of 0.2 mm and coarse particles with a diameter of 1.2 mm, maintaining a fine particle content of 35%, consistent with the original sample. The gradation curve employed in the simulation is depicted by the solid line in Figure 6.1. The generation process of the CFD-DEM sample follows the methodology described in earlier Chapters, and the final model is illustrated in Figure 6.2, where the DEM domain is a cube with dimensions of 12mm×12mm×12mm, while the CFD domain extends 36 mm in the length direction. To mitigate the impact of gravity on the results, an upward seepage erosion method is adopted. The microscopic parameters used in the simulation are detailed in Table 6.1.

The objective of this study is to investigate the influence of seepage velocity, confining pressure (mean stress) and stress ratio on solid-liquid mass exchange. To achieve this, a total of 11 samples are established with varying hydraulic gradients ($i = 2,3,4,6,8,12\text{m/m}$), mean stresses ($p = 50,100,150,200\text{kPa}$) and stress ratios ($\eta = q/p = 0, 0.3, 0.5, 0.75$,where q is deviatoric stress) are established. The details of these samples are provided in Table 6.2. The simulation time is determined based on the criterion that no further loss of fines occurs. However, slight differences in simulation time may arise due to different stress conditions, ranging from 8.5 to 12.5 seconds.

6.2.2 Results of the fines mass loss

Figure 6.3 shows the percentage of fines mass loss m_e, which is given by the ratio of cumulative lost mass and initial fines mass. Generally, the evolution of mass loss shows an initial high rate, followed by a decrease with increasing suffusion time, and eventually reaching a steady state where the loss of fine particles becomes negligible. These numerical results align well with observations from physical experiments (Marot et al., 2012; Chang and Zhang, 2013a; Ke and Takahashi, 2014b). As the hydraulic gradient (seepage velocity) increases, the fluid exerts a stronger drag force on fines, facilitating particle transportation and resulting in increased fines loss. It is noteworthy that the relationship between the maximum mass loss ratio and seepage velocity exhibits significant nonlinearity. Specifically, when the hydraulic gradient is below 2m/m, the specimen does not exhibit visible fines loss. As the hydraulic gradient increases to 3m/m, the mass loss slightly increases. However, when the hydraulic gradient is increased from 3 to 4m/m, the mass loss significantly increases. Subsequently, when the hydraulic gradient is

increased from 4 to 12m/m, the increase in mass loss becomes very limited. Laboratory experiments (Chang and Zhang, 2013b) have also confirmed such nonlinear behavior. On the other hand, an increase in mean stress enhances particle connection, thereby increasing erosion resistance and decreasing mass loss. Conversely, the presence of deviatoric stress leads to an anisotropic distribution of contact forces, increasing the likelihood of particle migration and resulting in more fines loss (Zhou et al., 2022; Liu et al., 2023b).

6.2.3 The model of fines mass loss

To derive the erosion law in the following section, which describes the rate of volumetric mass loss exchange from fine particles to the fluid, a cumulative mass loss model is first introduced. Based on the observations from Figure 6.3, it is evident that the evolution of the mass loss ratio follows the patterns of exponential functions. Therefore, the following exponential formula is proposed:

$$m_e = m_\infty[1-\exp(-\lambda_e v_f^{a_e}(p/p_{ref})^{b_e} t)] \tag{6.1}$$

where m_e is the mass loss ratio, and v_f denotes the seepage velocity. p and p_{ref} are the mean stress and reference stress, respectively. In this study, the p_{ref} is uniformly specified as 50kPa. t is the suffusion time. λ_e, a_e, b_e are soil-related material parameters. m_∞ is the maximum mass loss ratio when seepage erosion stabilizes. It is a function of seepage velocity, mean stress and stress ratio, given as:

$$m_\infty(v_f, p, \eta) = m_0 \frac{\exp(L_1 p/p_{ref} + L_2(\eta/M_p)^{c_e})}{1+\exp(L_3(v_f - v_{fc}))} \tag{6.2}$$

where M_p is the soil peak stress ratio (according to the DEM triaxial results, the peak stress ratio for HK-CDG is determined as 0.85 in this study), and v_{fc} is a critical seepage velocity.

m_0, L_1, L_2, L_3, c_e are fitting parameters.

Eqn. (6.2) indicates that for a given confining pressure and stress ratio, as the seepage velocity increases, m_∞ approaches m_0, and the mass loss does not increase infinitely. This is because, based on the tests conducted, there is always a portion of fines that remains in the soil regardless of the level of hydraulic gradient. All the unknown parameters in Eqn. (6.2) can be calibrated by fitting the data of the ultimate mass loss ratio m_∞ under different test conditions. Figure 6.4 presents the fitting results of Eqn. (6.2) and the calibrated parameters are listed in Table 6.3. Once the Eqn. (6.2) is determined, it can be substituted into Eqn. (6.1), allowing the unknown parameters in Eqn.(6.1) to be calibrated using the time evolution curve of the mass loss ratio obtained from CFD-DEM, as shown in Figure 6.5. From the fitting curves in Figure 6.4 and Figure 6.5, it can be found that the proposed mass loss ratio formula can well correspond to the results from CFD-DEM simulations for most cases.

To further validate the effectiveness of the model, the calculated results are compared with experiments conducted by Liang et al.(2017b) using gap-graded soils (as illustrated in Figure 6.6). The mean stress and deviatoric stress in the experiments were applied using confining and vertical loading systems, thus soil with different initial stress states could be obtained. Subsequently, the samples were subjected to an upward seepage flow through a water supply system. By adjusting the height of the upstream water tank, various hydraulic gradients could be imposed.

For the purpose of validation, three samples, featuring different hydraulic gradients, mean stresses, and stress ratios were selected from the experiments. It's noticed that in Eqs. (6.1)-(6.2), the seepage velocity of the specimen during suffusion is required. However, Liang et al. did not provide the complete variation of seepage velocity, but only the final hydraulic gradient. Therefore, it is assumed that the flow velocity (v_f) remains constant and satisfies Darcy's law to obtain the required velocity for calculations based on the permeability coefficient provided in their study. Additionally, the model also requires the value of the maximum stress ratio M_p, which was also not provided in their experiments. Hence, it is assumed that its value is 1. It is important to note that these assumptions do not affect the correctness of the model; they only impact the calibration of parameter magnitudes. If an accurate value for M_p is available for the specimen, only the magnitude of the parameter needs to be adjusted accordingly.

Three groups of results with different hydraulic gradients, mean stresses, and stress ratios were selected and plotted in Figure 6.7, where the dashed lines represent the predicted results from Eqs. (6.1)-(6.2). The parameter values used in the calculations are shown in Table 6.3. It can be observed that the proposed model successfully reproduces the main evolution of the experiments, indicating its effectiveness in capturing the suffusion process in gap-graded soils.

6.3 Continuous medium theory framework for seepage-erosion-mechanical coupling

As discussed in the Introduction to this thesis, the loss of fine particles during suffusion can be modeled within the continuous medium mechanics framework using the mass balance equations.

Following the development of a prediction formula for the fines mass loss in Section 6.2 using CFD-DEM, an explicit expression for the mass exchange rate required to solve the governing equations can be derived. Building on this foundation, this section will establish a computational framework for the seepage-erosion-mechanical coupling for gap-graded soils, integrating four-phase media theory and a soil constitutive model that incorporates the effects of erosion.

6.3.1 Four constituents model

The soil undergoing suffusion can be considered as a saturated soil. In previous studies, saturated soil has often been treated as a two-phase medium consisting of fluid and soil skeleton. However, erodible soils typically consist of coarse and fine particles. In this case, the fine particles can migrate within the pores with infiltrating water flow, while the coarse particles, serving as the soil skeleton, cannot be transported. Therefore, treating the soil as a two-phase medium fails to distinguish between the various modes of coarse and fine particle movement during erosion. Therefore, Schaufler et al. (2013a) proposed a more detailed distinction within the solid phase of saturated soil, separating it into the soil skeleton composed of coarse particles, fluid-like fines, and solid-like fines. As is illustrated in Figure 6.8, in a representative elementary volume of saturated soil, the volume of solid (dV) consists of four constituents: pure fluid (n^{ff}), eroded fluidized fine particles (n^{fp}, fluid-like), non-eroded erodible fine particles (n^{se}, solid-like), and the coarse skeleton (n^{ss}). The volume fraction of each constituent is determined as follows:

$$n^i = \frac{\mathrm{d}V^i}{\mathrm{d}V} \tag{6.3}$$

where $i = \{ff, se, ss, fp\}$, V^i is the volume of each corresponding constituent.

After neglecting the hydro-mechanical dispersion tensor, Schaufler et al. (2013) presented the mass balance equation for each term at the material point scale:

$$\frac{\partial\left(\rho^{i}\right)}{\partial t}+\operatorname{div}\left(\rho^{i}\mathbf{v}_{i}\right)=\rho^{ex,i} \tag{6.4}$$

Where $\rho^{ex,i}$ and $\mathbf{v}_i$ represent the mass exchange term and velocity corresponding to each constituent, respectively. The partial density ρ^{i} is defined as the ratio of the mass dm^{i} of constituent i to the volume dV of the RVE. The relationship between the partial density ρ^{i} and the effective density ρ^{iR} is as follows:

$$\rho^{i}=\frac{\mathrm{d}m^{i}}{\mathrm{d}V}=\frac{\mathrm{d}m^{i}}{\mathrm{d}V^{i}}\frac{\mathrm{d}V^{i}}{\mathrm{d}V}=\rho^{iR}n^{i} \tag{6.5}$$

The mass balance equations can be reduced to a balance equation represented by the volume fraction:

$$\frac{\partial\left(n^{i}\right)}{\partial t}+\operatorname{div}\left(n^{i}\mathbf{v}_{i}\right)=n^{ex,i} \tag{6.6}$$

where $n^{ex,i}$ is the volume mass exchange term for each constituent.

To further derive the final governing equations, it is assumed that the fluidized fine particles eroded from the soil and the fluent has the same velocity at any given time and coordinate location. Coarse particles (i.e., the solid skeleton) can deform but do not erode. The porosity field $\phi\left(\boldsymbol{x},t\right)$within the sample, the erodible fine content $f_c\left(\boldsymbol{x},t\right)$, and the concentration of fluidized fine particles $c\left(\boldsymbol{x},t\right)$ are defined as follows:

$$\phi=\frac{\mathrm{d}V_{v}}{\mathrm{d}V}=\frac{\mathrm{d}V^{ff}+\mathrm{d}V^{fp}}{\mathrm{d}V}=n^{ff}+n^{fp} \tag{6.7}$$

$$f_c=\frac{n^{se}}{n^{ss}+n^{se}}=\frac{n^{se}}{1-\phi} \tag{6.8}$$

$$c=\frac{n^{fp}}{n^{ff}+n^{fp}}=\frac{n^{fp}}{\phi} \tag{6.9}$$

When fine particles undergo a phase transition from solid to fluidized particles, the volume mass exchange is as follows:

$$-n^{ex,fp} = n^{ex,se} = \hat{n},\ n^{e\alpha,ss} = 0,\ n^{ex,ff} = 0 \tag{6.10}$$

where $\hat{n}$ is the volume exchange rate, i.e, the erosion law, which will be discussed in detail in the following section.

By combining Eqs. (6.3) to (6.10), the mass balance equations are obtained as follows (Yang, 2019):

$$-\frac{\partial \phi}{\partial t} + \operatorname{div}(\mathbf{v}_s) - \operatorname{div}(\phi \mathbf{v}_s) = \hat{n} \tag{6.11}$$

$$\frac{\partial (f_c)}{\partial t} - \frac{\partial (f_c \phi)}{\partial t} + \operatorname{div}(f_c \mathbf{v}_s) - \operatorname{div}(f_c \phi \mathbf{v}_s) = \hat{n} \tag{6.12}$$

$$\frac{\partial (c\phi)}{\partial t} + \operatorname{div}(c q_w) + \operatorname{div}(c\phi \mathbf{v}_s) = -\hat{n} \tag{6.13}$$

$$\operatorname{div}(q_w) + \operatorname{div}(\mathbf{v}_s) = 0 \tag{6.14}$$

where 'div' is the divergence operator; q_w is the volumetric flow rate, which is the flow passing through a unit area per unit time. Assuming the fluid satisfies Darcy's law, it can be determined as follows:

$$q_w = -\frac{k(f_c, \phi)}{\eta_k \bar{\rho}(c)} \operatorname{grad}(p_w) \tag{6.15}$$

where p_w is the pore pressure; η_k is the fluid's dynamic viscosity; $\boldsymbol{k}$ is the intrinsic permeability of the soil, which is a function of the fine particle content f_c and porosity $\boldsymbol{\phi}$ of the current soil; $\bar{\rho}$ is the mixed density of the water-soil mixture, which is a function of the concentration c. $\boldsymbol{k}$ and $\bar{\rho}$ are given by the following equations:

$$k = k_0 \left[1 - f_c(1-\phi)\right]^{3m_k} \tag{6.16}$$

$$\bar{\rho} = c\rho_s + (1-c)\rho_f \tag{6.17}$$

where ρ_s and ρ_f represent the densities of the solid and fluid, respectively; m_k is the

cementation exponent related to the pore geometry (Revil and Cathles Iii, 1999).

6.3.2 Implementation of erosion law

The volume exchange rate $\hat{n}$ in Eqs (6.11) to (6.14), also known as the erosion law, represents the rate at which fine particles are eroded. It can be derived from the mass loss ratio m_e. Taking the derivative of Eqn. (6.1) yields:

$$\frac{\partial m_e}{\partial t} = \lambda_e v_f^{a_e} (p / p_{ref})^{b_e} m_\infty \exp(-\lambda_e v_f^{a_e} (p / p_{ref})^{b_e} t) = \lambda_e v_f^{a_e} (p / p_{ref})^{b_e} (m_\infty - m_e) \tag{6.18}$$

Then, based on the definition of the mass loss ratio, which is the ratio between the eroded fines mass Δm_f and the initial fines mass m_{f0}, m_e can be rewritten as follows:

$$m_e = \frac{\Delta m_f}{m_{f0}} = \frac{\Delta m_f}{m_0 f_{c0}} = \frac{\Delta m_f / \rho_s}{m_0 f_{c0} / \rho_s} = \frac{\Delta V_f}{V_0 f_{c0}} \tag{6.19}$$

where m_0 is the initial total mass of soil, f_{c0} is the initial fine content. ρ_s is the soil density. ΔV_f and V_0 denotes the cumulative volume of eroded fines and the initial volume of soil, respectively. Similarly, differentiating Eqn. (6.19) yields:

$$\frac{\partial m_e}{\partial t} = \frac{1}{f_{c0}} \frac{\partial (\Delta V_f / V_0)}{\partial t} \tag{6.20}$$

Submitting $\hat{n} = \dfrac{\partial (\Delta V_f / V_0)}{\partial t}$ into Eqn. (6.20) and (6.18), the volume exchange rate can be expressed by:

$$\hat{n} = \lambda_e v_f^{a_e} (p / p_{ref})^{b_e} (m_\infty - m_e) f_{c0} \tag{6.21}$$

where m_∞ is the final mass loss ratio, given by Eqn.(6.2). $(m_\infty - m_e)$ denotes the residual fraction of the erodible fines.

It can be found that the newly proposed law (Eqn.(6.2) and Eqn.(6.21)) not only takes into account the seepage velocity but also incorporates the influence of mean stress p and stress

ratio η (q / p). Consequently, it provides a foundation for establishing a hydromechanical model that considers the suffusion process.

6.3.3 Critical state-based and fines-dependent mechanical model

In order to realize the hydromechanical modeling for suffusion, an appropriate mechanical constitutive model is of great importance. Yang et al. (2020b) pointed out that the influence of erosion on mechanical responses includes two aspects: first, the decrease of particles reduces the soil shear stiffness, leading to an increase in deformation of the granular assembly. Second, soil friction properties, for example, sliding resistance, can be changed due to erosion. Therefore, an appropriate constitutive relationship must reflect these characteristics. However, it is important to emphasize that the focus of this study is still on soil erosion, and the primary aim should be to describe the erosion process. When selecting the constitutive model, in addition to ensuring it captures the aforementioned characteristics, it is essential to maintain simplicity in form to avoid difficulties in achieving convergence when solving the governing equations. For this purpose, this study adopts a simple exponential constitutive function, which has been improved by Yin et al. (2018) and Wu (2019). This model takes into account the nonlinear elastic relationship, the nonlinear dilatancy relationship, and the critical state concept, thereby enabling the modeling of the impact of erosion on the mechanical behavior of the soil.

Basic exponential function

The stress ratio and shear strain of granular materials typically exhibit progressive nonlinear friction characteristics. This progressive relationship of friction can be represented by an exponential form, as follows:

$$\eta = b\left(1-e^{-a\gamma}\right) \tag{6.22}$$

In nonlinear constitutive modeling, an incremental form has to be considered. Therefore, Eqn. (6.22) is rewritten as:

$$\delta\eta = ab\left(1-\frac{\eta}{b}\right)\delta\gamma \tag{6.23}$$

Under triaxial testing conditions, the stress ratio $\eta = q/p'$ is defined as the ratio of the deviatoric stress $q\left(q=\sigma_a-\sigma_r\right)$ to the mean effective stress $p'\left(p'=\left(\sigma_a+2\sigma_r\right)/3\right)$, where σ_a and σ_r represent the axial and radial stresses, respectively. Therefore, Eqn. (6.23) under triaxial conditions can be further rewritten as follows:

$$\delta\eta = G_\eta(1-\frac{\eta}{M_p})\delta\varepsilon_d \tag{6.24}$$

where $\delta\varepsilon_d = 2(\delta\varepsilon_a-\delta\varepsilon_r)/3$ represents the deviatoric strain increment; M_p is the strength ratio; $G_\eta = 3G/p'$ is the initial stiffness; and G is the shear modulus. According to the definition of stress ratio η, the following relationship can also be obtained:

$$\eta = \frac{q}{p'} \Rightarrow \delta\eta = \frac{\delta q}{p'} - \frac{q}{p'^2}\delta p' = \left(\delta q - \eta\delta p'\right)\frac{1}{p'} \tag{6.25}$$

By combining Eqn. (6.25) and Eqn. (6.24), the deviatoric stress increment can be obtained as follows:

$$\delta q = 3G\left[(p'-\frac{q}{M_p})\delta\varepsilon_d\right] + \frac{q}{p'}\delta p' \tag{6.26}$$

Dilatancy is an important mechanical property of soil. To describe the volume deformation caused by shear, the dilatancy equation proposed by Roscoe and Burland (Roscoe and Burland, 1968) is used:

$$\frac{\delta\varepsilon_v^{in}}{\delta\varepsilon_d} = M_{pt} - \frac{q}{p'} \tag{6.27}$$

where $\delta\varepsilon_v^{in}$ represents the volumetric strain increment caused by shear, and M_{pt} is the phase

transition strength ratio.

The increment expression for the mean effective stress is as follows:

$$\delta p' = K\left(\delta\varepsilon_v - \delta\varepsilon_v^{in}\right) = K\left(\delta\varepsilon_v + (\frac{q}{p'} - M_{pt})\delta\varepsilon_d\right) \tag{6.28}$$

where K represents the bulk modulus, and $\delta\varepsilon_v = \delta\varepsilon_a + 2\delta\varepsilon_r$ is the volumetric strain increment.

Finally, the constitutive model is completely defined by:

$$\delta q = 3G\left[(p' - \frac{q}{M_p})\delta\varepsilon_d\right] + \frac{q}{p'}\delta p' \tag{6.29}$$

$$\delta p' = K\left(\delta\varepsilon_v + (\frac{q}{p'} - M_{pt})\delta\varepsilon_d\right) \tag{6.30}$$

Enhancement of nonlinear elasticity

To account for the change in soil stiffness induced by erosion, Yin et al. (2018) modified the nonlinear elastic relationship of the model as suggested by Richart et al. (1970):

$$G = G_0 \frac{(2.97-e)^2}{(1+e)}\left(\frac{p'}{p_{at}}\right)^n \tag{6.31}$$

$$K = K_0 \frac{(2.97-e)^2}{(1+e)}\left(\frac{p'}{p_{at}}\right)^n \tag{6.32}$$

where G_0 is reference bulk moduli, and K_0 is reference shear moduli. n is a model parameter, typically ranging from 0.5 to 0.7; and $p_{at} = 101.325\text{kPa}$ is the reference atmospheric pressure.

Enhancement of critical state concept

The concept of critical state was established by Roscoe and Schofield (1968) based on a series of triaxial test results. According to critical state theory, regardless of the initial state of the soil sample or the stress path it undergoes, the sample will reach the so-called critical state after a certain degree of shear deformation. At this point, only the shear strain continues to increase, while the mean effective stress and volume of the soil sample remain constant. Yin et al. (2018)

introduced the nonlinear critical state line (CSL) in the $e-\log p'$ plane, as proposed by Li and Wang (1998):

$$e_c = e_{c0} - \lambda\left(\frac{p'}{p_{at}}\right)^{\xi} \tag{6.33}$$

where λ represents the slope of the CSL, ξ is the model parameter controlling the nonlinearity, and e_{c0} is the critical void ratio at very low confining pressure.

After introducing the critical state, the dense state of the soil can be described by the ratio of e_c/e or the distance between e_c-e, where e is the current void ratio of the soil. e_c is the critical state void ratio corresponding to the current mean effective stress p', which can be calculated from the CSL expression defined in Eqn. (6.33). When $e_c/e<1$ or $e_c-e<0$,the soil is in a loose state. When $e_c/e>1$ or $e_c-e>0$,the soil is in a dense state. To further account for the impact of the dense state on the soil's stress-strain behavior, the dynamic peak friction angle ϕ_p and the dynamic phase transition angle ϕ_{pt} can be defined as follows:

$$\tan\phi_p = \left(\frac{e_c}{e}\right)^{n_p}\tan\phi_c \tag{6.34}$$

$$\tan\phi_{pt} = \left(\frac{e}{e_c}\right)^{n_d}\tan\phi_c \tag{6.35}$$

where ϕ_c is friction angle. n_{p} and n_{d} are model interlocking parameters, which, according to the suggestion of Biarez and Hicher (1994), can be taken as 1.

The dynamic peak friction angle indicates that, for soils in a loose state, the initial friction angle ϕ_p is less than the critical friction angle ϕ_c. In contrast, for soils in a dense state, the initial friction angle ϕ_p is greater than the critical friction angle ϕ_c. Upon reaching the soil's peak stress

state, shear dilation initiates, reducing interparticle interlocking forces. This degradation of frictional resistance leads to a decline in the peak friction angle, ultimately resulting in strain-softening behavior. The dynamic phase transition angle indicates that for soils in a loose state ($e > e_c$), ϕ_{pt} is greater than the critical friction angle ϕ_c, causing the soil to contract. Conversely, for soils in a dense state ($e < e_c$), ϕ_{pt} is less than the critical friction angle ϕ_c, leading the soil to exhibit dilative behavior. This allows the modeling of dense soils initially contracting before undergoing dilation. Using the dynamic peak friction angle and dynamic phase transition angle, the expressions for the peak strength ratio M_p and the phase transition strength ratio M_{pt} can be further derived as follows:

$$M_p = \frac{6\sin\phi_p}{3-\sin\phi_p} \tag{6.36}$$

$$M_{pt} = \frac{6\sin\phi_{pt}}{3-\sin\phi_{pt}} \tag{6.37}$$

Enhancement of nonlinear stress dilatancy

Extensive experimental observations show that the stress path of the soil in $p'-q$ space always increases almost vertically during undrained triaxial loading, indicating that during the initial shear phase, the volumetric strain is very small. Based on this, Yin et al. (2018) further refined the dilatancy relationship of the model, and the modified expression is as follows:

$$\frac{\delta\varepsilon_v^{in}}{\delta\varepsilon_d} = A_d\left(M_{pt} - \frac{q}{p'}\right)\left[1-\exp\left(-d\eta\right)\right] \tag{6.38}$$

where A_d and d is a constant controlling the magnitude of the stress-dilatancy.

By substituting Eqn. (6.38) into Eqn. (6.27), the improved expression for the mean effective stress increment can be obtained:

$$\delta p' = K\left(\delta\varepsilon_v - \delta\varepsilon_v^{in}\right) = K\left(\delta\varepsilon_v + A_d\left(\frac{q}{p'} - M_{pt}\right)\delta\varepsilon_d\left[1-\exp\left(-d\eta\right)\right]\right) \tag{6.39}$$

Fines-dependent critical state

When fine particles within the soil are eroded, the porosity as well as fine content vary correspondingly. Studies have illustrated that the mechanical response of gap-graded soils is highly dependent on fine content (Yin et al., 2014, 2016b). In order to correctly reflect the mechanical variation induced by erosion, the above model can further be enhanced. For the CSL in Eqn. (6.33), Yin et al. (2018) made the following corrections to e_{c0}:

$$\begin{aligned} e_{\mathrm{c0}} = & \left[e_{\mathrm{hc,cr0}} \left(1- f_{\mathrm{c}}\right) + a f_{\mathrm{c}} \right] \frac{1-\tanh\left[\zeta\left(f_{\mathrm{c}} - f_{\mathrm{th}}\right)\right]}{2} \\ & + e_{\mathrm{hf,cr0}} \left[f_{\mathrm{c}} + \frac{1- f_{\mathrm{c}}}{\left(R_{\mathrm{d}}\right)^{m}} \right] \frac{1+\tanh\left[\zeta\left(f_{\mathrm{c}} - f_{\mathrm{th}}\right)\right]}{2} \end{aligned} \tag{6.40}$$

where $e_{hc,cr0}$ and $e_{hf,cr0}$ are the reference critical void ratios for the pure sand ($f_c = 0$) and the pure silt ($f_c = 100$), respectively. $a, m, f_{\mathrm{th}}, \zeta$ are material constants, in which ζ controls the transition zone between the sandy silt and the silty sand. f_{th} is the threshold fines content from the coarse grains skeleton to the fine grains skeleton. R_d is the ratio of the mean size of coarse particles and the mean size of fine particles. By combining Eqs. (6.33) and (6.40), the effect of changes in fine content on the critical state line can be assessed.

6.3.4 The establishment of framework for the coupling of seepage-erosion-mechanics

The coupling framework in this study aims to realize the two-way full coupling between erosion and mechanical response. On the one hand, the stress state of the soil is considered through the proposed erosion law, which controls the erosion evolution. On the other hand, the effect of erosion on mechanical behaviour is considered through two aspects. Firstly, the erosion-induced f_c variation is directly linked to the position of CSL in the constitutive model. Secondly,

erosion-induced void ratio increase also changes the soil peak strength and stiffness. Using the above framework, the hydromechanical modeling can be implemented for internal erosion tests.

Unlike the traditional triaxial experiments, the soil specimen during the suffusion test is normally subjected to constant boundary stresses. Therefore, the strain change is actually induced by the variation of peak strength ratio and stiffness, as: (Yang et al., 2020b)

$$\delta\varepsilon_{\mathrm{d}} = -(\frac{M_{\mathrm{p}}}{G_{\eta}}\ln\left[\frac{M_{\mathrm{p}}-\eta}{M_{\mathrm{p}}}\right])^{(i)} + (\frac{M_{\mathrm{p}}}{G_{\eta}}\ln\left[\frac{M_{\mathrm{p}}-\eta}{M_{\mathrm{p}}}\right])^{(i-1)} \tag{6.41}$$

where the superscript (i) represents the current loading step and ($i-1$) is the previous loading step. After obtaining the shear strain increment $\delta\varepsilon_{\mathrm{d}}$, the volumetric strain increment $\delta\varepsilon_{\mathrm{v}}$ is calculated using the following equation:

$$\delta\varepsilon_{\mathrm{v}} = -\frac{p}{K^2}\delta K + A_{\mathrm{d}}\left(M_{\mathrm{pt}} - \frac{q}{p}\right)\delta\varepsilon_{\mathrm{d}}[1-\exp(-d\eta)] \tag{6.42}$$

The incremental void ratio includes two parts, e.g., void ratio induced by the body deformation and fine particle volume loss caused by erosion, given:

$$(\delta e)_{\mathrm{total}} = (\delta e)_{\mathrm{erosion}} + \delta\varepsilon_{v}(1+e) \tag{6.43}$$

After the above modifications, the simulation of the suffusion process can be easily implemented using numerical methods, with the computational flowchart shown in Figure 6.9. Here, (i) represents the current time step, and ($i-1$) refers to the previous time step. The governing differential equations can be solved using numerical methods (such as the finite difference method, FDM) in both time and space steps, with the main unknown variables being the soil displacement $u_s(\boldsymbol{x},t)$ ($\mathbf{v}_s(\boldsymbol{x},t)$), pore pressure $p_w(\boldsymbol{x},t)$, porosity $\phi(\boldsymbol{x},t)$, and the concentration of fluidized fine particles $c(\boldsymbol{x},t)$. Other unknowns can be explicitly determined

from these variables. Based on the computational framework in Figure 6.9, an FDM program is developed in MATLAB for simulating the suffusion of unit cells.

6.4 Validation and discussion

The framework presented in Section 6.3 is highly suitable for conducting triaxial suffusion tests, which involve subjecting soil to constant stress while observing erosion processes. It is noticed that Chang et al. (2011, 2013b) conducted suffusion tests using an adapted stress-controlled erosion apparatus. The evolution of suffusion under complex stress states, as well as the soil stress-strain response subjected to suffusion, are presented in their study, which can be used to validate the numerical model in this study.

6.4.1 Description of laboratory suffusion tests

Chang and Zhang (2013a) performed downward seepage erosion experiments on HK-CDG soil samples (Figure 6.1) under varying hydraulic gradients. The experimental setup consisted of an enhanced triaxial loading apparatus, a variable-pressure water supply system, and a soil-water collection system, as depicted in Figure 6.10. An LVDT displacement gauge was integrated with the loading unit, enabling precise measurement of axial deformation. The base of the experimental apparatus was modified into a hollow structure to facilitate the passage of soil particles. The soil samples, cylindrical in shape with a diameter and height of 100 mm, were subjected to either isotropic compression or anisotropic stress conditions, where the principal stress aligned with the direction of seepage. Following consolidation under isotropic pressure, axial compression was progressively applied to simulate the anisotropic stress states. Upon completion of the loading phase, a seepage flow, parallel to the principal stress of the sample,

was introduced through a water supply system connected to the triaxial apparatus. The applied water pressure followed a non-uniformly varying pattern. As is illustrated in Figure 6.11, each stage of the hydraulic gradient within the sample lasts 10 mins, and the increase magnitude is 0.15 m/m for $i \leq 1.0$ m/m, 0.25 m/m for 1.0 m/m $< i <$ 2.0 m/m, and 0.50 m/m for $i > 2.0$ m/m. For each gradient level, the hydraulic pressure was increased within the first 2 mins and then kept constant for the following 8 mins to ensure there was no more soil loss. Throughout the suffusion process, the external stress remained constant, while the weight of the eroded mass and the outflow rate were continuously monitored. Figure 6.12 presents the deformation of the sample before and after suffusion.

Before simulating the experiment using the numerical model proposed in Section 6.3, it is essential to calibrate the parameters involved in the model, which include soil physical parameters (e.g., ρ_s, ρ_f, k_0, m_k in Eqs.(6.16) and (6.17)), mechanical parameters (e.g., $K_0, G_0, n_p, n_d, d, A_d, \phi_c$ in Eqs.(6.31)-(6.32), (6.34)-(6.35) and (6.39)), CSL-related parameters (a, ξ, $e_{hc,cr0}, \zeta, f_{th}, e_{hf,cr0}, m, R_d$ in Eqs.(6.33) and (6.40)), and erosion-related parameters ($\lambda_e, a_e, b_e, c_e, L_1, L_2, L_3, v_{fc}$ in Eqs.(1)-(2)). The direct method to determine the necessary parameters involves conducting triaxial shear tests for mechanical parameters and CSL parameters, as well as triaxial suffusion tests for erosion-related parameters. However, in this study, these experiments were not conducted and instead referenced from existing literature. The soil physical parameters can be directly obtained from the values provided in the experiments. The mechanical parameters can be determined by fitting the stress-strain relationships reported

in the triaxial tests conducted by Chang and Zhang (2013b), as is shown in Figure 6.15(a) (Yang et al., 2020b). However, the determination of CSL-related parameters is more complex due to limited experimental data. Fortunately, Yin et al.(2014) have conducted a series of experiments on soil critical state for coarse-fine mixtures, which are similar to gap-graded soils, aligning well with the objectives of this study. Therefore, the CSL-related parameters are fitted using the results obtained by Yin et al. (2014). Figure 6.15(b) illustrates the fitting results compared to the experiments for CSL parameters. For the erosion-related parameters, they can be determined by fitting the mass loss results reported in the experiments. The erosion-related parameters are calibrated based on the results of the two groups labeled GS-C-1 and GS-C-5 in the experiments (Chang and Zhang, 2013a), where GS-C-1 represents erosion samples under 50kPa confining pressure, and GS-C-5 represents erosion samples under 50kPa confining pressure and 100kPa deviator stress. All calibrated parameter results are presented in Table 6.4.

6.4.2 Comparison between simulations and experiments

According to the previous calculation scheme and determined parameters, the simulation results are obtained and compared with the results from experimental samples GS-C-1, GS-C-5, GS-C-6(Chang, 2012). The erosion tests for these samples were conducted with a confining stress of 50 kPa and deviatoric stresses of 0, 100, and 150 kPa, corresponding to stress ratios of $\eta = 0$, 1.2 and 1.5, respectively. The results are shown in Figure 6.14.

Figure 6.14(a) presents the cumulative eroded soil weights for these tests. It is clear that the eroded mass rises with the stress ratio, highlighting the substantial impact of stress state on

erosion. This trend can be attributed to the loss of fine particles, which triggers a reconfiguration of the soil microstructure. As a result, the soil transitions from an anisotropic state to an isotropic state (Zhou et al., 2022; Liu et al., 2023b). Therefore, a more pronounced initial stress anisotropy leads to a more intense particle adjustment, resulting in a greater amount of mass loss. The findings indicate that the proposed model effectively replicates the overall erosion evolution process, with the final eroded mass at the stable stage increasing in line with the stress ratio. Furthermore, it should be noted that for sample GS-C-1 under isotropic stress, the mass loss exhibits a sharp increase between Time=100-180 min, and the simulation results successfully capture this significant rise during the same time period. However, there are also noticeable discrepancies between the model and the experimental results for samples GS-C-5 and GS-C-6 under anisotropic stress states. The model fails to accurately capture the turning point (i.e., critical gradient) that corresponds to the abrupt change in eroded mass. Specifically, the mass loss of sample GS-C-5 begins to increase rapidly around Time=200 min, whereas the model predicts this increase at around Time=120 min. This can be attributed to the fact that the numerical model employs the finite difference method, treating the soil as a representative elementary volume without accounting for spatial inhomogeneity. In contrast, experimental soil samples inherently exhibit variations in void ratio and fine content, leading to deviations from the model predictions.

Figure 6.14(b) illustrates the evolution of hydraulic conductivity. It is observed that after erosion occurs, the permeability of the soil increases as the particles decrease. Experimental findings

indicate that after reaching its peak, the permeability decreases during the later stages of suffusion. When comparing with numerical models, the proposed model in this study accurately predicts the growth process of permeability and the peak values under different stress conditions. However, unlike the experiments, the model-calculated permeability maintains a nearly constant value after reaching the peak, without exhibiting a decrease. This discrepancy can be attributed to the occurrence of local clogging within the specimens. In actual seepage processes, fine particles can be lost through the pores of the soil skeleton, but they can also undergo self-filtration, leading to the aggregation of fine particles within the pores and reducing local permeability. Unfortunately, the numerical model does not consider the heterogeneity of the specimens, thus is unable to account for local clogging phenomena or accurately reflect the decrease in permeability observed during the later stages of erosion.

Figure 6.14(c)-(d) depict the axial and radial strain induced by erosion. It is observed that soil deformation becomes more pronounced with increasing stress ratio. In general, the proposed model effectively captures both the rapid deformation phase and the subsequent stable stage of soil. However, it should be noted that there are still discrepancies observed for certain samples, such as sample GS-C-5. There are two main reasons for this discrepancy. Firstly, the parameters related to mechanical behavior in the model were fitted from a similar study, rather than directly from HK-CDG data, due to the lack of available data. This difference in parameter selection could affect the model's ability to accurately estimate the strains. Secondly, in the erosion tests, the stress state was maintained constant throughout, implying that the strains are solely

influenced by the eroded particles. As mentioned earlier, there are differences in the cumulative mass loss results between the model and experiments. Consequently, the strains predicted by the model also exhibit slight variations compared to the experimental data.

It is worth mentioning that Yang et al.(2020b) have also made a try to incorporate the influence of shear stress into the erosion law proposed by Uzuoka et al.(2012). Therefore, Figure 6.15 compares the erosion law proposed in this study with the one proposed by Yang et al and Uzuoka et al. The results show that under zero stress ratio, both models yield similar calculations. However, Uzuoka et al.'s model can not estimate the results for anisotropic stress conditions, and the accuracy of Yang et al.'s model diminishes under high stress ratios. It becomes challenging for their model to adequately capture the differences in cumulative mass loss and variations in permeability coefficient between the two groups of models, i.e., $\eta = 1.2$ and $\eta = 1.5$. Furthermore, it can be observed that all these models suffer from the same limitation of not considering particle clogging effects and non-uniformity. Consequently, there are discrepancies between the model predictions and experimental data regarding changes in the hydraulic permeability coefficient during the later stages of erosion. This highlights the need for improvement in future models to better account for these factors.

6.5 Influence of soil initial state on suffusion response

The above analysis indicates that the erosion law proposed in this paper based on CFD-DEM, as well as the established seepage-erosion-mechanics coupling method, can effectively simulate

suffusion within the framework of continuum mechanics. On this basis, a series of erosion simulations is carried out in this section to explore the impact of various influencing factors.

Figure 6.16(a) depicts the mass loss of soils with different void ratios e_0, revealing that denser samples exhibit lower mass loss under the same stress conditions. In the proposed model, the direct incorporation of void ratio into the erosion law is not employed. Instead, void ratio is considered in the calculation of CSL, mechanical stiffness, and hydraulic velocity. A higher void ratio results in increased hydraulic conductivity and, consequently, a larger seepage velocity under the same input gradient. Additionally, the influence of soil friction angle is investigated and presented in Figure 6.16(b). It is observed that a higher friction angle leads to increased resistance to erosion. In addition, as the friction angle increases, mass loss gradually decreases. At smaller friction angles, soil samples undergo greater deformation at the same stress level, leading to a sudden surge in mass loss. For example, in the case of $\phi_c = 33^\circ$, mass loss increases sharply at T = 200min. Figure 6.16(c) illustrates the impact of initial fines content f_{c0} on suffusion, revealing that it not only affects the final mass loss but also influences the erosion development process. The cumulative mass loss increases with higher fines content. Moreover, as fine content increases, the soil transitions from an underfilled to an overfilled state, causing fine particles to participate in more stress transfer and consequently exhibit greater erosion resistance. As a result, samples with higher fines content initiate suffusion at a relatively later stage compared to those with lower fines content, demonstrating that greater hydraulic gradients are required to induce particle migration in overfilled soils. Finally, Figure 6.16(d) investigates

the influence of size ratio R_d, which is defined as the ratio of coarse to fine particle sizes. The results obtained demonstrate that the current hydromechanical coupling model effectively captures the mass loss variations corresponding to different size ratios. Specifically, as the size ratio increases, the mass loss also exhibits an increasing trend. Xie et al. (2023) also noted that the larger the size ratio, the less contribution is made by the fine particles in bearing forces. Consequently, the resistance to erosion decreases, leading to higher mass loss.

6.6 Soil mechanical response subjected to suffusion

Previous studies (Ke and Takahashi, 2014c; Qian et al., 2021a) have reported variations in soil strength subsequent to suffusion. In this section, drained triaxial tests are simulated on pre- and post-suffusion samples to investigate the effect of soil strength by erosion using existing models. Samples with different initial void ratios and fine contents were selected and subjected to shear tests. Figure 6.17(a) illustrates the relationship between shear stress and axial strain before erosion. The results show that as the initial porosity decreases, the stress-strain behavior transitions from hardening to softening. This shift corresponds to a change in volume strain from dilation to contraction, as depicted in Figure 6.17(b). Following seepage erosion, the strength of specimens with different initial porosity ratios exhibits distinct variations. For initially dense specimens $(e_0 = 0.43, 0.45, \text{and } 0.47)$, the peak strength significantly decreases, and the stress-strain behavior shifts from softening to hardening. For example, the peak strength of a sample with an initial porosity ratio of 0.43 is approximately 330kPa before sufusion, but decreases to around 230kPa after sufusion. Additionally, no shear expansion behavior is observed in the porosity changes of these samples after suffusion. Conversely, for initially loose specimens

$(e_0 = 0.49)$, the peak strength increases after seepage erosion, and the changes in porosity show slight shear expansion. The different changes in sample strength can be attributed to the fact that while seepage erosion increases the soil's void ratio and reduces its strength, for gap-graded soils, when the fine content drops below a critical threshold (typically around 35%), the reduction in fine content actually enhances soil strength due to the greater load-bearing capacity of coarse particles (Shire et al., 2014; Yin et al., 2014; Taha et al., 2019). Thus, it can be concluded that initially dense specimens are more strongly affected by increased porosity, leading to reduced strength, while initially loose specimens are more influenced by reduced content, resulting in an increase in strength.

In addition, Figure 6.18 further investigates the mechanical response of samples with different initial fine contents f_{c0}. Prior to suffusion, it is observed that the soil strength decreases with an increase in f_{c0} when f_{c0}<35%, whereas it increases with an increase in f_{c0} when f_{c0}>35%. Such non-linear variation corresponds well with previous studies (Shire et al., 2014; Yin et al., 2014; Taha et al., 2019). Following erosion, the initially dense sample ($f_{c0} = 15\%, 25\%, \text{and } 50\%$) also displays a reduction in strength, whereas the initially loose sample ($f_{c0} = 35\%$) exhibits a slight increase in strength.

6.7 Summary

In this study, a novel erosion law has been proposed based on simulation results obtained from coupled CFD-DEM models. The erosion law takes into account both hydraulic conditions and soil stress states. Subsequently, it was integrated into a four-constituent continuum model,

coupled with a critical state-based fines-dependent constitutive model, enabling the realization of hydromechanical modeling of gap-graded soils with suffusion. To validate the proposed erosion with the framework, a series of erosion tests was simulated and compared with experimental data. Furthermore, the model was utilized to investigate the influence of significant factors on suffusion evolution and the subsequent variation in soil strength. The key findings and conclusions are summarized as follows:

(a) According to the CFD-DEM simulations, an exponential model is found appropriate to represent the evolution of mass loss induced by suffusion for samples under different seepage velocities, mean stress and shear stress ratios. By a set of appropriate parameters, the experimental observation can be well captured using the proposed erosion model;

(b) The established hydromechanical model achieves a two-way coupling between erosion and soil mechanical behavior. It incorporates the influence of stress on erosion through the erosion rate, while also accounting for the impact of erosion on stress through the fine content-related critical state theory. As a result, this framework effectively captures the essential characteristics of specimens subjected to various stress states and hydraulic conditions during suffusion;

(c) The current framework effectively showcases the influence of multiple factors on suffusion phenomena, underscoring its wide applicability in the field of suffusion analysis. Moreover, it successfully captures the variations in soil mechanical response resulting from suffusion. Drained triaxial tests reveal that erosion has a detrimental impact on the initial dense soil sample,

leading to a reduction in soil strength. Conversely, for the initial loose sample, erosion exhibits a subtle enhancement in peak strength.

Table 6.1 Summary of model parameters

Model parameters		
DEM	Young's modules, E	5×10^{7}
	Poisson's ratio, μ	0.3
	Friction coefficient, μ_c	0.3
	Rolling friction coefficient, μ_r	0.1
	Time step (s)	2×10^{-7}
CFD	Density, ρ_s (kg/m^3)	2.65×10^{3}
	Fluid viscosity, ν (Pa·s)	1×10^{-3}
	Density, ρ_f (kg/m^3)	1×10^{3}
	Cells (mm)	$1.2\times1.2\times1.2$
	Time step (s)	2×10^{-3}

Table 6.2 Summary of simulation samples

No.	i (m/m)	p (kPa)	η (q/p)	Initial void ratio e_0	Initial hydraulic conductivity k_0 (cm/s)	Simulation time (s)
1	2	50	0	0.335	2.10×10^{-3}	8.5
2	3	50	0			8.5
3	4	50	0			8.5
4	8	50	0			8.5
5	12	50	0			8.5
6	4	100	0	0.332	2.11×10^{-3}	8.5
7	4	150	0	0.328	2.11×10^{-3}	8.5
8	4	200	0	0.326	2.16×10^{-3}	8.5
9	4	50	0.3	0.321	2.06×10^{-3}	8.5
10	4	50	0.5	0.325	2.05×10^{-3}	12
11	4	50	0.75	0.335	2.12×10^{-3}	12.5

Table 6.3 Parameters of the mass loss ratio model

Soil	λ	a	b	c	m_0	k_1	k_2	k_3	v_{fc} (cm/s)	p_{ref} (kPa)
HK-CDG in this study	178.5	0.75	0.2	1	18.7	-0.15	0.4	8.3	0.8	50
Liang et al. (2017b)	32	1.5	-0.4	1	17	0.12	0.98	-20	0	20

Table 6.4 Parameters used in the hydramechanical model

Physical properties of HK-CDG soil	Density of fluid	ρ_f	1.00g/cm^3
	Density of soil	ρ_s	2.65g/cm^3
	Kinematic viscosity of fluid	η_k	$5.0\times10^{-6} m^2/s$
	Initial fines content	f_{c0}	0.35
	Initial permeability	k_0	$7.5\times10^{-5} m/s$
	Pore geometry index	m_k	4
	Initial void ratio	e_0	0.53
Mechanical constants of HK-CDG mixture	Elastic parameters	K_0	50MPa
		G_0	16.7MPa
		n	0.95
		n_p	1
		n_d	1
	Dilatancy parameters	d	18
		A_d	0.35
	CSL-related parameters	$e_{hc,cr0}$	0.776
		$e_{fc,cr0}$	0.87
		ξ	0.45
		λ	0.03
		a	0.751
		m	0.474
		ϕ_c	40.5
Erosion model parameters	Erosion rate controlling parameters	λ_e	1
		a_e	0.87
		b_e	-1.5
	Final mass loss controlling parameters	m_0	3.84
		c_e	8
		L_1	-0.05
		L_2	0.7
		L_3	-0.4
		v_{fc}	$4.2\ cm/s$

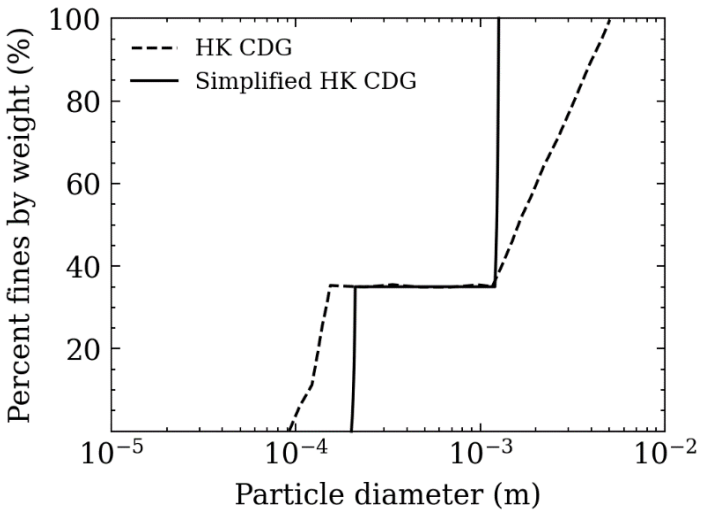

Figure 6.1 Grain-size distribution of soils in this study and experiment

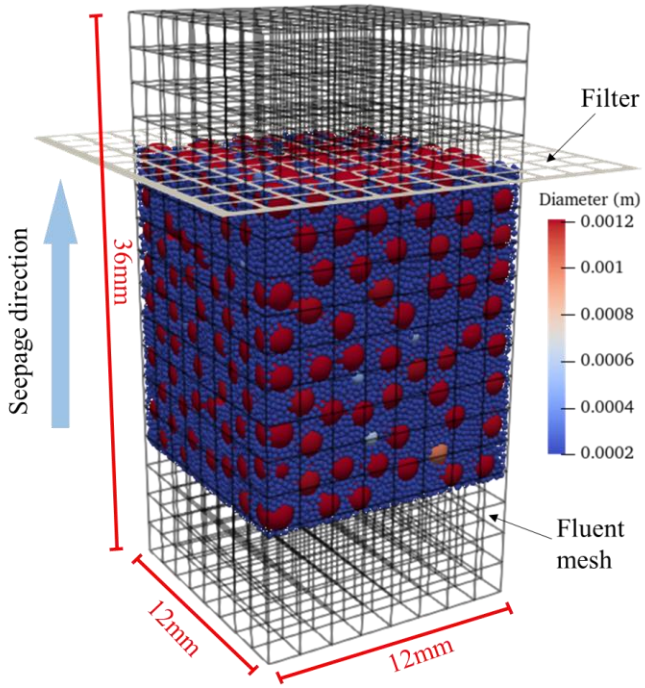

Figure 6.2 Illustration of CFD-DEM model

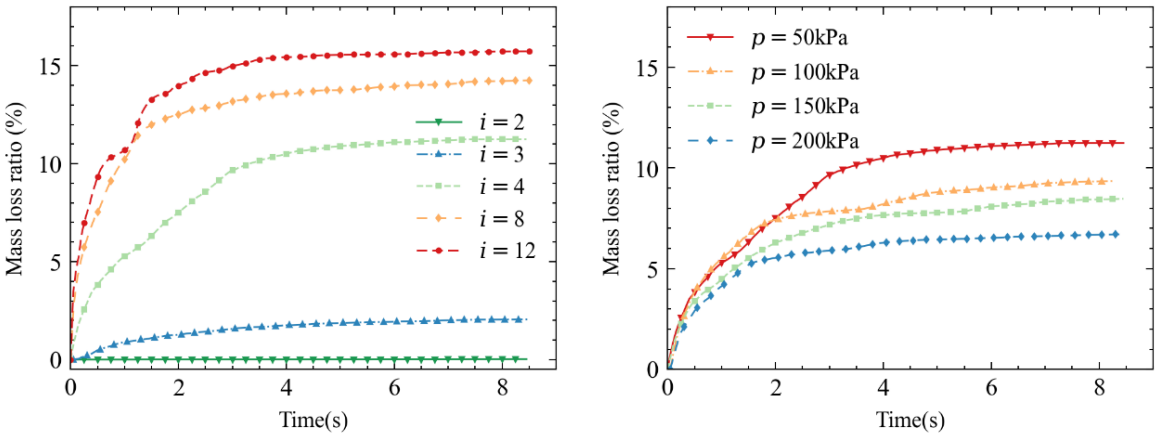

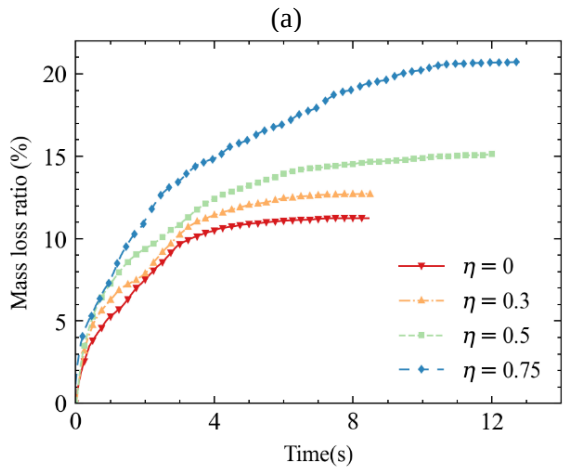

Figure 6.3 Fine particle mass loss ratio for samples under different: (a)confining pressure; (b) hydraulic gradient; (c) stress ratio

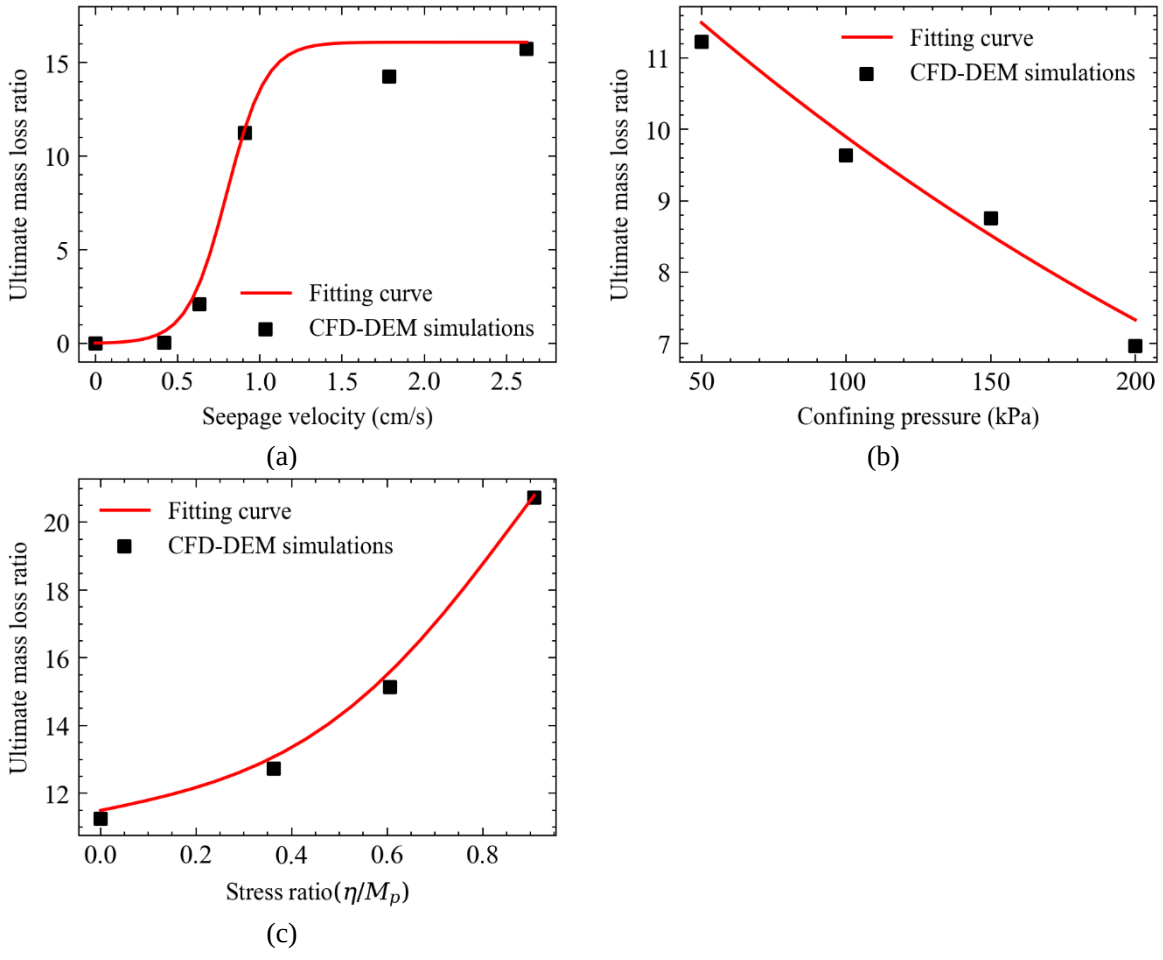

Figure 6.4 The fitting curve of ultimate mass loss ratio for different: (a) seepage velocity; (b) confining pressure; (c) stress ratio

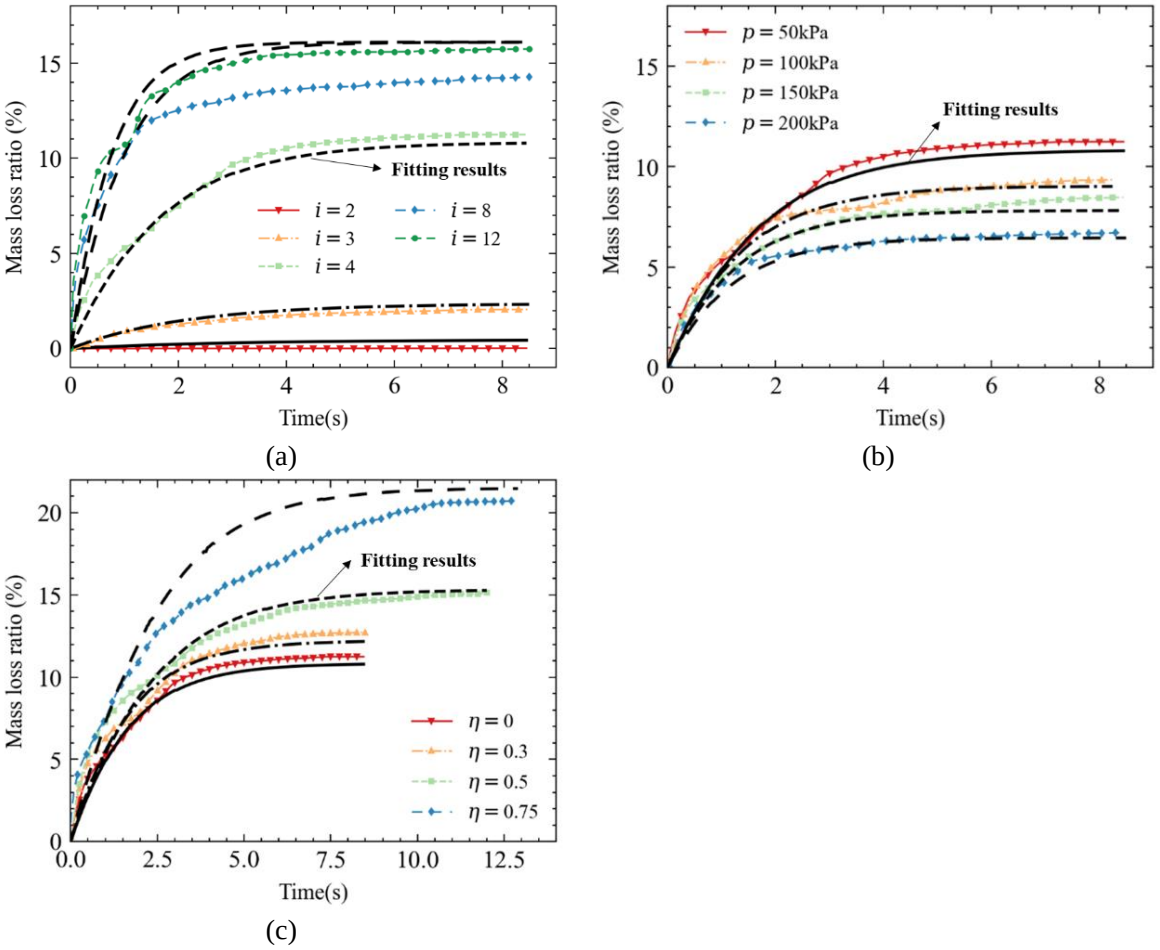

Figure 6.5 Fitting results of mass loss ratio versus time for cases under different: (a) seepage velocity; (b) confining pressure; (c) stress ratio

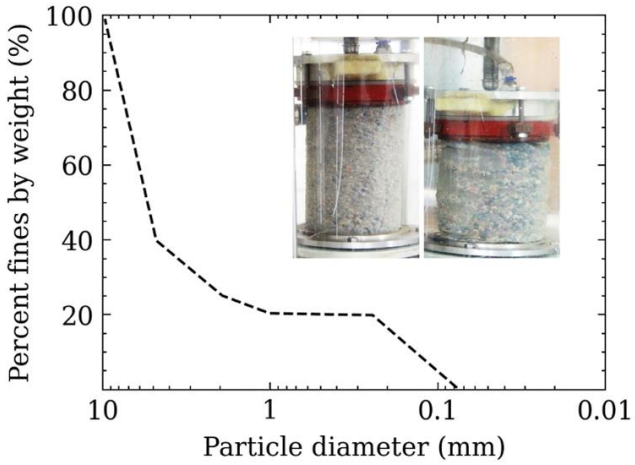

Figure 6.6 PSD of soils and suffusion samples in the study of Liang et al.(Liang et al., 2017b)

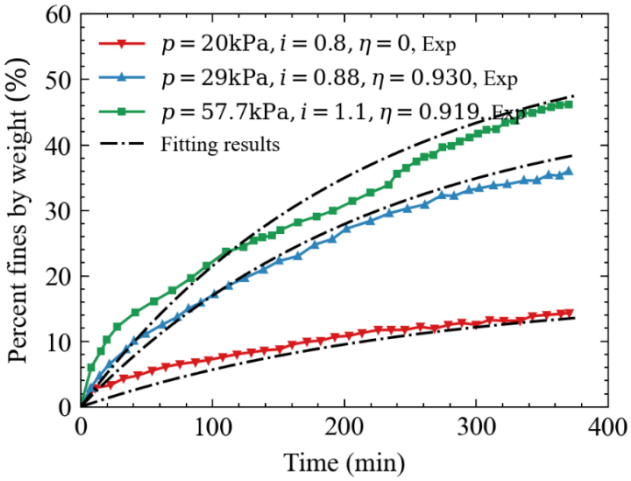

Figure 6.7 Comparison of results from experiments and fitting

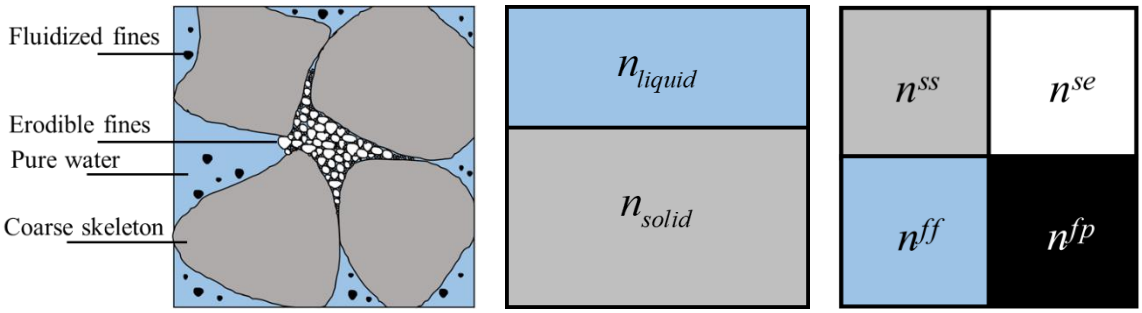

(a) (b) (c)

Figure 6.8 Simplified modeling of saturated soils: (a) Mesoscale REV; (b) two-constituents continuum model; (c) four-constituents continuum model

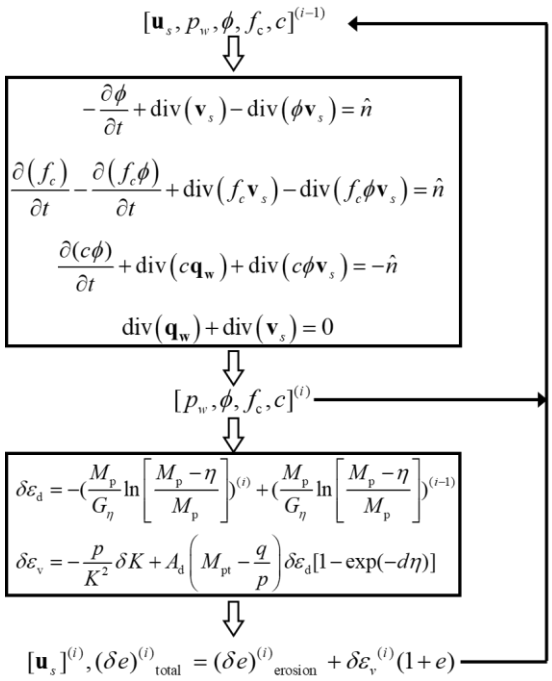

Figure 6.9 Seepage-Erosion-Mechanics coupling calculation flowchart

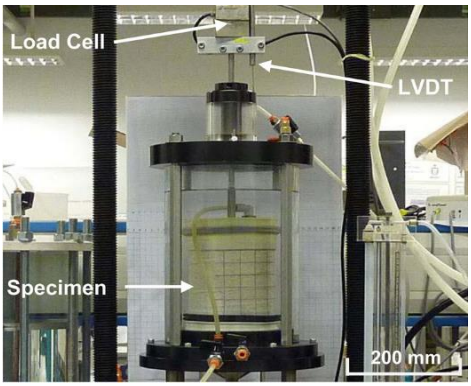

(a)

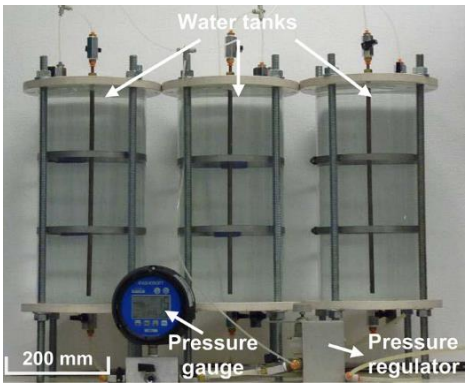

(b)

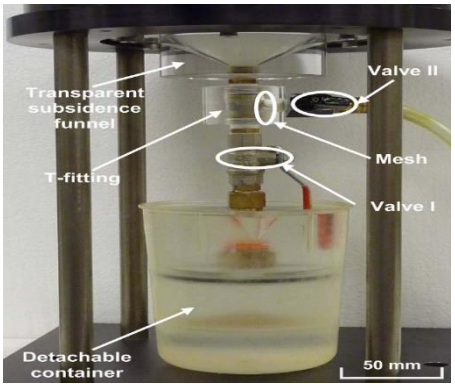

(c)

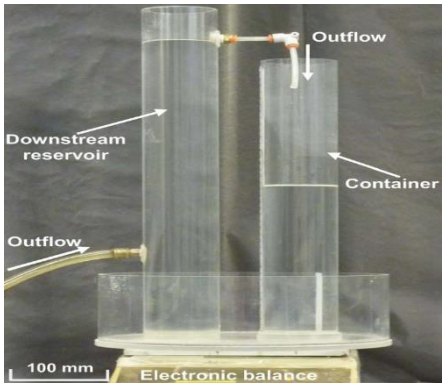

(d)

Figure 6.10 Triaxial Seepage Erosion Testing Equipment(Chang and Zhang, 2011): (a) Triaxial tesing system; (b) Water supply system; (c) Soil collection system; (d) Water collection system

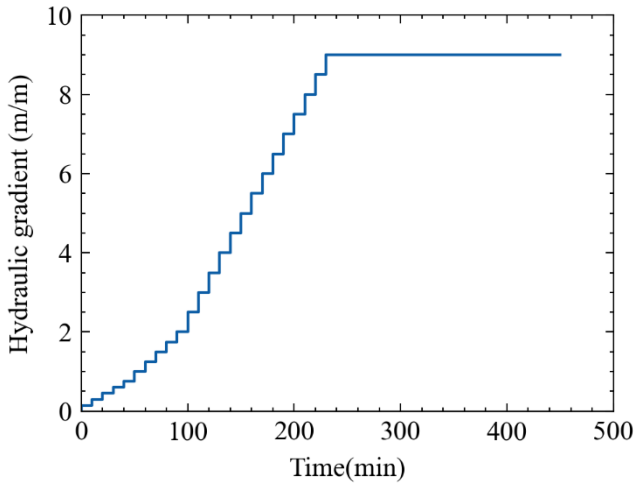

Figure 6.11 Hydraulic gradient applied during suffusion tests.

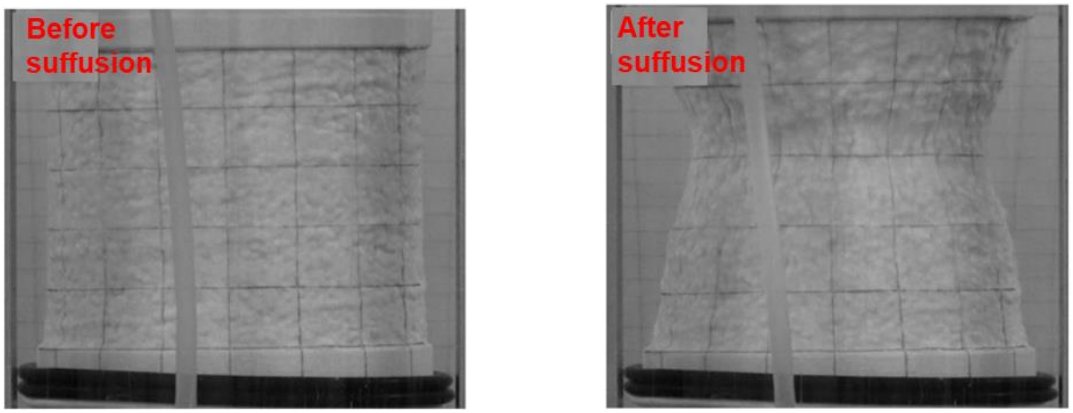

Figure 6.12 Deformation of specimen before and after suffusion (Chang and Zhang (2013b))

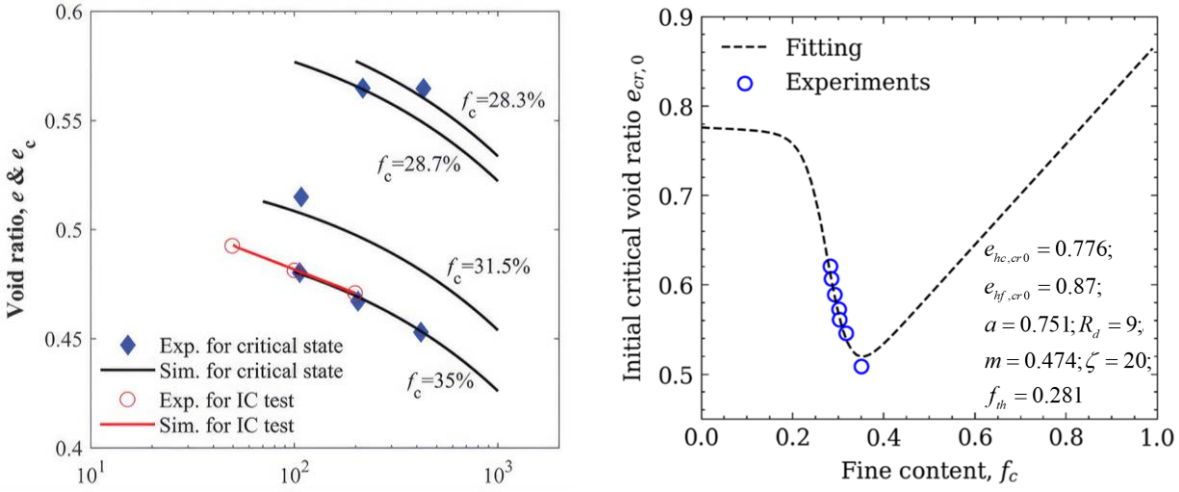

(a) (b)

Figure 6. 13 Determination of simulation parameters: (a) Determination of mechanical parameters; (b) Determination of CLS parameters

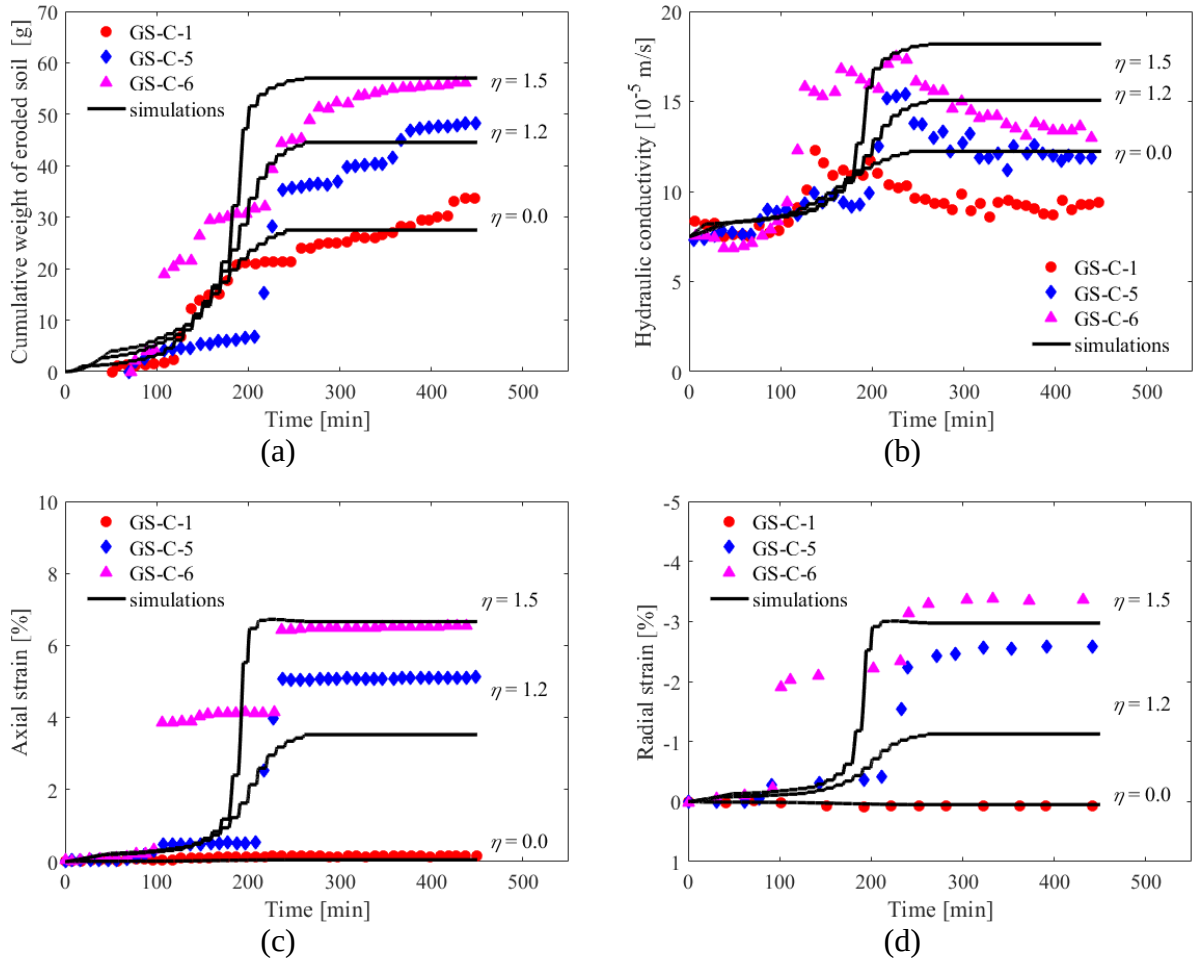

Figure 6.14 Comparison between experiments and numerical simulations: (a) cumulative mass; (b) evolution of hydraulic conductivity; (c) axial strain; (d) radial strain

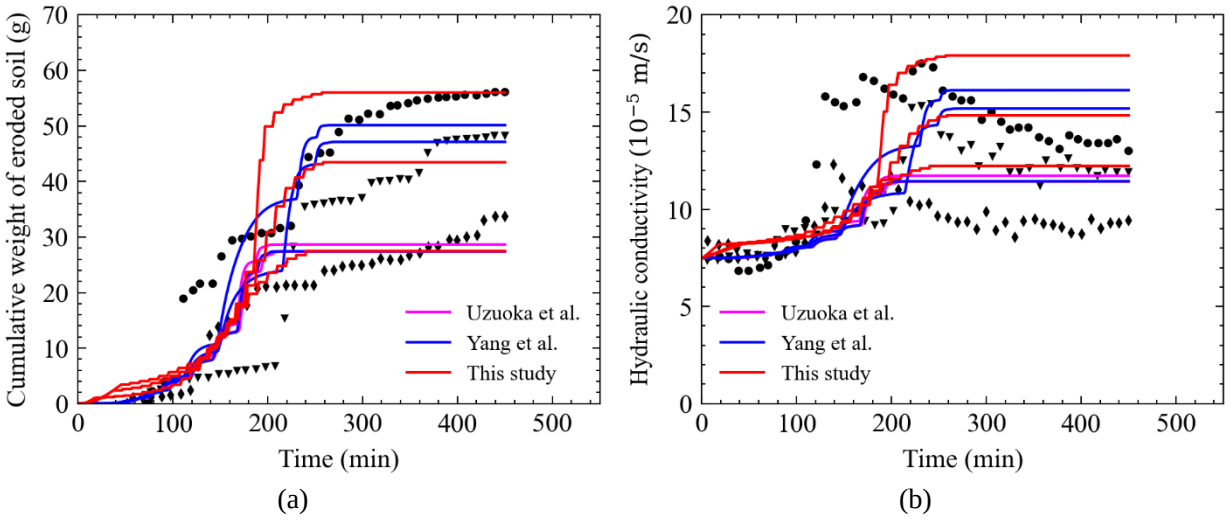

Figure 6.15 Comparison of different erosion laws: (a) Eroded soil mass; (b)Hydraulic conductivity

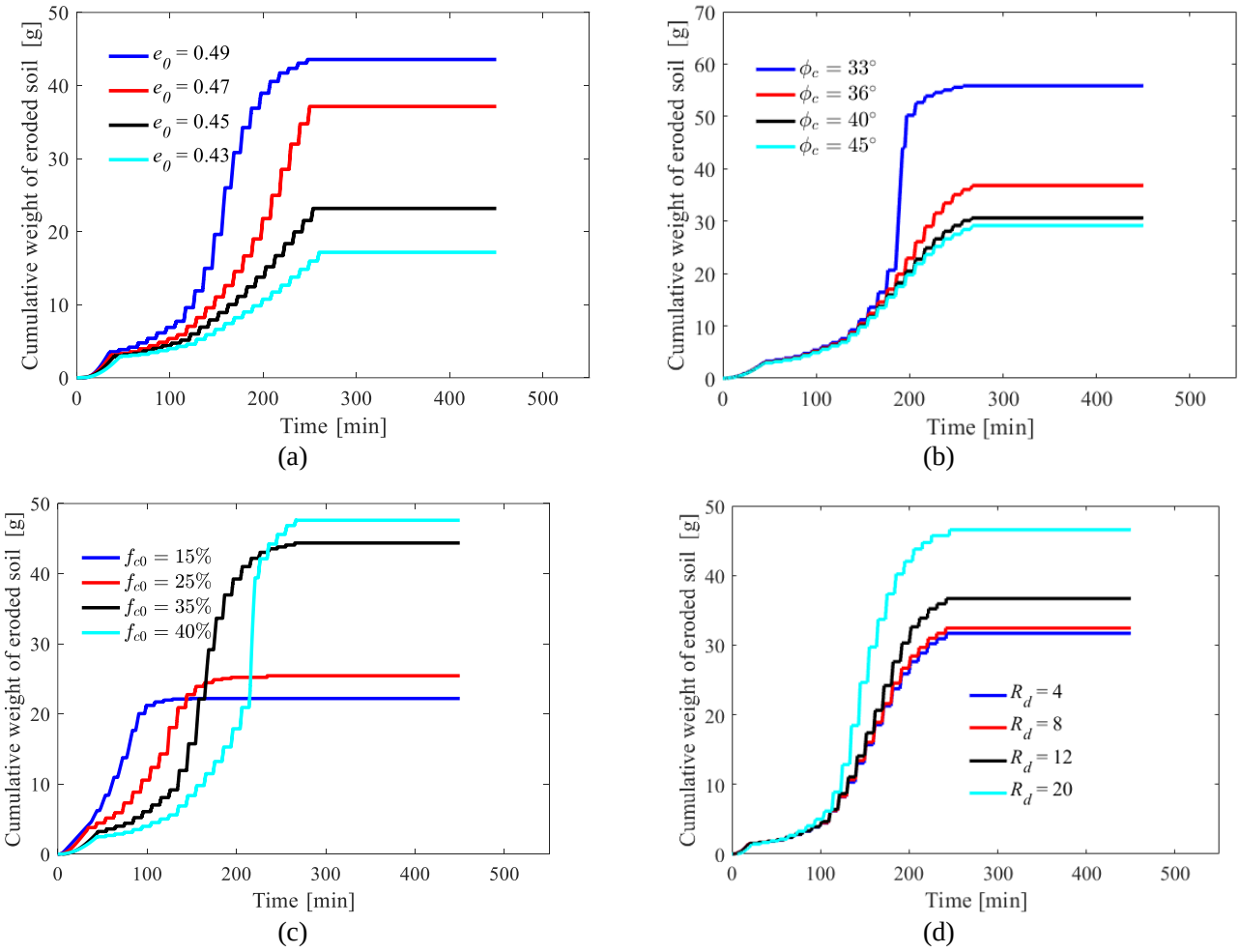

Figure 6.16 Cumulative mass loss for sample with different (a) void ratio; (b) friction angle; (c) fine content; (d) size ratio

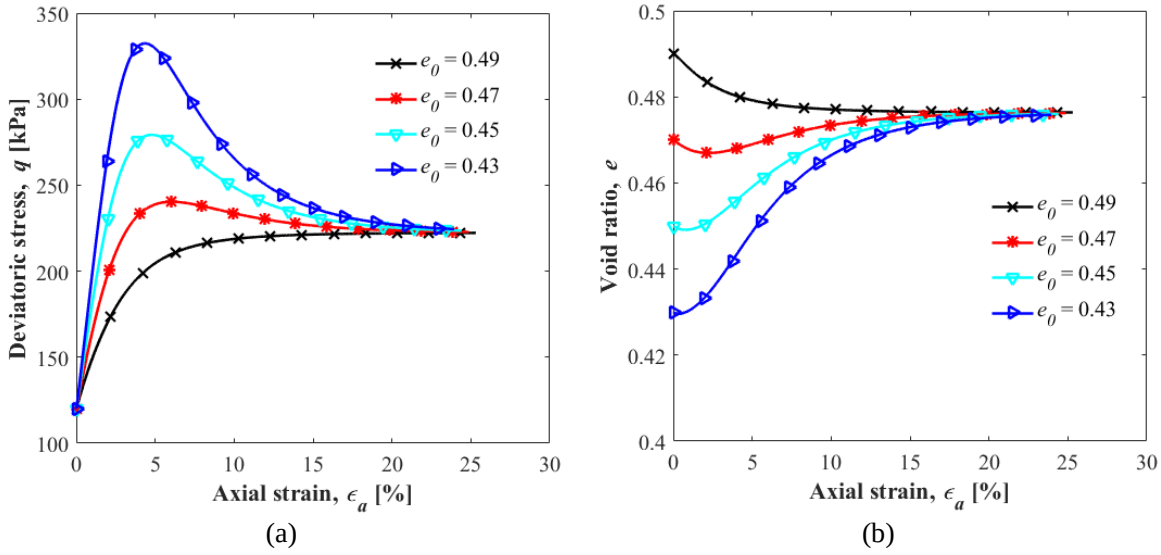

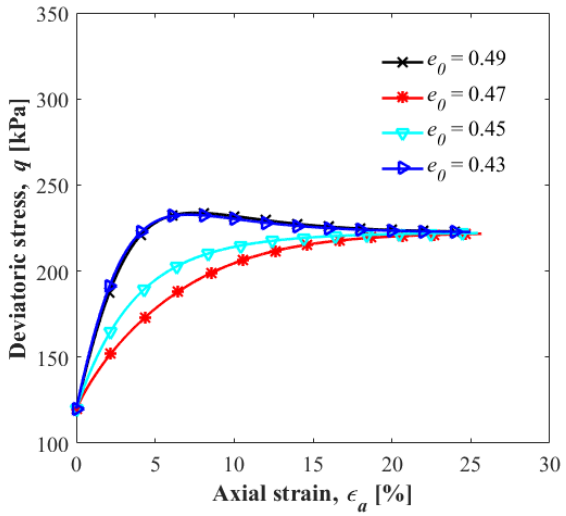

(c)

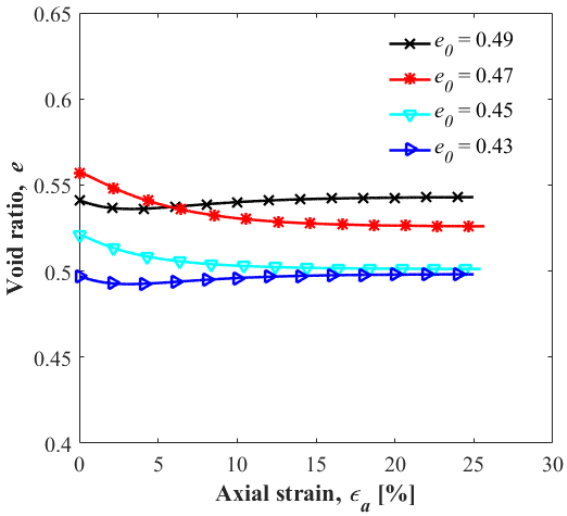

(d)

Figure 6.17 Results of drained triaxial tests for samples with different void ratios before and after erosion:

(a,c) deviatoric stress versus axial strain; (b,d) void ratio versus axial strain

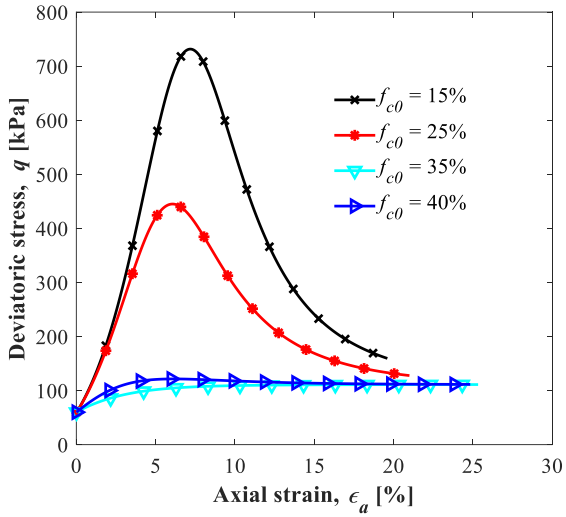

(a)

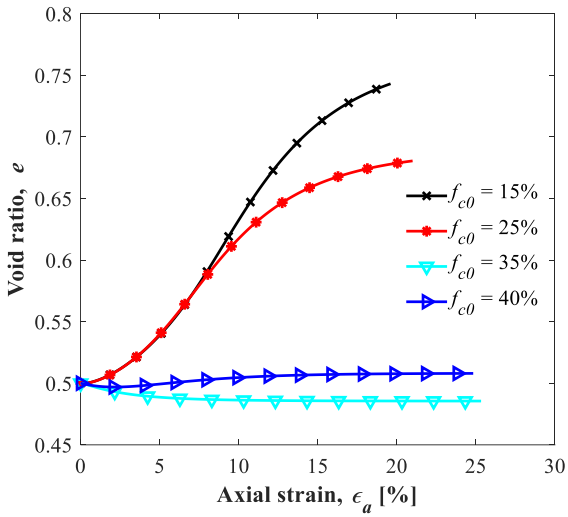

(b)

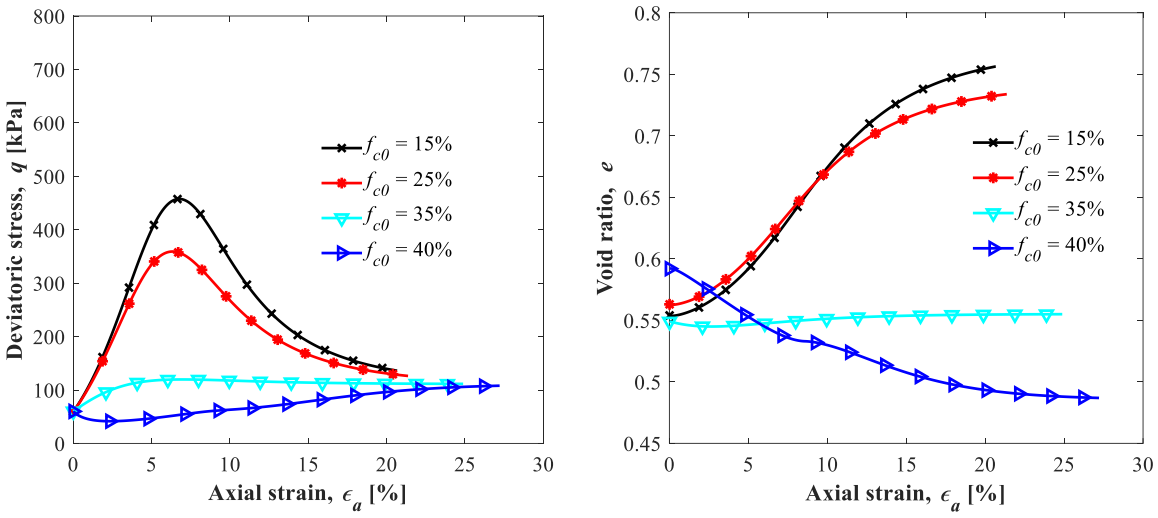

(c) (d)

Figure 6.18 Results of drained triaxial tests for samples with different fine contents before and after erosion:

(a,c) deviatoric stress versus axial strain; (b,d) void ratio versus axial strain.

CHAPTER 7 FINITE ELEMENT SIMULATION OF INTERNAL EROSION IN LARGE-SCALE DAMS BASED ON ABAQUS

7.1 Introduction

In Chapter 6, an erosion law based on CFD-DEM simulations is proposed, and a hydro-mechanical coupling framework is established, enabling the simulation of seepage erosion in the soil representative element volume within the continuum mechanics theory. To address the limitations of CFD-DEM methods, which are constrained by computational resources and cannot be applied to large-scale engineering problems, this chapter builds upon the research in Chapter 6 to further investigate numerical studies of suffusion at the engineering scale. To achieve this, the mass balance equations incorporating the proposed erosion law, along with the fines-dependent critical state constitutive model, are implemented into the ABAQUS finite element platform through its User Defined Element (UEL) subroutine. Finally, a case study of a dam engineering boundary value problem is presented, simulating the evolution patterns of suffusion in large-scale engineering models.

7.2 Hydro-mechanical coupling governing equations

The implementation of hydro-mechanical modeling for suffusion is achieved through the mass balance equations and stress balance equations. According to porous medium theory, the stress balance equations are given by:

$$\sigma_{ij,i} - w_i = 0 \tag{7.1}$$

where σ_{ij} represents the stress tensor ($i, j = 1, 2, 3$), w_i refers to the volumetric stress of

the soil.

Eqs. (7.1) and Eqs. (6.11)-(6.14) together form the governing equations for the hydro-mechanical coupling of suffusion, as follows:

$$\sigma_{ij,i} - w_i = 0 \tag{7.2}$$

$$\mathrm{div}(q_w) + \mathrm{div}(\mathbf{v}_s) = 0 \tag{7.3}$$

$$-\frac{\partial \phi}{\partial t} + \mathrm{div}(\mathbf{v}_s) - \mathrm{div}(\phi \mathbf{v}_s) = \hat{n} \tag{7.4}$$

$$\frac{\partial (c\phi)}{\partial t} + \mathrm{div}(cq_w) + \mathrm{div}(c\phi \mathbf{v}_s) = -\hat{n} \tag{7.5}$$

$$q_w = -\frac{k}{\eta_k \bar{\rho}(c)} \mathrm{grad}(p_w) \tag{7.6}$$

$$\frac{\partial (f_c)}{\partial t} - \frac{\partial (f_c \phi)}{\partial t} + \mathrm{div}(f_c \mathbf{v}_s) - \mathrm{div}(f_c \phi \mathbf{v}_s) = \hat{n} \tag{7.7}$$

The unknowns to be solved in the equations include the displacement of the soil ($u_s(\boldsymbol{x},t)$), pore water pressure ($p_w(\boldsymbol{x},t)$), porosity ($\phi(\boldsymbol{x},t)$), concentration of the fluid-like fine particles ($c(\boldsymbol{x},t)$), and fluid velocity ($q_w(\boldsymbol{x},t)$). Other unknowns involved in the equations, such as fine content (f_c), mixture density ($\bar{\rho}(c)$), permeability coefficient ($\boldsymbol{k}$), and soil skeleton velocity ($\mathbf{v}_s$), can be directly solved using the following equations:

$$f_c = 1 - \frac{(1+\varepsilon_v)(1-\phi_0)(1-f_{c0})}{1-\phi} \tag{7.8}$$

$$\bar{\rho} = c\rho_s + (1-c)\rho_f \tag{7.9}$$

$$k = k_0 \frac{\phi^{k_1}}{(1-\phi)^{k_2}} \tag{7.10}$$

$$\mathbf{v}_s = \frac{\partial u_s}{\partial t} \tag{7.11}$$

where ε_v represents the volumetric strain of the soil, ϕ_0 and f_{c0} denote the initial porosity and initial fine content, respectively. ρ_s and ρ_f are the densities of the soil

particles and the fluid, respectively. k_0 is the initial permeability coefficient, and k_1 and k_2 are constants related to the soil. Since f_c can be explicitly solved, Eqn (7.7) does not need to be considered as a separate governing equation, thus simplifying the calculations. Based on this, the erosion law derived from CFD-DEM in the previous chapter is substituted into Eqs. (7.2)-(7.6), resulting in the final governing equation as follows:

$$\sigma_{ij,i} - w_i = 0 \tag{7.12}$$

$$\mathrm{div}\left(q_w\right) + \mathrm{div}\left(\mathbf{v}_s\right) = 0 \tag{7.13}$$

$$-\frac{\partial \phi}{\partial t} + \mathrm{div}\left(\mathbf{v}_s\right) - \mathrm{div}\left(\phi \mathbf{v}_s\right) - \lambda_e q_w^{a_e} \left(p / p_{ref}\right)^{b_e} \left(m_\infty - m_e\right) f_{c0} = 0 \tag{7.14}$$

$$\frac{\partial (c\phi)}{\partial t} + \mathrm{div}\left(c q_w\right) + \mathrm{div}\left(c\phi \mathbf{v}_s\right) + \lambda_e q_w^{a_e} \left(p / p_{ref}\right)^{b_e} \left(m_\infty - m_e\right) f_{c0} = 0 \tag{7.15}$$

$$q_w = -\frac{k}{\eta_k \bar{\rho}(c)} \mathrm{grad}\left(p_w\right) \tag{7.16}$$

7.3 The derivation of the finite element form of the governing equations

To solve for the unknowns in the given equations, the ABAQUS User-Defined Element (UEL) is employed, enabling the implementation of nonlinear finite elements with user-defined degrees of freedom. Yang (2019) developed an 8-node plane strain element in the UEL. The calculation of displacement $u_s(\boldsymbol{x},t)$ is based on quadratic interpolation with 8 nodes, while the calculations of the other four variables ($\phi(\boldsymbol{x},t)$ $c(\boldsymbol{x},t)$ $q_w(\boldsymbol{x},t)$ $p_w(\boldsymbol{x},t)$) are based on linear interpolation with 4 nodes, as shown in Figure 7.1. The variables have been discretized spatially and expressed in terms of their nodal values as follows:

$$u_s = \mathbf{N}_2 \mathbf{u}_s,\ p_w = \mathbf{N}_1 \mathbf{p}_w,\ \phi = \mathbf{N}_1 \boldsymbol{\phi},\ c = \mathbf{N}_1 \mathbf{c},\ q_w = \mathbf{N}_1 \mathbf{q}_w \tag{7.18}$$

where $\mathbf{N}_1$ and $\mathbf{N}_2$ represent the order 1 and order 2 shape functions, respectively. By integrating the shape functions with the above partial differential equation, the Galerkin-weighted residuals can be obtained as follows:

$$R_1 = \int_{\mathrm{V}} \mathbf{B}_2^{\mathrm{t}} \boldsymbol{\sigma} \mathrm{dV} - \int_{\mathrm{V}} \mathbf{N}_2^{\mathrm{t}} w \mathrm{dV} - \oint_{\mathrm{S}} \mathbf{N}_2^{\mathrm{t}} \tau \mathrm{dS} \tag{7.19}$$

$$R_2 = -\frac{k}{\eta_k \bar{\rho}} \int_{\mathrm{V}} \left[-\mathbf{B}_1^{\mathrm{t}} \mathbf{B}_1 \mathbf{p}_w + \frac{k_1 + (k_2 - k_1)\phi}{\phi(1-\phi)} \mathbf{N}_1^{\mathrm{t}} \mathbf{p}_w^{\mathrm{t}} \mathbf{B}_1^{\mathrm{t}} \mathbf{B}_1 \phi - \frac{\rho_s - \rho_f}{\bar{\rho}} \mathbf{N}_1^{\mathrm{t}} \mathbf{p}_w^{\mathrm{t}} \mathbf{B}_1^{\mathrm{t}} \mathbf{B}_1 \mathbf{c} \right] \mathrm{dV} + \int_{\mathrm{V}} \mathbf{N}_1^{\mathrm{t}} \mathbf{m}^{\mathrm{t}} \mathbf{B}_2 \frac{\Delta u_s}{\Delta t} \mathrm{dV} + \oint_{\mathrm{S}} \mathbf{N}_1^{\mathrm{t}} v_n \mathrm{dS} \tag{7.20}$$

$$R_3 = \int_{\mathrm{V}} \left[\mathbf{N}_1^{\mathrm{t}} \left(\frac{\Delta \phi}{\Delta t} - \lambda_e \mathbf{q}_w{}^{a_e} (p / p_{ref})^{b_e} (m_\infty - m_e) f_{c0} \right) \right] \mathrm{dV} + \int_{\mathrm{V}} \left[(\phi - 1) \mathbf{N}_1^{\mathrm{t}} \mathbf{m}^{\mathrm{t}} \mathbf{B}_2 \frac{\Delta u_s}{\Delta t} + \mathbf{N}_1^{\mathrm{t}} \operatorname{grad}(\phi) \mathbf{N}_2 \frac{\Delta u_s}{\Delta t} \right] \mathrm{dV} \tag{7.21}$$

$$R_4 = \int_{\mathrm{V}} \left[\mathbf{N}_1^{\mathrm{t}} \left(\frac{\Delta (c\phi)}{\Delta t} - \lambda_e \mathbf{q}_w{}^{a_e} (p / p_{ref})^{b_e} (m_\infty - m_e) f_{c0} \right) \right] \mathrm{dV} + \int_{\mathrm{V}} \left[\mathbf{N}_1^{\mathrm{t}} \operatorname{grad}(c) \mathbf{q}_w + (c\phi - c) \mathbf{N}_1^{\mathrm{t}} \mathbf{m}^{\mathrm{t}} \mathbf{B}_2 \frac{\Delta u_s}{\Delta t} \right] \mathrm{dV} + \int_{\mathrm{V}} \left[\mathbf{N}_1^{\mathrm{t}} \operatorname{grad}(\phi) \mathbf{N}_2 c \frac{\Delta u_s}{\Delta t} + \mathbf{N}_1^{\mathrm{t}} \operatorname{grad}(c) \mathbf{N}_2 \phi \frac{\Delta u_s}{\Delta t} \right] \mathrm{dV} \tag{7.22}$$

$$R_5 = \int_{\mathrm{V}} \left[\mathbf{N}_1^{\mathrm{t}} \mathbf{q}_w \frac{\eta_k \bar{\rho}}{k} + \mathbf{N}_1^{\mathrm{t}} \mathbf{B}_1 \mathbf{p}_w \right] \mathrm{dV} \tag{7.23}$$

where $\mathbf{B}_1$ and $\mathbf{B}_2$ are the spatial derivatives of the shape functions $\mathbf{N}_1$ and $\mathbf{N}_2$, respectively.

In ABAQUS UEL, the Newton method is used to solve the nonlinear system of equations. The general computational format for each iteration step is as follows:

$$\begin{vmatrix} \frac{\partial R_1}{\partial u_s} & \frac{\partial R_1}{\partial p_w} & 0 & 0 & 0 \\ \frac{\partial R_2}{\partial u_s} & \frac{\partial R_2}{\partial p_w} & \frac{\partial R_2}{\partial \phi} & \frac{\partial R_2}{\partial c} & 0 \\ \frac{\partial R_3}{\partial u_s} & 0 & \frac{\partial R_3}{\partial \phi} & 0 & \frac{\partial R_3}{\partial q_w} \\ \frac{\partial R_4}{\partial u_s} & 0 & \frac{\partial R_4}{\partial \phi} & \frac{\partial R_4}{\partial c} & \frac{\partial R_4}{\partial q_w} \\ 0 & \frac{\partial R_5}{\partial p_w} & \frac{\partial R_5}{\partial \phi} & \frac{\partial R_5}{\partial c} & \frac{\partial R_5}{\partial q_w} \end{vmatrix}_{(m)} \begin{vmatrix} \delta u_s \\ \delta p_w \\ \delta \phi \\ \delta c \\ \delta q_w \end{vmatrix}_{(m+1)} = - \begin{vmatrix} R_1 \\ R_2 \\ R_3 \\ R_4 \\ R_5 \end{vmatrix}_{(m)} \tag{7.24}$$

where, (m) represents the iteration counter. The first matrix on the left-hand side is the Jacobian stiffness matrix, which consists of the partial derivatives of the Galerkin-weighted residuals. Taking the partial derivatives of the residual function yields the following:

$$\frac{\partial R_1}{\partial u_s} = \int_{\mathrm{V}} \mathbf{B}_2^{\mathrm{t}} \mathbf{D} \mathbf{B}_2 \mathrm{dV} \tag{7.25}$$

$$\frac{\partial R_1}{\partial p_w} = -\int_{\mathrm{V}} \mathbf{B}_2^{\mathrm{t}} \mathbf{m} \mathbf{N}_1 \mathrm{dV} \tag{7.26}$$

$$\frac{\partial R_2}{\partial u_s} = \frac{1}{\Delta t} \int_{\mathrm{V}} \mathbf{N}_1^{\mathrm{t}} \mathbf{m}^{\mathrm{t}} \mathbf{B}_1 \mathrm{dV} \tag{7.27}$$

$$\frac{\partial R_2}{\partial p_w} = -\frac{k}{\eta_k \bar{\rho}} \int_{\mathrm{V}} \begin{bmatrix} -\mathbf{B}_1^{\mathrm{t}} \mathbf{B}_1 + \frac{k_1 + (k_2 - k_1)\phi}{\phi(1-\phi)} \mathbf{N}_1^{\mathrm{t}} \boldsymbol{\phi}^{\mathrm{t}} \mathbf{B}_1^{\mathrm{t}} \mathbf{B}_1 \\ -\frac{\rho_s - \rho_f}{\bar{\rho}} \mathbf{N}_1^{\mathrm{t}} \mathbf{c}^{\mathrm{t}} \mathbf{B}_1^{\mathrm{t}} \mathbf{B}_1 \end{bmatrix} \mathrm{dV} \tag{7.28}$$

$$\begin{aligned} \frac{\partial R_2}{\partial \phi} = & -\frac{k}{\eta_k \bar{\rho}} \int_{\mathrm{V}} \begin{bmatrix} \frac{k_1 + (k_2 - k_1)\phi}{\phi(1-\phi)} \mathbf{N}_1^{\mathrm{t}} \mathbf{p}_w^{\mathrm{t}} \mathbf{B}_1^{\mathrm{t}} \mathbf{B}_1 \\ + \frac{(k_2 - k_1)\phi^2 + 2k_1\phi - k_1}{\phi^2 (1-\phi)^2} \mathbf{N}_1^{\mathrm{t}} \mathbf{p}_w^{\mathrm{t}} \mathbf{B}_1^{\mathrm{t}} \mathbf{B}_1 \boldsymbol{\phi} \mathbf{N}_1 \end{bmatrix} \mathrm{dV} \\ & - \frac{k}{\eta_k \bar{\rho}} \frac{k_1 + (k_2 - k_1)\phi}{\phi(1-\phi)} \int_{\mathrm{V}} \begin{bmatrix} -\mathbf{B}_1^{\mathrm{t}} \mathbf{B}_1 \mathbf{p}_w + \frac{k_1 + (k_2 - k_1)\phi}{\phi(1-\phi)} \mathbf{N}_1^{\mathrm{t}} \mathbf{p}_w^{\mathrm{t}} \mathbf{B}_1^{\mathrm{t}} \mathbf{B}_1 \phi \\ -\frac{\rho_s - \rho_f}{\bar{\rho}} \mathbf{N}_1^{\mathrm{t}} \mathbf{p}_w^{\mathrm{t}} \mathbf{B}_1^{\mathrm{t}} \mathbf{B}_1 \mathbf{c} \end{bmatrix} \mathbf{N}_1 \mathrm{dV} \end{aligned} \tag{7.29}$$

$$\frac{\partial R_2}{\partial c}=-\frac{k}{\eta_k\bar{\rho}}\int_{\mathrm{V}}\left[-\frac{\rho_s-\rho_f}{\bar{\rho}}\mathbf{N}_1^{\mathrm{t}}\mathbf{p}_w^{\mathrm{t}}\mathbf{B}_1^{\mathrm{t}}\mathbf{B}_1+\left(\frac{\rho_s-\rho_f}{\bar{\rho}}\right)^2\mathbf{N}_1^{\mathrm{t}}\mathbf{p}_w^{\mathrm{t}}\mathbf{B}_1^{\mathrm{t}}\mathbf{B}_1\mathbf{c}\mathbf{N}_1\right]\mathrm{dV}$$
$$+\frac{k}{\eta_k\bar{\rho}^2}\left(\rho_s-\rho_f\right)\int_{\mathrm{V}}\begin{bmatrix}-\mathbf{B}_1^{\mathrm{t}}\mathbf{B}_1\mathbf{p}_w+\dfrac{k_1+\left(k_2-k_1\right)\phi}{\phi(1-\phi)}\mathbf{N}_1^{\mathrm{t}}\mathbf{p}_w^{\mathrm{t}}\mathbf{B}_1^{\mathrm{t}}\mathbf{B}_1\phi\\ -\dfrac{\rho_s-\rho_f}{\bar{\rho}}\mathbf{N}_1^{\mathrm{t}}\mathbf{p}_w^{\mathrm{t}}\mathbf{B}_1^{\mathrm{t}}\mathbf{B}_1\mathbf{c}\end{bmatrix}\mathbf{N}_1\mathrm{dV} \tag{7.30}$$

$$\frac{\partial R_3}{\partial u_s}=\int_{\mathrm{V}}\left[\frac{(\phi-1)}{\Delta t}\mathbf{N}_1^{\mathrm{t}}\mathbf{m}^{\mathrm{t}}\mathbf{B}_2+\frac{1}{\Delta t}\mathbf{N}_1^{\mathrm{t}}\,\mathrm{grad}(\phi)\mathbf{N}_2\right]\mathrm{dV} \tag{7.31}$$

$$\frac{\partial R_3}{\partial \phi}=\int_{\mathrm{V}}\left[\frac{1}{\Delta t}\mathbf{N}_1^{\mathrm{t}}\mathbf{N}_1+\mathbf{N}_1^{\mathrm{t}}\mathbf{m}^{\mathrm{t}}\mathbf{B}_2\frac{\Delta u}{\Delta t}\mathbf{N}_1+\mathbf{N}_1^{\mathrm{t}}\frac{\Delta u^{\mathrm{t}}}{\Delta t}\mathbf{N}_2^{\mathrm{t}}\mathbf{B}_1\right]\mathrm{dV} \tag{7.32}$$

$$\frac{\partial R_3}{\partial q_w}=-\lambda a(f_c-f_{rhs})f_{c0}(p/p_{ref})^b\int_{\mathrm{V}}\mathbf{N}_1^{\mathrm{t}}(\mathbf{q}_w\mathbf{N}_1)^{a-1}\mathrm{dV} \tag{7.33}$$

$$\frac{\partial R_4}{\partial u_s}=\int_{\mathrm{V}}\left[\frac{c\phi-c}{\Delta t}\mathbf{N}_1^{\mathrm{t}}\mathbf{m}^{\mathrm{t}}\mathbf{B}_2+\frac{c}{\Delta t}\mathbf{N}_1^{\mathrm{t}}\,\mathrm{grad}(\phi)\mathbf{N}_2+\frac{\phi}{\Delta t}\mathbf{N}_1^{\mathrm{t}}\,\mathrm{grad}(c)\mathbf{N}_2\right]\mathrm{dV} \tag{7.34}$$

$$\begin{aligned}\frac{\partial R_4}{\partial \phi}&=\int_{\mathrm{V}}\left[\frac{c}{\Delta t}\mathbf{N}_1^{\mathrm{t}}\mathbf{N}_1+\mathbf{N}_1^{\mathrm{t}}\,\mathrm{grad}(\phi)\mathbf{q}_w+\frac{c}{\Delta t}\mathbf{N}_1^{\mathrm{t}}\mathbf{m}^{\mathrm{t}}\mathbf{B}_2\Delta u\mathbf{N}_1\right]\mathrm{dV}\\&+\int_{\mathrm{V}}\left[\frac{c}{\Delta t}\mathbf{N}_1^{\mathrm{t}}\Delta u^{\mathrm{t}}\mathbf{N}_2^{\mathrm{t}}\mathbf{B}_1+\mathbf{N}_1^{\mathrm{t}}\,\mathrm{grad}(c)\mathbf{N}_2\frac{\Delta u}{\Delta t}\mathbf{N}_1\right]\mathrm{dV}\end{aligned} \tag{7.35}$$

$$\begin{aligned}\frac{\partial R_4}{\partial c}&=\int_{\mathrm{v}}\left[\frac{\phi}{\Delta t}\mathbf{N}_1^{\mathrm{t}}\mathbf{N}_1+\mathbf{N}_1^{\mathrm{t}}\mathbf{q}_w^{\mathrm{t}}\mathbf{B}_1+(\phi-1)\mathbf{N}_1^{\mathrm{t}}\mathbf{m}^{\mathrm{t}}\mathbf{B}_2\frac{\Delta u_s}{\Delta t}\mathbf{N}_1\right]\mathrm{dV}\\&+\int_{\mathrm{V}}\left[\mathbf{N}_1^{\mathrm{t}}\,\mathrm{grad}(\phi)\mathbf{N}_2\frac{\Delta u}{\Delta t}\mathbf{N}_1+\frac{\phi}{\Delta t}\mathbf{N}_1^{\mathrm{t}}\Delta u_s{}^{\mathrm{t}}\mathbf{N}_2^{\mathrm{t}}\mathbf{B}_1\right]\mathrm{dV}\end{aligned} \tag{7.36}$$

$$\frac{\partial R_4}{\partial q_w}=\int_{\mathrm{V}}\left[-\lambda_e a_e\mathbf{N}_1^{\mathrm{t}}(\mathbf{q}_w\mathbf{N}_1)^{a_e-1}(p/p_{ref})^{b_e}(f_c-f_{rhs})f_{c0}+\mathbf{N}_1^{\mathrm{t}}\,\mathrm{grad}(c)\mathbf{N}_1\right]\mathrm{dV} \tag{7.37}$$

$$\frac{\partial R_5}{\partial p_w}=\int_{\mathrm{V}}\mathbf{N}_1^{\mathrm{t}}\mathbf{B}_1\mathrm{dV} \tag{7.38}$$

$$\frac{\partial R_5}{\partial \phi}=\int_{\mathrm{V}}\left[\mathbf{N}_1^{\mathrm{t}}\mathbf{q}_w\mathbf{N}_1\frac{\eta_k\bar{\rho}}{k}\frac{\left(k_1-k_2\right)\phi-k_1}{\phi(1-\phi)}\right]\mathrm{dV} \tag{7.39}$$

$$\frac{\partial R_5}{\partial c}=\int_{\mathrm{V}}\left[\mathbf{N}_1^{\mathrm{t}}\mathbf{q}_w\mathbf{N}_1\frac{\eta_k}{k}\left(\rho_s-\rho_f\right)\right]\mathrm{dV} \tag{7.40}$$

$$\frac{\partial R_5}{\partial q_w}=\int_{\mathrm{v}}\left[\mathbf{N}_1^{\mathrm{t}}\mathbf{N}_1\frac{\eta_k\bar{\rho}}{k}\right]\mathrm{dV} \tag{7.41}$$

It should be noted that due to the complexity of the entire solution system, and to ensure convergence of the program, the previously mentioned erosion law has been simplified.

From Eqs. (6.21) and (6.2), it can be seen that the complete erosion law consists of the following two parts:

$$\hat{n} = \lambda_e v_f^{a_e} (p / p_{ref})^{b_e} (m_\infty - m_e) f_{c0} \tag{7.42}$$

$$m_\infty = m_0 \frac{\exp(L_1 p / p_{ref} + L_2 (\eta / M_p)^{c_e})}{1 + \exp(L_3 (v_f - v_{fc}))} \tag{7.43}$$

Eqn. (7.43) represents the prediction of the final cumulative fine particle loss, while $(m_\infty - m_e)$ in Eqs. (7.42) represents the proportion of remaining erodible fine particles within the element. To avoid the complexity of deriving Eqn. (7.43) and creating an overly complicated Jacobian matrix, $(m_\infty - m_e)$ is substituted for $(f_c - f_{rhs})$ in equation (7.42) to simplify the computation, where the residual fine content, f_{rhs}, is a constant parameter. Based on this simplification, the non-linear equations can be written in a compact form as required by ABAQUS UEL:

$$\mathbf{AMATRX} \cdot \mathbf{d}_N = \mathbf{RHS} \tag{7.44}$$

where **AMATRX** is the Jacobian stiffness matrix composed of the partial derivatives (Eqs. (7.25)-(7.41)), **RHS** is the residual the residual nodal fluxes or forces defined in the subroutine, and $\mathbf{d}_N$ is the nodal vector of degrees of freedom.

7.4 Simulation of internal erosion in dams

In order to study the internal erosion at an engineering scale, this study establishes a two-dimensional foundation-dam model under plane strain conditions using the proposed analysis framework, as shown in Figure 7.2. The model is based on a real-world engineering case of a dam built on a sandy-silt alluvium formation over karstic limestones (Rafid, 2016), where a confined aquifer exists below the limestone layer. When there is a difference in the water levels between the alluvial layer and the

confined aquifer, seepage will induce internal erosion. The established numerical model has a total length of 34m and a total height of 10.5m, with the dam portion having a height of 6m and the foundation portion having a height of 4.5m. For convenience in calculation, the model uses a symmetric half-model, containing 104,654 UEL elements and 14,301 nodes. The symmetric plane (x = 0 m), the bottom plane (y = 0 m), and the right boundary (x = 34m) are all fixed boundaries and impermeable. Seepage points are simulated by setting nodes with a high permeability coefficient at the foundation bottom. This chapter only considers the loss of fine particles, with the initial fine content in the soil set to 0.4. From previous simulations, it is known that a significant portion of the fine particles within the element cannot be eroded by seepage flow. Therefore, a residual fine content f_{rhs} of 0.2 is specified. When the fine content within the element decreases from 0.4 to 0.2, the mass exchange rate becomes 0, and the element no longer experiences further particle loss. The parameters involved in the calculations are shown in Table 7.1, with the mechanical-related parameters referenced from the study of Yang et al. (2020a).

7.5 Results and discussion

Figure 7.3 shows the variation in fine content f_c with the duration of suffusion. It can be observed that by the 150th day, the soil area with reduced fine content extends from the seepage point to the dam slope. As the duration of erosion increases, the area with reduced fine particle content further expands. Centred on the seepage point, the soil range with the lowest fine content ($f_c = 0.2$) expands outward in a semicircular pattern.

By days 300 and 350, the content on the slope gradually stabilises, but the soil areas with the lowest fine content continue to expand outward from the seepage point.

Figure 7.4 shows the development of soil displacement. It can be observed that by the 150th day, the soil has not undergone significant displacement deformation. As the erosion time increases, displacement subsidence begins to appear on the slope surface by day 250. By day 350, significant soil displacement is observed across the dam slope, with the maximum displacement occurring at the toe of the slope. At this point, internal erosion has triggered a severe landslide disaster.

Figure 7.5 further illustrates the variation in fine content and displacement at specific node locations (slope crest, slope toe, and seepage points). It can be observed that, during suffusion, fine loss occurs rapidly near the seepage points. Compared to the slope crest, the slope toe responds to erosion earlier, and the erosion rate at the slope toe is also greater than that at the slope crest. By approximately 320 days, the fine content at both the slope crest and slope toe reaches a stable phase, with little to no further particle loss occurring thereafter. The node displacements shown in Figure 7.5(b) indicate that displacement development exhibits significant nonlinearity. Soil deformation becomes noticeable only after approximately 200 days, after which it enters a rapid development phase. Compared to the slope toe, displacement at the slope crest is greater. Comparing the changes in fine content and displacement at the same locations also reveals a noticeable lag in displacement development. For example,

around the 150th day, particle loss occurs at the slope toe, leading to a decrease in fine content, but the displacement at this location is nearly zero. It is only around the 300th day that deformation begins to appear at the slope toe.

Figure 7.6 shows the development of shear strain with erosion time. It can be observed that by the 150th day, a shear zone forms only near the seepage point. However, according to Eqn. (6.40), the reduction in fine content leads to a decrease in the critical state void ratio e_{c0} of the soil, making it more prone to failure. As a result, by the 250th day, two continuous shear zones have formed within the soil: one connecting the seepage point to the slope toe and the other connecting the seepage point to the slope crest. As internal erosion progresses further, a landslide begins to occur on the embankment. From the shear strain distribution at day 350, an arcuate failure surface can be clearly observed, indicating that the embankment has failed at this point.

7.6 Summary

Based on the secondary development of the ABAQUS UEL, this chapter establishes a numerical analysis framework for the hydro-mechanical coupling of internal erosion. Using the mass balance and stress balance governing equations, an 8-node plane strain element is developed, and the Jacobian stiffness matrix for finite element solving is derived. The solution of the governing equations is then implemented in ABAQUS. Through the plane strain finite element analysis of the dam on an engineering scale, the effect of internal erosion on the dam's mechanical response is investigated. The main

research conclusions are as follows:

(a) Through the secondary development of ABAQUS UEL, the erosion law from CFD-DEM is integrated into the governing equations for seepage-erosion-mechanics coupling, where the displacement field is solved using second-order shape functions, while the solutions for other field variables are obtained using first-order shape functions.

(b) Finite element analysis results show that when suffusion occurs in the foundation, the eroded area gradually expands from the seepage point to the dam slope. The farther from the seepage point, the slower the rate of fine particle loss. Corresponding to the change in fine content, the surface settlement exhibits significant nonlinearity and hysteresis.

(c) Suffusion causes an increase in the critical porosity and a corresponding decrease in the critical strength of the soil. During the progressive erosion process, plastic shear strain initially concentrates near the seepage point, then the shear zone gradually develops and eventually extends to the top and bottom of the slope, resulting in overall landslide failure.

Table 7.1 The parameters of the numerical model

Physical properties	Density of fluid	ρ_f	1.00g/cm^3
	Density of soil	ρ_s	2.65g/cm^3
	Kinematic viscosity of fluid	η_k	$5.0\times10^{-6} m^2/s$
	Initial fines content	f_{c0}	0.4
	Initial permeability	k_0	$7.5\times10^{-5} m/s$
	Permeability parameters	k_1	3
	Permeability parameters	k_2	2
	Initial void ratio	e_0	0.6
Mechanical constants of HK-CDG mixture	Elastic parameters	K_0	50MPa
		G_0	16.7MPa
		n	0.95
		n_p	1
		n_d	1
	Dilatancy parameters	d	18
		A_d	0.35
	CSL-related parameters	$e_{hc,cr0}$	0.805
		$e_{fc,cr0}$	1.03
		ξ	0.19
		λ	0.081
		a	0.751
		m	0.474
		ϕ_c	40.5
Erosion model parameters	Erosion rate controlling parameters	λ_e	1.1×10^{-7}
		p_{ref}	30kPa
		a_e	2
		b_e	0.5

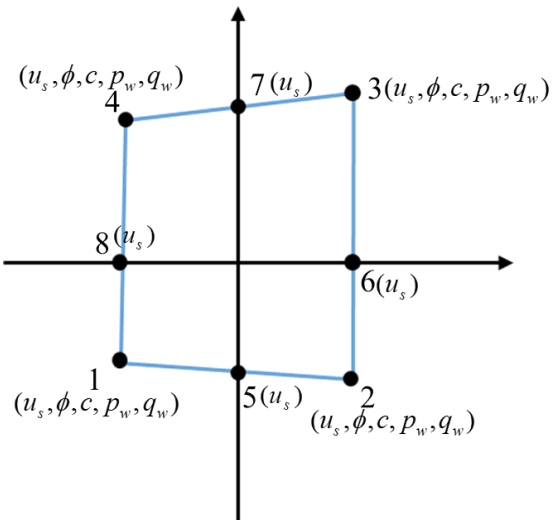

Figure 7.1 8-node plane strain element

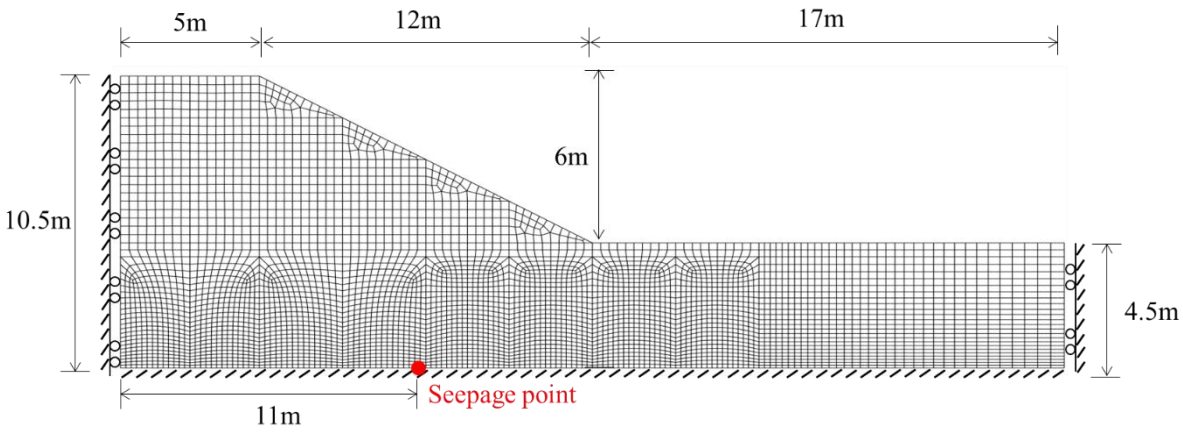

Figure 7.2 Diagram of FEM numerical model

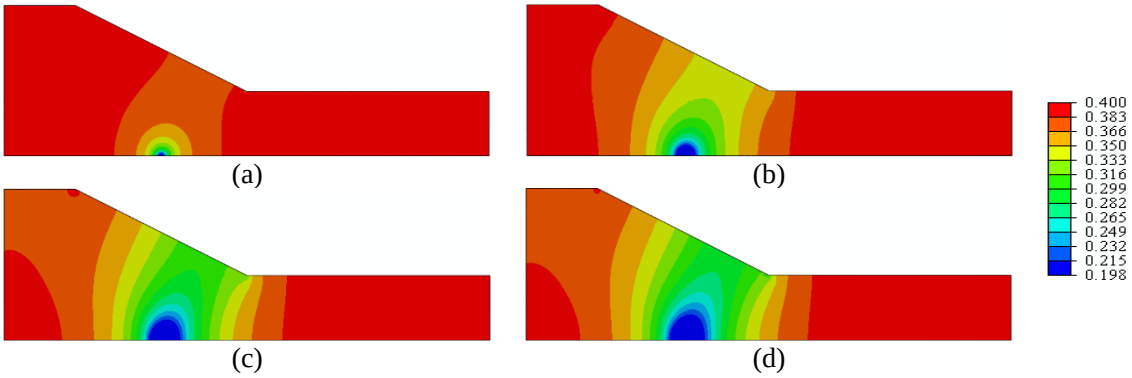

Figure 7.3 Variation of fine content f_c during erosion : (a) Day=150; (b) Day=250; (c) Day=300; (d) Day=350

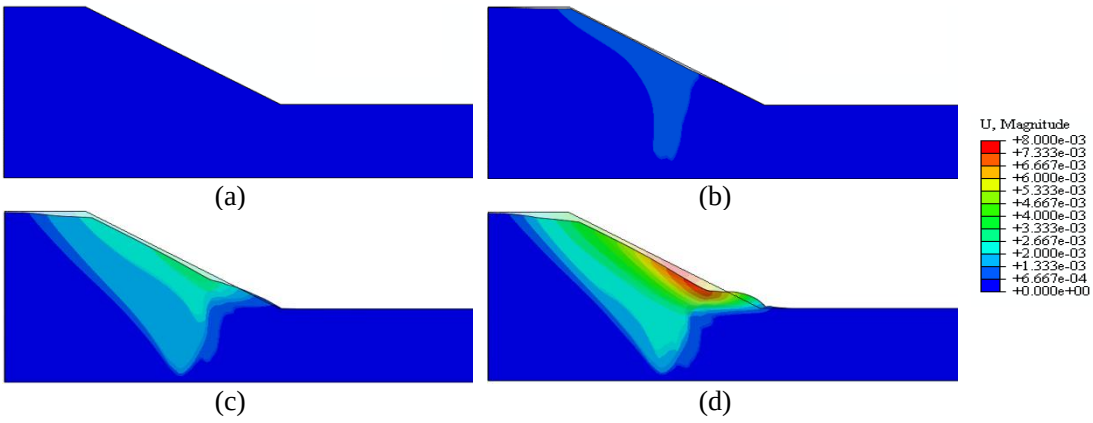

Figure 7.4 Variation in soil displacement during erosion (m) (Deformation amplification factor =250): (a) Day=150; (b) Day=250; (c) Day=300; (d) Day=350

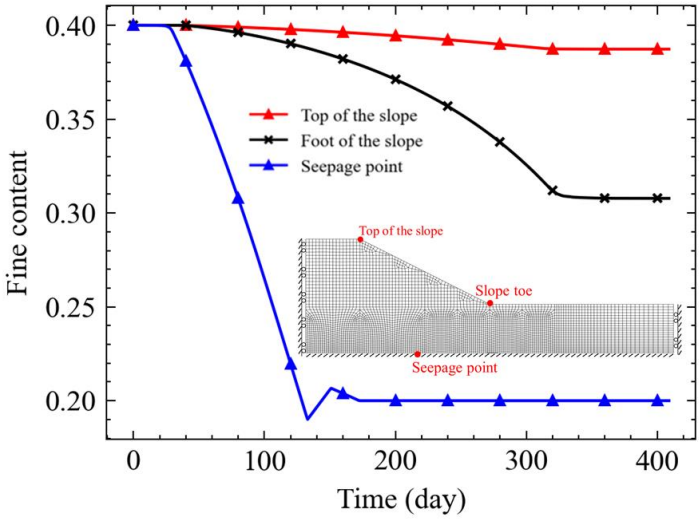

(a)

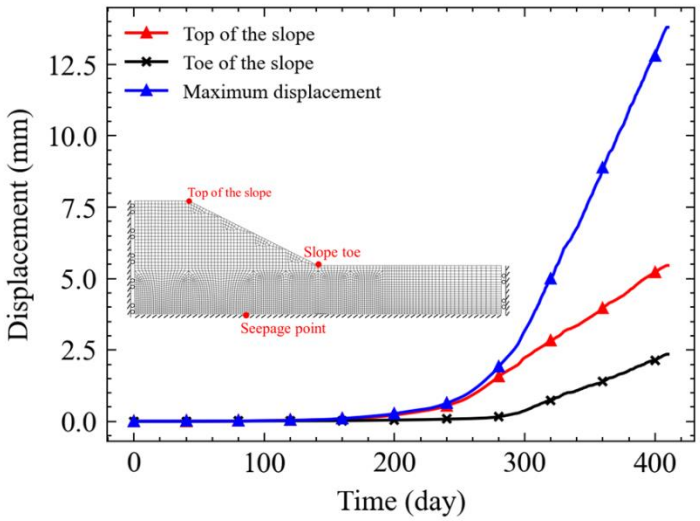

(b)

Figure 7.5 Changes in fine content and displacement at element nodes during erosion: (a) Fine content; (b) Displacement

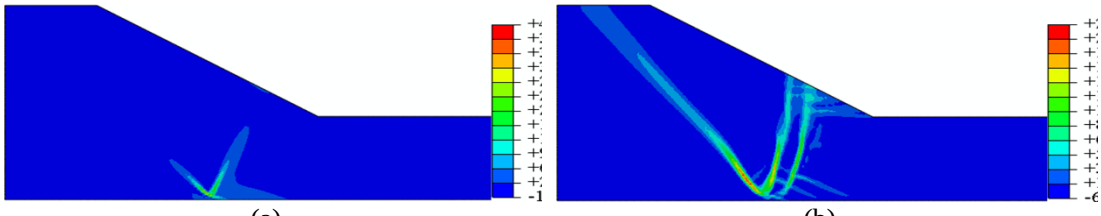

(a) (b)

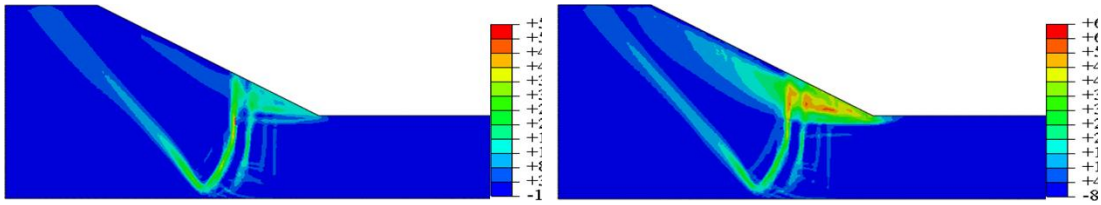

(c) (d)

Figure 7.6 Variation in shear strain during suffusion: (a) Day=150; (b) Day=250; (c) Day=300; (d) Day=350

CHAPTER 8 FINDINGS, CONCLUSIONS, AND RECOMMENDATIONS

8.1 Findings and conclusions

This study investigates internal erosion in sandy soils using a multiscale approach that integrates CFD-DEM and FEM methodologies. Within the framework of discrete media mechanics, the microscale CFD-DEM model was developed to investigate the effects of stress anisotropy and soil fabric anisotropy on erosion evolution. Subsequently, a mesoscopic CFD-DEM-FEM model was developed for tunnel seepage erosion simulations, examining the migration of particles and the mechanical response of the structure under varying operational conditions. To achieve the large-scale simulations for erosion in engineering problems, a stress-dependent erosion law was formulated based on CFD-DEM simulation results. This law was incorporated into a four-constituent porous media theory and integrated with an erosion-related constitutive model, thereby establishing a unified computational framework for coupled seepage-erosion-mechanics analysis. Further, the framework was implemented in ABAQUS through secondary development of a UEL subroutine, enabling simulations of internal erosion in foundation-dam systems. This approach successfully achieved a cross-scale linkage from microscopic particle interactions to macroscopic engineering behavior.

The main findings and recommendations for future research are summarized in the subsequent sections.

8.1.1 Effect of initial stress anisotropy on suffusion

The influence of stress anisotropy on soil erosion behavior was investigated at the RVE scale. Through CFD-DEM simulations, it was found that, compared to the initial isotropic stress state, samples with initial stress anisotropy experienced a significant increase in final mass loss. As particle loss occurred, the degree of initial stress anisotropy gradually decreased, approaching an isotropic state. The underlying microscopic mechanism can be attributed to the formation of a stable spatial isotropic stress structure. The turning point of the mass loss curve, along with the turning point on the particle surface velocity curve, could be used to define the critical hydraulic gradient. It was observed that the critical hydraulic gradient under the triaxial tension stress state was closer to that under the isotropic stress state but lower than that under the triaxial compression stress state. The microscopic mechanism behind this can be attributed to the alignment of the strong force chain network with the main direction of seepage in the triaxial compression stress state, which increased resistance to particle migration. Meanwhile, after applying seepage, the response of the coordination number under triaxial extension and isotropic compression stress states was greater than that under the triaxial compression stress state. This led to more fine particles detaching from coarse particles, resulting in a lower critical hydraulic gradient compared to triaxial compression.

8.1.2 Effect of initial fabric anisotropy on suffusion

The influence of natural sandy soil fabric anisotropy was investigated at the RVE scale through CFD-DEM simulations. The results demonstrated that as the bedding angle increased, the hindering effect of the coarse skeleton on fine particle migration diminished, resulting in greater mass loss in anisotropic soils. Meanwhile, both particle loss and soil strain increased as the bedding angle increased. Suffusion also led to an increase in the spatial distribution unevenness of fine particles, manifested as localized over-erosion and clogging of fine particles. During erosion, the compaction of coarse and fine particles changed differently. Fine particles became looser due to particle loss, while coarse particles became denser due to the increased external forces acting on them. Compared to the average void ratio, distinguishing between the void ratio in fine particles and that in coarse particles better reflected the changes between different components of gap-graded soil. Triaxial shear tests conducted on pre- and post-suffusion samples revealed that peak strength decreased with larger bedding angles, and fine particle loss further reduced soil strength. The initially anisotropic samples showed reduced fabric anisotropy during shear, whereas initially isotropic samples developed increasing anisotropy. The CFD-DEM simulations successfully calibrated material constants for erosion laws, establishing a link between microscale mechanisms and macroscopic predictions. Notably, fabric anisotropy showed negligible influence on these erosion law constants, suggesting its effects could be reasonably neglected when developing a new erosion law.

8.1.3 Soil-water-structure seepage erosion model

Internal erosion in tunnels was investigated at the meso-scale through a coupled CFD-DEM-FEM model. The results revealed that the evolution of seepage erosion could be classified into three modes based on tunnel crack width: stable mode, erosion-convergent mode, and erosion-divergent mode. As the crack location shifted from the tunnel crown to the invert, the amount of soil mass loss gradually decreased, with the least loss occurring when the crack was located at the bottom of the tunnel. Additionally, soil mass loss increased with both tunnel burial depth and rising groundwater levels.

In the early stages of seepage erosion, particle loss led to the formation of a soil arch, which temporarily supported the overburden pressure. The presence of soil arches delayed surface settlement relative to the loss of soil mass. However, with continued particle migration, the soil arch experienced progressive failure, accompanied by increasing surface subsidence. Wider cracks and higher groundwater levels significantly accelerated soil collapse, making the ground more susceptible to sudden settlement. Tunnel seepage erosion also altered the internal stress transmission mechanisms within the soil. Initially, the eroded particles bore part of the soil pressure load. As the soil arch effect developed, stress was redistributed toward the soil on both sides of the crack, resulting in a non-uniform horizontal distribution of effective stress, characterized by stress relaxation at the crack location and stress concentration on either side.

Increasing crack width and elevated groundwater levels exacerbated tunnel convergence deformation and tensile stress. Greater burial depth further intensified the convergence deformation around the tunnel waist, leading to a pronounced tensile stress state. Although soil mass loss decreased as the crack shifted from the tunnel crown to the invert, the structural constraints of the tunnel hindered stress transmission, ultimately resulting in more significant tunnel convergence deformation and the formation of a broader tensile stress zone.

8.1.4 Seepage-erosion-mechanics coupling framework

Based on observations from CFD-DEM numerical experiments, an erosion law for soil was developed that accounts for the effects of seepage velocity and stress state. This erosion law was incorporated into a four-constituent medium framework to simulate suffusion in sandy soils. The results demonstrated that an exponential function model effectively captures the mass loss induced by erosion under varying seepage velocities, mean stress levels, and stress ratios. The coupling between seepage, erosion, and mechanical behavior was achieved through the integration of the erosion law with constitutive mechanical models. The mechanical response influenced erosion primarily by affecting the fine particle loss rate and total mass loss, while erosion in turn impacted the mechanical behavior by modifying the critical state line of the soil.

The proposed framework successfully simulated mass loss evolution, deformation patterns, and permeability coefficient changes in representative element tests, with

validation results confirming the model's effectiveness. Parametric studies under different initial conditions showed the model's capability to capture mass loss variations with porosity, fine content, particle size ratio, and internal friction angle. Furthermore, mechanical response simulations showed that suffusion reduces the peak strength of initially dense specimens, while increasing the peak strength of initially loose specimens.

8.1.5 ABAQUS simulations for internal erosion

Based on a coupled seepage-erosion-mechanical numerical analysis framework, a continuum mechanics-based study was conducted to investigate suffusion in an engineering-scale dam. The framework was implemented through a user-defined element (UEL) subroutine in ABAQUS.

The numerical results demonstrated that foundation suffusion initiates at the seepage point and propagates toward the dam slope, with fine particle loss rates decreasing with distance from the seepage source. Surface settlement exhibited marked nonlinearity and hysteresis corresponding to variations in fine particle content. Progressive erosion induced continuous soil displacement until failure, with particle migration and pore enlargement increasing the soil's critical void ratio while reducing its shear strength. The failure mechanism analysis revealed that plastic shear strain initially localized near the seepage point, followed by gradual development of shear bands propagating toward both the slope crest and toe, ultimately leading to global slope instability.

8.2 Recommendations for future studies

This study presented a comprehensive multi-scale investigation of seepage-induced internal erosion in sandy soils, integrating microscopic and macroscopic analyses to establish fundamental erosion mechanisms and their engineering-scale consequences. However, some limitations exist, presenting opportunities for further development and improvement:

- While this study has systematically examined suffusion mechanisms through controlled single-factor analyses—such as stress anisotropy and fabric anisotropy—at small scales, the conclusions drawn under isolated conditions may be biased when multiple factors interact simultaneously. Future research should therefore focus on developing element-scale models that account for the coupled effects of multiple influencing factors to achieve a more comprehensive and realistic understanding of suffusion behavior.

- The mesoscale CFD–DEM–FEM framework developed in this study offers a simplified yet effective approach for investigating water–soil–structure interactions during seepage-induced erosion. However, it does not employ a fully bidirectional coupling scheme. The current implementation accounts for fluid–particle interactions (CFD–DEM coupling) and the influence of the fluid–particle system on structural response (CFD–DEM to FEM), but it neglects the feedback effects of structural deformation on particle dynamics and fluid flow (FEM to

DEM–CFD). This limitation highlights the need for future research to develop a fully coupled interaction scheme, which would enable more accurate and comprehensive simulations of erosion processes, particularly in scenarios where structural deformations significantly affect both granular behavior and seepage patterns.

- Although the proposed seepage–erosion–mechanical framework demonstrates satisfactory performance in simulating erosion evolution, both the erosion model and the mechanical model involve a large number of parameters, many of which are difficult to determine and calibrate. Future work could focus on developing simplified erosion and mechanical models that require fewer parameters, while still maintaining acceptable accuracy in simulation outcomes.

- With regard to the erosion criterion, this study successfully incorporated the effects of varying seepage velocities, mean stresses, and deviatoric stresses. However, the current criterion does not account for sample heterogeneity or particle clogging effects. Future work should therefore aim to improve the erosion criterion by incorporating the influence of soil heterogeneity, enabling a more realistic representation of erosion processes in natural soils.

- The work presented in this study is primarily centered on numerical theory and simulations, with limited support from laboratory experiments. Although the model

validation was performed through comparisons with experimental data reported in the literature, additional validation is necessary for practical engineering applications. Future research should therefore consider conducting laboratory experiments specifically designed to correspond with the numerical simulations, in order to enhance the reliability and applicability of the proposed models.

REFERENCES

Abate, G., Massimino, M.R., and Maugeri, M. 2015. Numerical modelling of centrifuge tests on tunnel–soil systems. Bulletin of Earthquake Engineering, **13**: 1927–1951. Springer.

Adhav, P., Besseron, X., and Peters, B. 2024. Development of 6-way CFD-DEM-FEM momentum coupling interface using partitioned coupling approach. Results in Engineering, **22**(April): 102214. Elsevier B.V. doi:10.1016/j.rineng.2024.102214.

Ahmed, A.A. 2013. Stochastic Analysis of Seepage under Hydraulic Structures Resting on Anisotropic Heterogeneous Soils. Journal of Geotechnical and Geoenvironmental Engineering, **139**(6): 1001–1004. doi:10.1061/(ASCE)GT.1943-5606.0000813.

Ai, J., Chen, J.-F., Rotter, J.M., and Ooi, J.Y. 2011. Assessment of rolling resistance models in discrete element simulations. Powder Technology, **206**(3): 269–282. Elsevier.

Al-Saigh, N.H., Mohammed, Z.S., and Dahham, M.S. 1994. Detection of water leakage from dams by self-potential method. Engineering Geology, **37**(2): 115–121. Elsevier.

Albaba, A., Schwarz, M., Wendeler, C., Loup, B., and Dorren, L. 2019. Numerical modeling using an elastoplastic-adhesive discrete element code for simulating hillslope debris flows and calibration against field experiments. Natural Hazards

and Earth System Sciences, **19**(11): 2339–2358. Copernicus GmbH.

Alobaid, F., Baraki, N., and Epple, B. 2014. Investigation into improving the efficiency and accuracy of CFD/DEM simulations. Particuology, **16**: 41–53. Elsevier.

Anandarajah, A., and Kuganenthira, N. 1995. Some aspects of fabric anisotropy of soil. Geotechnique, **45**(1): 69–81. Thomas Telford Ltd.

Azadbakht, S., Nouri, A., and Chan, D. 2020. An analytical model for estimation of internal erosion rate. Geomechanics and geoengineering: an international journal, **15**(1): 42–53. Taylor & Francis. doi:10.1080/17486025.2019.1602735.

Barrett, P.J. 1980. The shape of rock particles, a critical review. Sedimentology, **27**(3): 291–303. Wiley Online Library.

Biarez, J., and Hicher, P.-Y. 1994. Elementary mechanics of soil behaviour: saturated remoulded soils.

de Boer, R. 2000. Contemporary progress in porous media theory. Applied Mechanics Reviews, **53**(12): 323–70.

Brosh, T., Kalman, H., and Levy, A. 2014. Accelerating CFD–DEM simulation of processes with wide particle size distributions. Particuology, **12**: 113–121. Elsevier.

Burenkova, V. V. 1993. Assessment of suffusion in non-cohesive and graded soils. Filters in geotechnical and hydraulic engineering. Balkema, Rotterdam,: 357–360.

Chand, R., Khaskheli, M.A., Qadir, A., Ge, B., and Shi, Q. 2012. Discrete particle

simulation of radial segregation in horizontally rotating drum: Effects of drum-length and non-rotating end-plates. Physica A: Statistical Mechanics and its Applications, **391**(20): 4590–4596. doi:https://doi.org/10.1016/j.physa.2012.05.019.

Chang, D.S. 2012. Internal erosion and overtopping erosion of earth dams and landslide dams. Hong Kong University of Science and Technology,Hong Kong.

Chang, D.S., and Zhang, L. 2011. A stress-controlled erosion apparatus for studying internal erosion in soils. Geotechnical Testing Journal, **34**(6): 1–11. doi:10.1520/GTJ103889.

Chang, D.S., and Zhang, L.M. 2013a. Extended internal stability criteria for soils under seepage. Soils and Foundations, **53(4)**: 569–583. doi:10.1016/j.sandf.2013.06.008.

Chang, D.S., and Zhang, L.M. 2013b. Critical Hydraulic Gradients of Internal Erosion under Complex Stress States. Journal of Geotechnical and Geoenvironmental Engineering, **139**(9): 1454–1467. doi:10.1061/(asce)gt.1943-5606.0000871.

Chaplot, V. 2013. Impact of terrain attributes, parent material and soil types on gully erosion. Geomorphology, **186**: 1–11. Elsevier B.V. doi:10.1016/j.geomorph.2012.10.031.

Chen, F., Jiang, S., Xiong, H., Yin, Z. yu, and Chen, X. 2023a. Micro pore analysis of suffusion in filter layer using tri-layer CFD–DEM model. Computers and Geotechnics, **156**(March): 105303. Elsevier Ltd. doi:10.1016/j.compgeo.2023.105303.

Chen, F., Xiong, H., Wang, X., and Yin, Z.-Y. 2023b. Transmission effect of eroded particles in suffusion using the CFD-DEM coupling method. Acta Geotechnica, **18**(1): 335–354. doi:10.1007/s11440-022-01568-8.

Cheng, K., Wang, Y., and Yang, Q. 2018. A semi-resolved CFD-DEM model for seepage-induced fine particle migration in gap-graded soils. Computers and Geotechnics, **100**: 30–51. Elsevier.

Cheng, K., Zhang, C., Peng, K., Liu, H., and Ahmad, M. 2021. Un-resolved CFD-DEM method: An insight into its limitations in the modelling of suffusion in gap-graded soils. Powder Technology, **381**: 520–538. Elsevier B.V. doi:10.1016/j.powtec.2020.12.034.

Cheng, W.-C., Li, G., Liu, N., Xu, J., and Horpibulsuk, S. 2020. Recent massive incidents for subway construction in soft alluvial deposits of Taiwan: a review. Tunnelling and Underground Space Technology, **96**: 103178. Elsevier.

Chhabra, R.P., Agarwal, L., and Sinha, N.K. 1999. Drag on non-spherical particles: An evaluation of available methods. Powder Technology,. doi:10.1016/S0032-5910(98)00178-8.

Cividini, A., Bonomi, S., Vignati, G.C., and Gioda, G. 2009. Seepage-induced erosion in granular soil and consequent settlements. International Journal of Geomechanics, **9**(4): 187–194. American Society of Civil Engineers.

Cividini, A., and Gioda, G. 2004. Finite-Element Approach to the Erosion and Transport of Fine Particles in Granular Soils. International Journal of Geomechanics,. doi:10.1061/(asce)1532-3641(2004)4:3(191).

Crosta, G., and Prisco, C. di. 1999. On slope instability induced by seepage erosion. Canadian Geotechnical Journal, **36**(6): 1056–1073. NRC Research Press Ottawa, Canada.

Cundall, P.A., and Strack, O.D.L. 1979. A discrete numerical model for granular assemblies. Geotechnique,. doi:10.1680/geot.1979.29.1.47.

Davies, J.P., Clarke, B.A., Whiter, J.T., and Cunningham, R.J. 2001. Factors influencing the structural deterioration and collapse of rigid sewer pipes. Urban water, **3**(1–2): 73–89. Elsevier.

Dehnen, W., and Aly, H. 2012. Improving convergence in smoothed particle hydrodynamics simulations without pairing instability. Monthly Notices of the Royal Astronomical Society, **425**(2): 1068–1082. Blackwell Science Ltd Oxford, UK.

Deng, Z., Wang, G., Jin, W., Tang, N., Ren, H., and Chen, X. 2023. Characteristics and quantification of fine particle loss in internally unstable sandy gravels induced by seepage flow. Engineering Geology, **321**: 107150. Elsevier B.V. doi:10.1016/j.enggeo.2023.107150.

Ergun, S. 1952. Fluid flow through packed columns. Chem. Eng. Prog., **48**: 89–94. doi:citeulike-article-id:7797897.

Fannin, R.J., and Moffat, R. 2006. Observations on internal stability of cohesionless soils. Geotechnique, **56(7)**(7): 497–500. doi:10.1680/geot.2006.56.7.497.

Fell, R., and Fry, J.-J. 2007. The state of the art of assessing the likelihood of internal erosion of embankment dams, water retaining structures and their foundations. *In*

Internal erosion of dams and their foundations. CRC Press. pp. 9–32.

Foster, M., Fell, R., and Spannagle, M. 2000. The statistics of embankment dam failures and accidents. Canadian Geotechnical Journal, **37(5)**: 1000–1024. doi:10.1139/t00-030.

Fu, Y., Zeng, D., Xiong, H., Li, X., and Chen, Y. 2022. Seepage effect on failure mechanisms of the underwater tunnel face via CFD–DEM coupling. Computers and Geotechnics, **146**(December 2021). Elsevier Ltd. doi:10.1016/j.compgeo.2021.104591.

Gan, Z., Qian, J., and Lyu, Z. 2021. Dynamic responses of multilayered poroelastic ground under moving train loads considering effects of track irregularity. Transportation Geotechnics, **31**: 100660. Elsevier.

Gao, C. lu, Zhou, Z. qing, Yang, W. min, Lin, C. jin, Li, L. ping, and Wang, J. 2019. Model test and numerical simulation research of water leakage in operating tunnels passing through intersecting faults. Tunnelling and Underground Space Technology, **94**(July): 103134. Elsevier. doi:10.1016/j.tust.2019.103134.

Golshan, S., Sotudeh-Gharebagh, R., Zarghami, R., Mostoufi, N., Blais, B., and Kuipers, J.A.M. 2020. Review and implementation of CFD-DEM applied to chemical process systems. Chemical Engineering Science, **221**: 115646. Elsevier Ltd. doi:10.1016/j.ces.2020.115646.

Gong, J., Nie, Z., Zhu, Y., Liang, Z., and Wang, X. 2019. Exploring the effects of particle shape and content of fines on the shear behavior of sand-fines mixtures via the DEM. Computers and Geotechnics, **106**(October 2018): 161–176.

Elsevier. doi:10.1016/j.compgeo.2018.10.021.

Gu, D.M., Huang, D., Liu, H.L., Zhang, W.G., and Gao, X.C. 2019. A DEM-based approach for modeling the evolution process of seepage-induced erosion in clayey sand. Acta Geotechnica, **14**: 1629–1641. Springer.

Guo, N., and Zhao, J. 2016. Parallel hierarchical multiscale modelling of hydro-mechanical problems for saturated granular soils. Computer Methods in Applied Mechanics and Engineering, **305**: 37–61. Elsevier B.V. doi:10.1016/j.cma.2016.03.004.

Hu, G., Zhou, B., Yang, B., Wang, H., and Liu, Z. 2023. An insight into the interaction between fluid and granular soil based on a resolved CFD-DEM method. Computers and Geotechnics, **163**: 105722. Elsevier.

Hu, Z., Yang, Z.X., and Zhang, Y.D. 2020a. CFD-DEM modeling of suffusion effect on undrained behavior of internally unstable soils. Computers and Geotechnics, **126**. doi:10.1016/j.compgeo.2020.103692.

Hu, Z., Zhang, Y., and Yang, Z. 2019. Suffusion-induced deformation and microstructural change of granular soils: a coupled CFD–DEM study. Acta Geotechnica, **14**(3): 795–814. Springer Berlin Heidelberg. doi:10.1007/s11440-019-00789-8.

Hu, Z., Zhang, Y., and Yang, Z. 2020b. Suffusion-Induced Evolution of Mechanical and Microstructural Properties of Gap-Graded Soils Using CFD-DEM. Journal of Geotechnical and Geoenvironmental Engineering, **146**(5): 04020024. doi:10.1061/(asce)gt.1943-5606.0002245.

Huangfu, M., Wang, M.-S., Tan, Z.-S., and Wang, X.-Y. 2010. Analytical solutions for steady seepage into an underwater circular tunnel. Tunnelling and Underground Space Technology, **25**(4): 391–396. Elsevier.

Ibrahim, A., and Meguid, M.A. 2023. CFD-DEM simulation of sand erosion into defective gravity pipes under constant groundwater table. Tunnelling and Underground Space Technology, **131**(November 2021): 104823. Elsevier Ltd. doi:10.1016/j.tust.2022.104823.

Indraratna, B., Phan, N.M., Nguyen, T.T., and Huang, J. 2021. Simulating Subgrade Soil Fluidization Using LBM-DEM Coupling. International Journal of Geomechanics, **21**(5): 1–14. doi:10.1061/(asce)gm.1943-5622.0001997.

Ishii, M., and Mishima, K. 1984. Two-fluid model and hydrodynamic constitutive relations. Nuclear Engineering and design, **82**(2–3): 107–126. Elsevier.

Israr, J., and Indraratna, B. 2017. Internal Stability of Granular Filters under Static and Cyclic Loading. Journal of Geotechnical and Geoenvironmental Engineering, **143**(6): 04017012. doi:10.1061/(asce)gt.1943-5606.0001661.

Iwashita, K., and Oda, M. 1998. Rolling resistance at contacts in simulation of shear band development by DEM. Journal of engineering mechanics, **124**(3): 285–292. American Society of Civil Engineers.

Jäger, R., Mendoza, M., and Herrmann, H.J. 2017. Channelization in porous media driven by erosion and deposition. Physical Review E, **95**(1): 13110. APS.

Jensen, R.P., Bosscher, P.J., Plesha, M.E., and Edil, T.B. 1999. DEM simulation of granular media-structure interface: Effects of surface roughness and particle

shape. International Journal for Numerical and Analytical Methods in Geomechanics, **23**(6): 531–547.

Jiang, M., and Yin, Z.-Y. 2012. Analysis of stress redistribution in soil and earth pressure on tunnel lining using the discrete element method. Tunnelling and Underground Space Technology, **32**: 251–259. Elsevier.

Jing, L., Kwok, C.Y., Leung, Y.F., and Sobral, Y.D. 2016. Extended CFD–DEM for free-surface flow with multi-size granules. International Journal for Numerical and Analytical Methods in Geomechanics, **40**(1): 62–79. Wiley Online Library.

Ke, L., and Takahashi, A. 2014a. Experimental investigations on suffusion characteristics and its mechanical consequences on saturated cohesionless soil. Soils and Foundations, **54**(4): 713–730. Elsevier. doi:10.1016/j.sandf.2014.06.024.

Ke, L., and Takahashi, A. 2014b. Triaxial erosion test for evaluation of mechanical consequences of internal erosion. Geotechnical Testing Journal, **37**(2). doi:10.1520/GTJ20130049.

Ke, L., and Takahashi, A. 2014c. Experimental investigations on suffusion characteristics and its mechanical consequences on saturated cohesionless soil. Soils and Foundations, **54**(4): 713–730. Japanese Geotechnical Society. doi:10.1016/j.sandf.2014.06.024.

Kenney, T.C., and Lau, D. 1985. Internal stability of granular filters. Canadian Geotechnical Journal,. doi:10.1139/t85-029.

Khalil, T., Saiyouri, N., Muresan, B., and Hicher, P. 2013. Internal erosion of

chemically reinforced granular materials: a mathematical modeling approach. International journal for numerical and analytical methods in geomechanics, **37**(5): 491–502. Wiley Online Library.

Kloss, C., Goniva, C., Hager, A., Amberger, S., and Pirker, S. 2012. Models, algorithms and validation for opensource DEM and CFD-DEM. Progress in Computational Fluid Dynamics, **12**(2–3): 140–152. doi:10.1504/PCFD.2012.047457.

Kong, Y., Li, X., and Zhao, J. 2021. Quantifying the transition of impact mechanisms of geophysical flows against flexible barrier. Engineering Geology, **289**: 106188. Elsevier.

Korff, M., Mair, R.J., Van Tol, A.F., and Kaalberg, F. 2011. Building damage and repair due to leakage in a deep excavation. Proceedings of the Institution of Civil Engineers-Forensic Engineering, **164**(4): 165–177. Thomas Telford Ltd.

Lei, X., He, S., Chen, X., Wong, H., Wu, L., and Liu, E. 2020. A generalized interpolation material point method for modelling coupled seepage-erosion-deformation process within unsaturated soils. Advances in Water Resources, **141**(September 2019): 103578. Elsevier Ltd. doi:10.1016/j.advwatres.2020.103578.

Leung, C., and Meguid, M.A. 2011. An experimental study of the effect of local contact loss on the earth pressure distribution on existing tunnel linings. Tunnelling and Underground Space Technology incorporating Trenchless Technology Research, **26**(1): 139–145. Elsevier Ltd.

doi:10.1016/j.tust.2010.08.003.

Li, X.-S., and Wang, Y. 1998. Linear representation of steady-state line for sand. Journal of geotechnical and geoenvironmental engineering, **124**(12): 1215–1217. American Society of Civil Engineers.

Liang, W., Zhao, S., Wu, H., and Zhao, J. 2021. Bearing capacity and failure of footing on anisotropic soil: A multiscale perspective. Computers and Geotechnics, **137**(March): 104279. Elsevier Ltd. doi:10.1016/j.compgeo.2021.104279.

Liang, Y., Yeh, T.C.J., Wang, J., Liu, M., Zha, Y., and Hao, Y. 2019. Onset of suffusion in upward seepage under isotropic and anisotropic stress conditions. European Journal of Environmental and Civil Engineering, **23**(12): 1520–1534. Taylor & Francis. doi:10.1080/19648189.2017.1359110.

Liang, Y., Yeh, T.J., Wang, Y., Liu, M., Wang, J., and Hao, Y. 2017a. Numerical simulation of backward erosion piping in heterogeneous fields. Water Resources Research, **53**(4): 3246–3261. Wiley Online Library.

Liang, Y., Zeng, C., Wang, J.-J., Liu, M.-W., Yeh, T.-C.J., and Zha, Y.-Y. 2017b. Constant gradient erosion apparatus for appraisal of piping behavior in upward seepage flow. Geotechnical Testing Journal, **40**(4): 630–642. ASTM International.

Liao, S.-M., Liu, J.-H., Wang, R.-L., and Li, Z.-M. 2009. Shield tunneling and environment protection in Shanghai soft ground. Tunnelling and Underground Space Technology, **24**(4): 454–465. Elsevier.

Liu, Q.-W., Chen, R.-P., Wang, H.-L., Yin, Z.-Y., and Wu, H.-N. 2022a. Effect of particle shape on soil arching in the pile-supported embankment by 3D discrete-element method simulation. International Journal of Geomechanics, **22**(4): 4022027. American Society of Civil Engineers.

Liu, Q.-W., Wang, H.-L., Chen, R.-P., Yin, Z.-Y., Lin, X.-T., and Wu, H.-N. 2022b. Effect of relative density of 2D granular materials on the arching effect through numerical trapdoor tests. Computers and Geotechnics, **141**: 104553. Elsevier.

Liu, Y., Wang, L., Hong, Y., Zhao, J., and Yin, Z.Y. 2020. A coupled CFD-DEM investigation of suffusion of gap graded soil: Coupling effect of confining pressure and fines content. International Journal for Numerical and Analytical Methods in Geomechanics, **44**(18): 2473–2500. doi:10.1002/nag.3151.

Liu, Y., Wang, L., Yin, Z.Y., and Hong, Y. 2023a. Micromechanical investigation of suffusion and its consequence in gap-graded granular soil at the opening of underground structures using the coupled CFD-DEM method. Computers and Geotechnics, **158**(March): 105395. Elsevier Ltd. doi:10.1016/j.compgeo.2023.105395.

Liu, Y., Wang, L., Yin, Z.Y., and Hong, Y. 2023b. A coupled CFD-DEM investigation into suffusion of gap-graded soil considering anisotropic stress conditions and flow directions. Acta Geotechnica, **18**(6): 3111–3132. Springer Berlin Heidelberg. doi:10.1007/s11440-022-01734-y.

Liu, Y., and Yin, Z. 2024. Suffusion of irregular concave gap-graded sand with resolved CFD-DEM. Canadian Geotechnical Journal,.

Liu, Y., Yin, Z.Y., Wang, L., and Hong, Y. 2021. A coupled cfd–dem investigation of internal erosion considering suspension flow. Canadian Geotechnical Journal, **58**(9): 1411–1425. doi:10.1139/cgj-2020-0099.

Lu, H., and Gidaspow, D. 2003. Hydrodynamics of binary fluidization in a riser: CFD simulation using two granular temperatures. Chemical Engineering Science, **58**(16): 3777–3792. doi:10.1016/S0009-2509(03)00238-0.

Lü, X., Zeng, S., Zhao, Y., Huang, M., Ma, S., and Zhang, Z. 2020. Physical model tests and discrete element simulation of shield tunnel face stability in anisotropic granular media. Acta Geotechnica, **15**(10): 3017–3026. Springer.

Luo, Y., Luo, B., and Xiao, M. 2020. Effect of deviator stress on the initiation of suffusion. Acta Geotechnica, **15**(6): 1607–1617. Springer Berlin Heidelberg. doi:10.1007/s11440-019-00859-x.

Ma, Q., Wautier, A., and Zhou, W. 2021. Microscopic mechanism of particle detachment in granular materials subjected to suffusion in anisotropic stress states. Acta Geotechnica, **16**(8): 2575–2591. Springer Berlin Heidelberg. doi:10.1007/s11440-021-01301-x.

Mao, Y., Kong, Y., and Guan, M. 2022. GPU-accelerated SPH modeling of flow-driven sediment erosion with different rheological models and yield criteria. Powder Technology, **412**: 118015. Elsevier.

Markauskas, D., Kruggel-Emden, H., and Scherer, V. 2018. Numerical analysis of wet plastic particle separation using a coupled DEM-SPH method. Powder Technology, **325**: 218–227. Elsevier B.V. doi:10.1016/j.powtec.2017.11.021.

Marot, D., Le, V.D., Garnier, J., Thorel, L., and Audrain, P. 2012. Study of scale effect in an internal erosion mechanism: Centrifuge model and energy analysis. European Journal of Environmental and Civil Engineering, **16**(1): 1–19. doi:10.1080/19648189.2012.667203.

Marshall, A.M., Elkayam, I., Klar, A., and Mair, R.J. 2010. Centrifuge and discrete element modelling of tunnelling effects on pipelines. *In* Proceedings of the 7th International Conference on Physical Modelling in Geotechnics. pp. 633–637.

Meguid, M.A., and Dang, H.K. 2009. The effect of erosion voids on existing tunnel linings. Tunnelling and Underground Space Technology, **24**(3): 278–286. Elsevier.

Mei, R. 1992. An approximate expression for the shear lift force on a spherical particle at finite reynolds number. International Journal of Multiphase Flow, **18**(1): 145–147. doi:10.1016/0301-9322(92)90012-6.

Midgley, T.L., Fox, G.A., Wilson, G. V, Heeren, D.M., Langendoen, E.J., and Simon, A. 2013. Seepage-induced streambank erosion and instability: in situ constant-head experiments. Journal of Hydrologic Engineering, **18**(10): 1200–1210. American Society of Civil Engineers.

Moffat, R., and Fannin, R.J. 2011. A hydromechanical relation governing internal stability of cohesionless soil. Canadian Geotechnical Journal, **48**(3): 413–424.

Mu, L., Zhang, P., Shi, Z., and Huang, M. 2023. Coupled CFD–DEM Investigation of Erosion Accompanied by Clogging Mechanism under Different Hydraulic Gradients. Computers and Geotechnics, **153**(May 2022): 105058. Elsevier Ltd.

doi:10.1016/j.compgeo.2022.105058.

Mukunok, T., Kumano, N., Otan, J., and Kuwano, R. 2009. Visualization of three dimensional failure in sand due to water inflow and soil drainage from defective underground pipe using x-ray CT. Soils and Foundations, **49**(6): 959–968. doi:10.3208/sandf.49.959.

Nguyen, H.B.K., Rahman, M.M., and Fourie, A.B. 2020. Effect of Particle Shape on Constitutive Relation: DEM Study. Journal of Geotechnical and Geoenvironmental Engineering, **146**(7): 04020058. doi:10.1061/(asce)gt.1943-5606.0002278.

Nguyen, T.T., and Indraratna, B. 2020. A Coupled CFD–DEM Approach to Examine the Hydraulic Critical State of Soil under Increasing Hydraulic Gradient. International Journal of Geomechanics, **20**(9): 04020138. doi:10.1061/(asce)gm.1943-5622.0001782.

Oda, M. 1972. Initial fabrics and their relations to mechanical properties of granular material. Soils and foundations, **12**(1): 17–36. The Japanese Geotechnical Society.

Papamichos, E., Vardoulakis, I., Tronvoll, J., and Skjrstein, A. 2001. Volumetric sand production model and experiment. International Journal for Numerical and Analytical Methods in Geomechanics, **25**(8): 789–808. doi:10.1002/nag.154.

Park, K.-H., Owatsiriwong, A., and Lee, J.-G. 2008. Analytical solution for steady-state groundwater inflow into a drained circular tunnel in a semi-infinite aquifer: A revisit. Tunnelling and Underground Space Technology, **23**(2): 206–209.

Elsevier.

Pegah, E., Gu, X., and Liu, H. 2024. Fabric anisotropy of granular soils and its dependency on grading and particles specifications. Acta Geotechnica, **19**(11): 7619–7633. Springer.

Peng, S., Huang, W., Luo, G., Cao, H., and Pan, H. 2023. Failure mechanisms of ground collapse caused by shield tunnelling in water-rich composite sandy stratum: A case study. Engineering Failure Analysis, **146**(February): 107100. Elsevier Ltd. doi:10.1016/j.engfailanal.2023.107100.

Peng, Y., Ding, X., Xiao, Y., Deng, X., and Deng, W. 2020. Detailed amount of particle breakage in nonuniformly graded sands under one-dimensional compression. Canadian Geotechnical Journal, **57**(8): 1239–1246. NRC Research Press 1840 Woodward Drive, Suite 1, Ottawa, ON K2C 0P7.

Peng, Y., Liu, H., Li, C., Ding, X., Deng, X., and Wang, C. 2021. The detailed particle breakage around the pile in coral sand. Acta Geotechnica, **16**(6): 1971–1981. Springer.

Qian, J.G., Li Weiyi, Yin, Z.Y., and Yang, Y. 2021a. Influences of buried depth and grain size distribution on seepage erosion in granular soils around tunnel by coupled CFD-DEM approach. Transportation Geotechnics, **29**: 100574. doi:10.1016/j.trgeo.2021.100574.

Qian, J.G., Zhou, C., Yin, Z.Y., and Li, W.Y. 2021b. Investigating the effect of particle angularity on suffusion of gap-graded soil using coupled CFD-DEM. Computers and Geotechnics, **139**: 104383. doi:10.1016/j.compgeo.2021.104383.

Qin, T., Song, Z., Wang, C., and Liang, F. 2025. Two-point MPM study of fluidized grains in internal erosion around metro tunnel characterized by an erosion law. Computers and Geotechnics, **183**: 107227. Elsevier.

Rafid, A. 2016. Evaluation of the impact of a cavity upon an earth dike (analytical and numerical approaches).

Reddi, L.N., Xiao, M., Hajra, M.G., and Lee, I.M. 2005. Physical clogging of soil filters under constant flow rate versus constant head. Canadian Geotechnical Journal, **42**(3): 804–811.

Revil, A., and Cathles Iii, L.M. 1999. Permeability of shaly sands. Water Resources Research, **35**(3): 651–662. Wiley Online Library.

Richart, F.E., Hall, J.R., and Woods, R.D. 1970. Vibrations of soils and foundations.

Rochim, A., Ph, D., Marot, D., Sibille, L., Ph, D., and Le, V.T. 2015. Effects of Hydraulic Loading History on Suffusion Susceptibility of Cohesionless Soils. : 1–10. doi:10.1061/(ASCE)GT.1943-5606.0001673.

Roscoe, K., and Burland, J.B. 1968. On the generalized stress-strain behaviour of wet clay.

Sakaguchi, H., Nishiura, D., and Yamamoto, S. 2018. Multibillion particle DEM to simulate centrifuge model tests of geomaterials. *In* Physical Modelling in Geotechnics. CRC Press. pp. 227–232.

Sato, M., and Kuwano, R. 2015. Influence of location of subsurface structures on development of underground cavities induced by internal erosion. Soils and Foundations, **55**(4): 829–840. Elsevier. doi:10.1016/j.sandf.2015.06.014.

Schaufler, A., Becker, C., and Steeb, H. 2013. Infiltration processes in cohesionless soils. ZAMM-Journal of Applied Mathematics and Mechanics/Zeitschrift für Angewandte Mathematik und Mechanik, **93**(2-3): 138–146. Wiley Online Library.

El Shamy, U., and Sizkow, S.F. 2021. Coupled SPH-DEM simulations of liquefaction-induced flow failure. Soil Dynamics and Earthquake Engineering, **144**(November 2020): 106683. Elsevier Ltd. doi:10.1016/j.soildyn.2021.106683.

Shen, W., Peng, J., Qiao, Z., Li, T., Li, P., Sun, X., Chen, Y., and Li, J. 2024. Plowing mechanism of rapid flow-like loess landslides: Insights from MPM modeling. Engineering Geology, **335**: 107532. Elsevier.

Shen, Z., Wang, G., Huang, D., and Jin, F. 2022. A resolved CFD-DEM coupling model for modeling two-phase fluids interaction with irregularly shaped particles. Journal of Computational Physics, **448**: 110695. Elsevier Inc. doi:10.1016/j.jcp.2021.110695.

Sheorey, P.R., Loui, J.P., Singh, K.B., and Singh, S.K. 2000. Ground subsidence observations and a modified influence function method for complete subsidence prediction. International Journal of Rock Mechanics and Mining Sciences, **37**(5): 801–818. Elsevier.

Shin, J.H., Lee, I.K., Lee, Y.H., and Shin, H.S. 2006. Lessons from serial tunnel collapses during construction of the Seoul subway Line 5. Tunnelling and Underground Space Technology incorporating Trenchless Technology Research, **21**(3): 296–297.

Shire, T., O'Sullivan, C., Hanley, K.J., and Fannin, R.J. 2014. Fabric and Effective Stress Distribution in Internally Unstable Soils. Journal of Geotechnical and Geoenvironmental Engineering,. doi:10.1061/(asce)gt.1943-5606.0001184.

Skempton, A.W., and Brogan, J.M. 1994. Experiments on piping in sandy gravels. Geotechnique, **44**(3): 449–460. doi:10.1680/geot.1994.44.3.449.

Song, S.X., Yin, Z.Y., Liu, Y.J., Wang, P., and Cheng, Y.P. 2024. Investigation of Suffusion Under Torsional Shear Conditions With CFD-DEM. International Journal for Numerical and Analytical Methods in Geomechanics,: 4274–4290. doi:10.1002/nag.3844.

Steeb, H., Diebels, S., and Vardoulakis, I. 2007. Modeling internal erosion in porous media. *In* Computer Applications In Geotechnical Engineering. pp. 1–10.

Sterpi, D. 2003. Effects of the Erosion and Transport of Fine Particles due to Seepage Flow. International Journal of Geomechanics, **3**(1): 111–122. doi:10.1061/(asce)1532-3641(2003)3:1(111).

Stipić, D., Budinski, L., and Fabian, J. 2022. Sediment transport and morphological changes in shallow flows modelled with the lattice Boltzmann method. Journal of Hydrology, **606**: 127472. Elsevier.

Sun, X., Sakai, M., and Yamada, Y. 2013. Three-dimensional simulation of a solid–liquid flow by the DEM–SPH method. Journal of Computational Physics, **248**: 147–176. Elsevier.

Taha, H., Nguyen, N.S., Marot, D., Hijazi, A., and Abou-Saleh, K. 2019. Micro-scale investigation of the role of finer grains in the behavior of bidisperse granular

materials. Granular Matter, **21**(2): 1–17. Springer Berlin Heidelberg. doi:10.1007/s10035-019-0867-9.

Tang, Z., Gong, H., Wu, S., Zeng, Z., Wang, Z., Zhou, Y., Fu, D., Liu, C., Cai, Y., and Qi, L. 2023. Modelling of paddy soil using the CFD-DEM coupling method. Soil and Tillage Research, **226**: 105591. Elsevier.

Terzaghi, K. 1925. Erdbaumechanik auf bodenphysikalischer Grundlage. F. Deuticke.

Thevanayagam, S., and Mohan, S. 2000. Intergranular state variables and stress-strain behaviour of silty sands. Geotechnique, **50**(1): 1–23. doi:10.1680/geot.2000.50.1.1.

Tucker, G.E. 2004. Drainage basin sensitivity to tectonic and climatic forcing: Implications of a stochastic model for the role of entrainment and erosion thresholds. Earth Surface Processes and Landforms, **29**(2): 185–205. Wiley Online Library.

Uzuoka, R., and Borja, R.I. 2012. Dynamics of unsaturated poroelastic solids at finite strain. International Journal for Numerical and Analytical Methods in Geomechanics, **36**(13): 1535–1573. Wiley Online Library.

Uzuoka, R., Ichiyama, T., Mori, T., and Kazama, M. 2012. Hydro-mechanical analysis of internal erosion with mass exchange between solid and water. *In* Proceedings of 6th international conference on scour and erosion, Paris. pp. 655–662.

Vardoulakis, I., Stavropoulou, M., and Papanastasiou, P. 1996. Hydro-mechanical aspects of the sand production problem. Transport in porous media, **22**: 225–244.

Springer.

Wan, C.F., and Fell, R. 2008. Assessing the Potential of Internal Instability and Suffusion in Embankment Dams and Their Foundations. Journal of Geotechnical and Geoenvironmental Engineering, **134**(3): 401–407. doi:10.1061/(asce)1090-0241(2008)134:3(401).

Wang, P., Karatza, Z., and Arson, C. 2019. DEM modelling of sequential fragmentation of zeolite granules under oedometric compression based on XCT observations. Powder Technology, **347**: 66–75. Elsevier B.V. doi:10.1016/j.powtec.2019.02.050.

Wang, T., Wang, P., and Yin, Z.-Y. 2024. Numerical analysis of suffusion behavior under cyclic loadingwith coupled cfd-dem simulation. International Journal for Multiscale Computational Engineering, **22**(2). Begel House Inc.

Wang, X., Huang, B., Tang, Y., Hu, T., and Ling, D. 2022. Microscopic mechanism and analytical modeling of seepage-induced erosion in bimodal soils. Computers and Geotechnics, **141**: 104527. Elsevier Ltd. doi:10.1016/j.compgeo.2021.104527.

Wen, C.Y., and Yu, Y.H. 1966. A generalized method for predicting the minimum fluidization velocity. AIChE Journal, **12**(3): 610–612. doi:10.1002/aic.690120343.

Wu, Z. 2019. Mechanical modelling of sand considering simple shear condition and its application to pile foundation. Phd thesis,.

Wynn, T.M., Henderson, M.B., and Vaughan, D.H. 2008. Changes in streambank

erodibility and critical shear stress due to subaerial processes along a headwater stream, southwestern Virginia, USA. Geomorphology, **97**(3–4): 260–273. Elsevier.

Xie, X.C., Ceccato, F., Zhou, M.L., and Zhang, D.M. 2022. Hydro-mechanical behaviour of soils during water-soil gushing in shield tunnels using MPM. Computers and Geotechnics, **145**(February): 104688. Elsevier Ltd. doi:10.1016/j.compgeo.2022.104688.

Xie, Z., Wang, S., and Shen, Y. 2023. Roles of clusters in the migration of fines through porous media. Chemical Engineering Science, **265**. doi:10.1016/j.ces.2022.118217.

Xiong, H., Wu, H., Bao, X., and Fei, J. 2021. Investigating effect of particle shape on suffusion by CFD-DEM modeling. Construction and Building Materials, **289**: 123043. doi:10.1016/j.conbuildmat.2021.123043.

Xiong, H., Yin, Z.Y., Zhao, J., and Yang, Y. 2020. Investigating the effect of flow direction on suffusion and its impacts on gap-graded granular soils. Acta Geotechnica, **16(2)**: 399–419. Springer Berlin Heidelberg. doi:10.1007/s11440-020-01012-9.

Xiong, H., Zhang, Z., Sun, X., Yin, Z. yu, and Chen, X. 2022. Clogging effect of fines in seepage erosion by using CFD–DEM. Computers and Geotechnics, **152**: 105013. Elsevier Ltd. doi:10.1016/j.compgeo.2022.105013.

Xiong, H., Zhang, Z., Yin, Z.Y., Chen, X., and Zhou, W. 2024. Microscopic origins of shape effects on migration and clogging of fines in porous media using

coupled CFD-iDEM. Acta Geotechnica, **19**(8): 5001–5029. Springer Berlin Heidelberg. doi:10.1007/s11440-024-02281-4.

Xu, J., Wang, F., and Abegaz, R. 2025. State of the Art of CFD-DEM Coupled Modeling and Its Application in Turbulent Flow-Induced Soil Erosion. Geosciences, **15**(1): 21. MDPI.

Xu, W.J., and Dong, X.Y. 2021. Simulation and verification of landslide tsunamis using a 3D SPH-DEM coupling method. Computers and Geotechnics, **129**(November 2020): 103803. Elsevier. doi:10.1016/j.compgeo.2020.103803.

Yang, D., Liu, L., and Ji, S. 2023. Numerical analysis of interaction between sea ice and propeller based on coupled DEM-FEM model. Ocean Engineering, **268**(October 2022): 113469. Elsevier Ltd. doi:10.1016/j.oceaneng.2022.113469.

Yang, G.C., Jing, L., Kwok, C.Y., and Sobral, Y.D. 2021. Size effects in underwater granular collapses: Experiments and coupled lattice Boltzmann and discrete element method simulations. Physical Review Fluids, **6**(11): 114302. APS.

Yang, J. 2019. Analyses numériques de la problématique multi-physique des fontis au voisinage d'une digue ou d'un ouvrage linéaire. Ecole centrale de Nantes.

Yang, J., Yin, Z.Y., Hicher, P.Y., and Laouafa, F. 2017. A Finite Element Modeling of the Impact of Internal Erosion on the Stability of a Dike. *In* Poromechanics 2017 - Proceedings of the 6th Biot Conference on Poromechanics. pp. 354–361.

Yang, J., Yin, Z.Y., Laouafa, F., and Hicher, P.Y. 2020a. Three-dimensional hydromechanical modeling of internal erosion in dike-on-foundation. International Journal for Numerical and Analytical Methods in Geomechanics,

44(8): 1200–1218. doi:10.1002/nag.3057.

Yang, J., Yin, Z.Y., Laouafa, F., and Hicher, P.Y. 2020b. Hydromechanical modeling of granular soils considering internal erosion. Canadian Geotechnical Journal, **57**(2): 157–172. doi:10.1139/cgj-2018-0653.

Yang, J., Yin, Z.Y., Laouafa, F., and Hicher, P.Y. 2022. Numerical analysis of internal erosion impact on underground structures: Application to tunnel leakage. Geomechanics for Energy and the Environment, **31**: 100378. Elsevier Ltd. doi:10.1016/j.gete.2022.100378.

Yang, Z.X., Li, X.S., and Yang, J. 2008. Quantifying and modelling fabric anisotropy of granular soils. Géotechnique, **58**(4): 237–248. Thomas Telford Ltd.

Yao, L.M., Xiao, Z.M., Liu, J.B., and Zhang, Q. 2021. A new multi-field coupled dynamic analysis method for fracturing pipes. Journal of Petroleum Science and Engineering, **196**(June 2020): 108023. Elsevier B.V. doi:10.1016/j.petrol.2020.108023.

Ye, Z., and Liu, H. 2020. Modeling the Effects of Internal Erosion on the Structural Damage of a Shield Tunnel. International Journal of Geomechanics, **20**(6): 04020053. doi:10.1061/(asce)gm.1943-5622.0001691.

Ye, Z., and Liu, H. 2021. Investigating the relationship between erosion-induced structural damage and lining displacement parameters in shield tunnelling. Computers and Geotechnics, **133**(December 2020): 104041. Elsevier Ltd. doi:10.1016/j.compgeo.2021.104041.

Yerro, A., Rohe, A., and Soga, K. 2017. Modelling internal erosion with the material

point method. Procedia engineering, **175**: 365–372. Elsevier.

Yin, Z.-Y., Wu, Z.-X., and Hicher, P.-Y. 2018. Modeling Monotonic and Cyclic Behavior of Granular Materials by Exponential Constitutive Function. Journal of Engineering Mechanics, **144**(4): 1–13. doi:10.1061/(asce)em.1943-7889.0001437.

Yin, Z.-Y., Yang, J., Laouafa, F., and Hicher, P.-Y. 2020a. A framework for coupled hydro-mechanical continuous modelling of gap-graded granular soils subjected to suffusion. European Journal of Environmental and Civil Engineering,: 1–22. Taylor & Francis.

Yin, Z.-Y., Zhao, J., and Hicher, P.-Y. 2014. A micromechanics-based model for sand-silt mixtures. International journal of solids and structures, **51**(6): 1350–1363. Elsevier.

Yin, Z.Y., Chang, C.S., and Hicher, P.Y. 2010. Micromechanical modelling for effect of inherent anisotropy on cyclic behaviour of sand. International Journal of Solids and Structures, **47(14**–**15)**: 1933–1951. doi:10.1016/j.ijsolstr.2010.03.028.

Yin, Z.Y., Huang, H.W., and Hicher, P.Y. 2016a. Elastoplastic modeling of sand–silt mixtures. Soils and Foundations, **56(3)**: 520–532. doi:10.1016/j.sandf.2016.04.017.

Yin, Z.Y., Huang, H.W., and Hicher, P.Y. 2016b. Elastoplastic modeling of sand–silt mixtures. Soils and Foundations,. doi:10.1016/j.sandf.2016.04.017.

Yin, Z.Y., Wang, P., and Zhang, F. 2020b. Effect of particle shape on the progressive failure of shield tunnel face in granular soils by coupled FDM-DEM method.

Tunnelling and Underground Space Technology, **100**: 103394. Elsevier. doi:10.1016/j.tust.2020.103394.

Yio, M.H.N., Wong, H.S., and Buenfeld, N.R. 2017. Representative elementary volume (REV) of cementitious materials from three-dimensional pore structure analysis. Cement and Concrete Research, **102**(September): 187–202. Elsevier. doi:10.1016/j.cemconres.2017.09.012.

Yoo, C. 2017. Effect of water leakage in tunnel lining on structural performance of lining in subsea tunnels. Marine Georesources & Geotechnology, **35**(3): 305–317. Taylor & Francis.

Yu, R., Dong, X., Li, Z., and Fan, M. 2023. A coupled SPH–DEM model for erosion process of solid surface by abrasive water-jet impact. Computational Particle Mechanics, **10**(5): 1093–1112. Springer.

Yu, R., Hao, G., Yang, W., and Li, Z. 2024. An unresolved SPH-DEM model for simulation of ductile and brittle surface erosion by abrasive water-jet (AWJ) impact. Scientific Reports, **14**(1): 26115. Nature Publishing Group UK London.

Zeng, R., Wang, S., Zhang, Y., and Qu, T. 2025. CFD-DEM modeling of seepage in foam-conditioned soil. Computers and Geotechnics, **177**: 106818. Elsevier.

Zhang, D., Xie, X., Zhou, M., and Huang, Z. 2021. An incident of water and soil gushing in a metro tunnel due to high water pressure in sandy silt. Engineering Failure Analysis, **121**(September 2020): 105196. Elsevier Ltd. doi:10.1016/j.engfailanal.2020.105196.

Zhang, D.M., Gao, C.P., and Yin, Z.Y. 2019. CFD-DEM modeling of seepage erosion

around shield tunnels. Tunnelling and Underground Space Technology, **83**(February 2017): 60–72. Elsevier. doi:10.1016/j.tust.2018.09.017.

Zhang, D.M., Huang, Z.K., Yin, Z.Y., Ran, L.Z., and Huang, H.W. 2017. Predicting the grouting effect on leakage-induced tunnels and ground response in saturated soils. Tunnelling and Underground Space Technology, **65**: 76–90. Elsevier Ltd. doi:10.1016/j.tust.2017.02.005.

Zhang, D.M., Ma, L.X., Zhang, J., Hicher, P.Y., and Juang, C.H. 2015. Ground and tunnel responses induced by partial leakage in saturated clay with anisotropic permeability. Engineering Geology, **189**: 104–115. Elsevier.

Zhang, F., Wang, T., Liu, F., Peng, M., Furtney, J., and Zhang, L. 2020. Modeling of fluid-particle interaction by coupling the discrete element method with a dynamic fluid mesh: Implications to suffusion in gap-graded soils. Computers and Geotechnics, **124**(January): 103617. Elsevier. doi:10.1016/j.compgeo.2020.103617.

Zhang, P., and Yin, Z.-Y. 2021. A novel deep learning-based modelling strategy from image of particles to mechanical properties for granular materials with CNN and BiLSTM. Computer Methods in Applied Mechanics and Engineering, **382**: 113858. Elsevier.

Zhang, Z., Mao, M., Pan, Y., Zhang, M., Ma, S., Cheng, Z., and Wu, Z. 2022. Experimental study for joint leakage process of tunnel lining and particle flow numerical simulation. Engineering Failure Analysis, **138**(March): 106348. Elsevier Ltd. doi:10.1016/j.engfailanal.2022.106348.

Zheng, G., Cui, T., Cheng, X., Diao, Y., Zhang, T., Sun, J., and Ge, L. 2017a. Study of the collapse mechanism of shield tunnels due to the failure of segments in sandy ground. Engineering Failure Analysis, **79**(November 2016): 464–490. Elsevier. doi:10.1016/j.engfailanal.2017.04.030.

Zheng, Z., Zang, M., Chen, S., and Zhao, C. 2017b. An improved 3D DEM-FEM contact detection algorithm for the interaction simulations between particles and structures. Powder Technology, **305**: 308–322. Elsevier B.V. doi:10.1016/j.powtec.2016.09.076.

Zhou, C., Qian, J.G., and Yin, Z.Y. 2022. Microscopic investigation of the influence of complex stress states on internal erosion and its impacts on critical hydraulic gradients. International Journal for Numerical and Analytical Methods in Geomechanics, **46**(18): 3377–3401. doi:10.1002/nag.3454.